Ron DeSantis, *Governor*

Kevin Guthrie, *Executive Director*

HURRICANE LOSS MITIGATION PROGRAM 2025 ANNUAL REPORT

January 1, 2026

Prepared by
Florida Division of Emergency Management

DIVISION HEADQUARTERS
2555 Shumard Oak Boulevard
Tallahassee, FL 32399-2100

Telephone: 850-815-4000
www.FloridaDisaster.org

STATE LOGISTICS RESPONSE CENTER
2702 Directors Row
Orlando, FL 32809-5631

Contents

EXECUTIVE SUMMARY

Pursuant to section 215.559(6), Florida Statutes, this document provides a full report and accounting of activities and evaluation of such activities conducted by the Hurricane Loss Mitigation Program (HLMP). The period covered by this report is July 1, 2024, through June 30, 2025, or State Fiscal Year (FY) 2025. Section 215.559, Florida Statutes, establishes the Hurricane Loss Mitigation Program in the Florida Division of Emergency Management (FDEM). FDEM receives an annual appropriation of $10 million from the investment income of the Florida Hurricane Catastrophe Fund, authorized under the Florida General Appropriation Act and section 215.555(7)(c), Florida Statutes. The Shelter Development Program, Gulf Coast State College's (GCSC) Mobile Home Tie-Down Program, and Florida International University's (FIU) Hurricane Research Program account for a combined $6.5 million, or sixty-five (65%) percent of the $10 million appropriation. The remaining thirty-five (35%) percent is distributed as a community mitigation grant that includes flood and wind mitigation of Florida residences and public outreach and education about retrofits to citizens, local government officials, and their staff.

The Shelter Development Program and GCSC's Mobile Home Tie-Down Program have separate reporting requirements under section 252.385(3)(a), Florida Statutes, and section 215.559(2)(b)4., Florida Statutes, respectively. This report includes a project analysis of the Shelter Development Program, an annual report for the GCSC Mobile Home Tie-Down Program, a detailed summary of FIU's Hurricane Research Program progress, and a programmatic analysis of the Hurricane Loss Mitigation Program.

BACKGROUND

In the aftermath of Hurricane Andrew, the Florida Legislature created a series of programs to stabilize the economy and insurance industry. These programs consist of the following:

- Citizens Property Insurance Corporation (formed from a merger of the Florida Windstorm Underwriting Association and the Florida Residential Property and Casualty Joint Underwriting Association), the state insurance plan for residents unable to obtain a conventional homeowner's insurance policy;
- The Florida Hurricane Catastrophe Fund, section 215.555 Florida Statutes, a re-insurance fund established to limit insurance exposure after a storm; and
- The Bill Williams Residential Safety and Preparedness Act, which in 1999 created the Hurricane Loss Mitigation Program, section 215.559, Florida Statutes, with an annual appropriation of $10 million.

Section 215.559, Florida Statutes, establishes the Hurricane Loss Mitigation Program in the Florida Division of Emergency Management (FDEM). FDEM receives an annual appropriation of $10 million from the investment income of the Florida Hurricane Catastrophe Fund authorized under the Florida General Appropriation Act and section 215.555(7)(c), Florida Statutes. The annual appropriation provides funding to local governments, state agencies, public and private educational institutions, and non-profit organizations to support programs improving hurricane preparedness, reducing potential losses in the event of a hurricane, and providing research and education to reduce hurricane losses.

Specific Program Areas and Funding Levels

Shelter Development – Pursuant to section 215.559(1)(b), Florida Statutes, $3 million of the annual $10 million appropriation for the Hurricane Loss Mitigation Program directs retrofits to existing facilities and construction of new facilities to enable them for use as public shelters. A report of the state's shelter development program, entitled the Shelter Development Report, is prepared annually and separately submitted to the Governor and the Legislature pursuant to section 252.385(3)(a), Florida Statutes. The remaining $7 million of the appropriation is allocated according to different subsections in section 215.559, Florida Statutes, as described below.

Gulf Coast State College – Pursuant to section 215.559(2)(a), Florida Statutes, GCSC receives an annual allocation of $2.8 million, or forty (40%) percent of the remaining $7 million. GCSC administers these funds and uses them to mitigate future losses for mobile homes and to provide tie-downs for mobile homes in communities throughout Florida. See Appendix A for GCSC'S FY 2025 Annual Report.

Florida International University (FIU) – Pursuant to section 215.559(3), Florida Statutes, FIU receives $700,000, or ten (10%) percent, of the remaining $7 million. FIU administers these funds and dedicates them to hurricane research at the Type I Center of the State University System to support hurricane loss reduction devices and techniques. See Appendix B for FIU's FY 2025 Final Report.

Hurricane Loss Mitigation Program (HLMP) – The remaining $3.5 million provides grant funding to governmental entities, non-profit organizations, and qualified for-profit organizations as a means to improve the resiliency of residential, community, and government structures within their communities. HLMP advertises funding through a Request for Proposals (RFP), which utilizes a Benefit-Cost Analysis (BCA) for each of the submitted projects to ensure that the recommended mitigation retrofits remain cost-effective.

HURRICANE LOSS MITIGATION PROGRAM

The next sections will discuss program activities, analysis, goals, and recommendations for HLMP.

PROGRAM ACTIVITIES

HLMP Funding Distribution

In June 2024, FDEM issued a Call for Applications for Fiscal Year (FY) 2024-2025 projects. This application deadline was July 17, 2024. A review panel appointed by FDEM selected eligible applicants based on priority, need, benefit, available funding, and alignment with local mitigation strategy projects. FDEM received 55 applications. Based on the evaluation process, 14 projects became eligible for funding.

HLMP Outreach

In early 2024, FDEM issued a Call for Applications via FDEM Mitigation's GovDelivery Subscription service and posted the documents on the FDEM HLMP website.

The Program Manager of HLMP attended the 2025 Wall of Wind Challenge at FIU. This event is a judged competition for students to present strategies demonstrating mitigation concepts against hurricane force winds. The HLMP team also attended FIU's 2025 Eye of the Storm event, which is a community outreach event focused on presenting hurricane education, mitigation, and preparedness to the public.

Public Outreach efforts also continued throughout the year utilizing the FloridaDisaster.org website and FDEM Mitigation GovDelivery emails. This site provides potential recipients with the information and forms required to apply for the HLMP program. It also includes an additional hurricane retrofit guide to help citizens make informed decisions on preparing their homes for potentially hazardous weather.

Program Management

FDEM is working toward adopting successful processes that are utilized for the federal grant programs administered by the Mitigation Bureau. HLMP project and grant management training programs are continuously evolving to include the best practices experienced by all programs managed by the Bureau. Additionally, custom Scope of Work templates have been developed for the newly permissible mitigation project types that HLMP manages. These new scopes are Florida-specific, project-specific, and provide explicit instruction on the compliance requirements set forth by the State of Florida, FDEM, and the Bureau of Mitigation.

PROGRAM ANALYSIS

FY 2025 Recipients

Table 1.1 shows the awards and amounts spent to date for FY 2024-2025. All currently active projects are proceeding on schedule and are projected to close with most, if not all, funds spent.

Recipient	Award Amount	Spent to Date	Project Type
DEM-HL00080 City of Fellsmere	$194,000.00	$181,452.27	Public Building Wind Mitigation
DEM-HL00081 Miami Dade County - Community Action and Human Services Department	$194,000.00	$110,619.75	Residential Wind Mitigation
DEM-HL00082 Florida Keys Aqueduct Authority	$194,000.00	$194,000.00	Public Building Wind Mitigation
DEM-HL00083 City of Arcadia	$100,000.00	$32,356.77	Public Building Wind Mitigation
DEM-HL00084 City of Homestead	$194,000.00	$0.00	Public Building Wind Mitigation
DEM-HL00085 City of Lauderdale Lakes	$194,000.00	$139,274.00	Residential Wind Mitigation
DEM-HL00086 Flagler County Board of County Commissioners	$194,000.00	$193,904.27	Residential Wind Mitigation
DEM-HL00087 City of Atlantic Beach	$194,000.00	$194,000.00	Public Building Wind Mitigation
DEM-HL00088 Vizcaya Museum and Gardens	$194,000.00	$150,044.00	Public Building Wind Mitigation
DEM-HL00089 St. Lucie County Board of County Commissioners	$194,000.00	$12,150.36	Residential Wind Mitigation
DEM-HL00090 City of Bradenton	$194,000.00	$7,059.71	Residential Wind Mitigation
DEM-HL00091 Hernando County Fire and Emergency Program	$194,000.00	$173,098.00	Public Building Wind Mitigation
DEM-HL00092 City of Carrabelle	$194,000.00	$194,000.00	Residential Wind Mitigation
DEM-HL00093 Desoto County Board of County Commissioners	$194,000.00	$192,379.28	Public Building Wind Mitigation
DEM-HL00094 Centro Campesino Farmworker Center	$194,000.00	$194,000.00	Residential Wind Mitigation
Total	**$2,816,000.00**	**$1,968,338.41**	

Closed Projects

Table 1.2 shows all completed projects during FY 2024-2025, which had over $1.3 million spent retrofitting residential and public properties.

Closed Project	Award Amount	Amount Spent	Project Type
DEM-HL00066, Miami Dade CAHSD	$194,000.00	$194,000.00	Residential Wind Mitigation
DEM-HL00082, Florida Keys Aqueduct Authority	$194,000.00	$194,000.00	Public Building Wind Mitigation
DEM-HL00086, Flagler County BOCC	$194,000.00	$194,000.00	Residential Wind Mitigation
DEM-HL00087, City of Atlantic Beach	$194,000.00	$194,000.00	Public Building Wind Mitigation
DEM-HL00092, City of Carrabelle	$194,000.00	$194,000.00	Residential Wind Mitigation
DEM-HL00093, DeSoto County BOCC	$192,379.28	$192,379.28	Public Building Wind Mitigation
DEM-HL00094, Centro Campesino	$194,000.00	$194,000.00	Residential Wind Mitigation
Total	**$1,356,379.28**	**$1,356,379.28**	

FY 2026 New Projects

Table 1.3 shows all the approved HLMP projects for FY 2025-2026, which include both residential and non-residential wind mitigation projects.

Recipient	Award Amount	Project Type
DEM-HL00111, City of Dunedin	$250,000.00	Public Building Wind Mitigation
DEM-HL00112, City of Edgewater	$230,000.00	Public Building Wind Mitigation
DEM-HL00113 Flagler County BOCC	$250,000.00	Residential Wind Mitigation
DEM-HL00114, Fort Pierce Utility Authority	$250,000.00	Public Building Wind Mitigation
DEM-HL00115, Sarasota County	$250,000.00	Public Building Wind Mitigation
DEM-HL00116, Town of Ocean Ridge	$250,000.00	Public Building Wind Mitigation
DEM-HL00117, Village of Wellington	$224,920.00	Public Building Wind Mitigation
DEM-HL00118, City of Cooper City	$160,000.00	Public Building Wind Mitigation
DEM-HL00119, City of Homestead	$125,000.00	Public Building Wind Mitigation
DEM-HL00120, Town of Hypoluxo	$109,428.00	Public Building Wind Mitigation
DEM-HL00121, St. Lucie County	$250,000.00	Residential Wind Mitigation
DEM-HL00122, City of Bradenton	$250,000.00	Residential Wind Mitigation
DEM-HL00123, Eckerd College	$250,000.00	Public Building Wind Mitigation
Total	**$2,849,348.00**	

PROGRAM GOALS AND RECOMMENDATIONS

FDEM is committed to developing programs to educate the public on ways to reduce the impact of a disaster. Work must continue with Florida homeowners, local governments, non-profit organizations, and state agencies to reduce the risk of hurricane losses. Research must continue to develop stronger wind mitigation measures to protect the residents of Florida and increase structural survivability for residences. Additionally, more communities will have an opportunity to participate in the grant program through a comprehensive outreach program.

FDEM has the following goals for the Hurricane Loss Mitigation Program:

- Continue refining grant management activities in the Division of Emergency Management Enterprise System (DEMES) for better reporting and process improvement
- Where possible, leverage HLMP funds with other funds from federal, state, local government, or private sources
- Implement new programmatic changes to combat recognized challenges of the increase of material costs and short project timeline, as well as incorporate additional types of eligible projects
- Partner with FDEM Recovery and Mitigation Regional Coordinators to enhance HLMP outreach efforts

Observations

Grant recipients and contractors are continually under a confined time constraint for awarding and expending the appropriated funds within one fiscal year. Project solicitation, awarding, contracting, sub-contracting, construction, and project closeout must be completed by the end of each fiscal year. This condensed timeframe does not allow FDEM or its participants sufficient time to take full advantage of the funding provided.

Recommendations

Extend the funding and budget authority for the annual appropriation for up to three years. This would allow the contracts to start upon full execution and have a period of performance that would expire at the end of the second fiscal year.

SHELTER DEVELOPMENT PROGRAM

The next sections will discuss program activities, analysis, goals, and recommendations for the Shelter Development Program.

PROGRAM ACTIVITIES

Shelter Development Funding

In 2017, the Hurricane Loss Mitigation Program began managing the grant and contracting responsibilities of the Shelter Survey and Retrofit Program. In 2022, the program changed to the Shelter Development Program to encompass both the retrofitting of existing structures and the construction of new structures to be used as shelters. HLMP applies proven grant management processes to existing and new projects under the Shelter Development Program. With its resources available, the Mitigation Bureau's Finance Unit has been able to streamline processes for tracking shelter payments, contracting, and reporting.

HLMP staff also works with the Mitigation Bureau's Technical Unit to verify the work completed under the Shelter Development Program. Modernized Scopes of Work have been finalized with the collaboration of the Shelter Development Program, Technical Unit, and HLMP. New review processes and detailed requirements within the Scope of Work will strengthen regulation and monitoring while providing the recipient with a clearer understanding of their goals and objectives.

PROGRAM ANALYSIS

Executed Projects

Table 2.1 displays the shelter development agreements executed in FY 2024-2025, totaling $606,160.00.

Recipient	Award Amount
DEM-SD00042 Baker County, Division of Emergency Management	$606,160.00
TOTAL	**$606,160.00**

Closed Projects

Table 2.2 below summarizes the two projects closed during FY 2024-2025, totaling $215,000.00.

Recipient	Award Amount
DEM-SR00032, Alachua County BOCC	$200,000.00
DEM-SR00041, St Johns County School District (withdrawn)	$15,000.00
TOTAL	**$215,000.00**

Active Projects

Table 2.3 shows all twelve projects active at the end of FY 2025. The projects are divided into four major categories, including Engineering Study, Genset, Retrofit, and New Construction. An Engineering Study determines the viability of a building for retrofitting. A Genset project installs the necessary electrical components to connect a generator to a building. Retrofit projects focus on hardening the envelope of a building. New Construction projects provide envelope fenestration protection during the construction of a designated building.

Recipient	Projects	Project Type	# of Locations
HLMPSR17-020 A Multi Clay County BOCC	Orange Park High School	Engineering Study	5
	Asbury Lake Jr High School	Genset	
	Oakleaf High School	Retrofit	
	Fleming Island High School	Retrofit	
	Keystone Heights High School	Retrofit	
DEM-SR00001 Seminole County BOCC	Winter Springs High School	Retrofit	4
	Teague Middle School	Genset	
	Teague Middle School	Retrofit	
	Lawton Chiles Middle School	Genset	
	Lawton Chiles Middle School	Retrofit	
	Lyman High School	Genset	
	Lyman High School	Retrofit	
DEM-SR00005 Orange County BOCC	South Econ Rec Gym	Retrofit	3
	West Orange Rec Gym	Retrofit	
	Silver Star Rec Gym	Retrofit	
DEM-SR00018 Sarasota School Board	Taylor Ranch Elementary	Retrofit	3
	Gulf Gate Elementary	Retrofit	
	North Port High School	Retrofit	
DEM-SR00020 Lake School Board	East Ridge High School	Retrofit	13
	Eustis Middle School	Retrofit	
	Mt. Dora High School	Retrofit	
	Leesburg High School	Retrofit	
	Tavares High School	Retrofit	
	Umatilla High School	Retrofit	
	Eustis High School	Retrofit	
	Astatula Elementary School	Retrofit	
	Villages Elementary School	Retrofit	
	Lost Lake Elementary School	Retrofit	
	Leesburg Elementary School	Genset	
	Umatilla Elementary School	Genset	
	East Ridge Middle School	Genset	
DEM-SR00021 DeSoto School District	West Elementary School	Retrofit	2
	Nocatee Elementary School	Retrofit	
DEM-SR00030 The School Board of Polk County	Ben Hill Griffin JR Elementary School	Retrofit	3
	Frostproof Middle Senior School	Retrofit	
	Ft Meade Middle-Senior High School	Retrofit	
DEM-SR00037 Gadsden Board of County Commissioners	Gadsden County Community Hospital	Retrofit	1
	Gadsden County Community Hospital	Genset	
DEM-SR00038 Jefferson County School District	Jefferson County K-12 School	Retrofit	1
DEM-SR00039 School District of Indian River County	Treasure Coast Elementary School	Retrofit	1
DEM-SD00040 Sarasota County Schools	Sarasota Lorraine K-8 School	New Construction	1
DEM-SD00042 Baker County, Division of Emergency Management	MacClenny Primary School	Retrofit	1

PROGRAM GOALS AND RECOMMENDATIONS

Under the guidance of HLMP, the Shelter Development Program has grown in scope and efficiency. By collaborating with the FDEM's Infrastructure Section, the Program continues to eradicate shelter deficits throughout the state. From better reporting to improved funding accountability, the Program looks forward to providing greater resiliency and preparedness for future disasters throughout the state.

FDEM has the following goals to accomplish in the next Fiscal Year:

- Meet the Legislature's goal to eliminate the deficit of safe public hurricane evacuation shelter space in all regions of the state.
- Develop standards of cost-effectiveness towards new construction.
- Continue refining grant management activities in DEMES for better reporting and process improvement.
- Maintain a strong relationship between the Infrastructure staff and Mitigation staff.
- Coordinate with the Mitigation Technical Unit to increase integration within the Program.

Appendix A: FY 2024-2025 Annual Report for Mobile Tie-Down Program

2024-2025 ANNUAL REPORT
GULF COAST STATE COLLEGE
MOBILE HOME TIE-DOWN PROGRAM

Florida Statute (F.S.) 215.559 which governs the Hurricane Loss Mitigation Program and the Mobile Home Tie-down Program funding, awarded the project oversight to Gulf Coast State College (GCSC) effective July 1, 2022. The program is annually awarded two million eight-hundred thousand ($2,800,000) to inspect and improve tie-down anchoring on manufactured and mobile homes. The FY 2024-25 award funding was fully utilized.

Program Highlights:

- Demand for tie-down inspection and installation services remains high, and vendors continued to work through assignments as funding allowed. The program continues to serve mobile and manufactured homes installed 1999 and earlier, both with removable and non-removable type skirting.
- GCSC maintains regular communication with the MHTDP Advisory Council which includes DEM, Florida Highway Safety and Motor Vehicles, Manufactured Housing Division (FHSMV), Federation of Manufactured Home Owners of Florida (FMO), and Florida Manufactured Housing Association (FMHA).
- The 2024-25 Request for Proposals for vendor installation contracts (RFP#1 2024/25) was published April 10th, 2024; Proposals were due May 21st, and RFP Award Recommendations for Storm Ready Services and Top Notch Mobile Home Services was posted June 7th, and approved by the GCSC District Board of Trustees June 27th, 2024.
- FHSMV completed random inspections of a minimum of 10% of the homes for the Parks component. This inspection verifies the items as invoiced installed by the vendor according to 15C-1 and the manufacturer's specifications.
- The use of Quality Assurance Inspectors continued for the Individual component (FHSMV post-inspects parks). An additional support contract for post-installation quality assurance inspections for Individual Application homes was issued to HAS Inspections.
- At the end of the June 30 contract date, there was a small amount of contracted services funding remaining, and GCSC requested a budget amendment to move the remaining $2,370 to project administration for salary costs. This required a No Cost Extension (NCE) through December 2025, and the grant was fully utilized August 2025.

Final Numbers:

During FY 2024-25, Storm Ready Services continued assignments in partially completed parks from FY 2023-24 which did not require additional community meetings. Top Notch Mobile Home Services held three (3) community information meetings. The following deliverables were completed during this process:

- Community information sessions explaining program and answering homeowner questions.
- Intake training for the homeowners' association representatives.
- Visual inspections of all homes within the community.
- Collection of homeowner authorization forms.

These meetings were conducted with homeowner's association board members, park managers, FMO volunteers, and residents of each community. Form collection continued after community information meetings with the assistance of park representatives.

Gulf Coast State College installation vendors completed a total of seven hundred sixty-four (764) homes between parks and individual applications. The program was successfully completed in five (5) manufactured home communities, and three (3) partial parks, with work to be completed in FY 2025-26. Larger park progress and invoicing has been split into multiple parts, however FHSMV completed required post-installation inspections (minimum of 10%) upon each invoice/completion point.

Sixty-one (61) individual homes were also completed, in twenty-six (26) counties. HAS Inspections completed quality assurance post-installation inspections on a minimum of 10% of Individual homes completed by both vendors, in order to ensure tie-down improvements met FAC 15C-1 requirements. In total, twenty-eight (28) counties received program services.

The program historically averages 30% of the total number of park homes receive services due to number of homeowner sign-ups and eligibility of homes post-inspection. However, for FY 2024-25 we saw an average of 41% of homes received services in completed parks. One park had a completion rate of 68%. While large parks require multiple visits before completion, vendors met a higher average rate of park percentage completion this year.

In total, two million eight hundred thousand dollars ($2,800,000.00) was utilized of the FY 2024-25 DEM-HL00095 grant, or 100% grant utilization.

Parks Completed FY 2024-25 (Total Served vs Total Park Size)	**Address**	**City**	**County**	**# Homes Served**
Terra Mar Village Part 3, Final (93 of 318 total served)	109 Indian River Dr. N	Edgewater	Volusia	17
Lake Juliana Landings Part 3, Final (137 of 270 total served)	166 Juliana Blvd	Auburndale	Polk	58
Saddle Oak Part 4, Final (255 of 376 total served)	6045 SW 55th Ct	Ocala	Marion	143
Rolling Greens Village Part 4 (167 of 850 served so far)	1901 SE 58th Ave	Ocala	Marion	48
High Point Part 4 (443 of 1660 served so far)	8008 Baltic St	Brooksville	Hernando	126

Tidewater (53 of 125 served)	1701 NW 5th St	Deerfield	Broward	53
Orangebrook Harbor (89 of 247 served)	3318 Orange St	Hollywood	Broward	89
Sea Meadow Part 1 (169 of 445 served so far)	4290 Royal Manor Blvd	Boynton Beach	Palm Beach	169
Individuals (addresses vary), 26 Counties Served				61
Total Homes Served FY 2024-25 (28 Counties Total)				**764**

Moving Forward:

- RFP#1 2024/25 allows for contract renewals up to two (2) additional years. Both vendors wish to renew; SRS at the same rate, TN with an allowable 2.8% Cost of Business price adjustment increase. Recommendation was approved by the GCSC District Board of Trustees June 2025 pending the 2025-26 FDEM grant award execution.
- Several parks on the service and waiting lists have 800-1,600 homes. It can take multiple years to allow all interested homeowners the opportunity to be served in these large parks due to grant period and available funding.
- Vendors will continue to work through the park service list, with additional assignments pending funding availability.
- The park waiting list continues to grow, with one hundred fifty-nine (159) Park applications currently waiting for program services (including parks still in progress). There are also sixty-five (65) Individual applications pending services.
- Due to the size of the waiting list, the program is not returning to previously served parks at this time.

Please refer any questions relating to this report or the Program in general to:

Jennifer Shaw
Program Manager, MHTDP
Gulf Coast State College
jshaw6@gulfcoast.edu
488-201-6882

Appendix B:
FY 2024-2025 Annual Report for Florida International University

A Resource for the State of Florida

HURRICANE LOSS REDUCTION FOR HOUSING IN FLORIDA

FINAL REPORT
For the Period July 1, 2024 to June 30, 2025

A Research Project Funded by:
The State of Florida Division of Emergency Management
Through Contract #DEM-HL00096

Prepared by
The International Hurricane Research Center (IHRC)
Florida International University (FIU)

July 31, 2025

Final Report

Table of Contents

Section 1
Executive Summary

Four major research efforts were identified by the International Hurricane Research Center (IHRC) for the Hurricane Loss Mitigation Program (HLMP) Fiscal Year 2024-25. Funding was dedicated to areas of wind effects on photovoltaic (PV) systems, manufactured housing structural mitigation analysis, wind loads on irregular-shaped buildings, and education and outreach. In keeping with the comprehensive agenda of the research topics for this project, the IHRC organized a multidisciplinary team of researchers, students and support staff to complete the stated objectives. The following is a summary of research findings:

Research Area 1: Study of Wind Effects on Elevated Photovoltaic (PV) Systems – Solar Canopies (PIs Chowdhury and Elawady)

Elevated photovoltaic (PV) support structures and canopies, such as solar carports, have grown in popularity, and their U.S. market size is projected to increase from USD 112.60 million in 2024 to USD 291.40 million by 2034. As their use expands, it becomes increasingly important to ensure these structures can withstand extreme wind events and maintain safety standards. This study investigated the aerodynamic performance of elevated PV support structures (solar carports) under simulated wind flows, utilizing large-scale wind tunnel experiments conducted at the Wall of Wind Experimental Facility (WOW EF) at Florida International University (FIU). This research focused on understanding the wind loading effects on both single row and multiple row configurations, reflecting typical arrangement of elevated PV support structures. A total of 39 test cases were analyzed, with pressure taps installed on top and bottom surfaces of the PV panels to measure wind-induced pressures. These instrumented PV panels represent the most critical zones of the PV support structure according to ASCE 7-22. The key findings reveal that for an isolated, single-row solar carport, the most critical wind-induced negative pressures (suction) consistently occur at the windward edges and corners, with the intensity of this suction increasing at steeper tilt angles (e.g., 7° vs. 5° or 3°) due to more dominant airflow separation. While the presence of parked vehicles underneath the structures introduced localized pressure variations, it did not significantly alter the overall mean wind loads on the carport. The introduction of an upwind row reduced the negative pressure on the leading edge of the subsequent (downwind) row. This shielding was also observed in a three-row configuration. Conversely, the presence of a downwind-only row had a negligible impact on the wind loads of the structure in front of it. Data from these wind tunnel tests can inform the ASCE 7-22 standard wind load provisions and the current industry practice, ensuring these structures are better designed to handle hurricanes and other severe weather challenges.

Research Area 2 Part A: Manufactured Home Research (Sutley)

This report presents the research outcomes from Phase IV of the project carried out at the University of Kansas (KU), which consisted of the following three tasks: 1) Perform additional component and connection testing to gain necessary statistics for informing fragility functions and FEM; 2) Continue building collaborations with federal agencies and manufactured housing

industry to endorse testing full-scale manufactured homes; 3) Collaborate with partner institutions, FIU and UA, on their research tasks.

Task 1 executed full-scale connection tests of roof sheathing-to-rafter and roof-to-wall connections commonly found in Wind Zone II and Wind Zone III manufactured homes. The Phase IV testing focused on (a) completing endwall connection tests for roof to wall connections; (b) increasing the number of roof sheathing to rafter specimens tested for each unique connection design from past phases with attention to using a consistent cyclic protocol across a sufficient minimum number of specimens; and (c) investigating and designing enhanced connections in anticipation for Phase V. During Phases I and II the cyclic protocol was still being refined for what would work best for the finite element model. Phase IV focused on completing connection tests using the final cyclic protocol, which required additional tests for roof sheathing to rafter connections, ensuring a minimum number of tests had been done for all connections and designs. Task 2 strengthened relationships with federal partners, non-government organizations, as well as the broader research community. Task 3 consisted of passing all experimental data to the UA and FIU teams, as well as participating in team calls to collaborate on research design and process decisions. During Phase IV, the KU team submitted one manuscript for journal publication on roof the wall connection tests.

The connection-level experiments further demonstrated that screw connections and connections in stagger pattern perform substantially better and given that calculated capacities are not consistently conservative, calling out these structural details for critical load path connections is appropriate. Testing of remedial measures that enhance performance and full-scale wind tunnel testing of a manufactured housing unit is recommended to validate system level performance and to validate design measures that may improve performance.

Research Area 2B: Manufactured Home Research (Dao)

This research explored the validation of a 3D finite element method (FEM) developed to simulate the structural response of low-rise wood-frame buildings subjected to windstorms generated in a wind tunnel environment. It was determined that general hysteresis model effectively addresses limitations of existing models by automatically fitting experimental data and ensuring consistent behavior across different materials and connection types. The team also utilized FEM to assess the fragility of structural components subjected to wind pressure. Ten simulation cases were run using five randomly generated hysteresis curves for nails, tested across wind speeds ranging from 80 to 145 mph at a 195° wind direction. The analysis focused on identifying conditions that lead to roof openings and uplift failures, with probability distribution Lognormal used to compare FEM data against test results from roof sheathing and roof-to-wall nails. The new nail model offers a reliable tool for high-performance frame-building design, particularly in enhancing resilience against extreme wind events such as hurricanes and tornadoes.

This study represents a significant advancement in the dynamic analysis of lightweight frame structures subjected to turbulent cyclic wind loading. The 3D FEM framework provides a robust foundation for future research and development in the field of performance-based wind design.

The findings contribute to a deeper understanding of structural behavior under cyclic loading and support the development of advanced hysteresis modeling techniques. The newly developed model marks a major step forward in accurately capturing complex structural behaviors under dynamic loads, thereby enhancing the safety, reliability, and resilience of the built environment.

Research Area 3: Torsional Loads on Irregular-Shaped Buildings (PI: Zisis)

This study investigates how building shape and height affect wind pressures and structural forces in low-rise buildings through wind tunnel testing conducted at the WOW EF. Three building configurations, rectangular, L-shaped, and T-shaped, were evaluated at 1- and 3-story heights under simulated open terrain conditions. Pressure taps distributed across the building surfaces captured detailed pressure fields, allowing for the computation of mean ($\bar{C}_p$) and peak ($\hat{C}_p$, $\check{C}_p$) pressure coefficients. These data were integrated to derive directional base force coefficients, including torsional moments (C_T), lateral shear (C_{Sx}, C_{Sy}), and resultant force magnitudes (C_V). The findings show that non-rectangular buildings (L- and T-shaped) experience significantly higher torsional and shear demands than rectangular baselines, with amplification becoming more pronounced at increased heights. Peak suction pressures were notably stronger near inward corners and projections of irregular plans, with pressure coefficients reaching values as low as –4.26, indicating intense suction forces capable of stressing or lifting roof and wall elements. Resultant shear coefficients and torsional moments increased by up to 43% compared to rectangular counterparts, with taller configurations exhibiting more persistent asymmetries and stronger directional peaks under oblique winds. Vertical extension was found to intensify flow separation, pressure differentials, and vortex shedding effects, especially in buildings with asymmetric outlines.

This study offers critical insights for Florida's building codes, particularly regarding low-rise structures in hurricane-prone areas. These findings will enable engineers and architects to design more resilient irregular buildings, ultimately enhancing structural integrity and improving public safety against severe wind events, leading to reduced property damage and more effective disaster preparedness for citizens.

Research Area 4: Education and Outreach Programs to Convey the Benefits of Various Hurricane Loss Mitigation Devises and Techniques (PI: Erik Salna)

The IHRC developed and coordinated education and outreach activities to build on the foundation of previous work under this grant and showcased the hurricane-loss mitigation objectives of the HLMP. For the 2024-25 performance period, the below educational partnerships, community events, and outreach programs were developed:

Wall of Wind Mitigation Challenge (WOW! Challenge): March 20th, 2025
The IHRC implemented the Wall of Wind Mitigation Challenge (WOW! Challenge), a judged competition for South Florida high school students. As the next generation of engineers to address natural hazards and extreme weather, this STEM education event featured a competition between high school teams to develop innovative wind mitigation concepts and real-life human

safety and property protection solutions. The mitigation concepts were tested live at the FIU NSF-NHERI Wall of Wind (WOW) Experimental Facility (EF), located on FIU's Engineering Campus.

- The objective of the 2025 Wall of Wind Mitigation Challenge was for student teams to design a way to reduce the impact of wind scouring on a building's flat roof. Each team's task was to develop a mitigation solution that would improve the flat roof's aerodynamic performance to prevent pea gravel on the roof from being blown away by up-to-hurricane-force winds.
- The flat roof models were wind tested by the NSF-NHERI Wall of Wind experimental research facility at FIU to evaluate their performance.
- The high school teams prepared three components for the competition: a physical test, an oral presentation, and a written technical paper.
- The competition involved teams from nine South Florida high schools, including 135 students and nine teachers.
- *First Place* was awarded to TERRA Environmental Research Institute.
  Second Place was awarded to Florida Christian School.
  Third Place was awarded to South Miami Senior High School.
- A complete scoring summary can be found on the following link: 2025_CHALLENG_FINAL_SCORES.pdf

Media exposure resulted in great positive visibility for the IHRC, FIU and FDEM's message of mitigation:

- 2025 WOW Challenge Highlights Video: https://youtu.be/aGM7zTjtwm0?si=gN0f_W2Ep3T5bbYB
- THE BULLETIN, FDEM Mitigation Bureau, June 2025: Bulletin Volume 15 Issue 2
- CBS4-Miami: https://www.ihrc.fiu.edu/media/latest-media-coverage/cbs4-miami-fiu-wall-of-wind-challenge/

NOAA Hurricane Awareness Tour, Sarasota/Bradenton Airport: May 9th, 2025 (Cancelled)
The entire 2025 Hurricane Hunter Awareness Tour was cancelled.

Eye of the Storm (Science, Mitigation & Preparedness) Event: May 31st, 2025
The Museum of Discovery & Science (MODS), located in Fort Lauderdale, FL, assisted the IHRC in planning, coordinating, and facilitating this free admission public education event that showcased special hands-on, interactive activities and demonstrations teaching hurricane science, mitigation and preparedness.

- 6,105 visitors attended Eye of the Storm, showcasing special interactive activities and demonstrations teaching hurricane science, mitigation and preparedness.
- A Participant Post Survey showed 79.5% of respondents increased their knowledge about wind engineering and mitigating hurricane damage and 89.2% will be taking steps to mitigate hurricane damage.
- Event Flyer: 2025 Eye of the Storm – Hurricane (Science, Mitigation & Preparedness) Free Museum Event, Saturday, May 31st, 10am to 5pm | IHRC Website

Media exposure resulted in great positive visibility in the community for the IHRC, FIU and FDEM's message of mitigation.

- https://wsvn.com/news/local/broward/eye-of-the-storm-event-at-mods-in-fort-lauderdale-aims-to-ensure-floridians-are-hurricane-ready/#google_vignette
- https://www.news4jax.com/news/local/2025/05/31/fdem-hosts-press-conference-urges-floridians-to-make-final-preps-for-hurricane-season/
- https://app.criticalmention.com/app/#clip/view/022a8609-37e0-4245-acc2-5173459dc314?token=0e57270d-1c85-448e-b3ca-0788817604d7

International Hurricane Research Center

FLORIDA INTERNATIONAL UNIVERSITY

A Resource for the State of Florida

SECTION 2:

Study of Wind Effects on Elevated Photovoltaic (PV) – Solar Canopies

Report for the Period 2024-2025

A Research Project Funded by:

Florida Division of Emergency Management

Prepared by:

Arindam Gan Chowdhury, PhD.

Amal Elawady, PhD.

Graduate Students

Yonathan B. Adamu

Houssam Al Sayegh

Omar Metwally

July 31, 2025

Executive Summary

Elevated photovoltaic (PV) support structures, such as solar carports, have grown in popularity, and their U.S. market size is projected to increase from USD 112.60 million in 2024 to USD 291.40 million by 2034. As their use expands, it becomes increasingly important to ensure these structures can withstand extreme wind events and maintain safety standards. This study investigates the aerodynamic performance of elevated PV support structures (solar carports) under simulated wind flows, utilizing large-scale wind tunnel experiments conducted at the Wall of Wind Experimental Facility (WOW EF) at Florida International University (FIU). This research focuses on understanding the wind loading effects on both single row and multiple row configurations, reflecting typical arrangement of elevated PV support structures. A total of 39 test cases were analyzed, with pressure taps installed on top and bottom surfaces of the PV panels to measure wind-induced pressures. These instrumented PV panels represent the most critical zones of the PV support structure according to ASCE 7-22. The key findings reveal that for an isolated, single-row solar carport, the most critical wind-induced negative pressures (suction) consistently occur at the windward edges and corners, with the intensity of this suction increasing at steeper tilt angles (e.g., 7° vs. 5° or 3°) due to more dominant airflow separation. While the presence of parked vehicles underneath the structures introduced localized pressure variations, it did not significantly alter the overall mean wind loads on the carport. The introduction of an upwind row reduced the negative pressure on the leading edge of the subsequent (downwind) row. This shielding was also observed in a three-row configuration. Conversely, the presence of a downwind-only row had a negligible impact on the wind loads of the structure in front of it. Combined with the findings from the upcoming steps detailed in this paper, data from these wind tunnel tests can inform the ASCE 7-22 standard wind load provisions and the current industry practice, ensuring these structures are better designed to handle hurricanes and other severe weather challenges.

1 Introduction

Renewable energy is a critical component of the energy production needs of the State of Florida and the entire U.S. Renewable energy holds great promise because it is plentiful, never runs out, and has a strong capacity to lower carbon emissions (Aly 2021). Solar energy, as a sustainable and environmentally friendly power source, has become a key component in reducing dependence on

fossil fuels. The value of solar power as an eco-friendly energy source was recognized as early as 1911 (Aly 2021). Today, the global shift toward renewable energy has greatly sped up the use of solar panels in homes, businesses, and industries. This rapid expansion has brought increased attention to the design and installation of solar panel systems, which must withstand a variety of environmental forces. Among these forces, wind loads are particularly critical due to their substantial impact on the structural integrity, operational efficiency, and long-term durability of solar energy systems. An accurate estimation of wind loads is essential for designing solar panels that are both safe and cost-effective.

The majority of solar panels installations are either roof-mounted or ground-mounted (Aly 2016). Of these two, the most common one is roof-mounted. These systems can be installed on both flat and sloped roofs [see **Figure 1**].

a) b)

Figure 1 *Roof-mounted Solar Panel System a) Mibet Energy (2024) and b) ASCE7-22*

Ground-mounted solar systems, shown in **Figure 2** and **Figure 3**, are freestanding systems installed directly on the ground without usable space underneath (IBC 2024), typically categorized as low-rise structures.

Figure 2 *Ground-mounted Solar Panel System (Daniel 2023)*

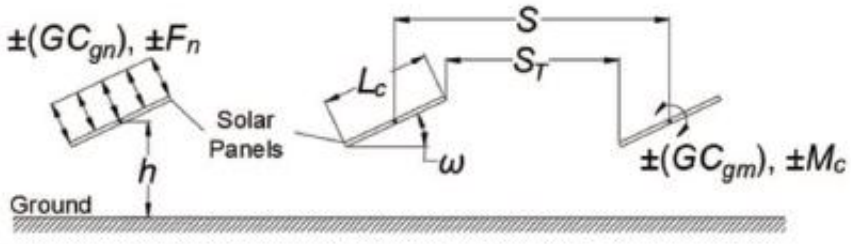

Figure 3 *Ground-mounted PV panel Systems (ASCE7-22)*

Another solar panel installation method is Elevated Photovoltaic (PV) Support Structure [**Figure 4**]. The 2024 edition of the International Building Code (IBC 2024) defines Elevated PV Support Structure as "an independent photovoltaic (PV) panel support structure designed with usable space underneath with minimum clear height of 7 feet 6 inches (2286mm), intended for secondary use such as providing shade or parking of motor vehicles."

Figure 4 *Elevated PV Support Structures as parking shades (Ecopower 2024)*

Elevated PV Support Structures are becoming popular as they offer numerous benefits to the public, being a source of clean, low-cost energy. Such solar structures are widely used in commercial properties, colleges and universities, sports stadiums, and large parking lots. The U.S. solar carport market was valued at USD 112.60 million in 2024 and is expected to reach approximately USD 291.40 million by 2034 (Precedence Research 2025). They can be built to create covered walkways or carports, at ground level, or in elevated locations. Today's elevated PV structures use space efficiently and effectively and provide a source of renewable energy; however, strong winds can significantly impact and damage such structures. **Figure 5** shows damages caused by Hurricane Irma and Hurricane Maria in 2017 to the solar carports (seen on the top and right side of the building in **Figure 5**b) in the Ron de Lugo Federal Building and Courthouse St. Thomas, U.S. Virgin Islands in addition to the roof-mounted PV panels. In spite of this, there are no explicit design provisions for these specific types of structures outlined in the current code provisions such as ASCE7-22. Therefore, this research aims to study wind effects on elevated photovoltaic (PV) support structures (solar carports for the purpose of this study) utilizing large-scale wind tunnel experiments conducted at the Wall of Wind Experimental Facility (WOW EF).

(a) (b)

(c)

Figure 5 *Ron de Lugo Federal Building and Courthouse St. Thomas, U.S. Virgin Islands (a) before (Akin 2021); (b) after (Helios Energy 2025) Hurricane Irma and Maria; (c) close-up on damaged solar carports.*

2 Methodology

2.1 Model, test configurations, and instrumentation

Based on several discussions with various PV industries, the team selected the most representative configurations to test. The selected test model consists of a 1:10 scale solar carport with full scale plan dimensions of 56’7.5” x 37’7.5” (17.25m x 11.47m) and 18’5” (4.93m) high at the mean roof height for tilt angles of 3°, 5° & 7°. The solar carport is a T-shaped structure [see **Figure 6**] that comprises of a 15x5 PV array roof on an interconnected framing system with 3 posts in the middle as supports at 27’ (8.23m) on-center spacing [see **Figure 7**]. Among the 75 PV panels 25 were instrumented with pressure taps (15 taps per panel) for wind pressure measurement with 8 taps on the top surface and 7 taps on the bottom surface [see **Figure 8**].

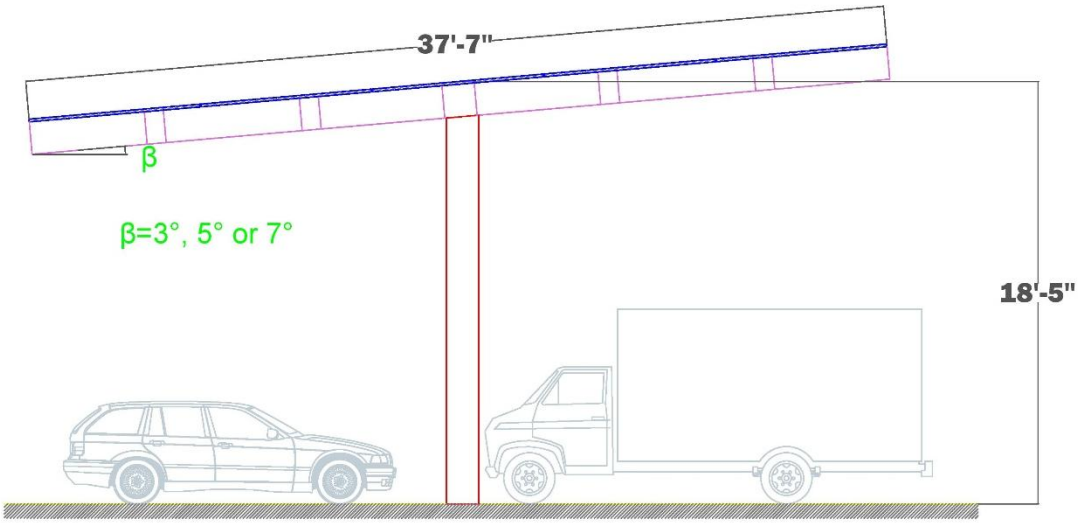

Figure 6 *Section view of solar carport model.*

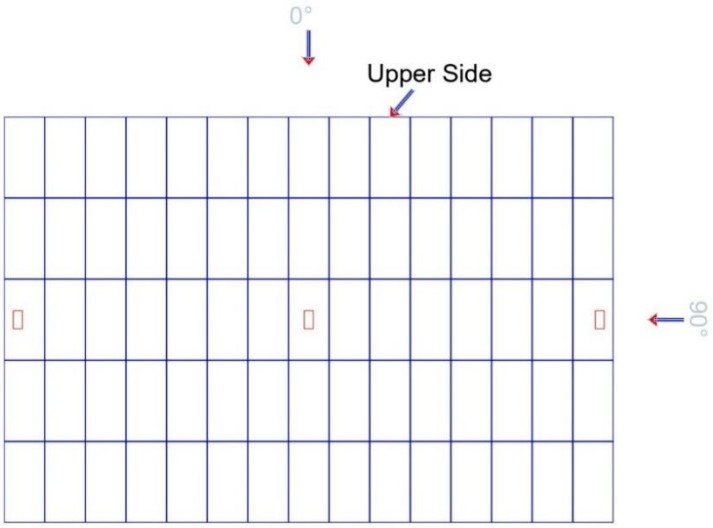

Figure 7 *Wind directions with respect to the upper side of the solar carport*

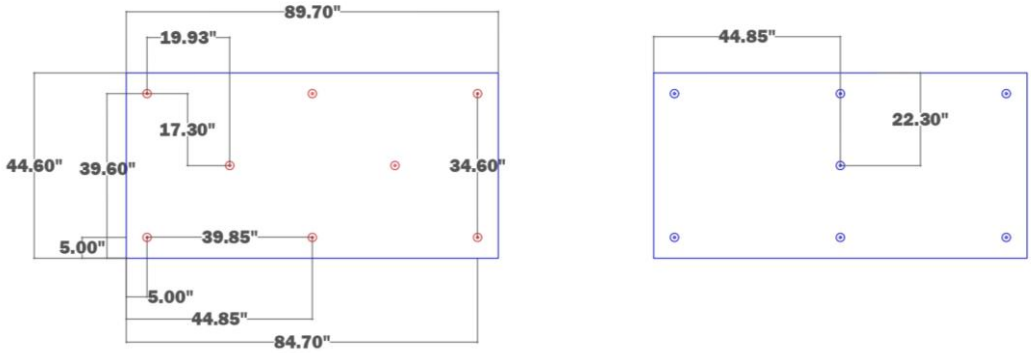

a) b)

Figure 8 *Panel pressure tap layout a) top surface and b) bottom surface*

Location of the 25 instrumented panels was selected based on the critical zone assignments (Zone 2 & 3) from ASCE7-22 for open buildings, mono-slope free roofs ($\theta \leq 45°$) as shown in **Figure 9** and **Figure 10**. According to ASCE7-22, an open building is a building that has each wall at least 80% open. The solar carport was subjected to aerodynamic testing before and after the presence of parked vehicles. An additional set of tests (results not included in this report) were also undertaken to assess the wind pressures on Zone 1 of the carport by moving the instrumented panels to the inner part of the array as presented in **Figure 11**. These test cases encompassed all scenarios earlier outlined for Zone 2 and Zone 3 cases.

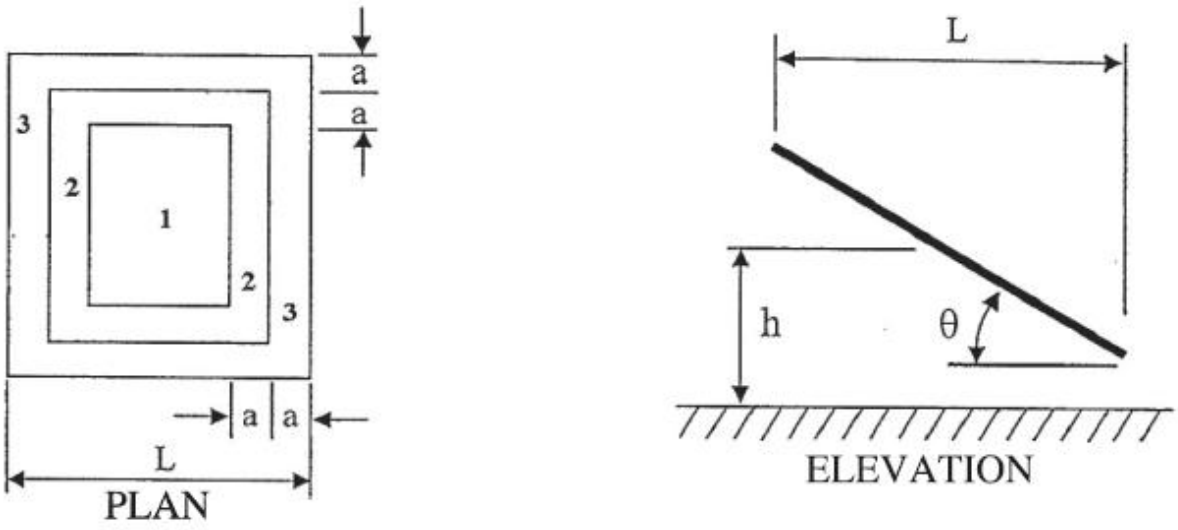

Figure 9 *ASCE 7-22 Zone Assignment for open buildings, mono-slope free roofs (θ ≤ 45°) (ASCE7-22)*

In **Figure 9**, 'a' is 10% of least horizontal dimension or 0.4, whichever is smaller but not less than 4% of least horizontal dimension or 3ft (0.9m); 'h' is mean roof height, ft (m); 'L' stands for the horizontal dimension of building, measured in the along-wind direction, ft (m), and θ is the angle of plane of roof from horizontal in degrees.

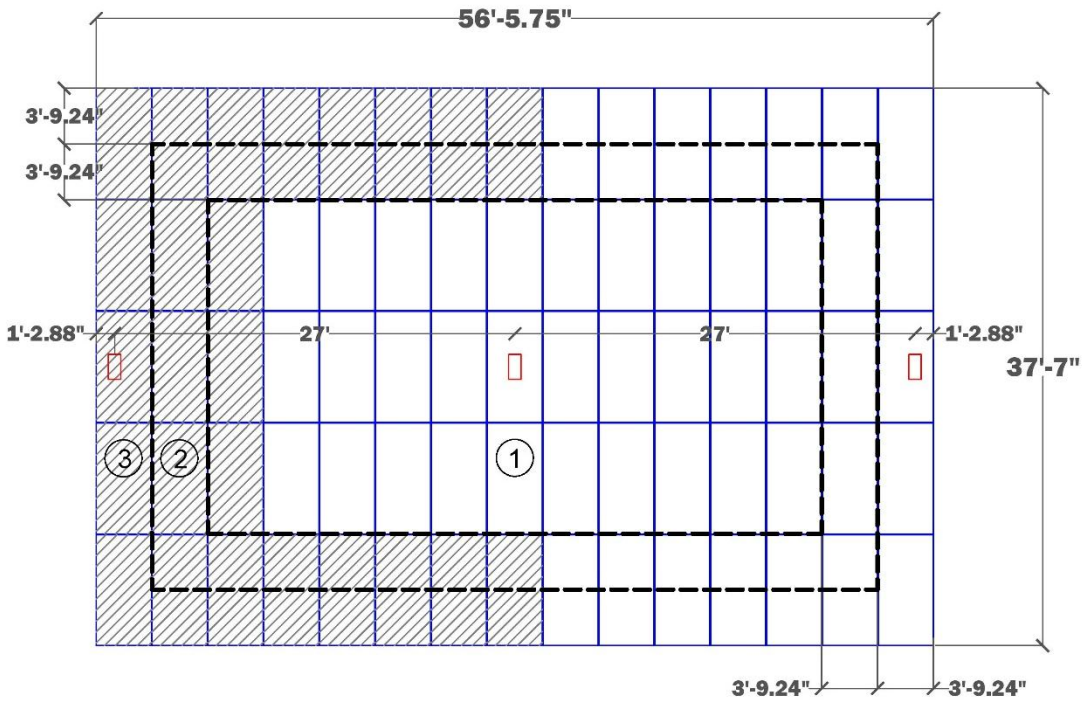

Figure 10 *Location of instrumented panels to cover Zone 2 and 3*

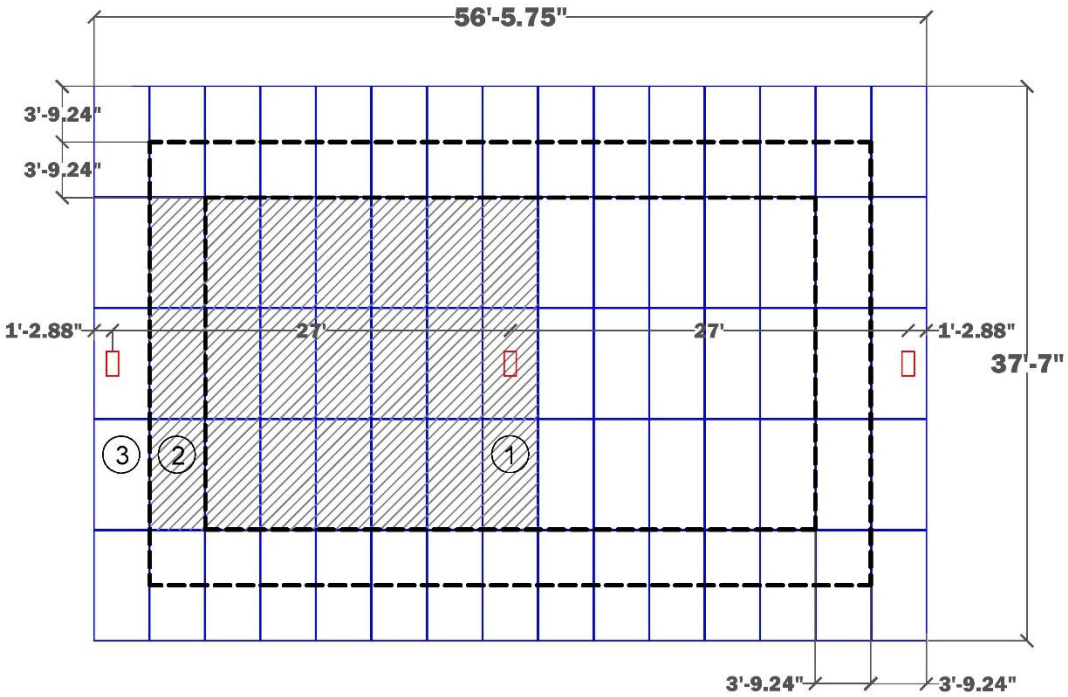

Figure 11 *Location of instrumented panels to cover Zone 1*

Additionally, to investigate the interference effects, tests were conducted for two and three rows of solar carports which represent the real-life scenarios with un-instrumented additional two rows [**Figure 12**]. These tests were conducted with a 12’ and 20’ full scale clear spacing between carport rows, which correspond to one-way and two-way traffic respectively, to investigate the effects of spacing on the wind loads.

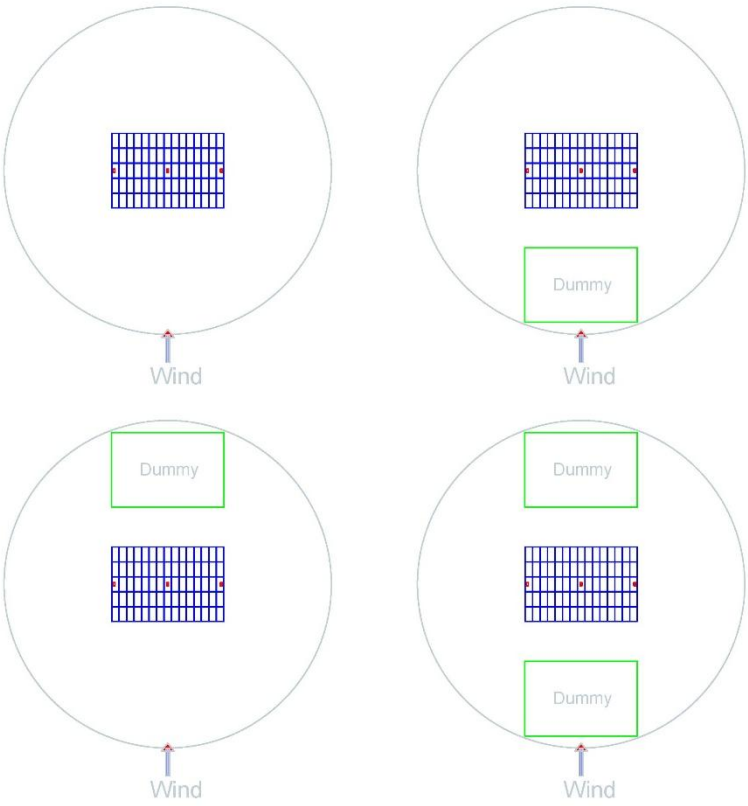

Figure 12 *Test configurations with the carport of interest located at the center*

The PV panels were 3D printed with integrated tubing for top and bottom pressure measurements. Dummy PV panels were cut out of 6mm (0.25in) thick polycarbonate sheets. All columns, beams and purlins, either for the instrumented or dummy carport, were made of steel. **Figure 13** shows a single solar carport row with and without the presence of vehicles. Car bodies of 1:10 were used to simulate the effects of parked vehicles. Multiple rows of carports can be seen in **Figure 14a, b and c**.

a) *b)*

Figure 13 *Single solar carport row a) without and b) with vehicle present*

(a) (b) (c)

Figure 14 *Dummy carport location (a) upwind, (b) downwind, and (c) upwind and downwind*

A total of 39 cases, each evaluated for 40 wind directions (0:10:350°, 45°, 135°, 225°, and 315°), were considered for the described experimental program. **Table 1** summarizes the various solar carport model configurations which can be grouped into 4 categories: single-row cases with no vehicles (Cases 1, 9, 17, 25, 30 and 35), single-row cases with vehicles (Cases 8, 16, 24, 29, 34 and 39), two-row cases (Cases 2, 3, 5, 6, 10, 11, 13, 14, 18, 19, 21, 22, 26, 27, 31, 32, 36, and 37), and three-row cases (Cases 4, 7, 12, 15, 20, 23, 28, 33 and 38). The selected tilt angles for the solar carports were 3°, 5° and 7°.

Table 1 *Test model configurations*

Test Case Name	Tilt Angle	Vehicle Present	Number of Carport Rows	Dummy Carport Location
Case_01_3Deg_Z2&3_NV_1	3°	No	One	N/A
Case_02_3Deg_Z2&3_NV_2_U	3°	No	Two (20ft)	Upwind
Case_03_3Deg_Z2&3_NV_2_D	3°	No	Two (20ft)	Downwind
Case_04_3Deg_Z2&3_NV_3_UD	3°	No	Three (20ft)	1 Upwind & 1 Downwind
Case_05_3Deg_Z2&3_NV_2_U	3°	No	Two (12ft)	Upwind
Case_06_3Deg_Z2&3_NV_2_D	3°	No	Two (12ft)	Downwind
Case_07_3Deg_Z2&3_NV_3_UD	3°	No	Three (12ft)	1 Upwind & 1 Downwind
Case_08_3Deg_Z2&3_V_1	3°	Yes	One	N/A
Case_09_5Deg_Z2&3_NV_1	5°	No	One	N/A
Case_10_5Deg_Z2&3_NV_2_U	5°	No	Two (20ft)	Upwind
Case_11_5Deg_Z2&3_NV_2_D	5°	No	Two (20ft)	Downwind
Case_12_5Deg_Z2&3_NV_3_UD	5°	No	Three (20ft)	1 Upwind & 1 Downwind
Case_13_5Deg_Z2&3_NV_2_U	5°	No	Two (12ft)	Upwind
Case_14_5Deg_Z2&3_NV_2_D	5°	No	Two (12ft)	Downwind
Case_15_5Deg_Z2&3_NV_3_UD	5°	No	Three (12ft)	1 Upwind & 1 Downwind
Case_16_5Deg_Z2&3_V_1	5°	Yes	One	N/A
Case_17_7Deg_Z2&3_NV_1	7°	No	One	N/A
Case_18_7Deg_Z2&3_NV_2_U	7°	No	Two (20ft)	Upwind
Case_19_7Deg_Z2&3_NV_2_D	7°	No	Two (20ft)	Downwind
Case_20_7Deg_Z2&3_NV_3_UD	7°	No	Three (20ft)	1 Upwind & 1 Downwind
Case_21_7Deg_Z2&3_NV_2_U	7°	No	Two (12ft)	Upwind
Case_22_7Deg_Z2&3_NV_2_D	7°	No	Two (12ft)	Downwind
Case_23_7Deg_Z2&3_NV_3_UD	7°	No	Three (12ft)	1 Upwind & 1 Downwind
Case_24_7Deg_Z2&3_V_1	7°	Yes	One	N/A

Case_25_3Deg_Z1_NV_1	3°	No	One	N/A
Case_26_3Deg_Z1_NV_2_U	3°	No	Two (20ft)	Upwind
Case_27_3Deg_Z1_NV_2_D	3°	No	Two (20ft)	Downwind
Case_28_3Deg_Z1_NV_3_UD	3°	No	Three (20ft)	1 Upwind & 1 Downwind
Case_29_3Deg_Z1_V_1	3°	Yes	One	N/A
Case_30_5Deg_Z1_NV_1	5°	No	One	N/A
Case_31_5Deg_Z1_NV_2_U	5°	No	Two (20ft)	Upwind
Case_32_5Deg_Z1_NV_2_D	5°	No	Two (20ft)	Downwind
Case_33_5Deg_Z1_NV_3_UD	5°	No	Three (20ft)	1 Upwind & 1 Downwind
Case_34_5Deg_Z1_V_1	5°	Yes	One	N/A
Case_35_7Deg_Z1_NV_1	7°	No	One	N/A
Case_36_7Deg_Z1_NV_2_U	7°	No	Two (20ft)	Upwind
Case_37_7Deg_Z1_NV_2_D	7°	No	Two (20ft)	Downwind
Case_38_7Deg_Z1_NV_3_UD	7°	No	Three (20ft)	1 Upwind & 1 Downwind
Case_39_7Deg_Z1_V_1	7°	Yes	One	N/A

To measure the wind-induced pressures, a total of 375 pressure taps (15 taps per panel) were installed on the carport model's surfaces, as shown in **Figure 8**. Specifically, a total of 200 pressure taps were installed on the top surface, and 175 taps on the bottom surface of the carport roof. The pressure taps were connected to a ZOC33/DSM4000 Scanivalve data acquisition system, which sampled pressures at a rate of 625 Hz. A tubing transfer function was used to correct the collected pressure data for distortion effects introduced by the tubing length (Irwin et al. 1979). **Figure 15** and **Figure 16** illustrate how the pressure taps were arranged to capture measurements in the three zones of the structure, in accordance with the zone assignment guidelines of ASCE 7-22 [See **Figure 9**].

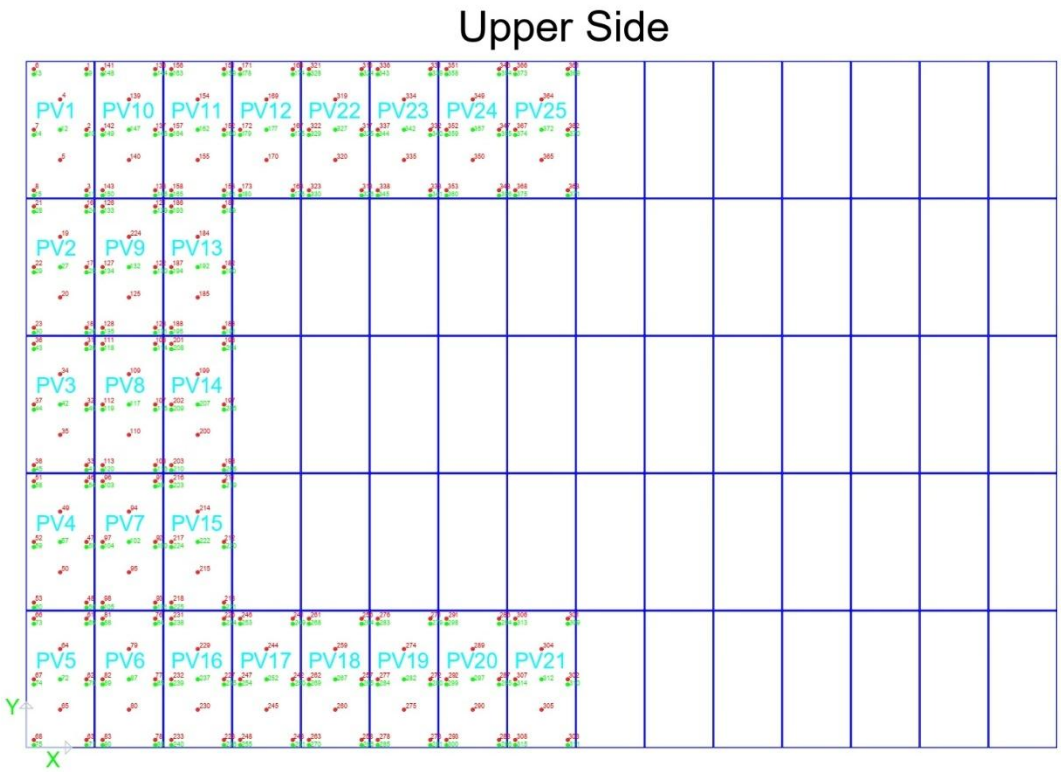

Figure 15 *Pressure Tap Layout for Zone 2 and 3*

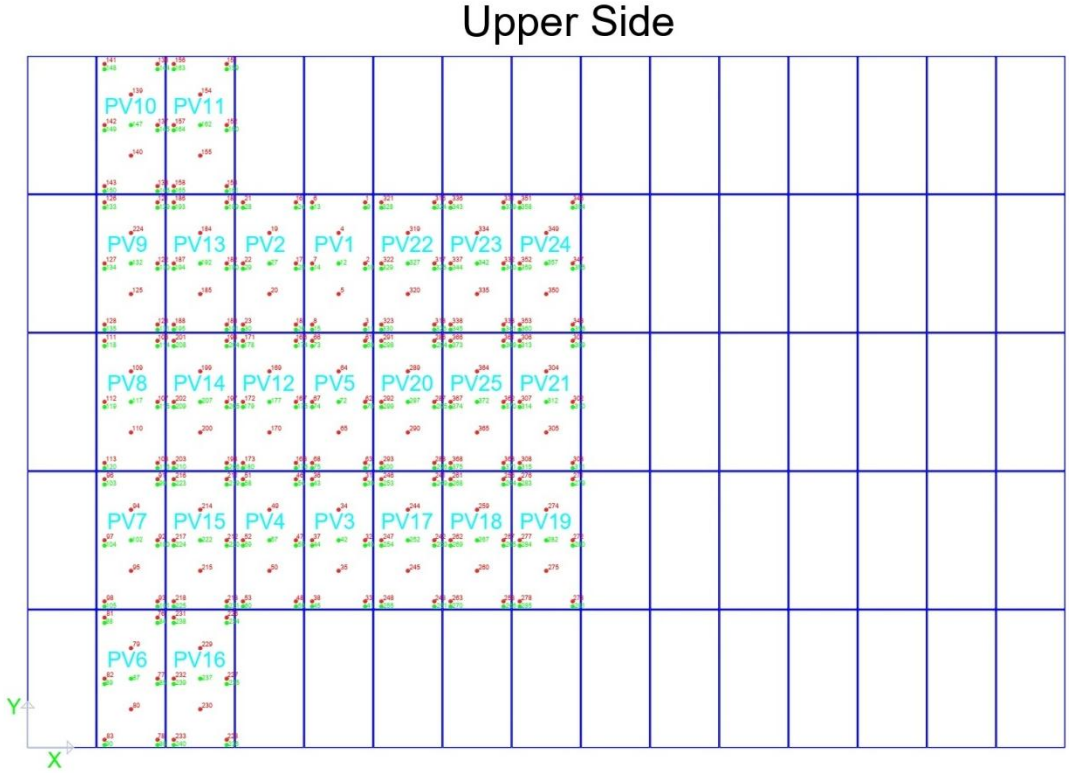

Figure 16 *Pressure Tap Layout for Zone 1*

2.2 Wind flow simulation and test protocol

The 12-fan WOW EF, shown in **Figure 17a**, is a full- and large-scale testing facility, capable of generating wind speeds up to 70 m/s (157 mph) and turbulence characteristics similar to those recorded in Category 5 hurricanes on the Saffir-Simpson scale (Chowdhury et al. 2017, 2018). Equipped with spires and floor roughness elements (**Figure 17b**), the WOW is capable of simulating Atmospheric Boundary Layer (ABL) wind flows under various terrain conditions. The WOW uses three triangular spires placed at the entrance of the flow management section, followed by an array of 150 roughness elements to produce the requisite atmospheric boundary layer conditions. The spire and floor roughness elements setup is shown in **Figure 17b**.

(a) (b)

Figure 17 *(a) 12-fan WOW EF; (b) spires and floor roughness elements*

The Turbulent Flow Instrumentation Pty Ltd.'s Cobra probes 232 and 239 were used to measure the free stream wind speeds for the profiles. A summary of the free stream wind speed measurement is shown in Table 1**.** The wind speed and turbulence intensity profile obtained from the free stream measurements for the 1:10 scale is presented in **Figure 19** and compared against the corresponding ESDU profiles. **Figure 20** shows the turbulence power spectra at the reference height of 0.56 m (22.1 inches). According to the ASCE 49-21 Standard for Wind Tunnel Testing for Buildings and Other Structures, the power spectra of velocity fluctuations measured between 60% and 100% of the roof height in wind tunnel simulations should align with the target mean velocity profile.

Figure 18 *Free flow measurement setup*

Table 2 *Summary for 1:10 Scale Exposure C Open Terrain*

Target Profile	1:10 open terrain (ASCE7 Exposure Category C)
Roughness Setup	Automatic roughness element at 15-degree angle, spires at 30-degree angle, no additional roughness blocks, see **Figure 18**.
Reference height (inch)	22.1 at mean roof height U_{mean}=22.38 m/s, U_{3sec}=24.14 m/s, Iu=12.3%, Lu=0.58m
Probe heights (inch)	4.42, 8.84, 13.26, 17.68, 22.1, 33.15, 39.78, 44.2, 55.25, 66.3
Profile location	Center of the turntable
Test fan throttle	45% (about 68 mph from the Pitot).
Data sampling	Data was sampled at 2000Hz for 2 minutes.
Note	Only 2 Cobra probes are good to use. Thus, a total of 5 measurement batches were conducted for 10 heights.

Figure 20 shows the power spectral density (PSD) of the WOW longitudinal velocity fluctuations at the mean roof height along with the full-scale Von-Karman PSD based on ESDU item 85020 (ESDU 2001) for a roughness length z_o = 0.03m. The mean wind velocity and turbulence intensity profiles are presented in **Figure 19**.

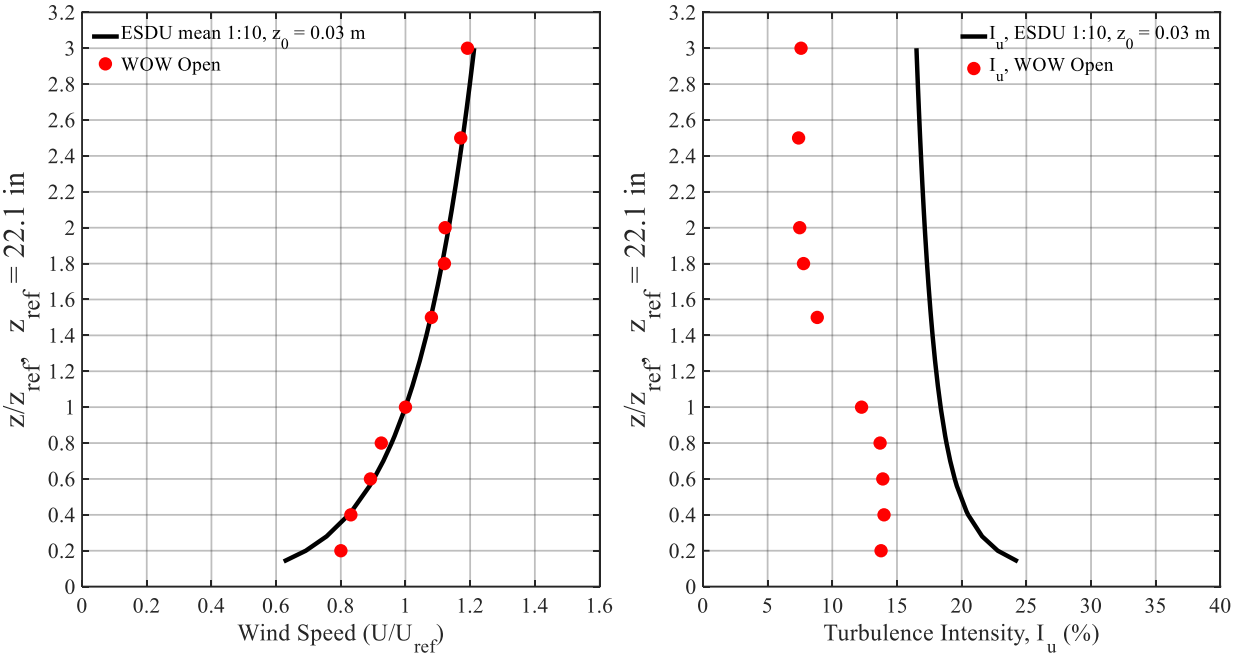

(a) Profiles of the normalized mean wind speeds (b) Profiles of the turbulence intensity

Figure 19 *ABL profiles for 1:10 open terrain (z_{ref} = 22.1" in the WOW).*

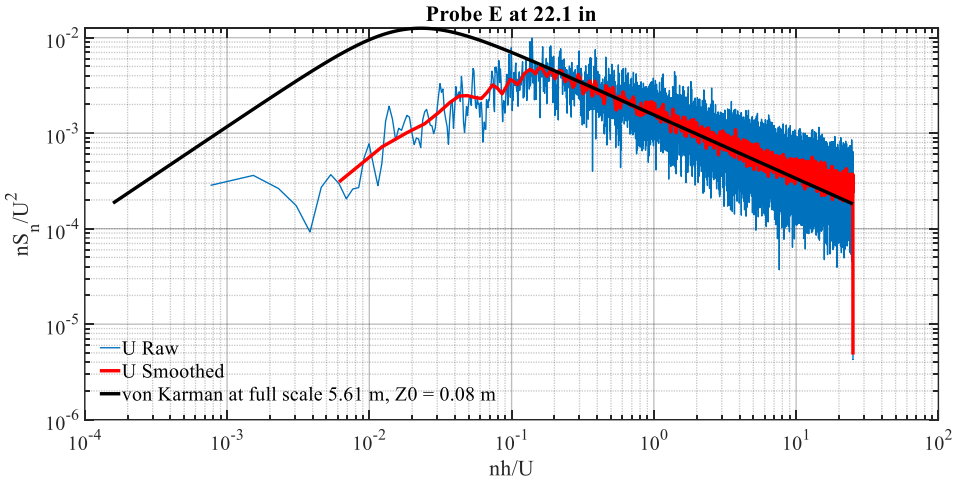

Figure 20 *PSD of the longitudinal wind velocity fluctuations*

The difference in the turbulence intensity profile between the WOW data and the ESDU is attributed to the missing low frequency component of the wind. That can be seen in **Figure 20**, where the power spectral density (PSD) spectra of the WOW and the Von Karman match except for the low-frequency part. Partial Turbulence Simulation (PTS), a validated procedure for large-

scale testing, was utilized to overcome this issue. In PTS, the missing low-frequency turbulence is compensated for during post-test analysis (Mooneghi 2016).

A summary of the simulated wind flow characteristics and those of the full-scale counterpart are presented in Table 3. The model was placed on the automated turntable and aerodynamic experiments were conducted for a 2-min duration at 40 wind directions (0:10:350°, 45°, 135°, 225°, and 315°).

***Table 3**. Wind flow characteristics*

Parameter	Full-scale	WOW Model (1:10)
Turbulence Intensity (%)	$I_{up} = 17.80$	$I_{um} = 12.30$
Integral length scale (m)	${}^{x}L_{up} = 62.80$	${}^{x}L_{um} = 0.58$
Mean roof height (m)	$H_p = 5.60$	$H_m = 0.56$
Sampling duration (min)	$t_p = 60$	$t_m = 2$
Mean wind speed (m/s)	$\overline{U}_p = 43.60$	$\overline{U}_m = 22.38$

2.3 Data Analysis

Wind-induced external pressure data were collected on the 3D printed panels of the solar carport model for the 39 test configurations. Time histories of the pressure coefficients $C_p(\theta, t)$ were calculated using Equation (1), where $P(\theta, t)$ is the pressure time series in Pa (psf), P_0 is the static reference pressure in Pa (psf), ρ is the air density in kg/m^3 (slugs/ft^3), θ is the wind azimuth, and $\overline{U}$ is the mean wind speed in m/s (mph) at the mean roof height.

$$C_p(\theta, t) = \frac{P(\theta, t) - P_0}{\frac{1}{2}\rho \overline{U}^2} \qquad (1)$$

Peak pressure coefficients, referenced by the 3-sec full-scale gust wind speed $\widehat{U}_{3s} = \overline{U}_{1hr}.\left(1 + 3.4I_{u,p}\right)$, were estimated for a 1-hr storm duration using Partial Turbulence Simulation with 120 subintervals. Specifically, the peaks were fitted into a Fisher Tippet Type-I distribution based on a non-exceedance probability of 0.78 (Lieblein 1974).

3 Results and Discussion

Results of the large-scale aerodynamic experiments on the solar carports are presented in this section for a range of wind directions. The mean and peak pressure coefficients on the single row solar carport model including the effects of parked vehicles are discussed in Section 3.1. The results of the interference effects on wind loads are then examined in Section 3.2 for the two and three row cases. In addition, the effects of tilt angle on the wind loads are assessed for both all the aforementioned cases.

3.1 Aerodynamics of a single carport row

3.1.1 Spatial distribution of pressure coefficients

The aerodynamics of the solar panels followed those of a typical bluff body subjected to wind flow. The distribution of mean pressure coefficients, $\bar{C}_p$, on the solar carport model with 5° tilt angle, single carport row (Case 9), is presented in **Figure 21** for normal (0° and 90°) and cornering (45° and 135°) wind directions. For normal winds, the highest suctions are observed at the windward edges under the separation bubble. The $\bar{C}_p$ values are -2.49 and -2.37 for 0° and 90° respectively. As the distance from the windward edge increases, $\bar{C}_p$ tend to decrease in magnitude for both normal directions due to flow reattachment. For cornering winds, high suctions were observed at the upwind corners and edges due to the formation of conical vortices [e.g., $\bar{C}_p(45°)$ = -1.88 and $\bar{C}_p(135°)$ = -1.00].

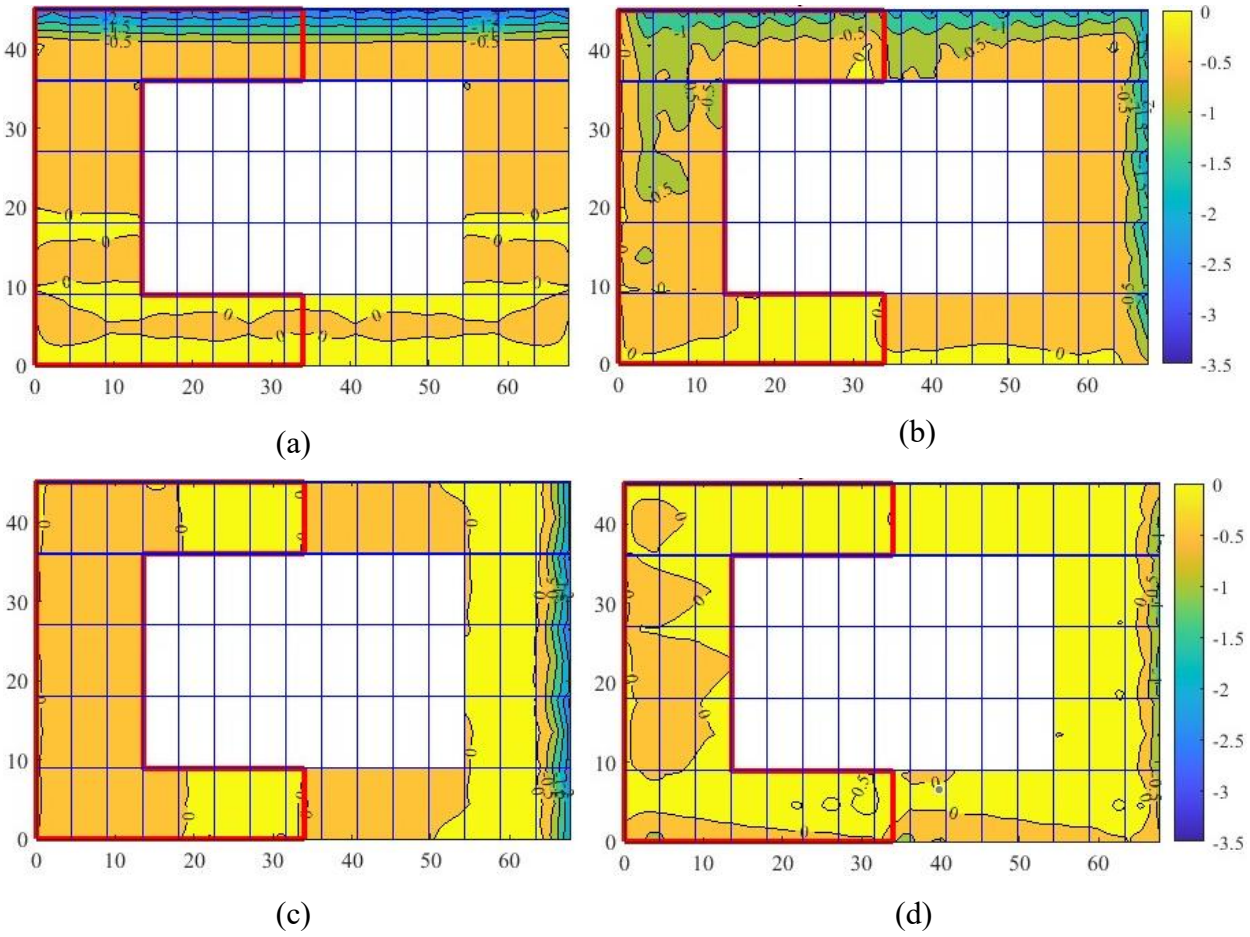

Figure 21 *$\bar{C}_p$ for Case 9 (single-row, 5° tilt with no vehicles): (a)* 0°*, (b)* 45°*, (c)* 90°*, and (d)* 135°

3.1.2 Effects of tilt angle on the wind loading

To understand the effects of tilt angle on the wind loading of a solar carport, three tilt angles were investigated: the commonly used 5° (Case 9 to 16 and Case 30 to 34), the less common 3° (Case 1 to 8 and Case 25 to 29), which is useful for long spans and 7° (Case 17 to 24 and Case 35 to 39), which, although not typically used, serves as a useful upper bound for the 5° case.

For the solar carport with 3° tilt angle (single carport row), mean pressure coefficients, $\bar{C}_p$, values are similar to that of the one with 5° tilt angle which is presented in Section 3.1.1 with slight increase for 0° and 135° wind directions. **Figure 22** shows that the maximum $\bar{C}_p$ values are -2.62, -1.81, -2.26, and -1.25 for 0°, 45°, 90°, and 135° wind directions respectively.

On the other hand, for the solar carport with 7° tilt angle (single carport row), a larger region of negative pressure is present. This could be because of the more aggressive flow separation that can

be attributed to the steeper angle of the PV panel. It can be observed, **Figure 23**, that the maximum $\bar{C}_p$ values are -2.49, -2.10, -2.17, and -0.83 for 0°, 45°, 90°, and 135° respectively.

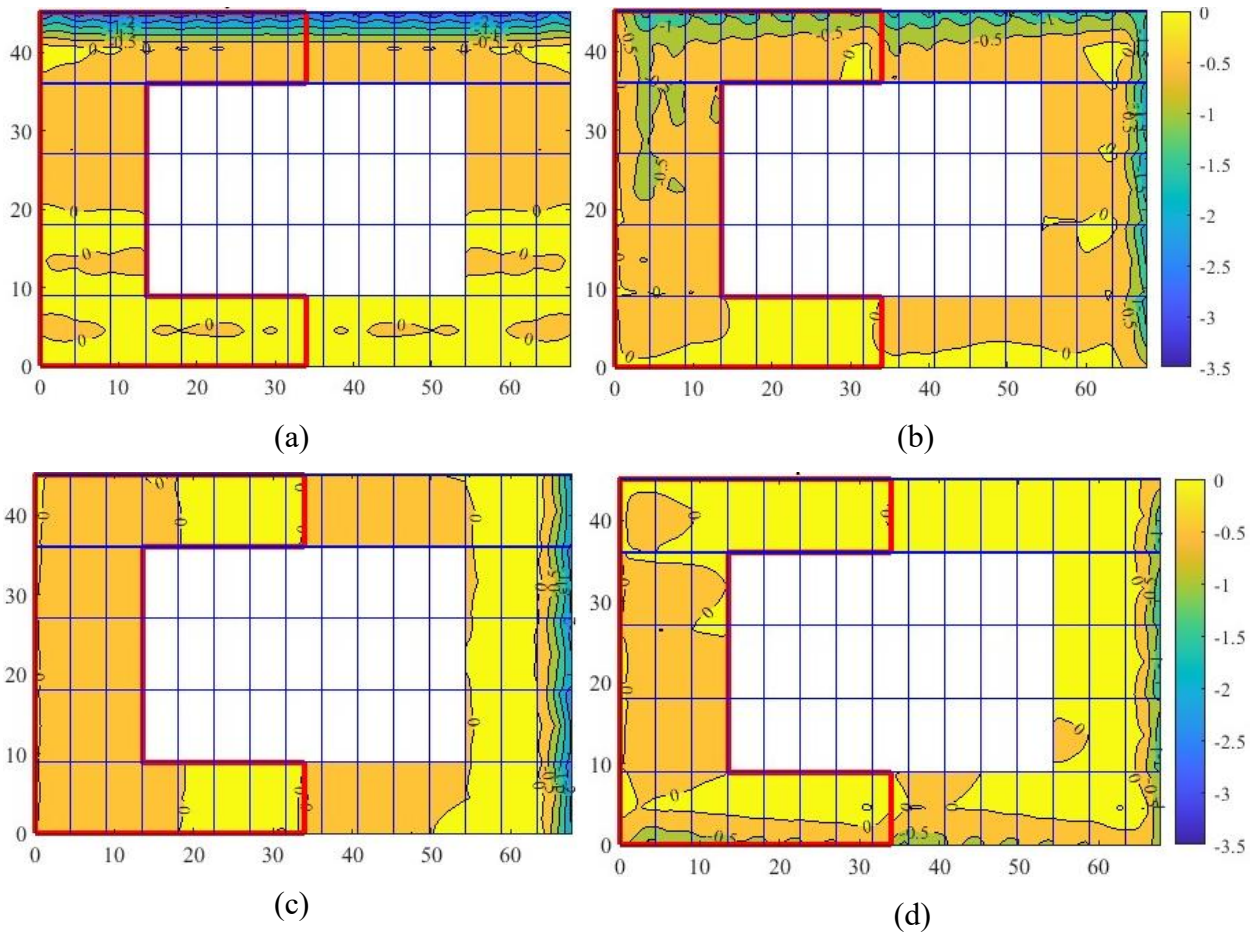

Figure 22 *$\bar{C}_p$ for Case 1 (single-row, 3° tilt with no vehicles): (a)* 0°*, (b)* 45°*, (c)* 90°*, and (d)* 135°

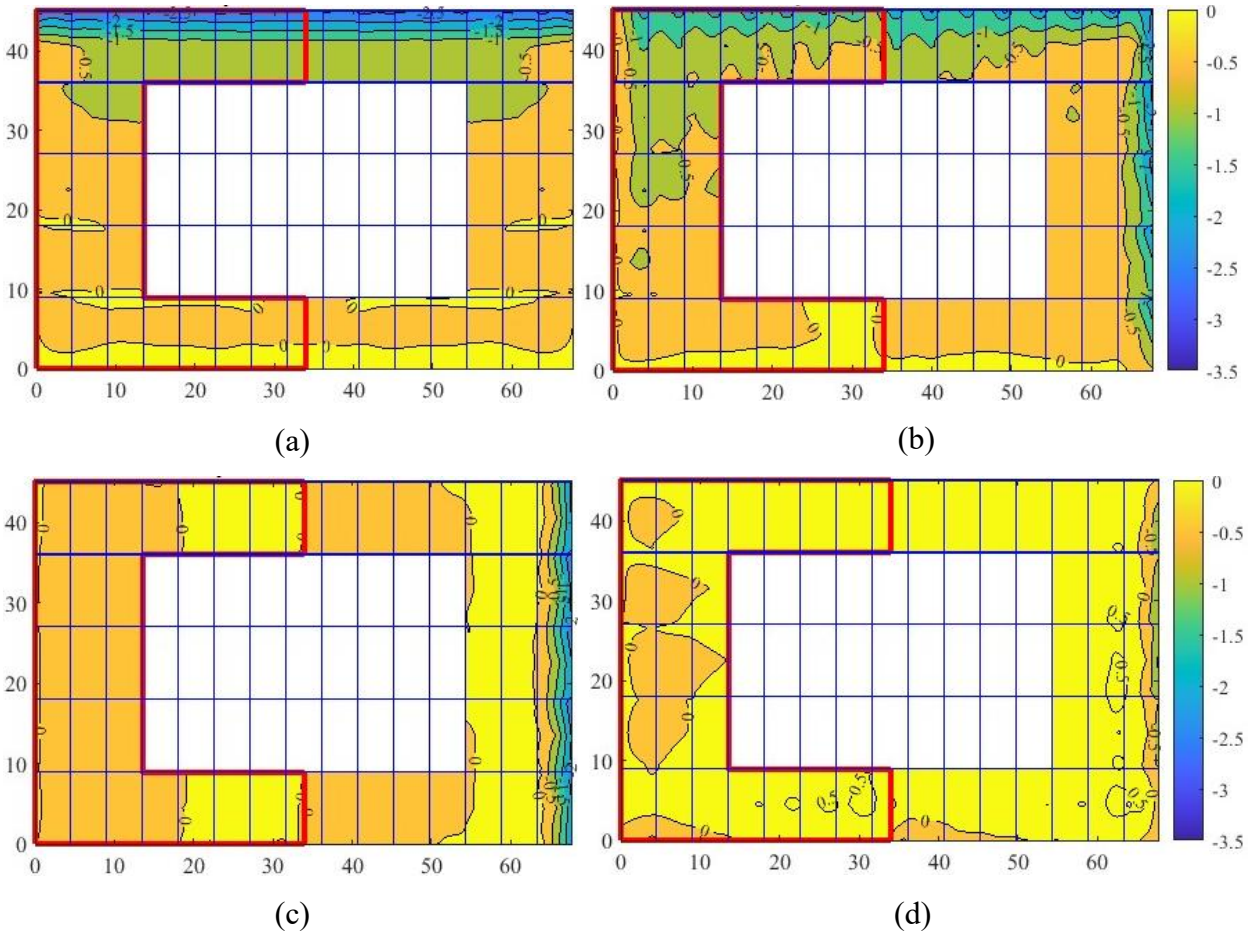

Figure 23 *$\bar{C}_p$ for Case 17(single-row, 7° tilt with no vehicles): (a)* 0°*, (b)* 45°*, (c)* 90°*, and (d)* 135°

3.1.3 Effects of the presence of parked vehicles

The presence of vehicles (Case 16) introduced significant local variations in the pressure distribution on the upper side of the structure. However, the overall mean pressure coefficients, $\bar{C}_p$, were comparable to the case without vehicles (Case 9). As shown in **Figure 24**, **Figure 22**, the most notable difference was observed for the 0° wind direction, where $\bar{C}_p$ in the central part of Zone 2 remained between -0.5 and -1.0 for Case 16 as opposed to values less than -0.5 for Case 9. For Case 16, maximum suction values of -2.46, -1.99, -2.11, and -1.18 were observed for 0°, 45°, 90°, and 135° wind directions, respectively.

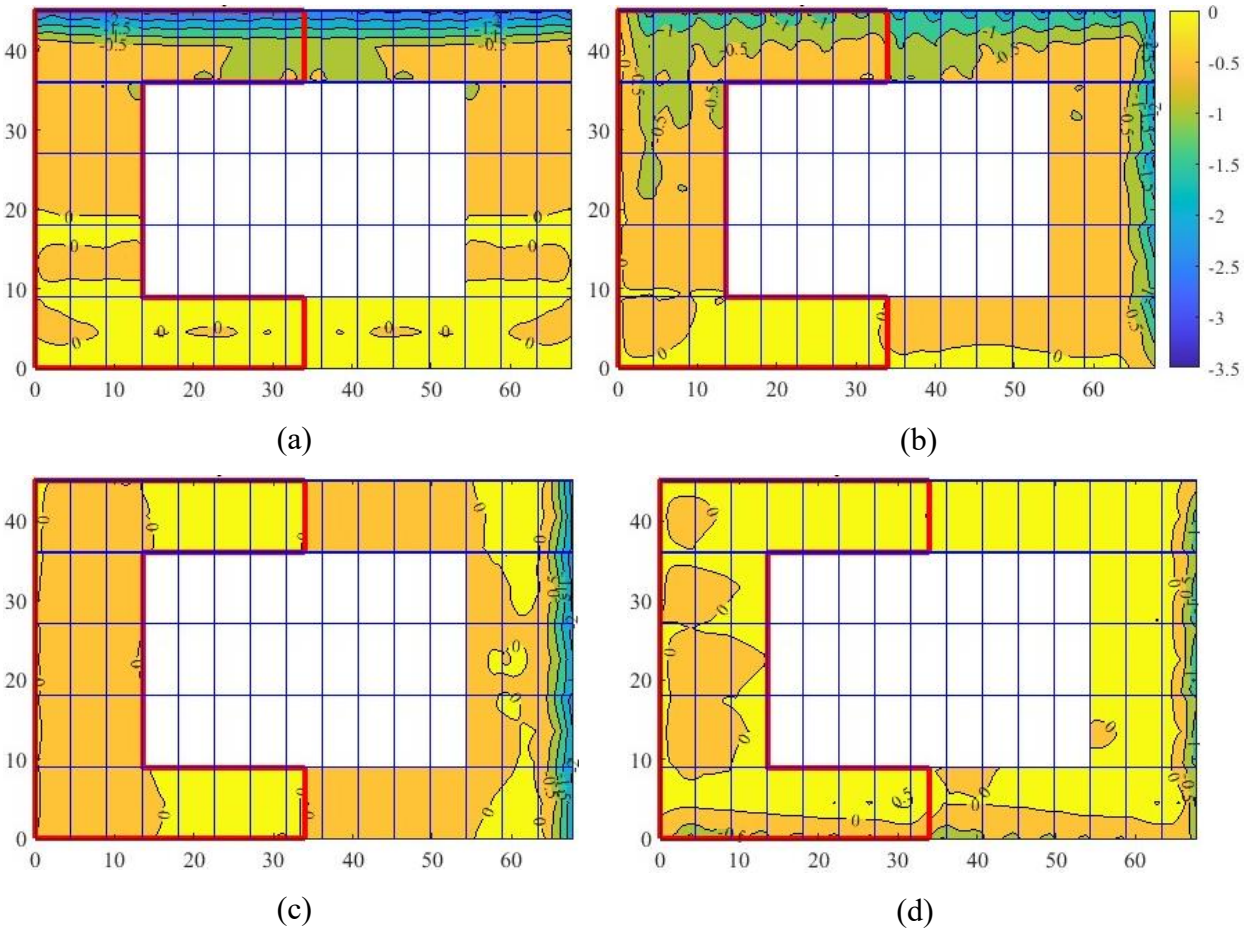

Figure 24 *$\bar{C}_p$ for Case 16 (single-row, 5° tilt with vehicles): (a)* 0°*, (b)* 45°*, (c)* 90°*, and (d)* 135°

3.2 Interference effects on the wind loading

3.2.1 Upwind-only cases

The introduction of an upwind row resulted in the reduction in the magnitude of the negative pressure in the leading edge of the instrumented solar carport [**Figure 25a**]. This can be taken to be due to the disruption of wind flow because of the upwind row that created a wake that envelops the second row. The mean pressure coefficient, $\bar{C}_p$, values on the leading edge appear to be lower than the single row case with a value of -2.31 (0° wind directions). For cornering winds, no changes were observed (-7.96, and -1.04 for 45° and 135° wind directions, respectively). Additionally, the pressure distribution across the entire structure appears to be more complex.

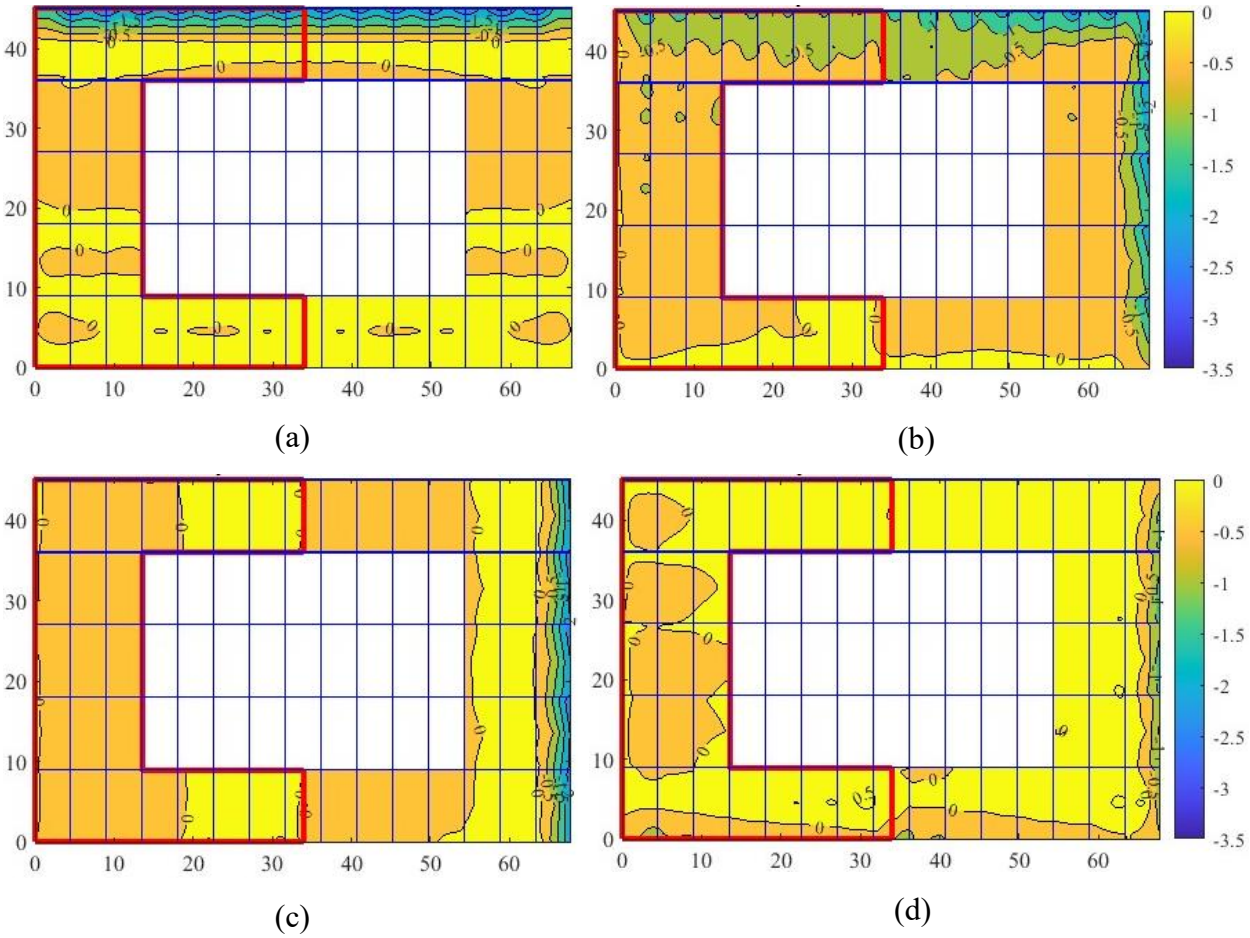

Figure 25 *$\bar{C}_p$ for Case 10 (two-row upwind, 5° tilt and 20ft spacing): (a)* 0°, *(b)* 45°, *(c)* 90°, *and (d)* 135°

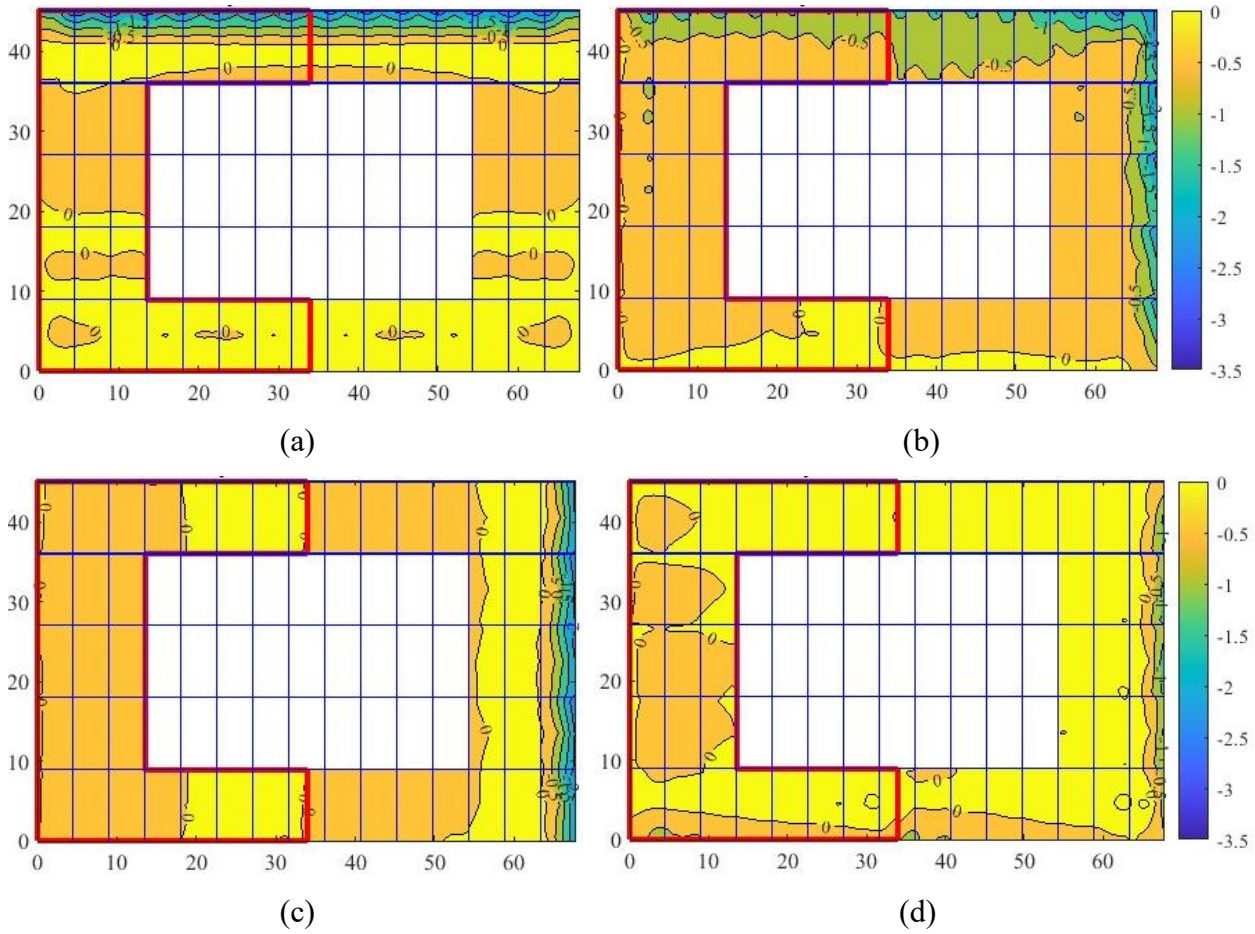

Figure 26 *$\bar{C}_p$ for Case 13 (two-row upwind, 5° tilt and 12ft spacing): (a)* 0°*, (b)* 45°*, (c)* 90°*, and (d)* 135°

3.2.2 Downwind-only cases

Compared to the benchmark single-row case (Case 9), the downwind-only cases display an almost identical pressure coefficient distribution, suggesting that the introduction of a downwind row has no significant effect on the wind loading. The $\bar{C}_p$ values are -2.59 and -2.11 for 0° and 90°, respectively, as shown in **Figure 27a** and **b**. For cornering winds, $\bar{C}_p(45°)$ = -1.89 and $\bar{C}_p(135°)$ = -1.02 were observed [See **Figure 27 c** and **d**].

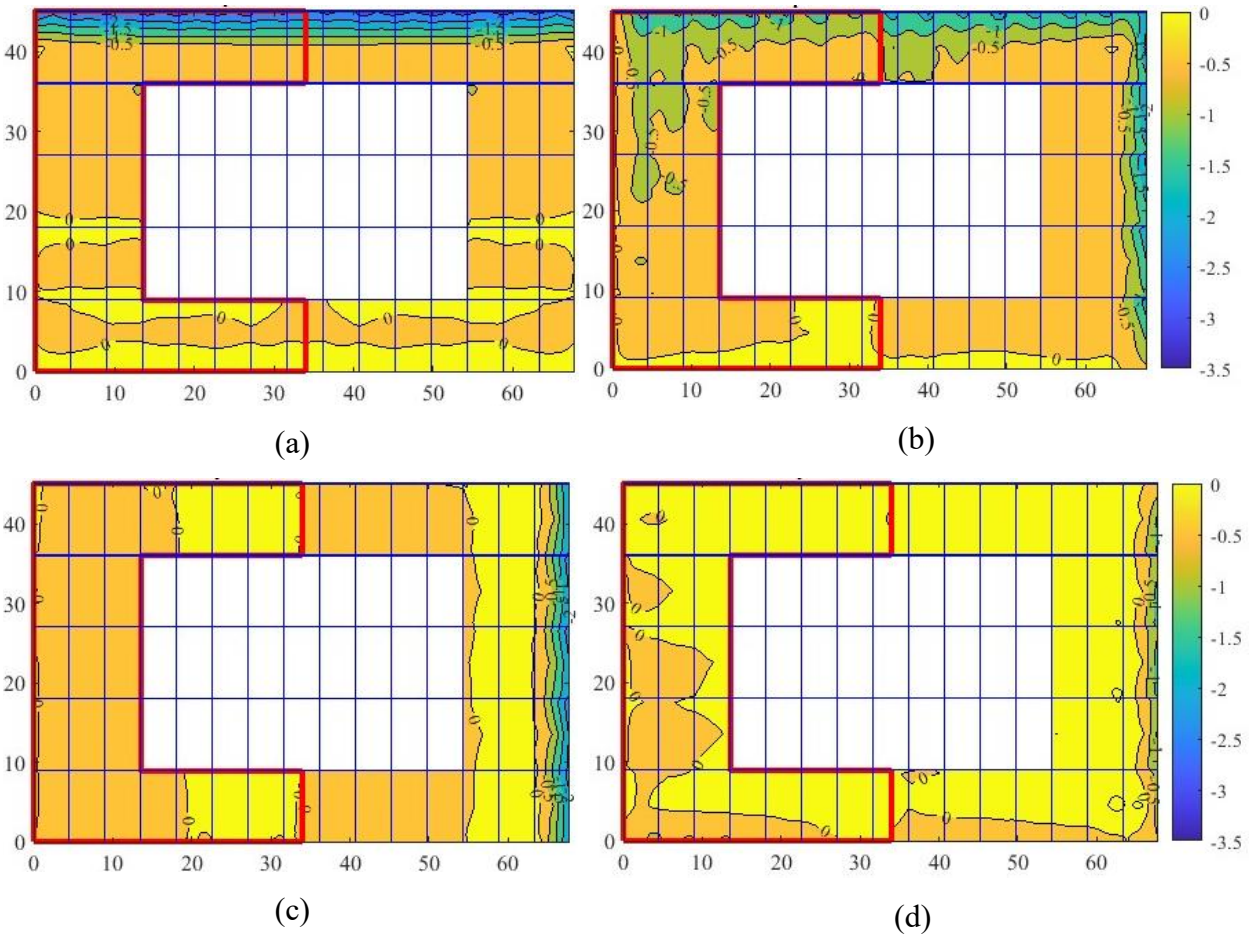

Figure 27 *$\bar{C}_p$ for Case 11 (two-row downwind, 5° tilt and 20ft spacing): (a)* 0°*, (b)* 45°*, (c)* 90°*, and (d)* 135°

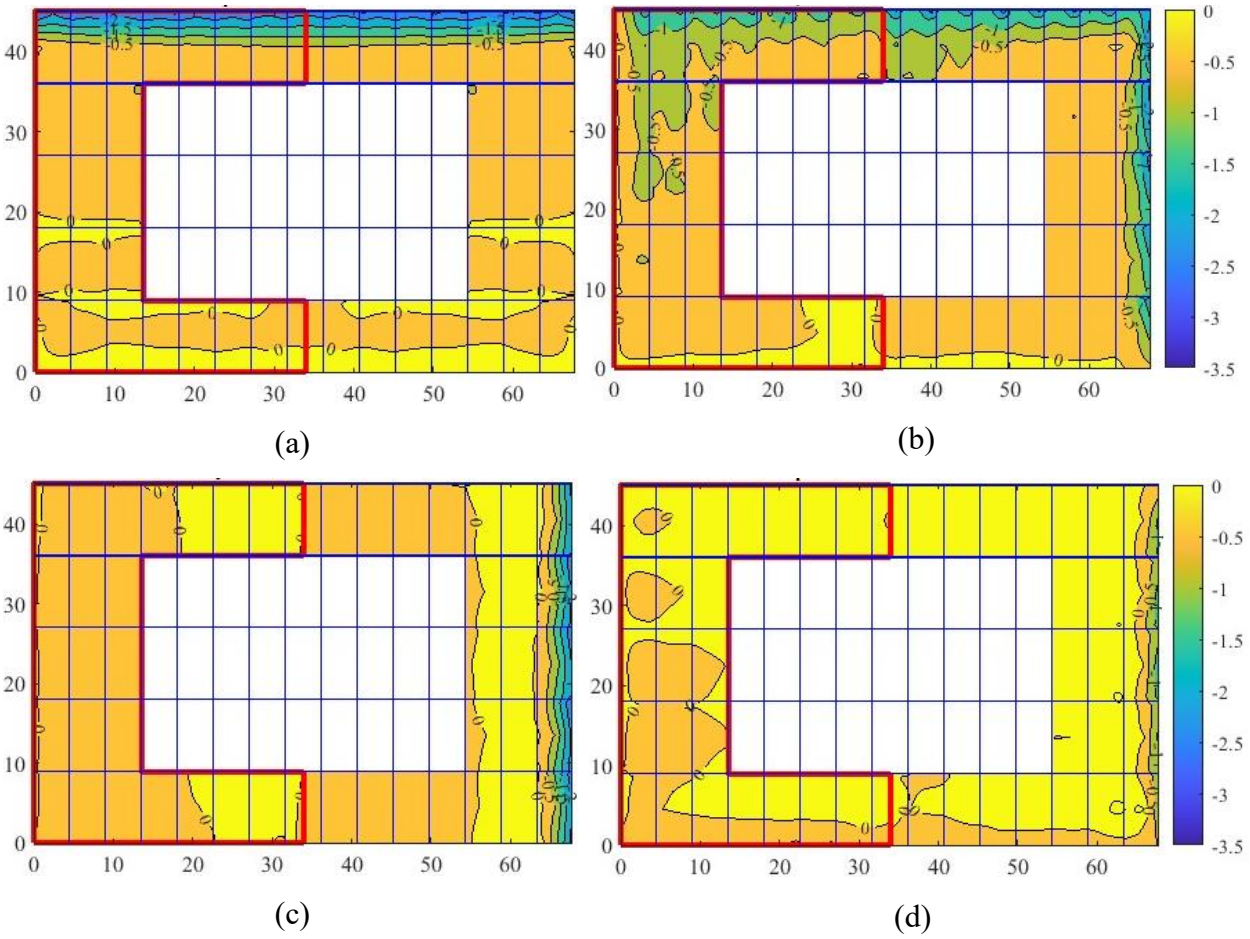

Figure 28 *$\bar{C}_p$ for Case 14 (two-row downwind, 5° tilt and 12ft spacing): (a)* 0°*, (b)* 45°*, (c)* 90°*, and (d)* 135°

3.2.3 Upwind and downwind cases

For the three row cases (with the addition of one upwind and one downwind row to the instrumented solar carport row), the leading edge experienced a slight reduction in the mean pressure coefficient value for 0° wind direction [$\bar{C}_p$= -2.40] compared to the benchmark single-row case (Case 9). However, no significant changes in $\bar{C}_p$ values were observed for 45°, 90° and 135° wind directions.

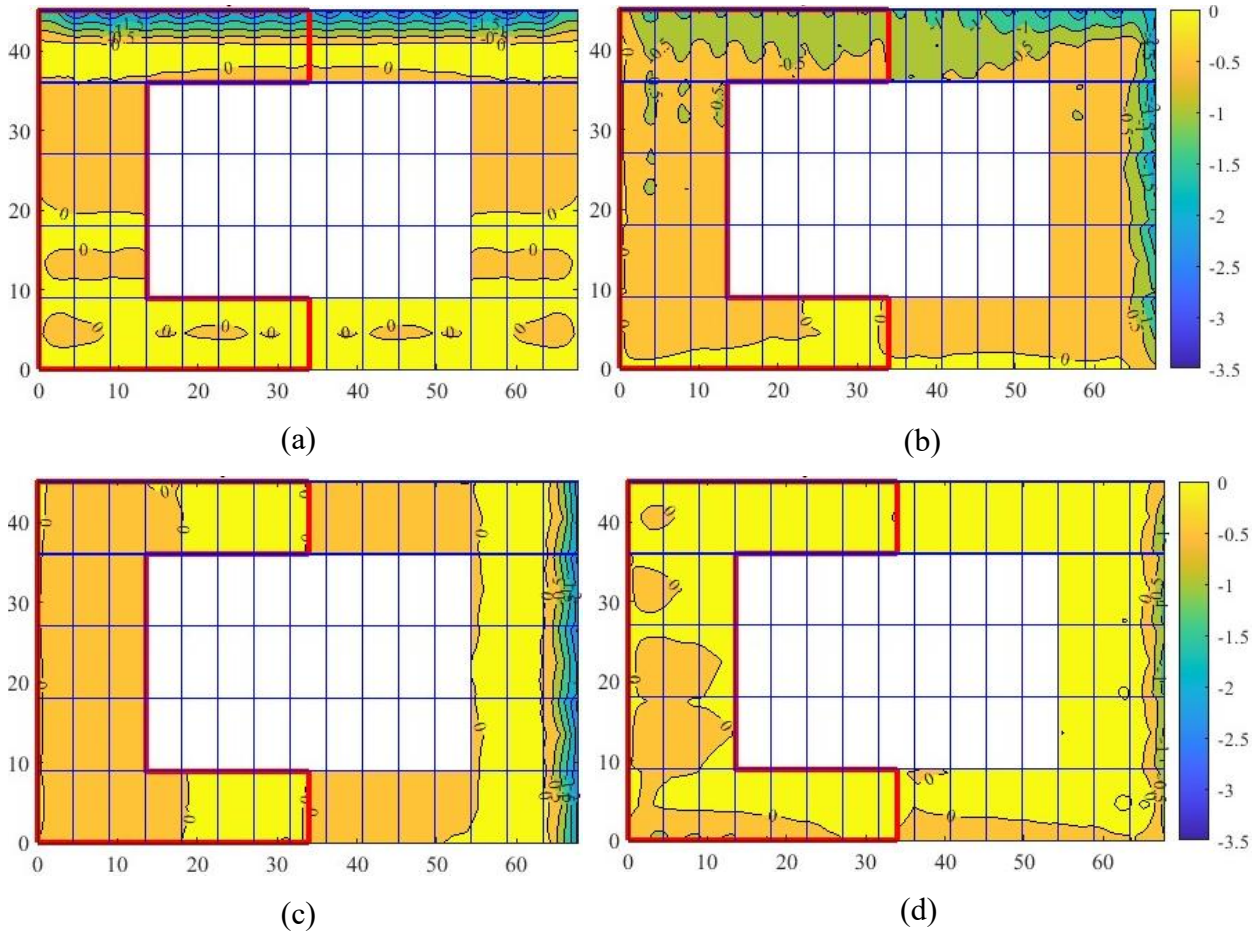

Figure 29 *$\bar{C}_p$ for Case 12 (three-row, 5° tilt and 20ft spacing): (a)* 0°*, (b)* 45°*, (c)* 90°*, and (d)* 135°

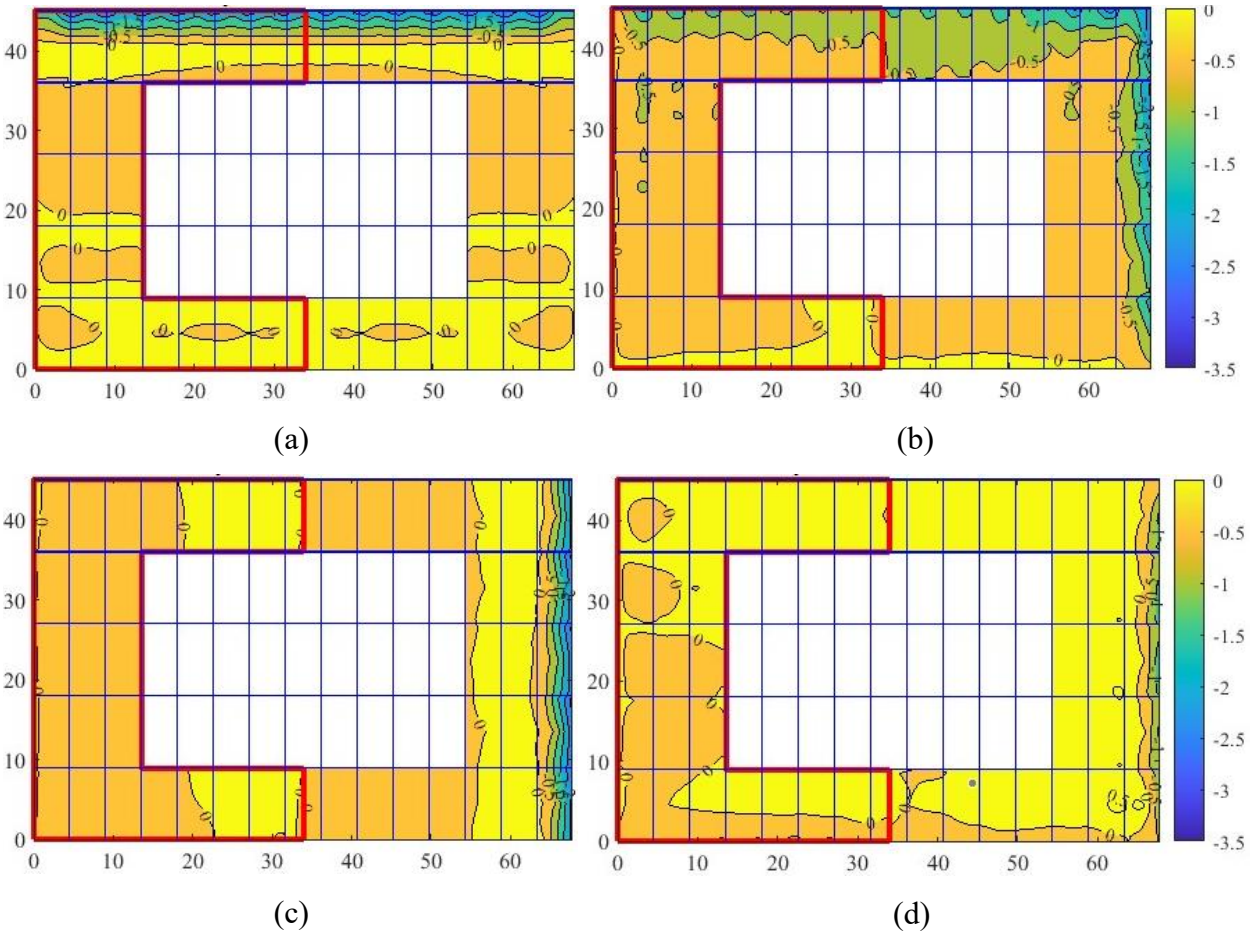

Figure 30 *$\bar{C}_p$ for Case 15 (three-row, 5° tilt and 12ft spacing): (a)* 0°*, (b)* 45°*, (c)* 90°*, and (d)* 135°

4 Concluding Remarks

This study evaluated wind loads on elevated photovoltaic (PV) support structures (solar carports for the purpose of this study), using a large-scale, state-of-the-art wind testing experimental facility, the Wall of Wind (WOW) Experimental Facility (EF) at Florida International University (FIU). The main objective was to investigate wind loads on single-row and multiple-row solar carports by considering various tilt angles and the presence of vehicles. This entailed conducting aerodynamic experiments on 39 test configurations that were subjected to simulated open-terrain boundary layer flows at the WOW EF. Statistical means of pressure coefficients, obtained from the collected pressure time histories, were used to assess wind effects on solar carports. Based on these results, the following concluding remarks are provided:

- The highest suction on a single row solar carport with a 5° tilt occurs at the windward edges during normal wind directions. As the distance from the windward edge increases, the magnitude of the pressure coefficient tends to decrease due to possible flow reattachment. For cornering winds on a single row, high suction was found at the upwind corners and edges.
- A larger region of negative pressure is present on a single carport with a 7° tilt angle compared to 3° and 5° tilt angles, which is attributed to more dominant flow separation.
- The presence of parked vehicles resulted in local pressure variations, but the overall mean pressure coefficients were comparable to the case without vehicles.
- The introduction of an upwind row reduces the magnitude of negative pressure on the leading edge of the solar carport due to the disruption of wind flow.
- The presence of only a downwind row has no significant effect on the wind loading of the carport, with a pressure coefficient distribution almost identical to the single row case.
- In a three-row configuration, the instrumented middle row experienced a reduction in the mean pressure coefficient on its leading edge for a 0° wind direction, however, no significant changes in pressure coefficient values were observed for 45°, 90°, and 135° wind directions.

These findings advance the understanding of wind loading and contribute to improving the design of solar carports to better withstand extreme weather events. Data from these wind tunnel tests will be invaluable in assessing the effectiveness of the current design approach, which is based on

ASCE 7-22 provisions for open buildings with mono-slope free roofs. These provisions were not originally intended for solar carports, which exhibit different aerodynamic behavior and are more susceptible to wind induced vibrations due to the flexible nature of the PV panel glass compared to mono-slope roofs. As a result, this research will inform updates to the ASCE 7-22 standard, ensuring that solar carports are more resilient against severe weather conditions.

The next steps, planned before the end of the year, include analyzing the behavior of peak pressure coefficients and the pressure coefficient distribution in Zone 1. These results will be compared with the provisions outlined in ASCE 7-22. Additionally, the findings will be evaluated against current industry practices to determine whether existing design methods are sufficient or if new provisions are needed for these types of structures. Another key focus of the study will be the investigation of roof mounted solar carports as well as quantifying wind-induced dynamic effects, which may necessitate further experimental testing.

Acknowledgment

The authors would like to acknowledge financial support from the State of Florida Division of Emergency Management (FDEM). The experiments at the WOW EF were greatly facilitated by the fine works of the WOW staff members Dr. Steven Diaz, Dr. Dejiang Chen, James Erwin, and Houssam Al Sayegh. The opinions, findings, conclusions, or recommendations expressed in this article are solely those of the authors and do not represent the opinions of the funding agencies.

References

Akin, B. (2021). "Feds Replacing and Upgrading Solar Systems on District Court Buildings". *https://stthomassource.com/content/2021/09/27/feds-replacing-and-upgrading-solar-systems-on-district-court-buildings-in-v-i/*. (2021, September 27).

Aly, M. A. (2016). “On the evaluation of wind loads on solar panels: The scale issue.” *Solar Energy*, 135(2016), 423–434.

Aly, M. A. and Whipple, J. (2021). “Wind Forces on Ground-Mounted Photovoltaic Solar Systems: A Comparative Study.” *Applied Solar Energy*, Bol. 57, No. 5, 444–471.

SCE. (2021). *Wind tunnel testing for buildings and other structures*. *ASCE Standard*, American

Society of Civil Engineers (ASCE), Reston, VA, USA.

ASCE. (2022). *Minimum Design Loads and Associated Criteria for Buildings and Other Structures*. American Society of Civil Engineers (ASCE), Reston, VA, USA.

Chowdhury, A. G., Vutukuru, K. S., and Moravej, M. (2018). "Full- and Large-Scale Experimentation Using the Wall of Wind to Mitigate Wind Loading and Rain Impacts on Buildings and Infrastructure Systems." *Proceedings of the 11th Structural Engineering Convention (SEC18)*, Jadavpur University, Kolkatta, India.

Chowdhury, A. G., Zisis, I., Irwin, P., Bitsuamlak, G., Pinelli, J. P., Hajra, B., and Moravej, M. (2017). "Large-scale experimentation using the 12-fan wall of wind to assess and mitigate hurricane wind and rain impacts on buildings and infrastructure systems." *Journal of Structural Engineering (United States)*, 143(7), 1–16.

Daniel, I. (2023). "Ground-mounted Solar Panels: Is it your best bet?". *https://www.integratesun.com/post/ground-mounted-solar-panels-is-it-your-best-bet/*. (2023, July 24).

Ecopower Solar (2024). "Solar Canopy Structures". *https://ecopowersolar.com*. (2025, June 25).

ESDU. (2001). "Characteristics of the Atmospheric Boundary Layer, Part II: Single Point Data for Strong Winds (Neutral Atmosphere) (Item 85020). Engineering Sciences Data Unit." Engineering Science Data Unit.

Helios Energy (2025). "Solar Projects: Ron de Lugo Federal Building and Courthouse St. Thomas, U.S. Virgin Islands". *https://heliosenergyus.com/projects/ron-de-lugo-federal-building-and-courthouse-st-thomas-u-s-virgin-islands/*. (2025, June 21).

International Building Code (2024). "2024 International Building Code (IBC)". *https://codes.iccsafe.org/content/IBC2024V1.0/chapter-2-definitions#IBC2024V1.0_Ch02_Sec202*. International Code Council, (2025, June 21).

Irwin, H., Cooper, K. R., and Girard, R. (1979). "Correction of distortion effects caused by tubing systems in measurements of fluctuating pressures." *Journal of Industrial Aerodynamics*, Elsevier, 5, 93–107.

Lieblein, J. (1974). *Efficient methods of extreme-value methodology*. *NBSIR 74-602*, Washington DC.

Mibet Energy (2024). "Solar Knowledge". *https://www.mbt-energy.com/knowledge/solar-panel-roof-mounting-brackets/*. (2024, July 19).

Mooneghi, M. A., Irwin, P., and Chowdhury, A. G. (2016). “Partial turbulence simulation method for predicting peak wind loads on small structures and building appurtenances.” *Journal of Wind Engineering and Industrial Aerodynamics*, Volume 157, 47-62.

Precedence Research (2025). "Solar Carport Market Siize and Forecast 2025 to 2034". https://www.precedenceresearch.com/solar-carport-market. (2025, February 06).

FIU International Hurricane Research Center
FLORIDA INTERNATIONAL UNIVERSITY

A Resource for the State of Florida

SECTION 3a:

Understanding Hurricane Effects on Manufactured Homes

Report for the Period 2024-2025

A Research Project Funded by:

Florida Division of Emergency Management

Prepared by
Elaina J. Sutley, PhD.
William Collins. PhD.

Graduate Students
Pedro Marquez
Andres Alvarado Cueva

Undergraduate Student
Mauricio Garcia

July 31, 2025

Executive Summary

This report presents the research outcomes from Phase IV of the project carried out at the University of Kansas (KU), which consisted of the following three tasks:

- Task 1: Perform additional component and connection testing to gain necessary statistics for informing fragility functions and FEM
- Task 2: Continue building collaborations with federal agencies and manufactured housing industry to endorse testing full-scale manufactured homes
- Task 3: Collaborate with partner institutions, FIU and UA, on their research tasks.

Task 1 executed full-scale connection tests of roof sheathing-to-rafter and roof-to-wall connections commonly found in Wind Zone II and Wind Zone III manufactured homes. The Phase IV testing focused on (a) completing endwall connection tests for roof to wall connections; (b) increasing the number of roof sheathing to rafter specimens tested for each unique connection design from past phases with attention to using a consistent cyclic protocol across a sufficient minimum number of specimens; and (c) investigating and designing enhanced connections in anticipation for Phase V. During Phases I and II the cyclic protocol was still being refined for what would work best for the finite element model. Phase IV focused on completing connection tests using the final cyclic protocol, which required additional tests for roof sheathing to rafter connections, ensuring a minimum number of tests had been done for all connections and designs. Task 2 strengthened relationships with federal partners, non-government organizations, as well as the broader research community. Task 3 consisted of passing all experimental data to the UA and FIU teams, as well as participating in team calls to collaborate on research design and process decisions. During Phase IV, the KU team submitted one manuscript for journal publication on roof the wall connection tests.

The connection-level experiments further demonstrated that screw connections and connections in stagger pattern perform substantially better and given that calculated capacities are not consistently conservative, calling out these structural details for critical load path connections is appropriate. Testing of remedial measures that enhance performance and full-scale wind tunnel testing of a manufactured housing unit is recommended to validate system level performance and to validate design measures that may improve performance.

1. Introduction

Across the U.S., Florida houses one of the highest percentages of residents living in manufactured housing (MH). Per U.S. Census Bureau data, approximately 7% of Florida households live in MHs, and just over 8% of new manufactured homes have been sold or shipped to buyers in the State of Florida in the past three years, since the start of this project. In recent years, Florida has continued to be impacted by high wind events, including hurricanes and tornadoes, that also continue to expose the disproportionate performance of and damage to MHs. The overall goal of this research is to provide the fundamental and practical knowledge needed to significantly reduce the physical vulnerability of manufactured homes to wind events through a quantitative capture of structural design levels for Wind Zone II and Wind Zone III MHs. Limited research, outside of this partnered project supported by the Florida DEM, has been conducted on the structural design and performance of MHs. Of the limited research that exists on MHs, the focus is on anchorage systems, and there is a dearth in coverage on many observed failure modes, including roof and wall cladding loss and system failure. In 2018 after Hurricane Michael, our team documented significant damage induced by key load path connections to MHs located in Florida. The field observations became the focus of this multi-phase project. Research documented in this report aims to advance code provisions, policies, and manufacturing processes, to better protect manufactured home residents.

This report presents the research from Phase IV of the project carried out at the University of Kansas (KU), which consisted of the following three tasks:

- Task 1: Perform additional component and connection testing to gain necessary statistics for informing fragility functions and FEM
- Task 2: Continue building collaborations with federal agencies and manufactured housing industry to endorse and/or sponsor testing full-scale manufactured homes
- Task 3: Collaborate with partner institutions, FIU and UA, on their research tasks

The methodology, results and conclusions are reported for Tasks 1, 2, and 3 throughout this report. As a primer for Task 1, it is important to note that Phase I focused on Roof Sheathing to Rafter (S2R) connections; Phase II on Wall to Floor (W2F) connections, and initiated Roof to Wall (R2W) connection tests. Phases I and II performed few (3 to 5) cyclic tests for each examined connection design. Phase III focused on increasing the number of tests (8 or more) for each connection design for S2R, W2F and R2W connections. Additionally, a new configuration for S2R connections was added in Phase III. During Phase I and II, the cyclic protocol changed based on feedback from the UA team and their work on the finite element model. In Phase IV, the KU team (a) completed endwall connection tests for roof to wall connections; (b) increased the number of specimens tested for each unique roof sheathing to rafter connection design from past phases with attention to using a consistent cyclic protocol across a sufficient minimum number of specimens; and (c) investigated and designed enhanced connections in anticipation for Phase V. All tested connections are based on input from HUD and based on the structural drawings provided to the team by Clayton Homes and the Federal Emergency Management Agency, are considered typical for Wind Zones II and III.

Regarding Task 3, importantly, the research reported in this chapter fits into a multi-university collaborative project that includes researchers at the University of Alabama (UA) and Florida International University (FIU). The UA team is developing an advanced finite element model

(FEM) of a manufactured home, whose connections are informed by the test data obtained from KU. The FIU team has performed wind tunnel tests to obtain necessary wind pressure coefficients and system-level validation for the collaboration work. During each phase, all experimental data generated at KU is cleaned and passed to the UA and FIU teams, and the group has collaborated on two peer-reviewed manuscripts (one led by UA and one led by KU), and next steps for the full-scale testing planned for Phase V at the FIU Wall of Wind which aims to validate the FEM and the increased capacity of remedial measures designed and tested at KU.

The report is organized with a brief background to provide context to the study, which is followed by the methodology, results, and conclusions for each task.

2. Background

The design of manufactured homes is governed by the U.S. Department of Housing and Urban Development standard *Manufactured Home Construction and Safety Standards, Part 3280*, (termed HUD Code herein) which has not seen significant updates to its hazard design criteria since 1994, and in which the wind hazard maps and tabulated design pressures are developed from and reference use of the 1988 version of ASCE/ANSI 7 *Minimum Design Loads and Associated Criteria for Buildings and Other Structures*. While site-built housing, and all other built structures have benefited from 35 years of technical and statistical advancements in wind engineering, provisions for manufactured homes have remained stagnant. Past events have demonstrated manufactured housing units to be particularly vulnerable to windstorms, including hurricanes and tornadoes. Manufactured housing uses wood frame construction that is constructed fundamentally differently from site-built housing necessitating the need for MH to be studied specifically.

Our 2018 post-Hurricane Michael field reconnaissance demonstrated high variability in manufactured home construction, within and across Wind Zones, which correlates to performance (Sutley et al. 2020). There is no publicly available information on how manufactured homes are constructed. However, Clayton Homes shared their structural drawings with our team for Wind Zone II and III homes; a representative from HUD also provided some additional context on how the Clayton Homes designs vary from those from other manufacturers. The specimens tested here come from those design and construction insights. Quantifying connection capacity and cyclic performance becomes a critical first step in understanding and quantifying system level performance, and thus is the target of this research.

3. Methodology

3.1 Stakeholder Engagement

During Phase I, the stakeholder engagement task had an intentional structure which involved hosting meetings with an advisory board to gain feedback on important decisions early in the project, to build new connections for the project team with relevant experts, and to stimulate interest and momentum in the study of manufactured housing. Phase II continued building on many of the decisions made during Phase I, and leveraged new relationships gained during Phase I to facilitate focused conversations instead of large advisory group discussions.

Phase II stakeholder engagement did not include any group meetings, and instead relied on individual discussions via phone calls, emails and social media (LinkedIn and Facebook) communications.

Phase III similarly maintained direction based on the Phase I meetings, and maintained connections built during the prior two years, including additional meetings with individuals in the broader research community, the Urban Institute, Clayton Homes and strong relationships with the Institute for Business and Home Safety (IBHS), the Applied Technology Council (ATC), Headwaters Economics, the Federal Emergency Management Agency's (FEMA) Mitigation group, as well as FEMA's Individual Assistance group, who will all be critical in the translation of this research to practice.

Phase IV has similarly maintained direction based on the Phase I meetings, finally completing the initial scope of planned tests and shifting to focus on remedial measures in Phase V. Relationships with the broader research community and manufactured housing stakeholders have continued. Clayton Homes, the Lincoln Institute, and FEMA have continued to be generous with sharing information to help the team expand their knowledge. FEMA has also committed three de-commissioned full-scale manufactured housing units for full-scale testing at the Wall of Wind in Phase V.

3.2 Connection Tests

As described in the Introduction, Phase IV focused on completing endwall connection tests for the Roof to Wall (R2W) connections and increasing the number of tests for Roof to Rafter (S2R) connections using a consistent cyclic protocol for cyclic characterization. All tested connections are based on input from HUD and based on the structural drawings provided to the team by Clayton Homes and are considered typical for Wind Zones II and III. For the testing, the KU team used a two-step quasi-static cyclic testing protocol, which started with monotonic testing to inform the cyclic testing phase. This section details the test configuration, nomenclature, setup and load protocol.

The methodology has not changed from previous phases, and thus this section is mostly repeated for convenience from the Phase III report.

3.2.1 Test configuration

The HUD Code requires connections to be engineered to resist specified pressures but does not detail connection design or fastener schedules. For the S2R connection, a 150-mm (6-in.) fastener spacing was adopted per the International Building Code (2018) for hurricane-prone regions. Table 1a lists the fastener diameter, length, thread patterns, and wood material properties for the S2R connections per the National Design Specification (2018). Table 1b provides the same details for the R2W connections.

Table 1a: Geometric Properties of Roof Sheathing to Rafter (S2R) Connection

Component	Description	Geometric Properties
Rafter	Spruce-Pine-Fir (SPF)	38.1-mm x 88.9-mm (1.5-in. x 3.5-in.)
	Southern Yellow Pine (SYP)	38.1-mm x 88.9-mm (1.5-in. x 3.5-in.)
Sheathing	Oriented Strand Board (OSB)	11.1-mm (7/16-in.) thick
	3-Ply Plywood	12.7-mm (0.5-in.) thick

Fastener	Type	Length mm (in.)	Shank Diameter mm (in.)	Head Diameter mm (in.)	Thread Length mm (in.)
Smooth Shank Nail	8d common	60.33 (2.38)	2 3/8 (0.11)	7.15 (9/32)	n/a
Screw	#8	50.8 (2.0)	2.819 (0.11)	10.82 (0.43)	33 (1.3)

Table 1b: Geometric Properties of Roof to Wall (R2W) Connection

Location	Component	Material	Geometric Properties, mm (in.)
Sidewall	Stud	Spruce-Pine-Fir (SPF)	38.1x 88.9 (1.5x 3.5)
	Top Plate	Spruce-Pine-Fir (SPF)	38.1 x 88.9 (1.5 x 3.5)
	Edge Rail	Spruce-Pine-Fir (SPF)	19.1 x 88.9 (0.75 x 3.5)
	Bottom Chord	Spruce-Pine-Fir (SPF)	38.1 x 38.1 (1.5 x 1.5)
	Top Chord	Spruce-Pine-Fir (SPF)	38.1 x 63.5 (1.5 x 2.5)
Endwall	Stud	Spruce-Pine-Fir (SPF)	38.1x 88.9 (1.5x 3.5)
	Top Plate	Spruce-Pine-Fir (SPF)	38.1 x 88.9 (1.5 x 3.5)
	Ceiling	Gypsum board	12.7 x 88.9 (0.5 x 3.5)
	Bottom Chord	Spruce-Pine-Fir (SPF)	38.1 x 38.1 (1.5 x 1.5)

Component	Type	Length mm (in.)	Width mm (in.)	Shank Diameter mm (in.)	Head Diameter mm (in.)	Crown Length mm (in.)
Staple	15 Gauge	63.5 (2.5)	N/A	1.83 (0.072)	N/A	11.1 (0.438)
	16 Gauge	31.8 (1.25)	N/A	1.59 (0.0625)	N/A	11.1 (0.438)
Smooth Shank Nail	Clipped Head	76.2 (3)	N/A	3.3 (0.131)	7.3 (0.286)	N/A
		50.8 (2)	N/A	2.5 (0.099)	6.1 (0.242)	N/A
Strap at sidewall	26 Gauge	368.3 (14.5)	38.1 (1.5)	N/A	N/A	N/A
Strap at endwall	26 Gauge	152.4 (6)	38.1 (1.5)	N/A	N/A	N/A

3.2.2 Test matrices

The test matrix for each connection type is defined based on the available drawings and HUD documentation. Lumber and sheathing for this study were purchased locally, with all lumber graded No. 2 or better. Fasteners were installed using a pneumatic tool fitting the specified fastener (nails or staples), while screws were installed using a cordless drill.

Sheathing to Rafter

In Wind Zone II MH, nails are typically used for roof sheathing-to-rafter connections, as specified by the HUD representative's documentation to our team and confirmed by post-hurricane field observations. Screws are rarely used but were tested in this study to explore potential capacity increases. Table 2a summarizes the component details and number of tests for the S2R connection specimens. These configurations include a single field fastener on 203-mm x 203-mm (8-in. x 8-in.) sheathing, two field fasteners spaced 150 mm (6 in.) center-to-center on 203-mm x 203-mm (8-in. x 8-in.) sheathing, and two fasteners, one field and one edge, spaced 150 mm (6 in.) center-to-center on 203-mm x 203-mm (8-in. x 8-in.) sheathing with the edge fastener located 9.5-mm (3/8-in) from the edge of the sheathing. Figure 1 presents an example of each geometric configuration (CFG) with fastener location.

a) b) c)

Figure 1: S2R specimens: (a) single field fastener on 203-mm x 203-mm (8-in. x 8-in.) sheathing; (b) two field fasteners spaced 150-mm (6-in.) center-to center on 203-mm x 203-mm (8-in. x 8-in.) sheathing; (c) two fasteners, one field and one edge, spaced 150-mm (6-in.) center-to center on 203-mm x 203-mm (8-in. x 8-in.) sheathing with edge fastener at 9.5-mm (3/8-in) from sheathing edge.

Table 2a: Roof Sheathing to Rafter (S2R) Test Matrix

Type	ID	Name	Sheathing Type and Size	Fastener	Monotonic Tests*	Cyclic Tests**
A	1	O-N-F1	OSB 203 mm x 203 mm (8 in. x 8 in.)	(1) 8d Nail	3	8
	2	O-S-F1		(1) #8 Screw	3	8
	3	P-N-F1	Plywood 203 mm x 203 mm (8 in. x 8 in.)	(1) 8d Nail	3	8
	4	P-S-F1		(1) #8 Screw	3	8
B	5	O-N-F2	OSB 203 mm x 203 mm (8 in. x 8 in.)	(2) 8d Nail	3	8
	6	O-S-F2		(2) #8 Screw	3	8
	7	P-N-F2	Plywood 203 mm x 203 mm (8 in. x 8 in.)	(2) 8d Nail	3	8
	8	P-S-F2		(2) #8 Screw	3	8

C	9	O-EN-F2	OSB 203 mm x 203 mm (8 in. x 8 in.)	(2) 8d Edge Nail	3	8
	10	O-ES-F2		(2) #8 Edge Screw	3	8
	11	P-EN-F2	Plywood 203 mm x 203 mm (8 in. x 8 in.)	(2) 8d Edge Nail	3	8
	12	P-ES-F2		(2) #8 Edge Screw	3	8

Roof to Wall

The sidewall and endwall connections are illustrated in Figure 3. After assembly, holes were drilled for fixture installation. Additionally, for the sidewall connection, a mending plate was used to facilitate construction of the sidewall connection, as shown in Figure 3b. During specimen preparation, it was frequently observed that the staples pulled through the straps during installation, even when the staple gun pressure was carefully calibrated. Table 2c presents the configurations for the seven unique configurations (CFG).

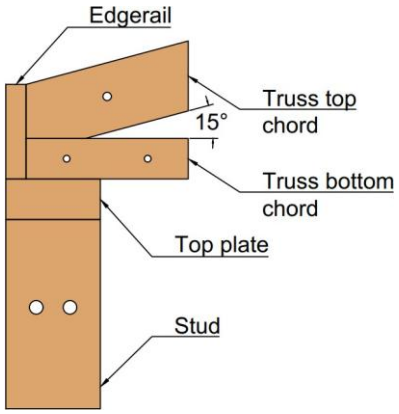

a)

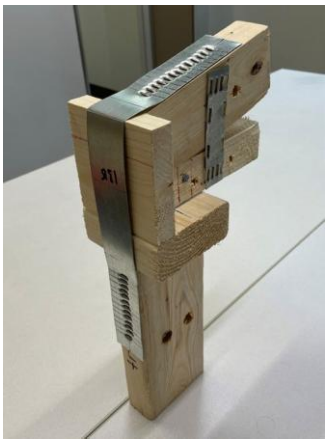

b)

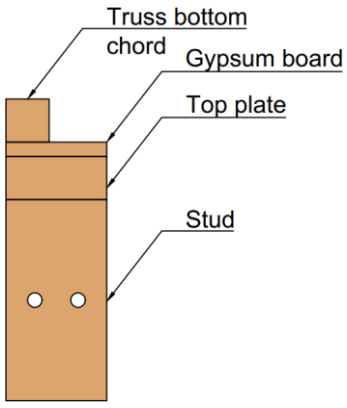

c)

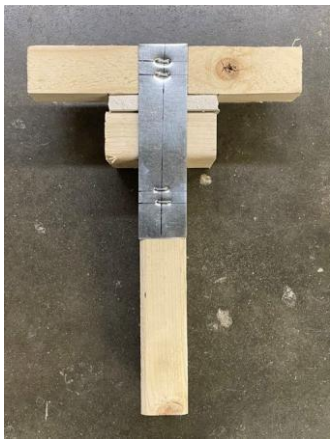

d)

Figure 3. Roof to Wall connections: a) Sidewall side view illustration of wood components; b) Sidewall picture of the specimen c) Endwall side view illustration of wood components; d) Endwall front view picture of the specimen

Table 2c: Roof to Wall (R2W) Test Matrix

CFG	Fastener	Pattern	Species	Monotonic Tests	Cyclic Tests	Wall Location
1	(6) 3.3-mm (0.131-in.) Nails-R	Row	SPF	3	8	Sidewall
2	(6) 3.3-mm (0.131-in.) Nails-S	Stagger	SPF	3	8	Sidewall
3	(13) 16 Gauge Staples-R	Row	SPF	3	8	Sidewall
4	(13) 16 Gauge Staples-S	Stagger	SPF	3	8	Sidewall
5	(2) 3.3-mm (0.131-in.) Nails-R	Row	SPF	3	8	Endwall
6	(2) 15 Gauge Staples-R	Row	SPF	3	8	Endwall
7	(4) 2.5-mm (0.099 in.) Nails-2R	Row	SPF	3	8	Endwall

3.2.3 Test Name Nomenclature

The S2R connection test names indicate the test type, sheathing material, rafter lumber species, fastener type, count, and location, with the last three digits representing the specimen number. Monotonic and quasi-static cyclic tests are represented by M and C, respectively. For example, M-O-S-SPF-F1-001 refers to the first monotonic test (M) on OSB (O) sheathing with screws (S) to an SPF rafter (SPF) with one field fastener (F1). For edge fasteners, E is added before the fastener type.

For R2W connections, additional letters indicate 'R' for roof connection, fastener type and pattern: 3.3 mm (0.131 in.) nails are designated A (row) and B (stagger), 2.9 mm (0.113 in.) nails are M (row) and N (stagger), 2.5 mm (0.099 in.) nails are G (row) and H (stagger), 15-gauge staples are J (row) and K (stagger), and 16-gauge staples are D (row) and E (stagger). Therefore, if a R2F specimen uses a spruce-pine-fir floor joist, a fastener pattern of six nails with a diameter of 3.3-mm (0.131-in.) in a row, and is the first specimen of the set, the label for the specimen is RM-6A-SPF-001.

3.2.4 Test Fixture

A steel fixture was designed and fabricated for each connection type to be compatible with a 266-kN (60-kip) capacity Baldwin screw-drive test frame. Each fixture uses a 57.2-mm (2.25-in.) wide plate with a thickness of 25.4 mm (1 in.) and a length sufficient to pass through the Baldwin grips and attach to the associated grips. These fixtures enabled the transfer of both monotonic and cyclic forces to the connections.

Sheathing to Rafter

The S2R test fixture consists of a bottom sheathing grip made from A36 steel plate with dimension 76.2-mm x 457.2-mm x 25.4-mm (3-in. x 18-in. x 1-in.), top sheathing grip is a hollow square section (HSS) with dimension 254-mm x 101.6-mm x 12.7-mm (10-in. x 4-in. 0.5-in.), as shown in Figure 4. A 101.6-mm (4-in.) opening along one side of the 254-mm (10-in.) length of the HSS was made to create allowance for holding the sheathing. While the bottom holds the rafter fixed in place, the top fixture grip transfers force through the sheathing into the fasteners, mimicking wind uplift on roof sheathing by attempting to extract the fasteners vertically from the rafter. To enable fully reversed displacement during cyclic loading, clamps were used to attach the sheathing to the top grip as shown in Figure 4b.

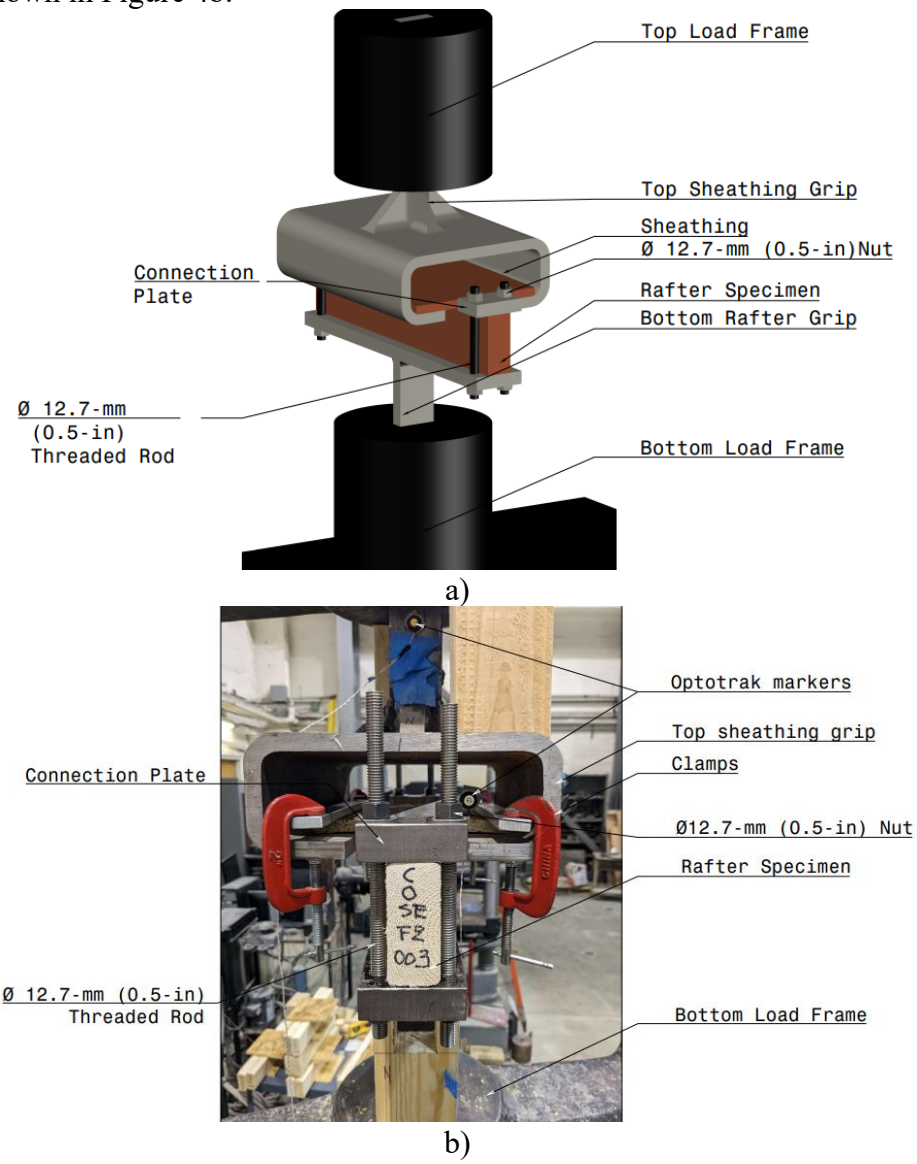

Figure 4: Roof Sheathing to Rafter (S2R) Test Fixture: (a) Schematic; (b) Photograph in lab

Roof to Wall

For theR2W tests, a steel fixture was designed and fabricated for each connection type to be compatible with a 266-kN (60-kip) capacity Baldwin screw-drive test frame. The RTW connection

fixture for the sidewall is shown in Figure 5, and the RTW connection fixture for the endwall is shown in Figure 6. Each fixture incorporated a 57.2 mm (2.25 in.) wide, 25.4 mm (1 in.) thick steel plate of sufficient length to pass through and attach to the Baldwin grips. These fixtures enabled the transfer of both monotonic and cyclic loads to the connection. The connection fixture consisted of a steel frame with two independent gripping assemblies, one for the roof structure and one for the wall stud. Fixtures were constructed from welded A36 steel plates. The bottom grip secured the stud using two 12.7 mm (0.5 in.) threaded rods that passed through the stud and a pair of 158.8 mm × 33.35 mm × 25.4 mm (6.25 in. × 5.25 in. × 1 in.) side plates. These plates were welded to a base plate measuring 158.8 mm × 260.4 mm × 25.4 mm (6.25 in. × 10.25 in. × 1 in.), which connected to the main plate that passed through the Baldwin grips.

As shown in Figure 5, the sidewall connection was secured using two 6.4 mm (0.25 in.) diameter bolts into the bottom chord and one 7.9 mm (0.313 in.) diameter threaded rod into the top chord. These fasteners passed through the roof structure and two 152.4 mm × 146.1 mm × 25.4 mm (6 in. × 5.75 in. × 1 in.) steel plates that were welded to a 158.8 mm × 165.1 mm × 25.4 mm (6.25 in. × 6.5 in. × 1 in.) base plate. The bottom chord bolts were evenly spaced, and the top chord threaded rod was aligned with the bolt furthest from the connection joint.

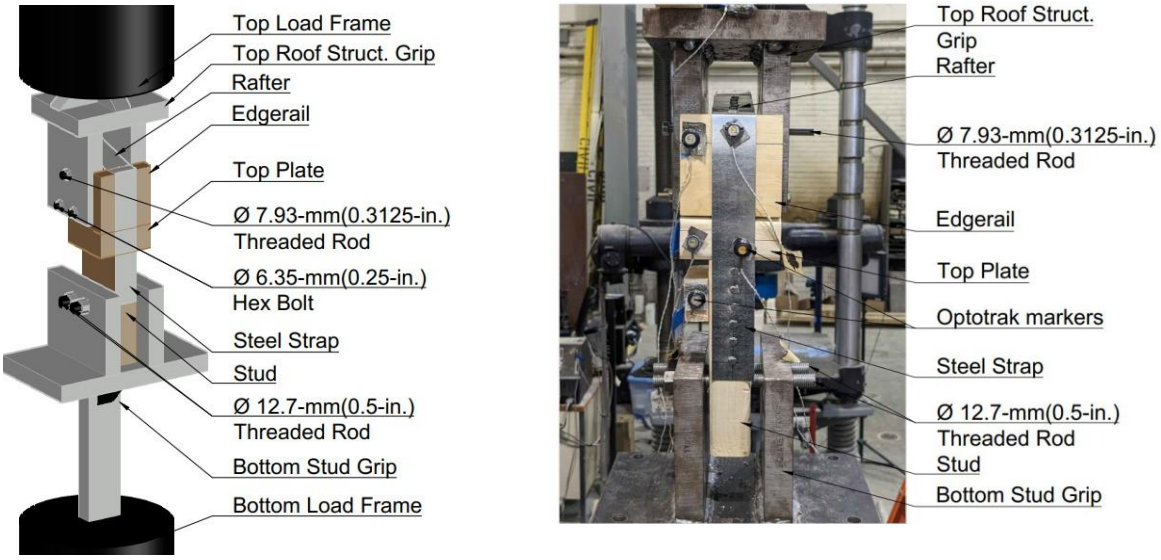

a) b)

Figure 5. Roof-to-wall fixture for sidewall connections: (a) schematic; (b) photograph in lab

As shown in Figure 6, the endwall connection featured a similar steel frame composed of two separate grips: one securing the bottom chord and the other the wall stud. The fixture was fabricated from welded A36 steel plates. For the stud grip, two 12.7 mm (0.5 in.) threaded rods passed through the stud and a pair of 127 mm × 120.7 mm × 25.4 mm (5 in. × 4.75 in. × 1 in.) plates to hold it in place. These plates were welded to a base plate measuring 127 mm × 158.8 mm × 25.4 mm (5 in. × 6.25 in. × 1 in.), which was connected to a plate interfacing with the Baldwin grip. The bottom chord was secured by clamping a 50.8 mm × 152.4 mm × 25.4 mm (2 in. × 6 in. × 1 in.) connection plate to each side using 12.7 mm (0.5 in.) threaded rods. These plates pressed

the chord against a top steel plate measuring 330.2 mm × 152.4 mm × 25.4 mm (13 in. × 6 in. × 1 in.), which was also connected to a plate interfacing with the Baldwin grip.

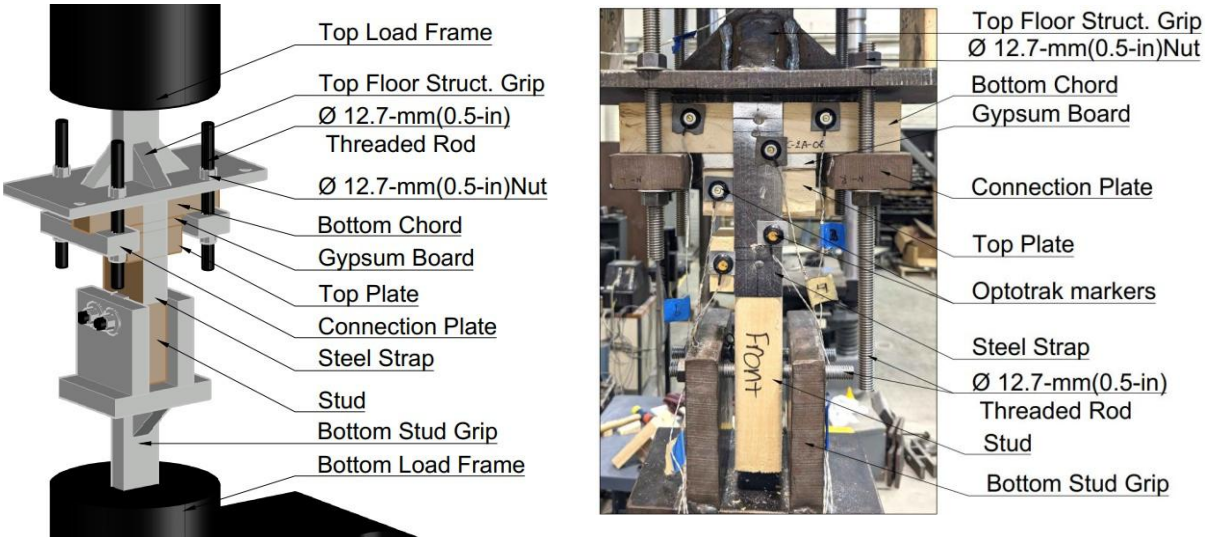

a) b)

Figure 6. Roof-to-wall fixture for endwall connections: (a) schematic; (b) photograph in lab

3.2.5 Load Protocol

The two-part load protocol included monotonic testing and a two-step quasi-static cyclic protocol based on FEMA 461 (2007) procedures are shown in Figure 7. The monotonic test, performed at a constant displacement rate of 2.54 mm/min (0.1 in./min) per ASTM D 1761 (2020), determined the displacement amplitude for cyclic tests. FEMA 461 requires identifying a displacement for initial damage, Δ_0, and performing at least six cycles before this point and ten cycles before reaching Δ_m, the displacement for maximum load. The displacement corresponding to initial damage was difficult to characterize for these types of connections and the initial damage displacement was approximated at 3.4%. Considering the requirement of six cycles before initial damage, a total of 16 cycles were planned. However, differentiating cycles by 40 percent showed that many cycles had minimal significance due to small displacements. Therefore, only four cycles were performed before reaching the initial damage displacement.

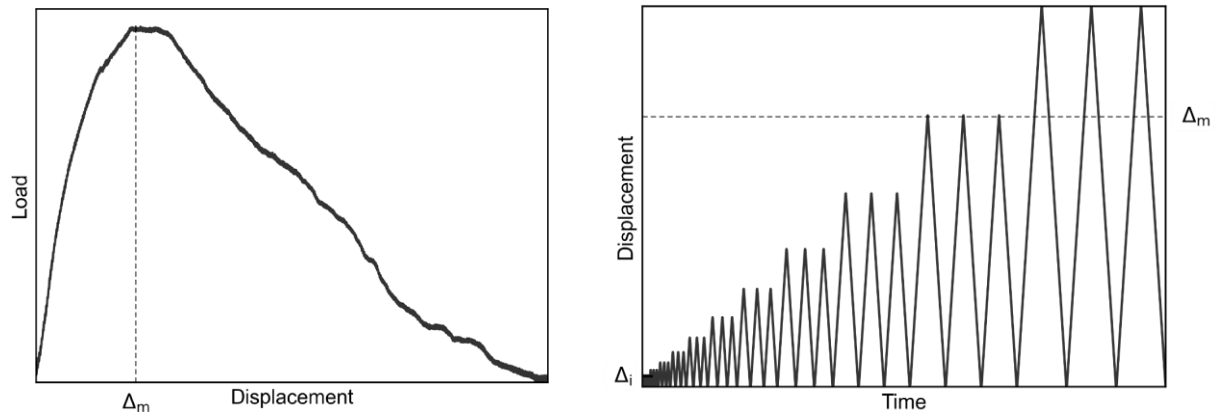

a) b)

Figure 7. Load protocol representation: a) monotonic, b) cyclic

FEMA 461 requires each cycle to load the specimen to the specified displacement twice. For each specified displacement, the specimen was unloaded to the starting location of the specimen. The load protocol was modified in Phase II to provide critical details capturing the load displacement relationship for purposes of developing the finite element model. This modification included adding a displacement of two-thirds of the cycle displacement into each cycle. In the third phase of testing, the protocol was further changed to include three complete cycles for each displacement.

The load response was recorded using the load frame's built-in force transducer at a rate of 10 Hz. Three Optotrak markers measured vertical displacement at various locations, as shown in Figure 4b for the S2R tests and Figure 5b for R2W test. For the S2R tests, markers were attached to the top sheathing grip to measure crosshead displacement and the sheathing centerline to remove sheathing bending from the crosshead displacement. For the R2W endwall connection, markers were attached to the top plate grip to measure crosshead displacement, the left and right sides of the top plate to accurately measure the displacement of the connection, and the stud to measure relative displacement between the plate and the stud. For the R2W sidewall connection, a marker was attached to the roof truss grip to measure crosshead displacement, the edgerail even with the nail placed in the member, the top plate, the stud, and the extents of the strap between the fasteners visible during testing. By tracking the top plate, stud, and edgerail the relative displacement between each of the members in the connection could be tracked.

4. Results

4.1 Stakeholder Engagement

There are limited tangible results to report for the stakeholder engagement, beyond that many conversations with federal agencies and non-governmental organizations did take place, as well as conversations with a manufacturer. There was considerable expressed interest in this research program and commitment of an in-kind contribution of three manufactured homes for full-scale wind tunnel testing in Phase V.

4.2 Roof Sheathing to Rafter Connection Tests

This section presents the results of the S2R tests and compares them to the calculated capacities based on the 2018 National Design Specification from the American Wood Council.

4.2.1 Capacity Evaluation

Single Fastener

The results from cyclic testing across four different configurations are summarized in Table 3. The results showed significant performance variability, with screwed connections outperforming nailed ones by an average factor of 3.39 and exhibiting less variability, as indicated by coefficients of variation (COVs) below or equal to 11%. Additionally, the type of sheathing impacted capacity, increasing it by an average of 16% from OSB to plywood. Displacements in screwed connections were up to 2.7 times greater than in nailed connections. Changing the sheathing from OSB to plywood increased displacement by 85% in nailed connections and by 20% in screwed connections. The cyclic-to-monotonic ratios showed no consistent pattern suggesting the superiority of either cyclic or monotonic loading. However, cyclic capacity dropped to 74% for configuration 3 (P-N-F1), indicating that cyclic effects can decrease connection capacity. Nailed connections exhibited a significant underperformance compared to the calculated capacities, reaching only 84% and 91% for configurations 1 and 3 respectively.

Table 3: Summary of cyclic testing for one fastener (Type A)

ID	Name	Avg. Cyclic Peak Load, N (lbf)	COV	Avg. Displacement, mm (in.)	Cyclic/Monotonic Ratio	Measured/Calculated Ratio
1	O-N-F1	628 (141)	0.27	1.11 (0.04)	1.03	0.84
2	O-S-F1	1976 (444)	0.11	4.54 (0.18)	0.96	1.24
3	P-N-F1	681 (153)	0.18	2.05 (0.08)	0.74	0.91
4	P-S-F1	2478 (557)	0.08	4.27 (0.17)	1.15	1.55

As shown in Figure 8, outliers are observed in configurations 1, 2, and 3. These outliers have no specific cause identified during testing and are attributed to inherent material variability. It was also observed that screwed connections have wider ranges even though they exhibit lower COVs. This is because screws show significantly higher means which reduces the relative impact of variability on the COV. For plywood sheathing, the mean is above the median, indicating a positively skewed distribution. In contrast, OSB shows a symmetric distribution for nails and a positively skewed distribution for screws.

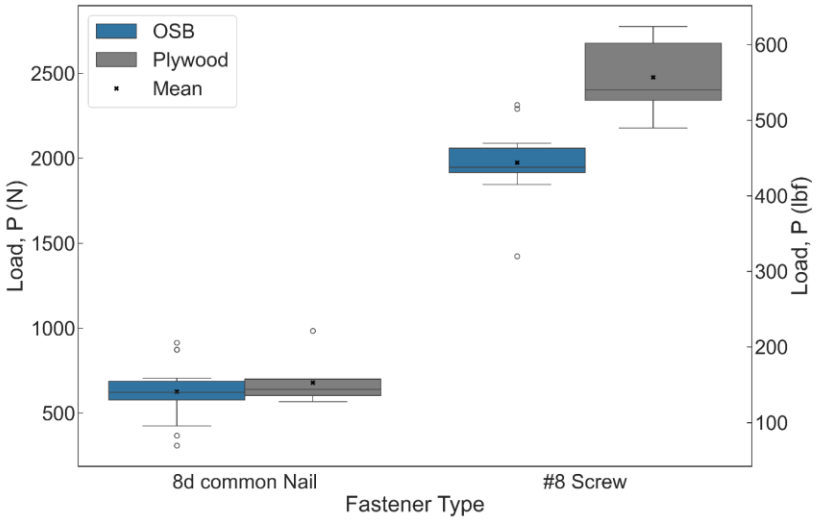

Figure 8: Single fastener comparison for sheathing and fastener types

The two failure modes for connection type A are illustrated in Figure 9. The predominant failure mode in cyclic testing was pull-out, except for configuration 2 (O-S-F1) where the predominant failure mode was pull-through. This behavior is expected, as pull-through failures depend on the strength and frictional resistance of the interacting components. Screws provide greater frictional resistance than nails, while OSB sheathing is less resistant than plywood. Cyclic failure modes resemble monotonic failure modes, with the only exception being configuration 4 (P-S-F1), where pull-through dominated monotonic failures.

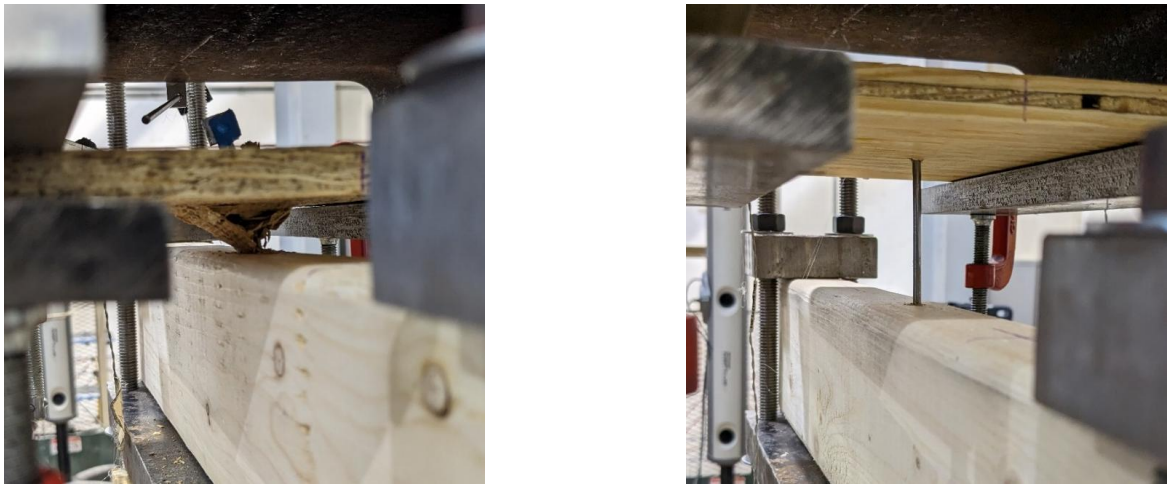

a) b)

Figure 9: Single Fastener Failure Modes: a) Pull through failure for a screwed connection with OSB sheathing (ID 2); b) Pull out failure for a nailed connection with plywood sheathing (ID 3).

Typical cyclic force-deformation curves for cyclic testing, derived from the monotonic tests and the modified FEMA 461 protocol are shown in Figure 10. These plots correspond to tests where the peak load values were close to the average for each specific configuration. A clear difference in capacity between nailed and screwed connections was observed. The plots also show that the

OSB sheathing connection with nails underperformed compared to the NDS calculated capacity, as also indicated in Table 3. In contrast, the OSB sheathing connection with screws demonstrated adequate performance, exceeding the calculated capacity by 26%.

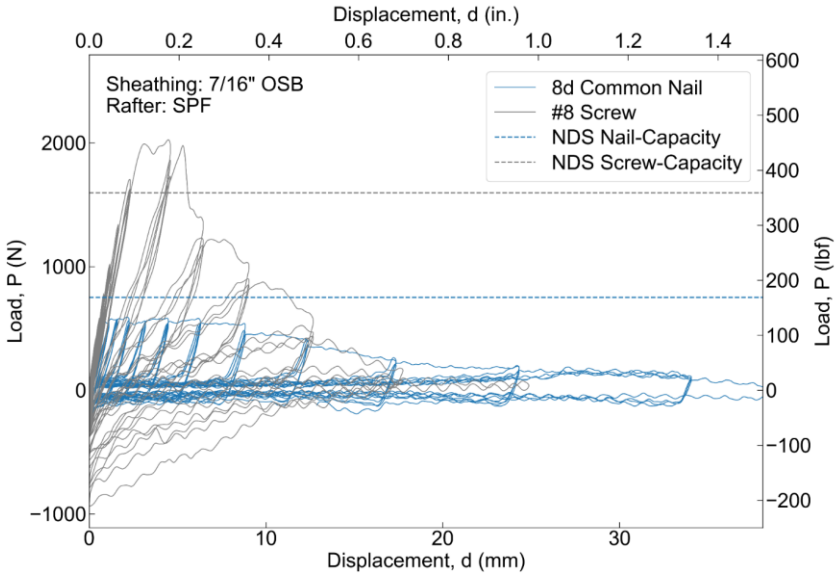

Figure 10: Cyclic force-deformation curve for single fastener, configurations 1 (O-N-F1) and 2 (O-N-F2)

Double Fastener

Table 4 follows the same structure as Table 3 to present the results of double fastener connections across four different configurations. The results showed a similar pattern to the single fastener connection, with screwed connections outperforming nailed ones by an average factor of 3.39 and exhibiting less variability, as indicated by COVs below or equal to 12%. The sheathing type had a more pronounced impact for this connection, increasing capacity by an average of 39% from OSB to plywood. Displacements were also significantly larger for screws, up to 2.18 times that of nailed connections. The sheathing type reduced displacements by 14% in nailed connections but increased them by 39% in screwed connections. The cyclic-to-monotonic ratios indicated that cyclic loading only caused a significant reduction for configuration 6 with a 7% decrease. Comparison with the calculated capacities on the other hand indicates a clear overestimation of load capacity for configurations 5, 6 and 7. Similar to the single fastener connection, the OSB with nail connection had the lowest ratio, reaching only 68% of the calculated capacity.

Table 4: Summary of cyclic testing for double fastener (Type B)

ID	Name	Avg Cyclic Peak Load, N (lbf)	COV	Avg Displacement, mm (in.)	Cyclic/Monotonic Ratio	Measured/Calculated Ratio
5	O-N-F2	1,033 (232)	0.20	3.24 (0.13)	0.99	0.68
6	O-S-F2	2,897 (651)	0.12	5.52 (0.22)	0.93	0.91
7	P-N-F2	1,191 (268)	0.23	2.80 (0.11)	1.11	0.79

8	P-S-F2	4,735 (1,064)	0.08	7.69 (0.30)	1.12	1.48

The significant impact of sheathing type on load capacity is highlighted in Figure 11, with screws showing up to a 63% increase when paired with plywood. This improvement is attributed to plywood's uniform, robust layered veneer composition, which enhances fastener holding capacity and load distribution. The trend of improved performance with screws and plywood is evident. However, variability in nailed connections, likely due to inherent material properties, is reflected by the presence of outliers, with no anomalies observed during testing. Nailed configurations are positively skewed, likely due to the presence of an outlier, while screwed configurations are symmetric.

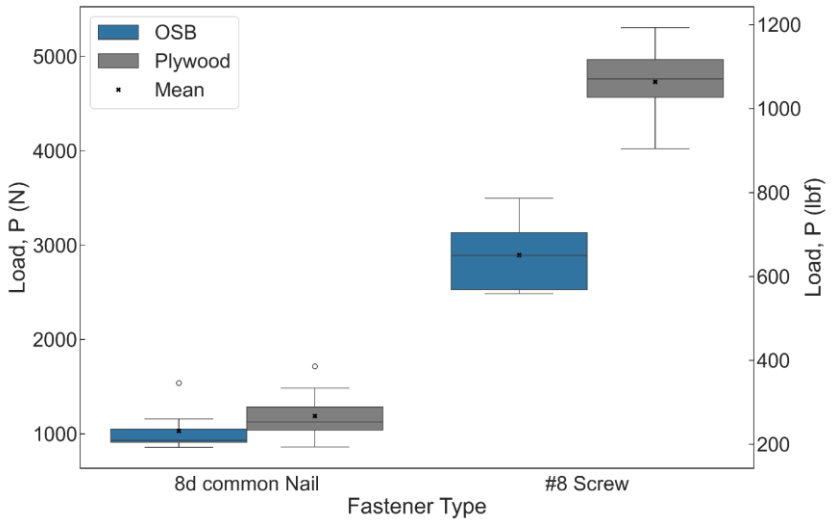

Figure 11: Double Fastener comparison for sheathing and fastener types

The two failure modes observed for connection type B are shown in Figure 12. No single failure mode dominated across all configurations. Pull-out failure occurred in configurations 5 (O-N-F2) and 7 (P-N-F2), while pull-through failure was observed in configurations 6 (O-S-F2) and 8 (P-N-F2). The inherent characteristics of screws, compared to nails, increase the likelihood of pull-through failures due to their stronger engagement with the sheathing. Cyclic failure modes generally mirrored monotonic ones, except for configuration 6 (O-S-F2), where monotonic testing exhibited a mixed mode with each fastener showing a different failure mode.

a) b)

Figure 12: Double fastener failure modes: a) Pull-out failure for a nailed connection with OSB sheathing (ID: 5); b) Pull-through failure for a screwed connection with Plywood sheathing (ID: 8).

Figure 13 illustrates a typical cyclic force-deformation curve for this connection type, highlighting the effect of sheathing type with the same fastener type. OSB sheathing with nails showed significant discrepancy from the calculated capacity, whereas plywood sheathing achieved the calculated capacity. As previously noted, the plots represent tests with peak values near the average for each configuration.

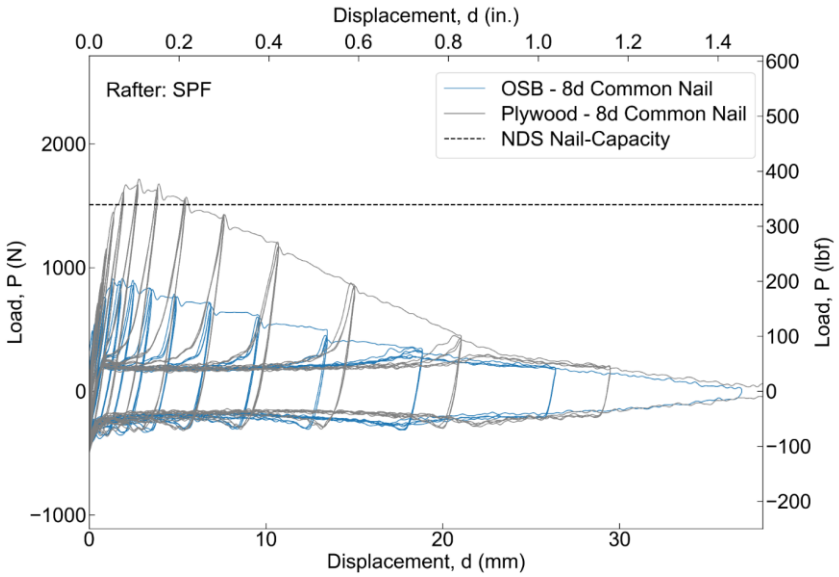

Figure 13: Cyclic force-deformation curve for double fastener, configurations 5 and 7

4.2 Roof to Wall Connection Tests

Sidewall

Table 5 presents the results of cyclic tests performed for sidewall configurations. Staggered patterns outperformed row patterns, increasing strength by 51% in nailed connections and by 6% in stapled connections. In addition, connections using the staggered pattern exhibited lower variability, with

coefficients of variation (COV) below 12%. Displacement measurements were approximately 35% larger in the staggered patterns compared to the row pattern. To further understand the variability in connection behavior, Figure 14 presents the distribution characteristics observed during testing. Nailed connections exhibited significant variability in the row pattern and followed a left-skewed distribution. While the row pattern had a symmetric distribution, it contained noticeable outliers. In contrast, stapled connections demonstrated more consistent behavior, though both connection types still followed a left-skewed distribution.

As summarized in Table 5, the cyclic-to-monotonic strength ratios revealed a reduction in capacity for all configurations. Nailed connections experienced an average decrease of approximately 3%, while stapled connections exhibited a more substantial reduction of about 7%. All tested connections underperformed relative to their calculated capacities, with reductions reaching as low as 62%.

Table 5. Summary of monotonic and cyclic results for Sidewall

ID	Name	Avg Cyclic Peak Load, N (lb)	COV	Avg Disp., mm (in.)	Cyclic/Monotonic Ratio	Measured /Calculated Ratio
1	(6) 3.3-mm (0.131-in.) Nails-R	3456 (777)	0.26	24.44 (0.96)	0.95	0.62
2	(6) 3.3-mm (0.131-in.) Nails-S	5220 (1173)	0.04	39.11 (1.54)	0.99	0.93
3	(13) 16 Gauge Staples-R	5051 (1135)	0.12	34.02 (1.34)	0.92	0.90
4	(13) 16 Gauge Staples-S	5376 (1208)	0.11	39.83 (1.57)	0.93	0.96

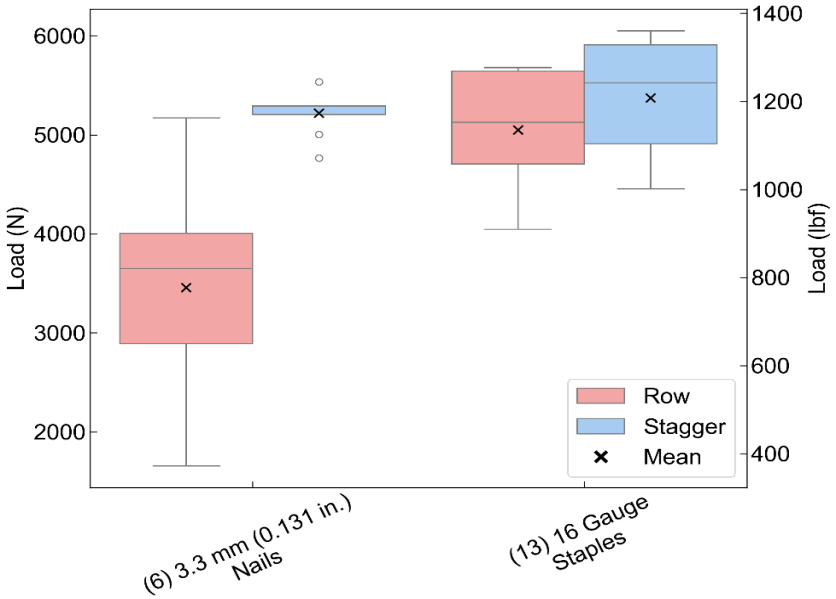

Figure 14. Sidewall connections, comparing fastener types and patterns

Figures 15a and 15b illustrate the failure modes observed in the sidewall connections. In Configuration 1, row splitting was the dominant failure mode, occurring in 95.2% of the specimens; the remaining failures were due to strap rupture. In Configuration 2, strap failure was predominant, occurring in 87.5% of the cases, while the rest exhibited row splitting. Configurations 3 and 4 exhibited strap failure exclusively. Across all configurations, cyclic loading produced failure modes consistent with those observed under monotonic loading.

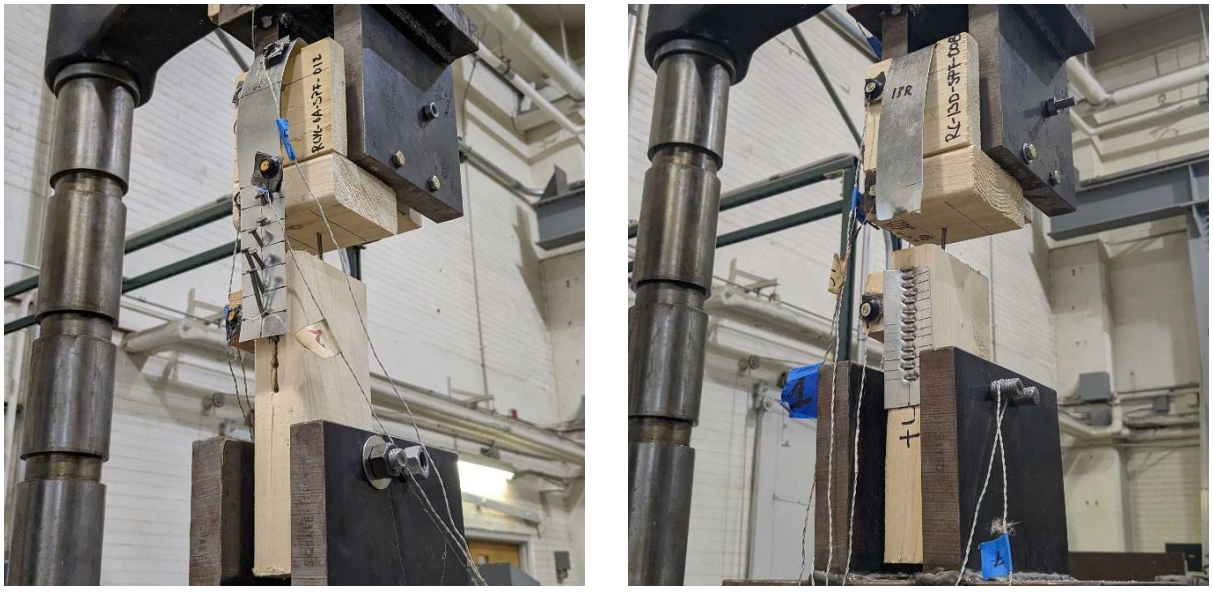

a) b)

Figure 15. Sidewall common failure modes: a) row splitting (ID 1); b) strap failure (ID 3)

Figure 16 illustrates representative cyclic force-deformation curves for this connection type. The trend indicated the outperforming of stagger patterns. It also indicates the difference between row splitting for row patterns and strap failure for stagger patterns. The plots correspond to tests with peak values close to the average for each configuration.

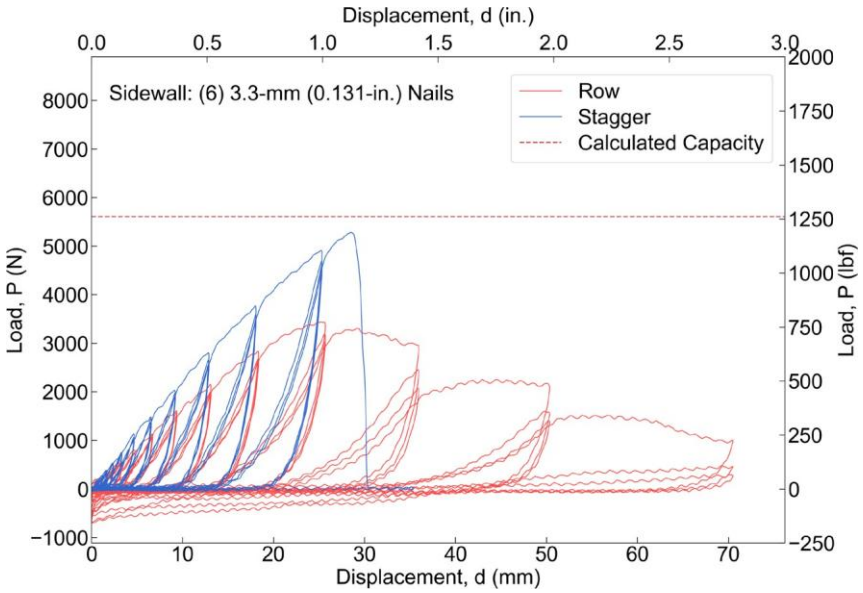

Figure 16. Cyclic force-deformation, sidewall, configurations 1 and 2

Endwall

Table 6 summarizes the cyclic test results for Endwall connections. For the same number of fasteners, stapled connections showed a higher capacity. The coefficient of variation remained below 10% in all cases. No capacity reduction was observed between monotonic and cyclic testing. Figure 17 further explode these findings and presents the distribution of each configuration. Configuration 5 exhibits a symmetrical, compact distribution but with two outliers. Configurations 6 and 7 show slight right and left skewness, respectively. Both have wider distributions than configuration 5 but no outliers. Additionally, as shown in Table 6, tested capacities for all configurations were similar or exceeded calculated values.

Table 6. Summary of monotonic and cyclic results for Endwall

ID	Name	Avg Cyclic Peak Load, N (lb)	COV	Avg Disp., mm (in.)	Cyclic/ Monotonic Ratio	Measured /Calculated Ratio
5	(2) 3.3-mm (0.131-in.) Nails-R	2431 (546)	0.06	11.53 (0.45)	1.03	1.02
6	(2) 15 Gauge Staples-R	2752 (618)	0.10	14.98 (0.59)	1.30	2.08
7	(4) 2.5-mm (0.099 in.) Nails-2R	3437 (772)	0.07	14.02 (0.55)	1.09	1.26

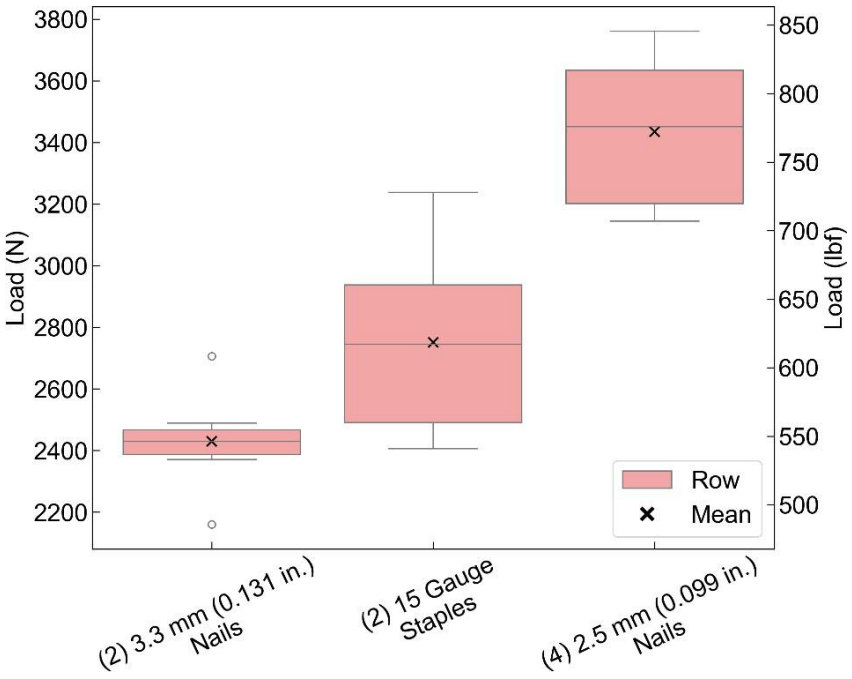

Figure 17. Sidewall connections, comparison fasteners types and patterns

Figures 18a and 18b illustrated the failure modes of Endwall connections. For configuration 5 the main failure mode was pull-out (50% of cases), followed by row splitting with 37.5% and strap failure 12.5%. For configuration 6 pull-out also controlled with a 63.6% and the remaining failures were pull-through. Configuration 7 was completely controlled by pull-out. Cyclic failure modes closely resembled monotonic ones across all configurations, with the only exceptions being strap and pull through failures which were not observed.

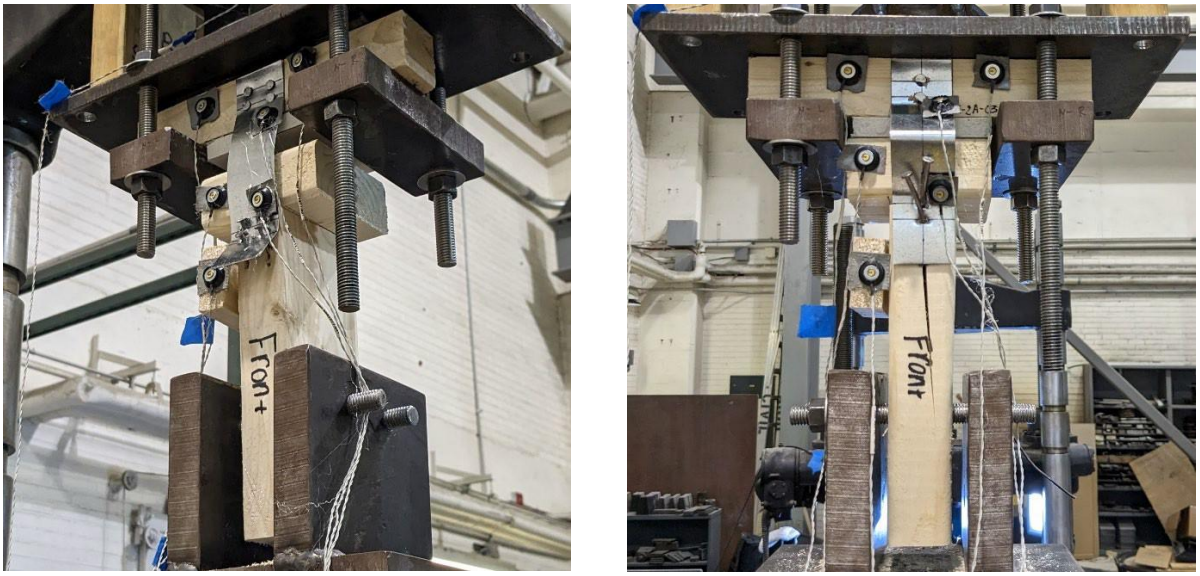

a) b)

Figure 18. Endwall common failure modes: a) pull-out (ID 7); b) row splitting (ID 5)

Figure 19 illustrates typical cyclic force-deformation curves for this connection type. Configuration 5 is slightly lower than the calculated capacity and configuration 6 significantly exceed the calculated capacity as showed in Table 6. The plots correspond to tests with peak values close to the average for each configuration as mentioned previously.

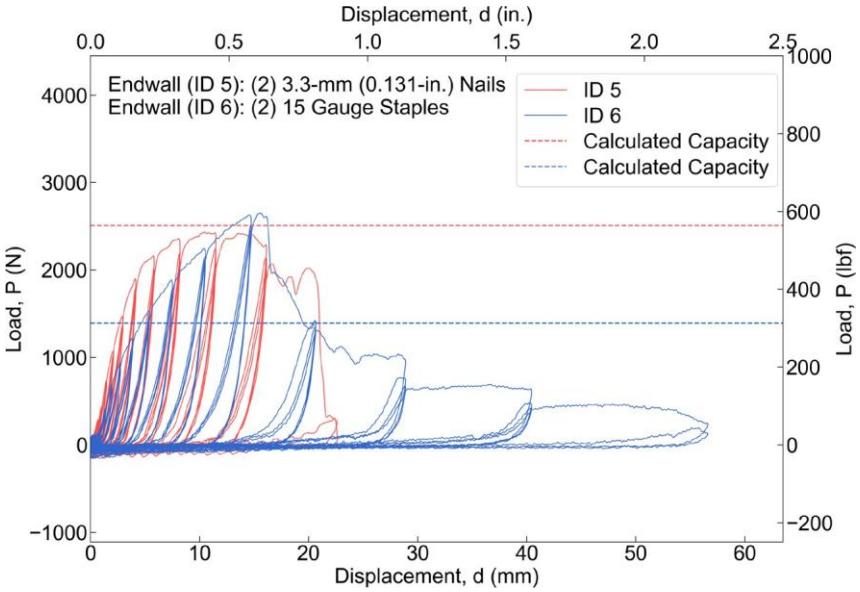

Figure 19. Cyclic force-deformation, endwall, configurations 5 and 6

Conclusions

Stakeholder Engagement

Through conversations with relevant stakeholders, there is significant interest in this research to quantify and improve the wind performance of manufactured homes, and in full-scale wind tunnel testing of a manufactured housing unit. It is critical to maintain engagement with relevant stakeholders to enable continued and additional research on manufactured housing, as well as for translation of the research findings.

Components and Connection Tests

Sheathing to Rafter Connections

Several observations emerge from this experimental study, each highlighting the need for adjustments to current practices to improve structural performance. One key observation is the underperformance of the most common connection types, specifically nails used with OSB and plywood sheathing. This behavior was evident in OSB sheathing configurations O-N-F1 (Type A) and O-N-F2 (Type B), which demonstrate measured-to-calculated capacity ratios of 84% and 68%, respectively. These results suggest that these widely used connections may be inadequate for extreme wind events and highlight the reduction in capacity due to grouping effects (discussed later in this section). For connection type C, results show that having a fastener close to the edge further reduces its capacity, reaching values as low as 71% for OSB and 63% for plywood. The National Design Specification (NDS) may need to account for these effects to more accurately represent the actual behavior of these connections.

The following key findings provide valuable insights into the performance of different connection configurations and materials.

- Nailed connections, particularly with OSB sheathing, exhibited reduced capacities, with measured-to-calculated ratios as low as 68%. Fasteners placed near the edge showed further decreased capacity, emphasizing the possible need for adjustments in design standards to account for edge influence.
- OSB connections experienced a notable 22% reduction in capacity due to fastener grouping, whereas plywood connections were less affected. Increasing fastener density does not always result in proportional capacity gains.
- Plywood sheathing consistently outperformed OSB, with capacity increases up to 49%. Screwed connections provided higher capacities (measured-to-calculated ratios up to 1.55) but exhibited lower ductility compared to nails, which showed greater energy dissipation and damping. Future studies would consider testing ring shank nails as fasteners. Ring shank nails might have higher capacity and ductility.
- Cyclic loading significantly reduced connection capacity for nailed connection, with reductions up to 35% compared to monotonic results. This suggests that current design standards, which rely on monotonic data, may not fully capture actual performance in high-wind conditions. Testing standards should adopt cyclic capacity values to estimate allowable load designs in high-wind regions.
- Failure modes remained consistent between cyclic and monotonic loading, with pull-out prevailing except where friction and sheathing strength caused pull-through. Screws increased pull-through likelihood, while edge fasteners in connection type C showed mixed failures.

Roof to Wall Connections

When comparing cyclic to monotonic capacities, a reduction was observed only at the sidewall location, averaging 5% with a maximum of 8%. Although modest, this reduction is still concerning because sidewalls experience the highest load demands in the structure.

Staggered fastener patterns offer improved performance, up to 51% for nailed configurations, this improvement is primarily due to the prevention of row splitting failure. Additionally, based on COVs, stagger patterns also present less variability, 7 % vs 19 % in average. These finding suggests that stagger patterns can be considered as a preferred pattern in design to maximize strength and minimize uncertainty.

Analysis of the failure modes indicates that most sidewall configurations fail due to strap rupture, implying that the strap strength alone governs the connection capacity. This suggests that the current connection detailing fully mobilizes the strap's strength, leaving no reserve capacity to accommodate higher demand levels. Additionally, the use of thin straps makes the connection susceptible to pull-through failure when staples are used, a failure mode observed during specimen construction and testing. This premature failure altered the connection behavior and occurred unexpectedly early during testing. These observations are consistent with findings reported by Marshall (1993) and suggest that using a thicker strap could mitigate this failure mode and improve overall capacity. Consequently, the results underscore the need for improved connection detailing or alternative strategies to ensure code compliance and enhance performance in structurally critical sidewall regions.

The following findings summarize the structural performance of the tested configurations.

- Sidewall connections exhibit capacity deficiencies, with cyclic loads reducing strength by up to 8%, and all configurations underperforming relative to NDS predictions, some as low as 62% due to row splitting.
- Staggered fastener patterns increase nailed connection strength by up to 51%, reduce row-splitting failures, lower capacity variability (COV: 7% vs. 19%).
- Observed failure modes indicate strap rupture dominates sidewall failures, suggesting that existing detailing fully utilizes strap capacity without reserve, necessitating improved connection strategies.
- Thin straps compromise connection performance by increasing susceptibility to premature pull-through failure, particularly when stapled. This underscores the need for further testing with thicker straps to evaluate their influence on connection behavior.

References

American Housing Survey (AHS) (2019). 2019 Florida – General Housing Data – All Occupied Units. Accessed July 24, 2022. https://www.census.gov/programs-surveys/ahs/data/interactive/ahsTablecreator.html?s_areas=00012&s_year=2019&s_Tablename=TABLE1&s_bygroup1=1&s_bygroup2=1&s_filtergroup1=1&s_filtergroup2=1

AF&PA. (2005). *National Design Specification for Wood Construction." Chapter 11: Dowel Type Fasteners, AF & PA American Wood Council*, Washington D. C.

American Society of Civil Engineers (ASCE) (2022). Minimum Design Loads for Buildings and Other Structures, Standard 7. American Society of Civil Engineers, Reston, VA.

American Society for Testing and Materials (ASTM) (2020). Standard Test Methods for Mechanical Fasteners in Wood and Wood-Based Materials, ASTM D1761. West Conshohocken, PA.

Clayton Homes. (2023). Manufactured Homes. Maryville, TN United States.

Federal Emergency Management Agency (FEMA) (2007). Interim Testing Protocols for Determining the Seismic Performance Characteristics of Structural and Nonstructural Components, FEMA 461. Prepared by the Applied Technology Council for the Federal Emergency Management Agency, Washington, D.C.

National Design Specification (NDS) (2018). National Design Specification for Wood Construction, 2018 Edition. ANSI/AWC-NDS 2018. American Wood Council, Leesburg, VA.

Marshall, R. D. (1993). Wind Load Provisions of the Manufactured Home Construction and Safety Standards—A Review and Recommendations for Improvement (NIST Interagency/Internal Report (NISTIR) 5189). National Institute of Standards and Technology.

Sutley, E.J., Vazquez, K., Dao, T., Kim, J., Hunt, J., and Johnston, B. (2020). "Performance of Manufactured Housing during Hurricanes Irma and Michael." ASCE *Journal of Performance of Constructed Facilities*, 34(4). DOI 10.1061/(ASCE)CF.1943-5509.0001486.

U.S. Department of Housing and Urban Development (HUD) (2022). 24 Code of Federal Regulations Part 3280, Manufactured Home Construction and Safety Standards. Washington, D.C.

FIU International Hurricane Research Center
FLORIDA INTERNATIONAL UNIVERSITY

A Resource for the State of Florida

SECTION 3b

Numerical Analysis of Manufactured Homes Under Hurricane Effects: Hysteresis Model for Connections

Report for the Period 2024-2025

A Research Project Funded by:

Florida Division of Emergency Management

Prepared by
Dr. Thang Dao

Graduate Student
Vuong Nguyen Van Do

July 31, 2025

Executive Summary

This report presents the outcomes of research Tasks 2 and 3 for the year 2024 (Task 1 was included in the previous report), along with all three research tasks completed in 2025. A summary of results from each task is provided below, with detailed discussions in the subsequent sections of this report.

2024 – Task 2: Finite Element Method (FEM) Modeling for Retrofit Design Selection

This task focused on using FEM to evaluate various retrofit strategies for low-rise frame buildings, particularly in response to wind-induced damage. The analysis emphasized identifying damage patterns in roof sheathing under varying wind speeds and directions, and highlighted frame regions with high internal axial loads that may pose structural risks. Displacements at nail connections in oriented strand board (OSB) roof panels were also examined. Detailed findings are presented in Sections 1 through 5.

2024 – Task 3: Validation of FEM with Full-Scale Testing Data

Following large-scale (1:4) wind tunnel tests at Florida International University (FIU) and nail withdrawal cyclic loading tests at the University of Kansas (KU), the UA team collaborated with KU and FIU to validate the FEM results. The FEM successfully replicated the observed roof sheathing damage and showed good agreement with hysteresis curves from the KU experiments under dynamic wind loading. This validation supports the use of FEM for retrofit assessment. Results from this task are presented in Section 6. The UA research team has completed the

validation process by comparing the FEM results with experimental data using cumulative distribution function (CDF) and fragility analysis, confirming that the proposed FEM model is suitable for predicting the response of MUs under wind loads.

2025 – Task 1: Calibration of Hysteresis Model Using New Experimental Data

Building on work from 2024, the novel hysteresis model was further refined and calibrated using KU-provided data from new connection tests. The model effectively captured the cumulative damage behavior of structural components under cyclic loading. The comparison between experimental results and the model's predicted response is illustrated in Figures 12 and 13, and described in Section 5.

2025 – Task 2: Fragility Assessment Using FEM Under Varying Wind Intensities

This task utilized FEM to assess the fragility of structural components subjected to wind pressure. Ten simulation cases were run using five randomly generated hysteresis curves for nails, tested across wind speeds ranging from 80 to 145 mph at a 195° wind direction. The analysis focused on identifying conditions that lead to roof openings and uplift failures, with probability distribution Lognormal used to compare FEM data against test results from roof sheathing and roof-to-wall nails. Findings are detailed in Section 7, with conclusions in Section 8.

2025 – Task 3: Multi-Institutional Collaboration with FIU and KU

The UA team continued active collaboration with FIU and KU, conducting regular meetings to exchange experimental data and track progress on wind tunnel and cyclic loading tests. This

partnership has been essential for validating the FEM in simulating nail failures, roof sheathing damage, and hysteresis behavior across different scenarios.

1. Introduction

Natural disasters such as windstorms, hurricanes, and tornadoes have consistently ranked among the most costly and deadly events over the past several decades [1]. Many regions around the world have been severely affected by extreme wind phenomena, resulting in significant damage to residential buildings and critical infrastructure. Recent wind load assessments have further highlighted the vulnerability of a large number of facilities to these hazards [2]. Particularly concerning is the devastating impact on affordable housing, which in some cases has been completely destroyed.

As the affordable housing crisis continues to intensify in the United States, manufactured home units (MHUs) have emerged as a promising solution to meet the long-term housing needs of rural and low-income communities. However, MHUs remain highly susceptible to wind-induced damage, in part due to inadequacies in current building codes – especially those related to structural connections and components. While there has been limited progress in developing numerical modeling approaches for light-frame wood construction (LFWC) under wind loads, it is important to note that MHUs differ significantly from conventional LFWC in several aspects: member sizes, construction materials, assembly methods, structural mass, and failure mechanisms. As such, MHUs require distinct modeling approaches and evaluation frameworks. Much of the past research on wind effects has focused on estimating wind pressures through laboratory-based wind tunnel testing. Notable efforts include full-scale and large-scale experimental studies such as the Southern Shores Project [3] and the Florida Coastal Monitoring Program [4]. However, these experiments are resource-intensive and demand highly specialized facilities, limiting their scalability.

In recent decades, the Finite Element Method (FEM) has become a widely accepted and powerful tool for analyzing the behavior of mechanical and structural systems. Nonlinear FEM models have been extensively used not only for the design of new wood structures but also for evaluating the performance of existing buildings under various loading scenarios [5–11]. Among the key factors influencing the performance of timber and hybrid structures are the mechanical behaviors of their connections. Numerous studies have modeled timber connections of various configurations and material combinations, shedding light on their critical role in overall structural response and failure modes.

A critical yet underexamined challenge lies in understanding how wind forces are transmitted through light timber-frame structural systems, particularly in the presence of vibration and nail connection degradation. Research in this area has been limited due to the high costs and logistical demands of large-scale field monitoring and laboratory experiments. To address this gap, this study proposes a new nail connection model, calibrated with experimental data, and integrates its parameters into a three-dimensional finite element (3D FEM) framework. This approach aims to more accurately capture the structural response of timber buildings under wind loads, especially with regard to localized failures and cumulative damage behavior.

This study is driven by two primary considerations. First, timber frame-shell construction is increasingly adopted across the United States as a cost-effective solution for low-income housing, particularly in one- and two-story configurations [23]. These structures demonstrate favorable resistance to dynamic wind loads due to timber's high strength-to-weight ratio and the energy-dissipating ductility of nail connections. Second, recent updates to U.S. wind-resistant design standards, such as the HUD guidelines [23] and ASCE/SEI 7-22 [32], have introduced revised

national wind hazard maps. These changes underscore the importance of accurately assessing both global and localized wind load effects on structural behavior. In this context, a simplified linear nail model is adopted to enhance understanding of the durability and performance of wind-resistant timber-frame structures.

Several studies are presented on the combined experimental and finite element modeling approach. It is noted that the behavior of the nail-connection model can be calculated through analytical methods [12]. However, this method is quite limited in analyzing the global and local behavior of timber frame structures. Therefore, more experiments on the connection of 3D nails and brackets need to be performed on the material behavior to better complement this global study. Dynamic and quasi-static tests for shear walls or full-scale models for timber houses should be performed to compare with the 3D FEM model. Because the nonlinear dissipation phenomenon in the frame building is primarily at the connections, where many simplified nail models are used to reflect the load-displacement paths developed based on the analytical and FEM [13, 14] by fitting the experimental data at the joints. Besides that, other methods also relied on the previous multi-scale ideas introduced by several researchers [15, 16], which required response laws that represented the evolution of load-displacement paths on different scales. Many constitutive laws for material behaviors have been developed over the years, from the nonlinear simple monotonic [17] to the hysteretic models that consist of complicated loads [18, 19], in which the proposed models could precisely capture the damage progress of structures under wind loads.

Namely, the simple model introduced by Richard et al. [15] was based on the strength degradation of accumulated factors in one direction, which used the previous step strength of unloading. Meanwhile, the constitutive laws used the exponential functions for the peaks of backbone curves,

and cyclic hysteresis had been proposed by Ayoub [20], which considered the trilinear functions in which the damage process was described in detail and listed as the fundamental degradations of strength, unloading stiffness, accelerated stiffness reduction, etc. Pang et al. [21] investigated the evolutionary parameter hysteretic model (EPHM) to define the exponential functions for the backbone curves, loading, and unloading hysteretic cycles. However, the accumulated damage was not considered in the calculations. The next research was examined by Xu and Dolan [16] for the BWBN method, which presented the strength reduction, and the dependent stiffness could provide a precise fitting on the experimental cyclic reverse tests for the nail connections and shear walls. However, this model was not based on physical parameters such as loads, displacements, and stiffness. Later, Humbert [22] carried out a new model that satisfied the shortcomings of Richard et al. [15], in which using the exponential function could lead to discontinuous and rigorous analytical problems in the numerical models [22]. To the author's knowledge, all constitutive laws must be detailed to pass the necessary conditions to facilitate the numerical methods to become a robust approach that well predicts the physical characteristics, such as variations of the defined displacement, load, and stiffness. The most important attention for this issue is the nail connection to be able to handle the behaviors of the frame system imposed by the lateral forces, complicated load-displacement paths, and well capture the experimental test data. Therefore, this is the most common feature for all load-displacement models to describe the constitutive law at the nail connection and frame building response to the lateral loads.

In this study, a new hysteretic constitutive model for the connections between the frame and sheathings is proposed, and its applications to the general nail model have been introduced. With over 100 nail tests, hysteretic withdrawal cyclic experiments are implemented between nails, roof sheathing, and wall sheathing.

The calibration of the nail rule has been made in detail, with special emphasis on how to account for the variability of experimental results. The first example uses test data from a withdrawal fastener test to calibrate the model, demonstrating its ability to accurately track hysteresis forces and energy dissipation. The second step is to take account of the hysteresis input data with a displacement protocol into a 3D finite element method to validate the model's capability to handle varying windstorm directions to predict the failure at roof sheathing, further confirming its accuracy and effectiveness enhance its applicability in performance-based design and research, making it a valuable tool for structural engineering. Furthermore, the evaluation of the 3D FEM model from wind tunnel experiments with various wind directions and velocities is designed to examine the responsiveness to wind loads and the versatility of the proposed numerical model.

The objective of the framework is to develop a 3D finite element model that combines a coupled frame-shell structure – a nonlinear hysteresis multi-degree-of-freedom (MDOF) nail connection model – and considers the damage accumulation at nails to analyze the behavior of a frame-wood mobile building subjected to dynamic wind loading. The full complex wood building is tested at a 1:4 scale using a wind tunnel experiment before implementing the 3D finite element model, which is also described at the corresponding scale. A numerical model for the nonlinear relationship of load and displacement at the nail connection is specifically proposed in this study, which can extract high accuracy with the numerical results from the complex withdrawals for hysteresis loading, such as Rafter and roof-sheathing and Wall points. The parameters calibrated from the specific model, such as Backbone, loading, unloading curves, and time-integrated damage rates, will be used as reliable input characteristics for the 3D FEM model in analyzing the transient dynamic wind conditions using the displacement control. In addition, the wind pressure in the time steps taken by the wind tunnel test will be measured at the taps and interpolated at the nail

connection as the external wind forces. The newly developed nonlinear hysteresis model evidences the validity of the complex load and displacement curves for two cyclic reversed analyses of nails and screw connections, as compared to the experimental withdrawal tests. The 3D frame-shell wood building FEM under the dynamic wind load field is in good agreement to estimate the dynamic performances of the full-scale structure, accurately identifying the location and the first damage appearance at the roof sheathing due to the different wind directions, such as 90^0, 135^0, and 180^0. As a result, the 3D FEM coupled with MDOF nail connection could be considered as a potential and reliable approach to well predict the light frame low-rate building during past hurricanes.

2. Data Analysis

The single-story building model was tested by the FIU research team at the 12-fan Wall of Wind (WOW) wind tunnel facility at Florida International University. The structure, designed according to U.S. standards for low-income housing [31], consists of a system of wooden frames interconnected through structural components and sheathed with oriented strand board (OSB) panels. The specifications of the frame system, including connecting beams and OSB panels, are detailed in Table 1.

The selected building geometry is rectangular with a gable roof, constructed using conventional framing techniques. To simulate the behavior of a wood-frame structure under extreme wind conditions, a wind-speed range of $60\ mph - 140\ mph$ was applied to a $1{:}4$ scale model. This wind speed range was chosen based on experimental observations indicating roof sheathing failures due to nail withdrawal and loosening. The results, presented in the following section, are used to validate the proposed hysteresis model and its nonlinear dynamic response through

comparison with numerical FEM simulations. The time-history external pressure coefficients $C_p(\theta, t)$ are computed using Equation (1), where $P(\theta, t)$ represents the time-varying pressure [in $Pa\ (psf)$], P_0 is the static reference pressure [$Pa\ (psf)$], ρ is the air density [in $kg/m^3 (slugs/ft^3)$], θ is the wind azimuth angle, and $\bar{U}$is the mean wind speed [in $m/s\ (mph)$] measured at the mean roof height.

$$C_p(\theta, t) = \frac{P(\theta, t) - P_0}{\frac{1}{2}\rho \bar{U}^2} \tag{1}$$

Table 1. *Composed of structural members in the MHU building (2023 FIU Report)*

No.	Member type	Section	Standard size	Area (in^2)
1	Roof sheathing	7/16 OSB	-	-
2	Truss bottom chord	$2 \times 2\ (SPF)$	1.5×1.5	2.25
3	Ridge	$2 \times 4\ (SPF)$	1.5×3.5	8.25
4	Strut horizontal/ diagonal members	$2 \times 2\ (SPF)$	1.5×1.5	2.25
5	Truss top chord	$2 \times 3\ (SPF)$	1.5×2.5	3.75
6	Wall Bottom plate	$1 \times 4\ (\neq 3 - SPF)$	0.75×3.5	2.2625
7	Wall Stud	$2 \times 4\ (Stud - SPF)$	1.5×3.5	5.25
8	Wall Stud	$4 \times 2\ (Stud - SPF)$	1.5×3.5	5.25
9	Wall Top Plate	$2 \times 4\ (\neq 3 - SPF)$	1.5×3.5	5.25
10	Connection End-wall/Sidewall	ST12	-	0.078125
11	Edge rail	$1 \times 4\ (SPF)$	0.75×3.5	2.2625
10	Floor Sheathing	7/16 OSB	-	-
11	Nail	8d	-	-
13	Floor Joist	$2 \times 6\ (\neq 2 - SPF)$	-	-

The force $C_F(\theta,t)$ and moment $C_M(\theta,t)$ coefficients with the time series along the x,y,z directions. These represent to the drag, lift and overturning moment that depend on the different wind directions are expressed from Eq.(2), in which d_i in m (ft) refers to the moment arm, is defined from the pressure taps to the height of the model on the load cells, H in m (ft) relating to the mean height of the roof and A_i refers to the tributary area at each pressure tap spot.

The force coefficients $C_F(\theta,t)$ and moment coefficients $C_M(\theta,t)$, defined as time-dependent values along the x, y, and z directions, represent the drag, lift, and overturning moment, respectively, and vary with wind direction. These coefficients are calculated using Equation (2), where d_i (in meters or feet) denotes the moment arm, measured from each pressure tap to the height of the model at the load cells. H (in meters or feet) is the mean roof height, and A_i is the tributary area associated with each pressure tap location.

$$C_{Fx}(\theta,t)=\frac{\sum_i\left(C_{P_{East,i}}(\theta,t)-C_{P_{East,i}}(\theta,t)\right)A_i}{\sum_i A_i},\ C_{Fy}(\theta,t)=\frac{\sum_i\left(C_{P_{South,i}}(\theta,t)-C_{P_{North,i}}(\theta,t)\right)A_i}{\sum_i A_i} \quad (2)$$

$$C_{Fz}(\theta,t)=\frac{\sum_i\left(C_{P_{Roof,i}}(\theta,t)-C_{P_{Floor,i}}(\theta,t)\right)A_i}{\sum_i A_i},C_{Mx}(\theta,t)=\frac{\sum_i C_{F_{y,i}}(\theta,t)d_i}{H},\ C_{My}(\theta,t)=\frac{\sum_i C_{F_{x,i}}(\theta,t)d_i}{H}$$

Table 2. *Experimental setting for wind load test. (2023 FIU Report)*

No.	Wind angles	Position	Wind speed (mph)	Measure methods
Test 1	0^0 or 180^0	North to south	60- 140	Sp, LVDT
Test 2	90^0	East to west	60- 140	Sp, LVDT
Test 3	45^0 or 225^0		60- 140	Sp, LVDT

For the roof sheathing, Linear Variable Differential Transformers (LVDTs) were used to measure displacements at locations LGS 007, 009, and 010. Additionally, Celesco SP-2 string

potentiometers were employed to capture upward displacements at all interior roof-to-wall connection frames, specifically at locations LGS 011, 008, 004, 005, and 006. These instruments were mounted on rigid lumber pieces attached to the top plates, as illustrated in Figure 1.

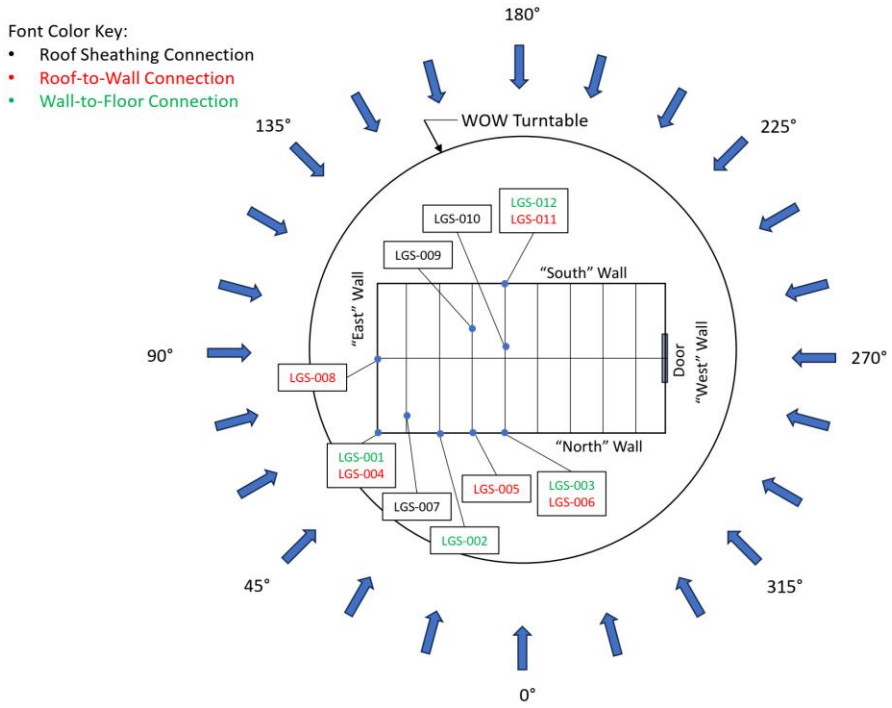

Figure 1. Observation points for roof sheathing deformation under wind load in the numerical model (2023 FIU Report)

Data from the wind tunnel tests for the wind angles and their speeds tabulated in Table 2 will be integrated into the finite element model to calculate nodal forces based on wind pressures measured from 376 pressure taps, as shown in Figure 2. These nodal forces are derived from the wind pressures acting on the surfaces of the side and roof sheathings and represent the transmitted loads applied to the structural system

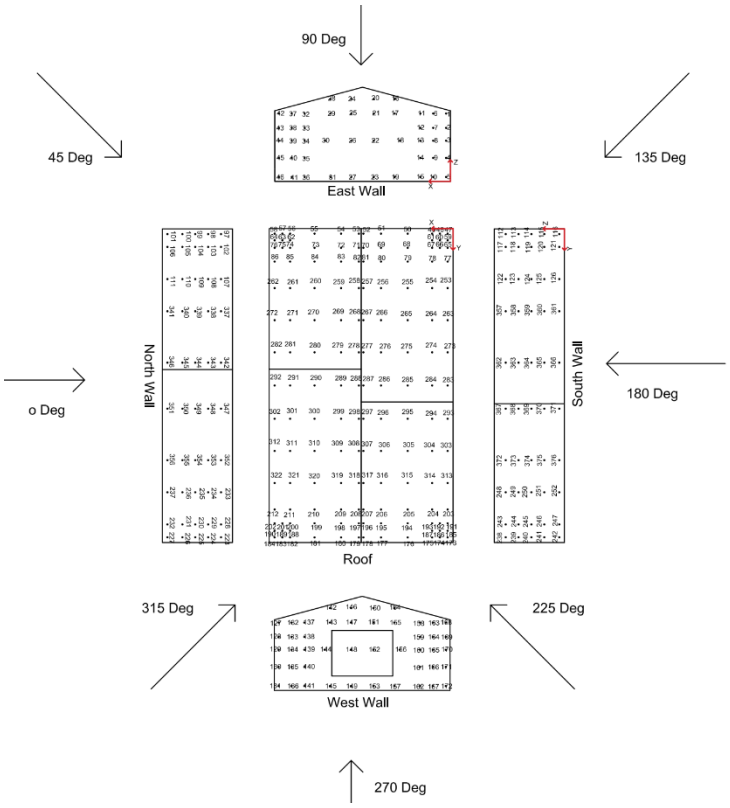

Figure 2. Distribution of wind taps (circular symbols) on the 1:4-scale mobile home model for various wind angles – WOW facility, FL (2023 FIU Report)

3. Nail Withdrawal Cyclic Loading Test

The roof sheathing-to-rafter (S2R) connection is one of the most critical joints in the structural analysis of low-rise mobile frame buildings, as it is particularly vulnerable to windstorm-induced loads. To evaluate its performance, each connection was first subjected to monotonic tensile loading to determine the displacement corresponding to the maximum nail capacity. This value was then used to establish the parameters for the quasi-static cyclic loading protocol.

According to the HUD Code [23], specific connection designs and anchorage procedures for such joints have not been standardized, despite the clear need for safe and reliable connections capable of resisting wind-induced impact loads. For this study, a fastener spacing of 150 mm (6 inches)

was adopted for the S2R connections, in accordance with the International Building Code (2006) recommendations for hurricane-prone areas. Table 3 presents the fastener specifications – diameter, length, and thread pattern – as well as the geometric properties of the wood materials used, based on the National Design Specification (NDS 2018) [24].

Table 3. *Geometric Properties of Roof Sheathing to Rafter (S2R) for withdrawal test. (2024 KU Report)*

Element	**Type**	**Actual size mm (in)**	**Smooth Shank Diameter mm (in)**	**Head diameter mm (in)**	**Thread length mm (in.)**
Smooth Shank nail	8d common	60.33 (2.38)	2 3/8 (0.11)	7.15 (9/32)	Other place
Description			**Geometric properties**		
Sheathing	Oriented Strand Board (OSB)		11.1-mm (7/16-in.) thick		
	3 ply plywood		12.7-mm (0.5-in.) thick		
Rafter	Spruce-Pine-Fir (SPF)		38.1-mm x 88.9-mm (1.5-in. x 3.5-in.)		
	Southern Yellow Pine (SYP)		38.1-mm x 88.9-mm (1.5-in. x 3.5-in.)		

Table 4. *Elastic material properties- sheathing panel, wall studs and nail. (2024 KU Report)*

Material properties	**Elastic modulus** ksi, (MPa)	**Poisson's ratio**	**Density** kg/m^3
7/16 OSB	1116	0.42	615.15
Wall studs (Spruce pine fir No.1)	1200	0.42	418.39
Smooth Nail shank (8d)	29000	0.28	7850

Table 5 summarizes the details of the S2R connection specimens that were manufactured and tested. Each S2R specimen featured a single anchor connecting to a $203\ mm \times 203\ mm$ ($8\ in. \times 8\ in.$) sheathing panel. A total of 40 specimens were tested, comprising two types of rafters: 20 specimens were subjected to monotonic loading, and the remaining 20 to cyclic loading.

Table 5. *Roof Sheathing to Rafter (S2R) Test Matrix (2023 KU Report)*

Sheathing type	Rafter type	Fastener	Monotonic test	Cyclic test
OSB	SPF	Nail	5	5
	SYP	Nail	5	5
Plywood (3-ply)	SPF	Nail	5	5
	SYP	Nail	5	5

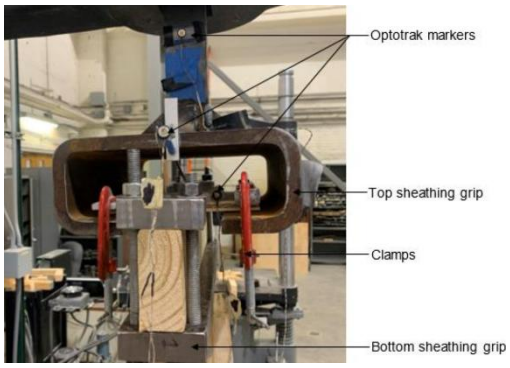

Figure 3. Roof Sheathing to Rafter (S2R) Test Fixture (2024 KU Report)

The nominal dimension of the rafter is 2×4 inches, with an actual size of $38.1mm \times 88.9mm$ ($1.5\ in. \times 3.5\ in.$), and it is fabricated from either Southern Yellow Pine (SYP) or Spruce-Pine-Fir (SPF). Rafters were connected to oriented strand board (OSB) or 3-ply plywood using 8d plain smooth shank nails, installed with a pneumatic nail gun. According to both the HUD Code and post-hurricane field investigations of manufactured homes, screws are seldom used in

practice. Instead, nails are the predominant fastening method for securing roof sheathing to rafters in typical wood-frame homes built to withstand Wind Zone II conditions. The S2R specimens, shown in Figure 3, were tested under both monotonic and quasi-static cyclic loading protocols.

To perform both monotonic and cyclic loading tests, a custom steel fixture was designed and fabricated to fit the Baldwin screw-drive test frame, which has a load capacity of $266\ kN$ $(60\ kip)$. The fixture consists of a $57.2\ mm$ $(2.25\ in.)$ wide steel plate with a thickness of $25.4\ mm$ $(1\ in.)$ and a length sufficient to extend through the Baldwin handles and engage the associated fixtures. Additional steel pads were used to ensure that the monotonic and cyclic loads were fully transmitted to the connection specimens. Both monotonic and cyclic tests were conducted at a constant displacement rate of $2.54\ mm/min$ $(0.1\ in./min)$, in accordance with $ASTM\ D1761\ (2020)$. The displacement amplitude for the cyclic test was determined based on the monotonic test results. Specifically, the full amplitude was divided into sixteen cycles to gradually approach the displacement corresponding to the peak load. To monitor deformation, a marker was attached to the fastener head to measure the relative displacement between the sheathing and the fastener. Crosshead displacement was measured using a marker placed on the top of the sheathing grip, as illustrated in Figure 4.

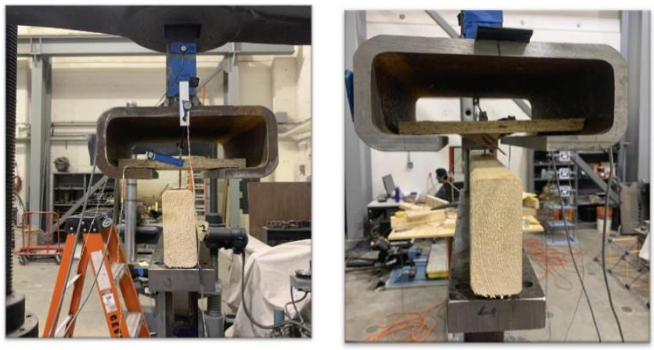

Figure 4. S2R single fastener failures (2024 KU Report)

A total of 20 specimens were tested under cyclic loading, exhibiting the same failure modes as observed in the monotonic tests, specifically, pull-through and pull-out failures in all nail connections. The results from the cyclic withdrawal tests, consisting of five data sets for nails in roof sheathings and five for nails in roof-to-wall connections, conducted by the KU team, will be used to calibrate the input parameters for the in-house finite element code. These parameters include loading and unloading behavior, backbone curves, and damage evolution characteristics.

4. Finite-Element Formulation

Failures in wood-frame structures subjected to wind loads typically occur at the connections between structural components, such as nails fastening oriented strand board (OSB) sheathing to roof trusses, rather than within the members themselves. To accurately simulate force and moment transfer from OSB to truss members, nail connections are modeled following the approach of Dao and van de Lindt [28], using nonlinear general spring elements with six degrees of freedom (three translational and three rotational) at each node, with axial stiffness interpreted from a new hysteresis model. The OSB roof sheathing is modeled using eight-node plate and shell elements, while truss members, beams, and columns are represented with beam elements. Shear walls, when present, are modeled using nonlinear spring elements. The governing equations for the 3D member and shell elements are detailed in a 2023 report by the University of Alabama research team.

In order to transfer the force and moment from the OSB to the truss members, the nail is modeled as a spring with six components including three components in translation and three components in rotation. As previously mentioned, the OSB is modeled using shell elements and the truss members are modeled as beam elements. Now, imagine the forces and moments need to be transferred from one node on the OSB to another node on a truss element via the nails. At the element level, the spring equation can be written simply as

$$[K]_S\{U\}_S = \{F\}_S \quad (3)$$

$$\{U\}_S = \{U\}_i - \{U\}_j \quad (4)$$

where $\{U\}_S$ is the spring displacement, $\{U\}_i$ is the displacement at node *i* on the OSB and $\{U\}_j$ is the displacement at node *j* on the truss, $[K]_S$ is the secant spring stiffness matrix for the six components, and $\{F\}_S$ is the spring force. The spring stiffness matrix $[K]_S$ is estimated at each load level based on the $\{U\}_S$ just obtained and the curves from experimental data. The bending component of the stiffness matrix follows the beam bending stiffness equation described before (1), and the axial component is modeled using the hysteresis curve described in the next section. The element stiffness matrix is transformed into global coordinates and then added to the global stiffness matrix. It should be noted that some details of finite element modeling integration are not obvious. For example, when integrating the nail model into a finite element program, node *i* and *node j initially have the same coordinates (before loading). Therefore,* the nail direction vector should be specified and used to create the transformation matrix. The positive directions (node *i* to node *j*, translational and rotational) should also be selected so that they can be checked at each load step. It is observed that when the nail stiffness matrix is integrated into the global matrix system, the anchor's behavior is predominantly governed by axial parameters. Other displacement and rotational responses are controlled by the intrinsic stiffness properties of the nail. To accurately capture the nail's behavior, both positive and negative displacements are computed using calibrated coefficients. To avoid unrealistic negative relative-deformation between sheathing and frame under compression wind loading, such as that illustrated in Figure 5, the relative displacement at their connection is constrained to zero for connections in compression.

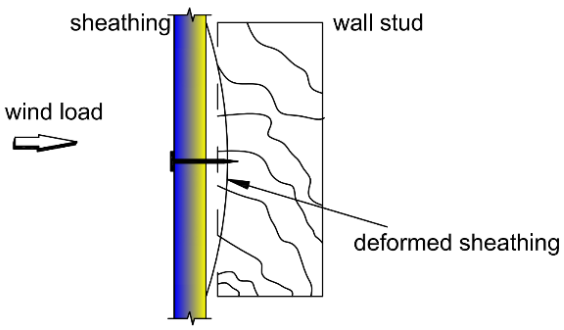

Figure 5. Nail model development for sheathing deformation due to wind load.

The new data fitted used in the model will be presented in the next section, such as Figure 7-Figure **9** for nails at roof sheathing and roof to wall, respectively.

5. Results in a 3D finite element model of a frame-shell wood building

The 3D finite element model of the wood-frame building was developed using beam elements, shell (plate) elements, and two-node general translation-rotation nail elements. Figure 6 shows a schematic of the full-frame shell model, highlighting the nail connections at the roof sheathing (red nails) and the roof-to-wall joints (yellow nails). The structural frame was modeled using Euler beam elements, while the sheathing panels, assumed to be isotropic OSB, were modeled using eight-node plane stress elements. Material properties, including elastic modulus and density, were assigned based on the National Design Specification [24] and APA guidelines [30]. The constitutive behavior of the components was implemented using an in-house code. The 3D FEM model consists of 566 beam elements, 6,201 nodal points, 1,696 shell elements, and 500 nail connections between the framing and the sheathing at the side walls and roof. The mesh was configured such that the nodes of the beam and shell elements coincide, ensuring compatibility at the interfaces. This configuration, with six degrees of freedom at the matched nodes, facilitates accurate analysis of displacements and structural responses of the frame building.

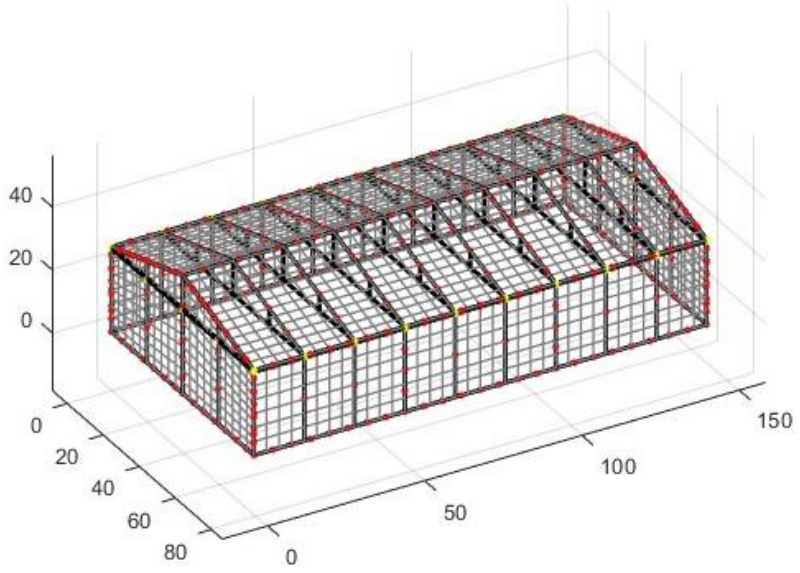

Figure 6. 3D FEM model and nail connections

The measurement positions, shown in Figure 1, are defined as follows: LGS 009 corresponds to Point No. 1 (nail 405) and LGS 007 to Point No. 2 (nail 388), both located at the midpoints of the inclined roof sheathing. In contrast, LGS 005 represents both Point No. 4 (nail 390) and Point No. 5 (nail 383), which are situated at the connections between the wall and roof sheathing. These points were used to evaluate displacements induced by wind tunnel effects during the testing period. The numerical FEM results were analyzed for various wind directions ranging from 90° to 270°, at 15° intervals, as illustrated in Figure 1. It is observed that roof sheathing experiences greater deformation compared to wall sheathing. This behavior is attributed to the lower load-carrying capacity of the nails connecting the roof-sheathing, in contrast to the more robust nail connections used in the wall, as shown in Figure 7-Figure **9**.

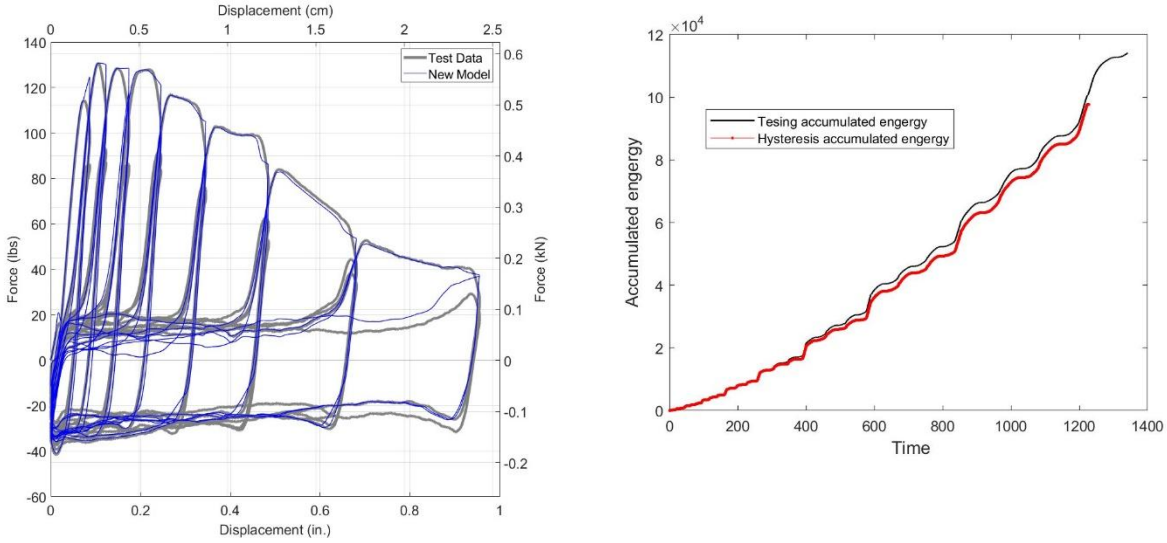

(a) b)

Figure 7. Validation of the proposed calibrated hysteresis model with experimental test at the roof sheathing: a) Hysteresis, b) Accumulated energy

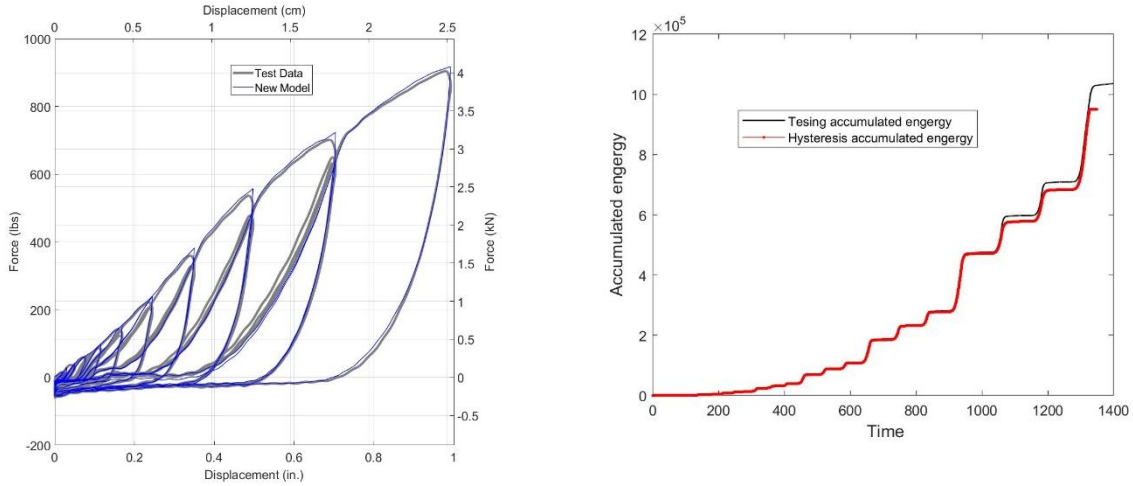

a) b)

Figure 8. Validation of the proposed calibrated hysteresis model with experimental test at the roof to wall: a) Hysteresis, b) Accumulated energy

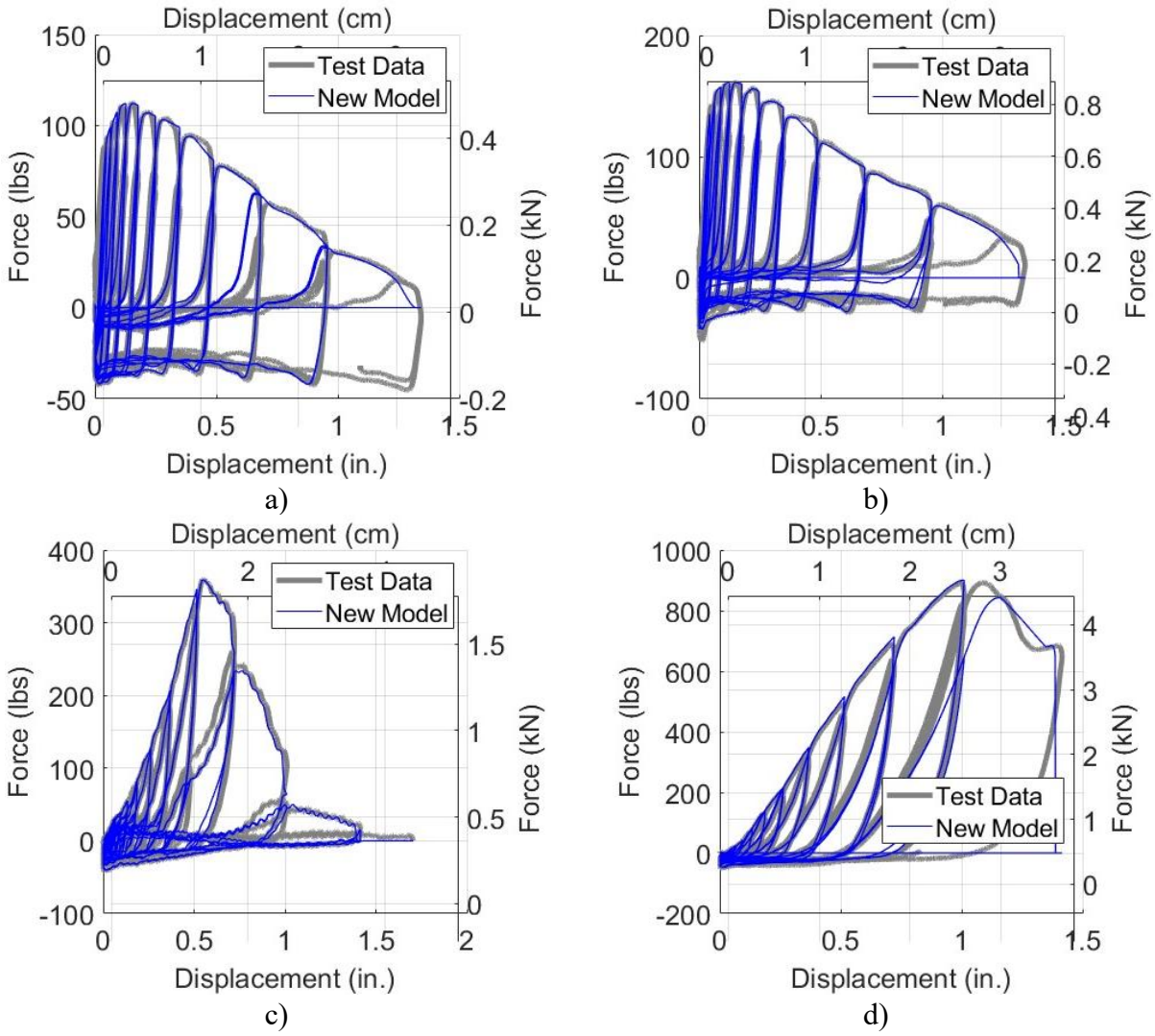

Figure 9. Validations of the proposed calibrated hysteresis model with experimental tests: a) Roof sheathing No.5, b) Roof sheathing No.12, c) Roof to wall No.23, d) Roof to wall No.28

The displacement magnitudes of the roof sheathing vary with changes in wind direction along the longitudinal edge of the building frame. The deformations predicted by the 3D FEM analysis at each interval are illustrated in Figure 10. Under wind directions ranging from 90° to 135° at a wind speed of 140 mph, the roof sheathing exhibits minimal deformation, as indicated by the small deflections in the closed-door condition. However, as the wind direction shifts between 150° and 210°, deformation gradually increases, with a sudden and significant deflection observed in the 8-

ft OSB sheathing. In contrast, the 4-ft OSB sheathing remains largely undeformed under the same wind conditions. When the wind direction shifts to 225°, 240°, 255°, and 270°, the deformation pattern reverses: roof deflection on the windward side decreases, while deformation on the leeward side increases with wind angle. This increase is attributed to the presence of an open door at the end of the building (Figure 1), which allows higher wind pressure to act on the leeward roof sheathing. As a result, both the 8-ft and 4-ft OSB sheathings show significant deformation. The variation in roof deformation closely reflects realistic trends influenced by wind speed and direction.

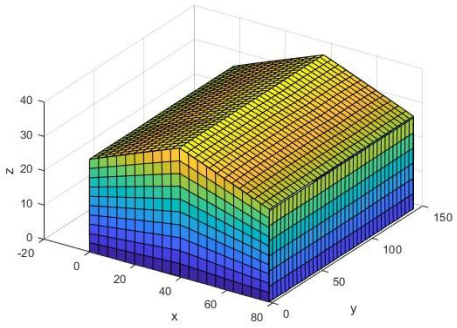

(a) Wind speed 140mph, Wind direction 90^0 -135^0

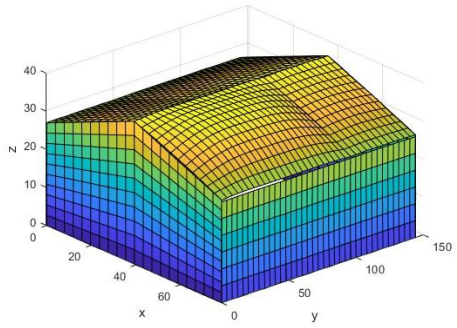

(b) Wind speed 140mph, Wind direction 150^0 -210^0

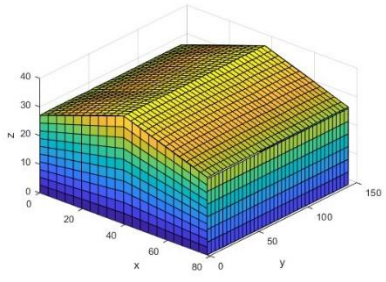

(c) Wind speed 140mph, Wind direction 225^0

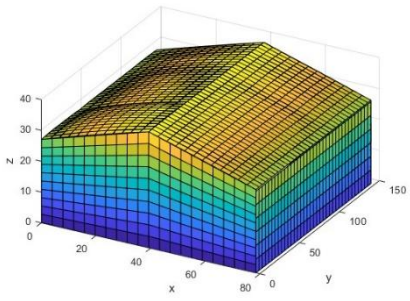

(d) Wind speed 140mph, Wind direction 240^0

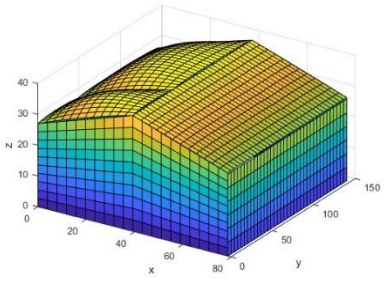

(e) Wind speed 140mph, Wind direction 255^0

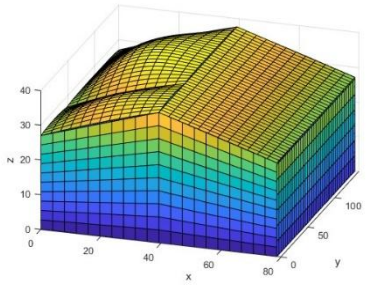

(f) Wind speed 140mph, Wind direction 270^0

Figure 10. Roof sheathing deformation due to wind load directions: (a) $90^0 - 135^0$, (b) $150^0 - 210^0$, (c) $225^0 - 270^0$ (Coordinates are in inches)

The wind speeds of 26.82 m/s (60 mph) and 62.58 m/s (140 mph) correspond to a Category 1 tropical storm and a Category 1 hurricane, respectively, based on the Saffir–Simpson Hurricane Wind Scale. These scenarios are referred to as Test 1 and Test 2, as summarized in Table 6. Deflections at sample points LGS 009 (nail 405), LGS 007 (nail 404), and LGS 011 (nail 390) are plotted in Figure 11 for various wind directions ranging from 90° to 270°, as predicted by the 3D finite element model (FEM). Under the 140 mph wind condition, the deflection patterns at these points exhibit symmetry on the windward roof sheathing, with respect to 15° increments in wind direction.

The roof sheathing exhibited increased deformation under wind directions between 240° and 270° at a wind speed of 62.58 m/s (140 mph), transitioning from closed to open conditions. Due to turbulent wind loads, the roof sheathing began to vibrate, creating openings between the roof and wall sheathing. These openings allowed wind to infiltrate the structure, increasing internal pressure and contributing to progressive damage. As a result, roof sheathing failure was observed, characterized by both nail pull-out and pull-through mechanisms. Additionally, wind pressure data recorded from 376 pressure taps during the wind tunnel experiment corroborates the deformation

patterns observed. Specifically, the greatest deformations occurred under wind directions between 240° and 270°, as shown in Figure 10, corresponding to the peak wind pressures illustrated in Figure 12. These findings align with the wind directions affecting the local opening at the end of the gable frame building.

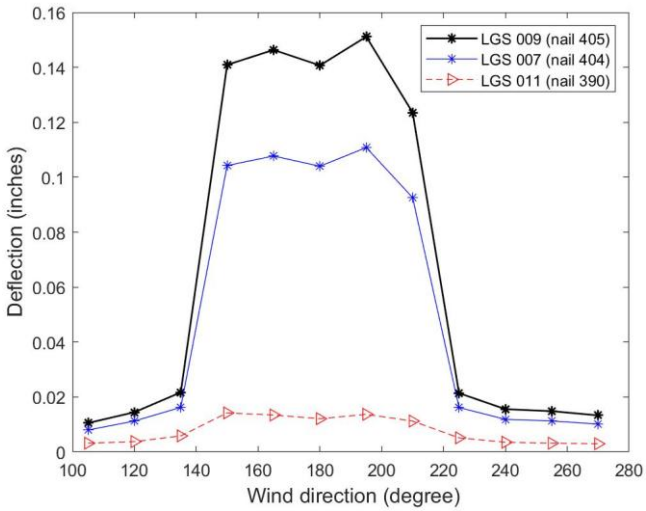

Figure 11. Windward roof sheathing deformation due to wind load range 90^0-270^0 : (a) LGS 009 (nail 405), nearly LGS 007 (nail 404), LGS 011 (nail 390)

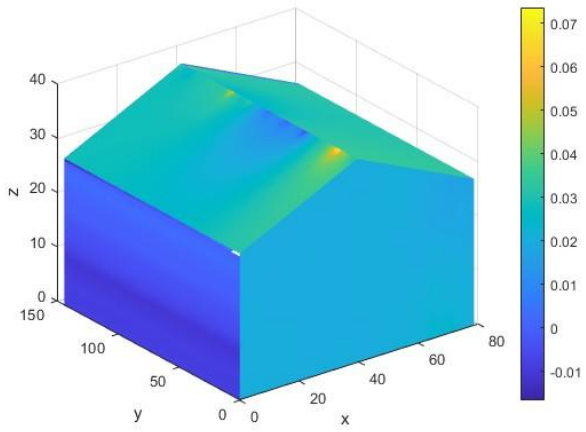

(a) Wind speed 140mph, Wind direction 225^0

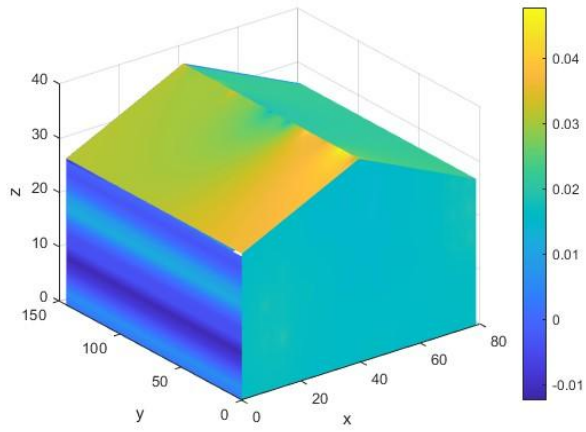

(b) Wind speed 140mph, Wind direction 240^0

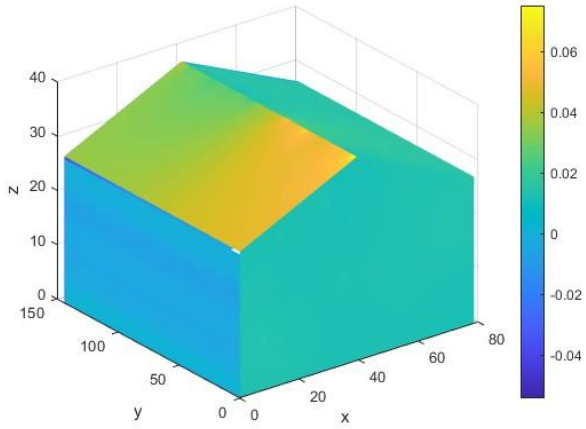

(c) Wind speed 140mph, Wind direction 255^0

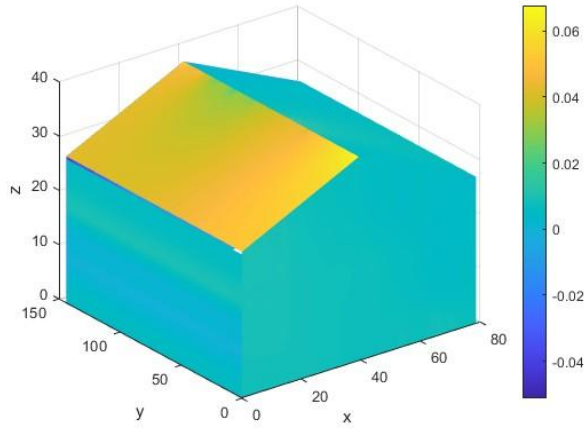

(d) Wind speed 140mph, Wind direction 270^0

Figure 12. Wind pressure distribution on building surface : (a) 225^0 , (b) 240^0, (c) 255^0, (d) 270^0

The displacements at the observed locations due to wind effects depend on the wind tunnel test duration, wind speed, and wind direction. Symmetrical deflections at points on opposite sides of the roof are expected to exhibit similar amplitudes when the wind direction is within the ranges of 0°–45° and 285°–360°. The displacement variation at points on the leeward roof sheathing follows a consistent trend when the wind direction is mirrored across the longitudinal centerline of the frame building. Furthermore, the displacement patterns show strong agreement between the finite element (FE) simulations and the experimental measurements. The 3D FEM simulations effectively capture the displacement responses at both windward and leeward roof locations, particularly under changes in wind direction at 15° intervals.

Internal Forces in the Building Under Wind Loads

The analysis presents a simplified yet effective 3D finite element method (FEM) for estimating internal forces in the structural frame, accounting for varying wind directions. Based on

simulations conducted over the wind loading period, the maximum internal forces at critical connections were predicted. The 3D FEM identifies high-risk elements within the frame, providing valuable insights for structural design. This enables designers to select appropriate structural elements, optimize material choices, and enhance performance through advanced simulations or experimental validation.

The computed internal force resultants incorporate considerations such as potential failure consequences, structural reliability, and safety factors related to materials and loads – ensuring the overall stability and safety of the system. Axial forces in the frame are determined using a linear connection model between beams and a nonlinear connection model between beams and roof panels through a general nail system.

The results, illustrated in Figure 13–Figure 15, highlight critical locations where elevated internal axial forces occur. These locations, detailed in Table 1, correspond to specific beam cross-sections that must be evaluated under different wind directions (90°, 135°, and 180°). Figure 13a–Figure 15a show the time-varying internal force magnitudes in the beams during the wind tunnel tests. At a wind speed of 140 mph, the internal forces range from 0.07 to 0.1 kips for the three wind directions. These values remain within the allowable limits for tensile and compressive forces, as defined by the wood design standard [31].

Risk-prone areas are marked with red circles, indicating the elements where internal forces peak and structural safety must be carefully assessed. For each wind direction, both compressive and tensile forces in frame members should be considered to ensure compliance with practical safety design standards.

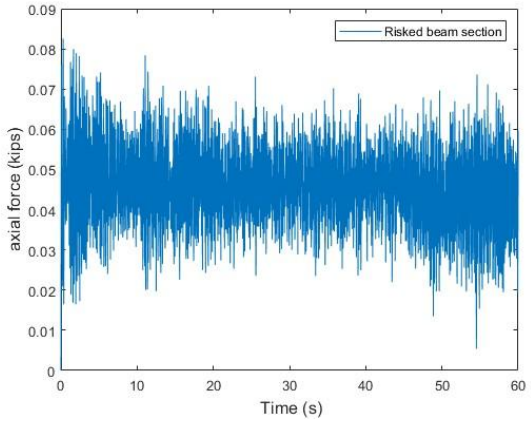

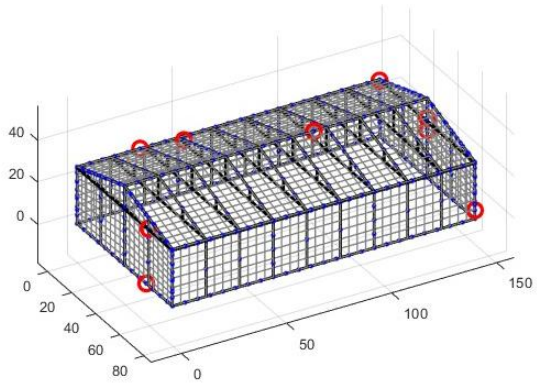

(a) Variation of internal forces at the risk frame element (Section 5)

b) Potential locations at wind direction (180^0)

Figure 13. Internal force and risked location of frame due to wind direction (180^0): (a) maximum internal force, b) considered risky potential locations.

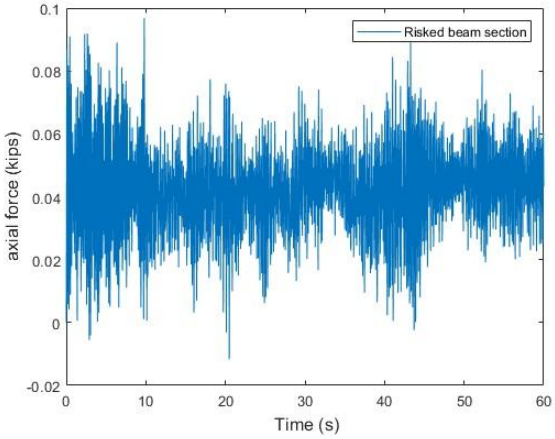

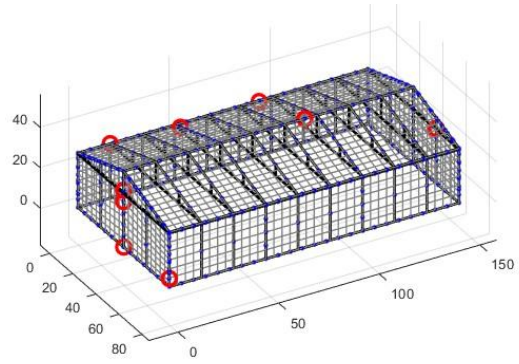

(a) Variation of internal forces at the risk frame element (Section 7)

b) Potential locations at wind direction (90^0)

Figure 14. Internal force and risked location of frame due to wind direction (90^0): (a) maximum internal force, b) considered risky potential locations.

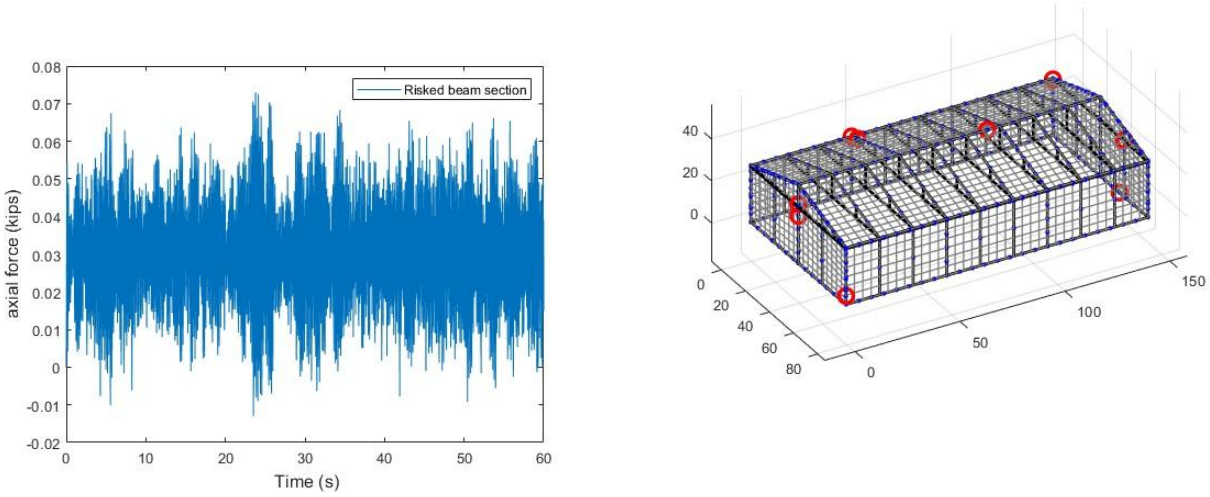

(a) Variation of internal forces at the risk frame element (Section 4)

b) Potential locations at wind direction (45^0)

Figure 15. Internal force and risked location of frame due to wind direction (45^0): (a) maximum internal force, b) considered risky potential locations.

6. Validation of 3D FEM Against Experimental Data

The response of the wood-frame building tested at the Wall of Wind (WOW) facility was predicted using a newly developed hysteresis-based 3D finite element modeling approach. In the experiment, a 1:4 scale model of the modular housing unit (MHU) was subjected to dynamic wind forces from various directions, as illustrated in Figure 16. The corresponding wind speeds used in the test are summarized in Table 6.

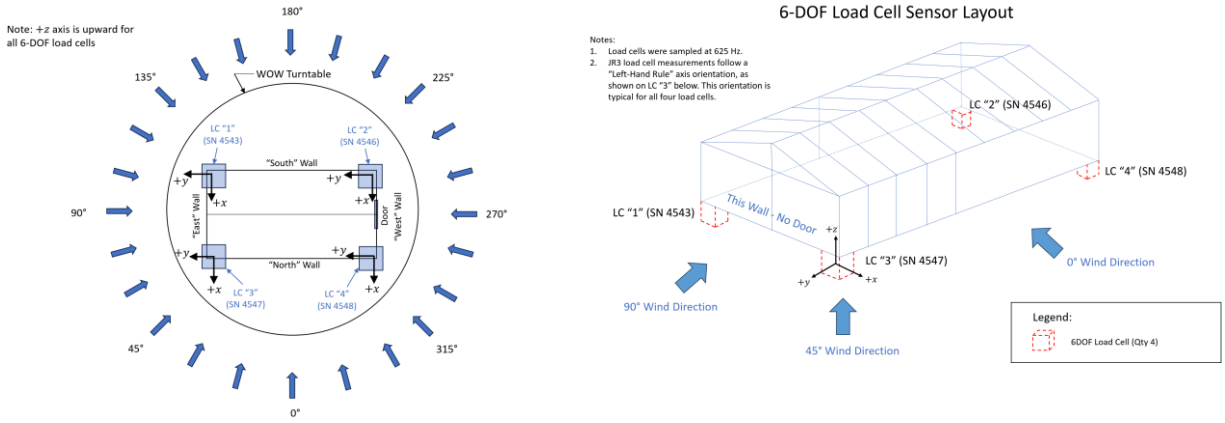

(a) b)

Figure 16. Plan View Showing Wind Load Directions and 6-DOF Load Cell Orientation. (2023 FIU Report)

Table 6. Numerical parametric study

Test type	Wind direction	Wind speed	Locations
Test 1	0-180^0 (15^0)	26.82 m/s (60mph)	LVDT, Sp
Test 2	0-180^0 (15^0)	62.58 m/s (140mph)	LVDT, Sp

The structural behavior of the building is analyzed in detail under wind loads from three principal directions: 0° and 180° (North–South), 90° (East–West), and the diagonals at 45° and 225° relative to the building's longitudinal axis. When wind loads are applied, forces are progressively transferred from the roof sheathing and shear walls to the wood frame and ultimately to the nail connections—identified as the most critical points for assessing the structural stability. Nail failures under these conditions are evaluated using the nonlinear hysteresis model developed in this study.

In timber systems, failure commonly initiates at the nails [26], which serve as primary connectors and carry the majority of structural loads. While previous studies have primarily focused on nail behavior under linear conditions [25-27], the complex nonlinear hysteresis response of nail connections under wind loading remains insufficiently understood [28]. This research addresses

that gap, providing a more comprehensive analysis of nonlinear behavior critical to the performance of wood-frame buildings under wind-induced loads.

In these examples, to evaluate the dynamic wind response of the low-rise wood-frame building, the laboratory test results must be interpreted within the appropriate context of the 1:4 scale MHU models. Additionally, the influence of nonstructural components, such as mass and damping ratios, is considered to more accurately represent the dynamic behavior of full-scale wood buildings subjected to high-acceleration wind loads. To integrate nail behavior into the proposed nonlinear spring-nail model within the 3D finite element framework, Table 7 presents the damage-related parameters for nails connecting the roof sheathing, while Table 8 provides the corresponding parameters for nails connecting the sheathing panels to the framing system, referred to here as shear walls.

Table 7. Hysteresis damage parameters of the roof sheathing

ID	$Unload\ displacement\ (in)$	$r_{0i}(in)$	a_i	b_i
1	0.0000	0.0000	0.0000	0.0000
3	0.0226	1.3162	0.0087	0.0080
4	0.0867	1.2521	0.0141	0.0257
5	0.1231	1.2157	0.0203	0.0238
6	0.1740	1.1647	0.0362	0.1118
7	0.2454	1.0934	0.0311	0.0344
8	0.3452	0.9935	0.0342	0.0372
9	0.4851	0.8537	0.0316	0.0367
10	0.6809	0.6579	0.0345	0.0329

Table 8. Hysteresis damage parameters of the roof to wall

ID	$Unload\ displacement\ (in)$	$r_{0i}(in)$	a_i	b_i
1	0.0000	0.0000	0.0000	0.0000
3	0.0226	1.3746	0.0029	0.0900
4	0.0303	1.3669	0.0280	0.1314
5	0.0499	1.3473	0.0126	0.1086
6	0.0774	1.3199	0.0301	4.2725
7	0.1158	1.2814	0.0004	5.1028
8	0.1694	1.2278	0.0006	3.9797
9	0.2447	1.1525	0.0003	3.9524
10	0.3500	1.0473	0.0686	0.0000
11	0.4974	0.8998	0.1226	0.0000
12	0.7037	0.6935	0.5721	0.0000

In the 3D finite element model, the wood frame components are represented by beam elements, while the wall and roof sheathing—constructed from OSB-type panels—are modeled using shell elements. These components are interconnected through nail connections. The shell elements consist of eight nodes, allowing for both in-plane and out-of-plane deformations. Each node possesses six degrees of freedom, which are fully compatible with the Euler–Bernoulli beam elements, also defined with six degrees of freedom at each end. This compatibility ensures proper integration of the elements into a complete wood structural system.

At all connection points within the wood-frame building, the axial translational spring forces are derived from hysteresis curves obtained from experimental tests. Other translational and rotational spring components are treated as variables that contribute to the global stiffness matrix during the

3D finite element analysis. The force–displacement behavior, backbone curves, and loading–unloading responses of the generalized nonlinear springs are computed using a calibration algorithm based on cyclic withdrawal tests conducted on the wood frame building.

To capture reversed-cyclic behavior, the model incorporates damage accumulation features, including strength degradation, stiffness reduction, and pinching effects. The model parameters are experimentally calibrated following the procedures outlined in Section 4, ensuring an accurate representation of the connection behavior under dynamic wind loading.

The first example demonstrates the validation of numerical dynamic responses of a 1:4 scale low-rise wood-frame building against wind tunnel data obtained from the Wall of Wind (WOW) facility in Florida (APA), using simulations performed with an in-house code. Two experimental measurement points are selected to assess the accuracy of the proposed FEM approach: LGS 009, located on the roof sheathing, and LGS 007, positioned near the roof-to-wall connection, as shown in Figure 1.

Figure 17 and Figure **18** show the cumulative distribution functions (CDFs) of displacement values based on the FEM model with lognormal fits at wind speeds of 80 mph, 100 mph, 120 mph, and 140 mph for measurement points LGS 009 and LGS 007, respectively. For each wind speed, ten displacement values were simulated by randomly selecting nail configurations (from experimental data) and their corresponding locations on the roof sheathing. These simulated displacements were then compared with experimental measurements at the same locations. Wind tunnel test results from FIU indicate that the displacements at LGS 009 correspond to CDF values of 0.99, 0.92, 0.70, and 0.33 at 80 mph, 100 mph, 120 mph, and 140 mph, respectively. In contrast, the corresponding CDF values for LGS 007 are 5.42×10^{-12}, 0.8279, 0.1052, and 0.1908.

In these figures, the solid blue point represents the experimental displacement, the red curve shows the lognormal CDF fitted to the FEM-simulated displacements, and the green point marks the corresponding CDF value of the experimental displacement.

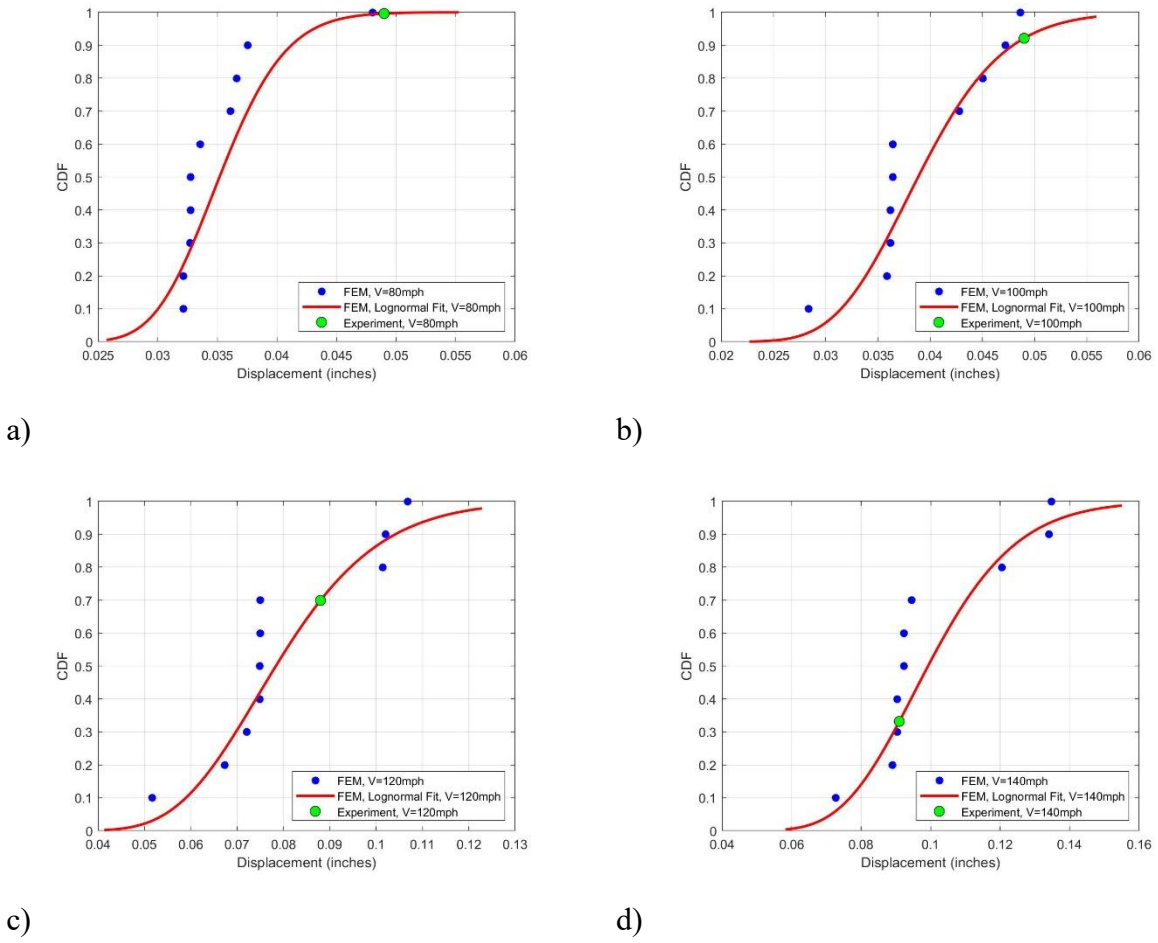

Figure 17. Comparison between FEM and Experimental test: a) 80 mph, b) 100 mph, c) 120 mph, d) 140 mph, for the displacement at LGS 009 (measured point)

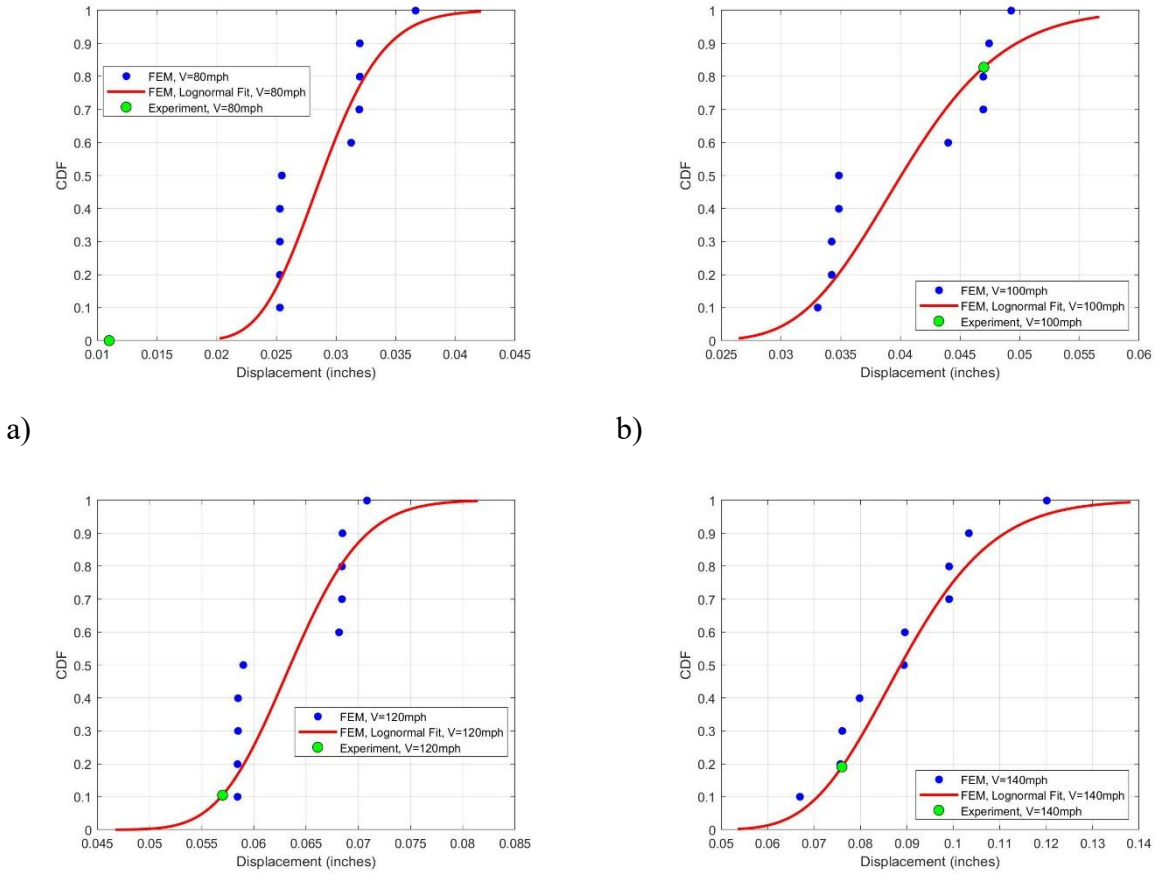

Figure 18. Comparison between FEM and Experimental test: a) 80 mph, b) 100 mph, c) 120 mph, d) 140 mph for the displacement at LGS 007 (measured point)

The results indicate that the FEM model is well-suited for analyzing and evaluating wind-induced responses in wood-frame structures, particularly when the cumulative probability falls within the statistically significant range of 0.1 to 0.9. The model demonstrates improved displacement prediction accuracy at higher wind speeds – a reasonable trend given that, under strong wind loads, the structural response is primarily governed by the nonlinear behavior of nail connections. In contrast, at lower wind speeds, the response is more influenced by the stiffness of the roof sheathing, whose statistical variability was not incorporated into the FEM model. Moreover, due

to signal noise in the experimental data, the model tends to be more reliable in predicting larger displacements than smaller ones. To improve accuracy across all wind speeds, increasing the number of randomly selected nail positions beyond ten could help produce a more representative displacement distribution. The research team plans to expand the analysis to include additional cases for greater reliability. Despite these limitations, the current findings demonstrate that the FEM model is a dependable tool for evaluating the structural performance of manufactured housing units under dynamic wind loads, particularly when simulated results align closely with experimental measurements.

In a second example, the FEM model is applied at a wind speed of 145 mph, where large displacements and potential roof sheathing failures are more likely at specific nail locations. Experimental data under various wind directions are used to identify nail failure zones, observe significant roof sheathing deformations, and validate the nonlinear axial behavior of nails, as characterized by hysteresis-based cyclic withdrawal test data.

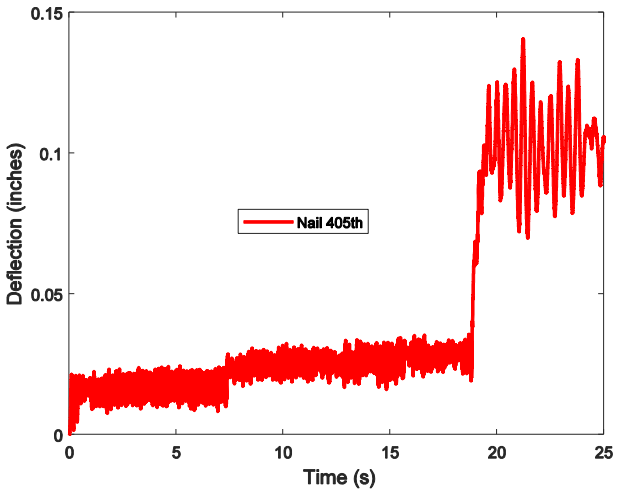

Figure 19. Displacement time history of nail connection No.1 (405) at failure

As shown in Figure 19 and Figure 6, the numerical deflections predicted by the 3D FEM model of the low-rise wood-frame building reach approximately 0.02 inches at the peak response of nail No. 1 (405) during each dynamic windstorm event. The accumulated displacement remains nearly constant within the 0–20 second time range, and the magnitude induced by wind loading is relatively small compared to the cyclic displacements observed in the withdrawal tests. This suggests that the dynamic displacements from wind loading correspond only to the initial cycles of the withdrawal test, and the resulting forces in the nonlinear nail elements under these conditions are relatively low.

After the nails received wind loads transferred from the walls and roof sheathing, the internal axial forces in the spring-nail elements were redistributed throughout the entire wood-frame structure due to nonlinear hysteresis effects – unlike the linear behavior observed in previous nail models [25-27]. During the 60-second simulation period, which captured significant deformations in both the roof and shear wall systems of the 1:4 scale low-rise wood-frame building, the displacement of Nail No. 1 (405) gradually increased, temporarily stabilized, and then experienced sudden failure at approximately the 20-second mark. At that point, the nail reached a peak displacement of around 0.15 inches, corresponding to the maximum nonlinear response and energy absorption. Following failure, the system's dynamic response progressively stabilized over the remaining simulation period (20 to 60 seconds), completing the deformation process under continued wind loading.

Notably, the displacement magnitudes of Nails No. 2 (404), No. 3 (390), No. 4 (397), and No. 5 (398) differed from that of Nail No. 1, exhibiting smaller amplitudes depending on their relative

positions. As shown in Figure 20, these nails were located in the failure region of the roof sheathing, which exhibited failure patterns consistent with those reported in Ref. [29].

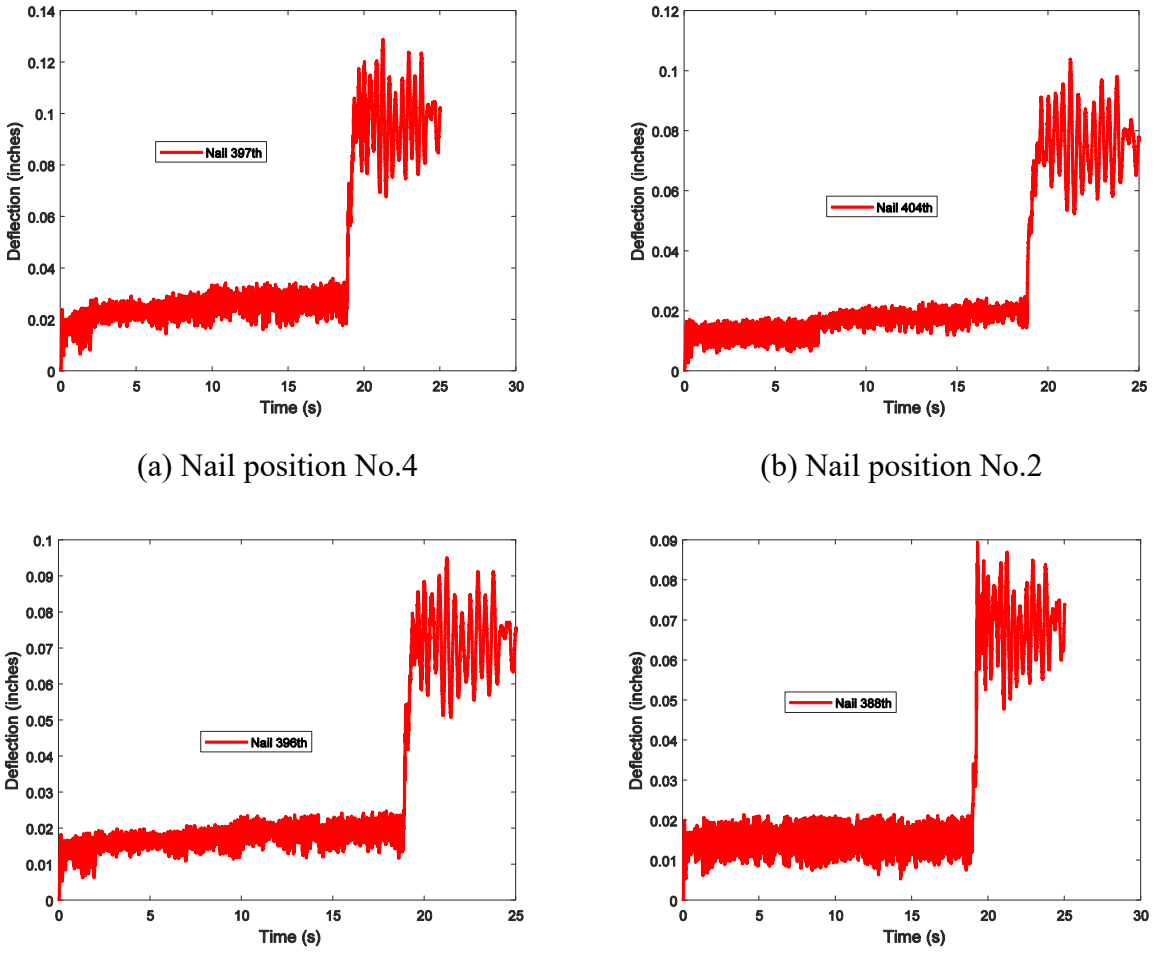

(a) Nail position No.4

(b) Nail position No.2

(c) Nail position No.3

(d) Nail position No.5

Figure 20. Nail response time histories

Figure 21 shows that the large deformations observed in the risk areas of the roof sheathing during testing at the WOW facility in Florida closely match the numerical predictions. In these regions, wind loads cause nail pull-out failures at damaged locations. The significant deformation of the nail is fully consistent with experimental observations, particularly at Nail No. 1 (405), which was withdrawn under wind loading perpendicular to the long edge of the 8-ft OSB panel designed

according to standard specifications [30]. This withdrawal resulted in cracking the roof surface. In contrast, the adjacent OSB panel of smaller dimensions did not exhibit failure.

The observed deformation pattern reflects substantial structural damage to the frame of the low-rise building, comparable to failures seen in real-world applications. To mitigate this risk, structural reinforcement is recommended, specifically, by increasing the number of nails to enhance the strength of the connection and ensure that the wood-frame structure performs reliably and remains stable under varying wind directions.

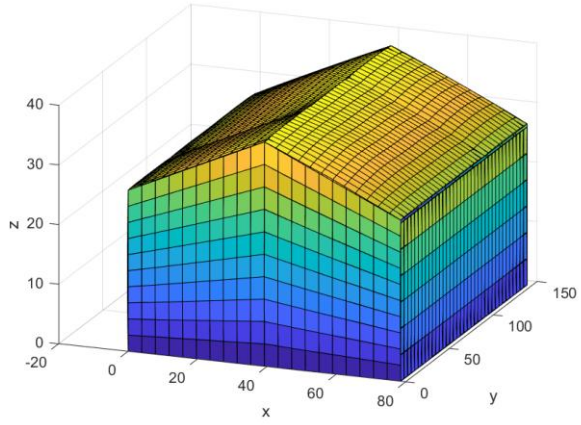

(b) 0-15s

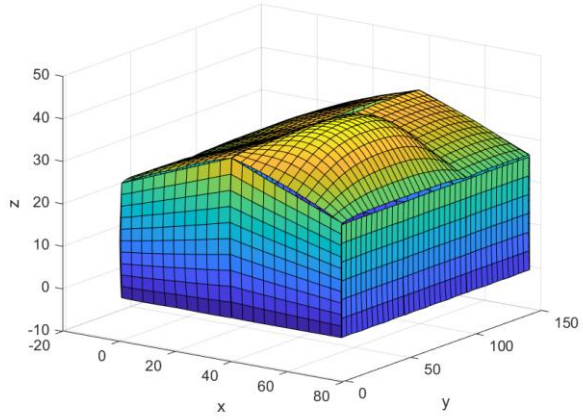

b) 20 sec

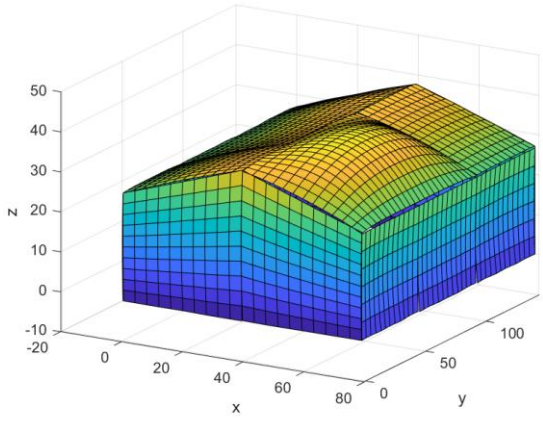

c) 30 sec

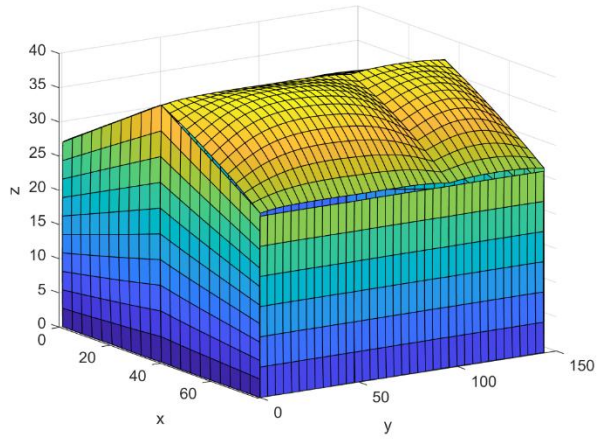

d) 60 sec

Figure 21. Comparison of failure modes between numerical and experimental roof sheathing deformations at different times under dynamic wind loading at 0° direction

The loading peaks generated by dynamic windstorms in the wind tunnel appear as a random time series throughout the test duration. Extracting these peak values for comparison with numerical responses, based on hysteresis data from a fixed loading protocol, is essential for evaluating the accuracy of the hysteresis algorithm implemented in the 3D nonlinear finite element model. Notably, the loading and unloading peaks observed in cyclic nail withdrawal tests differ significantly from those produced by dynamic wind loads in the WOW FL experiment. However, as shown in Figure 22, the generalized spring model under wind loading, derived from the 3D FEM, demonstrates hysteresis behavior that aligns reasonably well with the cyclic test data. This correlation is due to the fact that wind-induced axial force peaks in the nails generally follow the load-displacement path established in the withdrawal tests.

It is evident that when the magnitude of these wind-induced axial forces exceeds the predefined loading protocol or deviates from the load-displacement path, damage begins to accumulate and progressively increases at each nail connection in the low-rise wood-frame building model during wind tunnel testing. Conversely, when the peak force remains below the hysteresis threshold, the response is considered non-damaging, and the displacement simply oscillates around the equilibrium position without initiating failure.

The results indicate that when wind loads act perpendicular to the longitudinal axis of a low-rise frame building, the nails near the edges of the roof sheathing are the most vulnerable. This region experiences a significant concentration of wind energy, consistent with predictions from design standards, leading to damage accumulation in the nails and eventual failure, as observed in the FEM model.

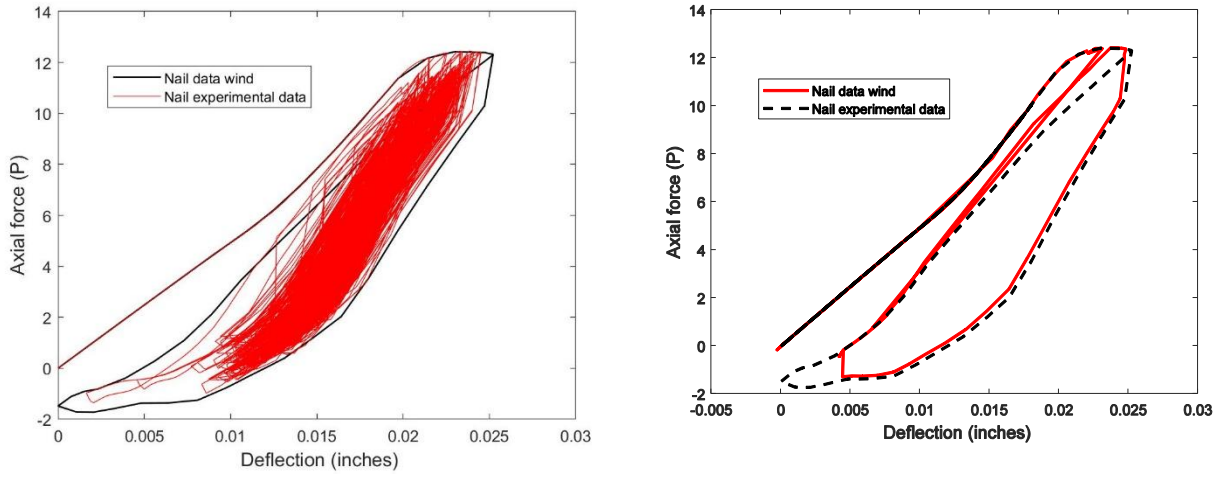

a) b)

Figure 22. Comparison to load-displacement hysteresis at the nonlinear nail connection under the wind dynamic load at $0^0/180^0$ and the Wind tunnel experimental data: a) dynamic variation peaks under wind load, b) maximum load-displacement curve under wind load.

The comparison results shown in Figure 24 and Figure 26 are consistent and reasonable for wind directions of 90° and 45°/135°, respectively. The internal axial forces developed in the nail connections under dynamic wind loads closely follow the hysteresis trajectories observed in the cyclic load tests of the sheathing-to-roof connections. It is evident that the nails at the roof-to-wall connections possess greater load-carrying capacity and do not experience axial forces that exceed the critical threshold on the load–displacement curve. As a result, these connections remain well within the safe zone under dynamic wind loading. In contrast, nails at roof sheathing connections are more susceptible to damage. Wind-induced vibrations can cause accumulated deformation and

progressive damage in these nails, potentially leading to withdrawal or even failure under large displacements.

A clear pattern is observed in Figure 23 and Figure 24 for wind loading applied at 90°, perpendicular to the short edge of the 1:4 scale low-rise wood-frame building (E–W direction). The wind speed remains consistent with the other tested directions (0°/180° and 45°/135°) at 140 mph. Under this condition, the load-displacement responses of the most highly loaded nails remain below the ultimate threshold established by the experimental cyclic loading data. As a result, the structure, including nails in critical regions, did not exhibit significant deformations in the roof sheathing under the 90° wind load.

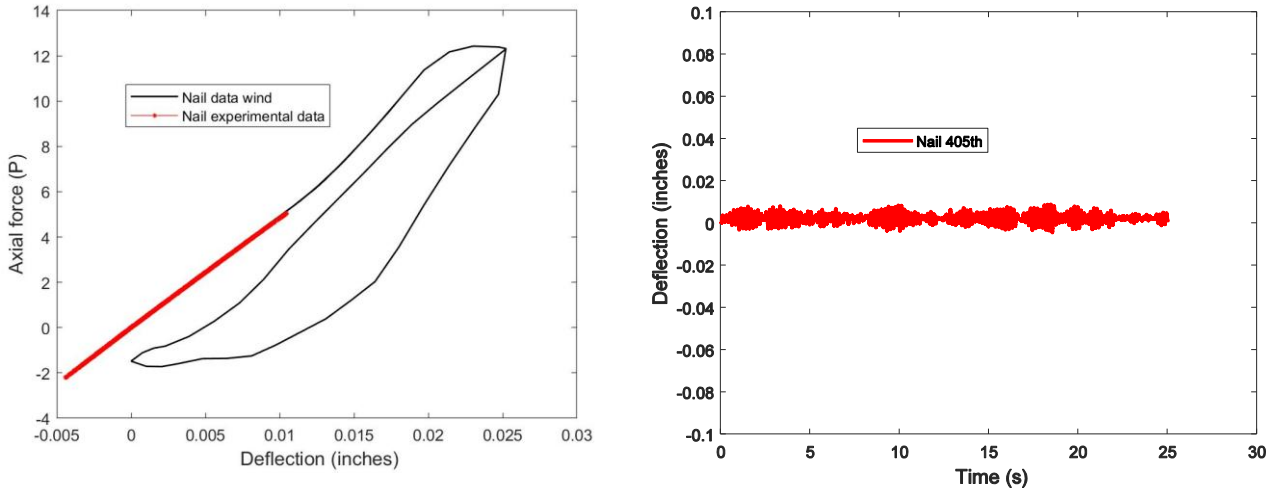

(a) b)

Figure 23. Nail responses under 90° wind load direction: a) Load–displacement path comparing dynamic FEM responses at the failure nail with experimental data; b) Time history of dynamic displacement at Nail 405 under 90° wind direction.

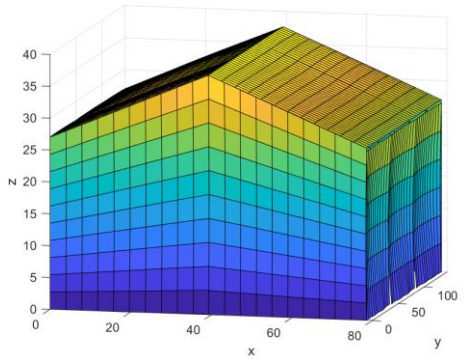

Figure 24. Dynamic roof deformations from 0 to 60 seconds under 90° wind loading

As shown in Figure 16, wind energy generated in the wind tunnel experiment was applied to the frame of the low-rise building at angles of 45° and 135° relative to the longitudinal axis of the structure. The numerical results from the 3D FEM model, presented in Figure 25 and Figure 26, indicate that the nonlinear axial force–displacement response and displacement time history of the most highly loaded nail closely match the behavior observed in the cyclic tests of the roof-sheathing connection. Moreover, the internal axial force in the nail remains below the threshold defined by the cyclic load-displacement curve, further validating the consistency between the wind tunnel testing results on the 1:4 scale MHU at the WOW FL facility and the FEM predictions. These findings are supported by the nonlinear spring model used for the nail connections between the wood frame and sheathing panels, confirming that the connection system remains stable under wind loading from these directions.

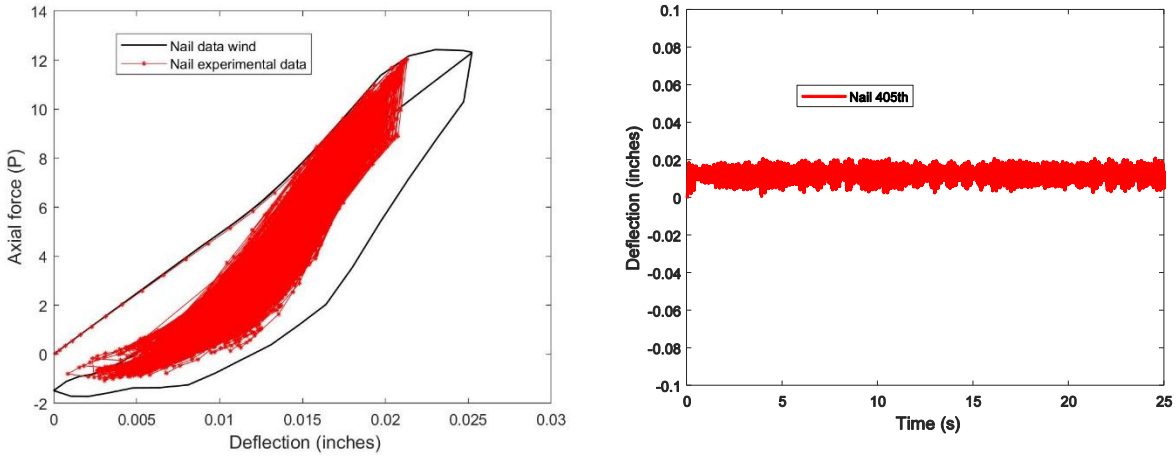

(a) b)

Figure 25. Nail responses under 45° wind load direction: a) Load–displacement path comparing dynamic FEM response at the failure nail with experimental data; b) Time history of dynamic displacement at Nail 405 under 45° wind direction.

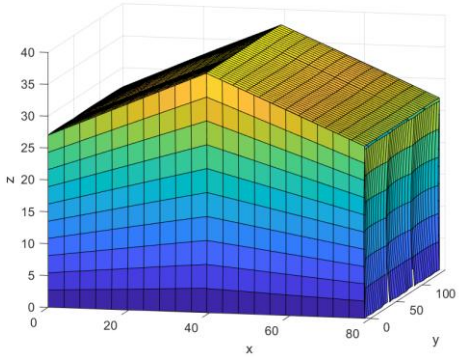

Figure 26. Dynamic roof deformations from 0 to 60 seconds under 45° wind loading

7. Fragility analysis

To estimate the statistical behavior of roof sheathing and roof-to-wall openings, a series of finite element (FE) analyses was conducted using the proposed nonlinear nail model. Displacements were evaluated at LGS 009 (Nail 405) on the roof sheathing and at LGS 007 (Nail 387), located near the roof-to-wall connection (Figure 1). Five experimentally measured hysteresis curves were randomly assigned to simulate nail behavior across 10 different cases, each subjected to wind

pressures of 80, 85, 90, 95, 100, 110, 120, 130, and 145 mph at a wind direction of 135°. An 8d nail, commonly used in light-frame wood construction, was used in the cyclic withdrawal tests to reflect realistic performance.

Based on these simulations, the probability of roof displacement, or the structure's capacity to resist uplift forces, can be evaluated using the following limit condition:

$$g(X) = R - (W - D)$$

where $\boldsymbol{X} = [WL\ DL\ R]^T$ is the vector of variables:

- WL represents the random wind load uplift pressure,
- DL is the random dead load, and
- R is the random uplift resistance at a certain limit, computed using the 3D finite element model based on the roof sheathing configuration and the arrangement of nails.

The conditional probability that the connection displacement D exceeds a specified threshold d, given a wind speed $V = v$, is defined as the *connection fragility*. It quantifies the likelihood of failure in a structural connection subjected to both wind and dead loads and can be expressed as:

$$P(V) = P(g(X) \leq 0 | V = v) = P(D \geq d | V = v)$$

where V represents the wind speed demand. In this study, the fragility model is used to evaluate the probability of damage to both the roof sheathing and the roof-to-wall connections.

Error! Not a valid bookmark self-reference. presents the calculated values of the coefficient of variation (COV), coefficient of determination (R^2), and Kolmogorov–Smirnov (KS) statistics at displacement thresholds of d=0.068d = 0.068d=0.068 in. and d=0.042d = 0.042d=0.042 in. for the roof sheathing and the

nail position near the roof-to-wall connection. At $d = 0.068\ in.$, the COV is approximately $0.1457\ in.$, indicating that the data vary by about 14.57% from the mean value. This relatively low COV reflects limited data dispersion and suggests that the model yields consistent results, which is desirable in FEM simulations, especially when variability is introduced by randomly placed nails.

The lognormal model explains approximately 98.33% of the data variability ($R^2 = 0.9833$), indicating an excellent fit. This highlights the model's effectiveness in capturing the deformation and damage behavior of structural components. Statistically, the lognormal distribution offers the most accurate representation of the displacement data.

The Kolmogorov–Smirnov (KS) statistic, which quantifies the maximum difference between the empirical cumulative distribution function (CDF) and the theoretical lognormal CDF, is relatively low and consistent ($KS = 0.44$). This suggests that the deviations between the empirical and fitted distributions are not statistically significant, supporting the plausibility of the data originating from the lognormal distribution. Similarly, at the threshold displacement of $d = 0.00019\ in.$, the lognormal model demonstrates strong performance for roof-to-wall nail connections, further validating its suitability for modeling connection fragility under wind loads.

Table 9. Evaluations for Lognormal fit with FEM data at roof-sheathing (d=0.068, 0.09 inches) and roof-to-wall (d=0.00014, 0.00019 inches) nail tests.

Distribution	COV	R^2	KS Statistic
d=0.068 inches	0.1457	0.9833	0.4444
d=0.09 inches	0.3727	0.9498	0.6667
d=0.042 inches	0.0644	0.9915	0.3750
d=0.069 inches	0.1221	0.9950	0.6250

Figure 27 and Figure 28 compare the fragility distributions derived from the lognormal fit with the results obtained from finite element analysis (FEA), which accounts for wind pressure–induced

displacements at the roof sheathing and roof-to-wall connections, respectively. The x-axis represents wind-induced pressure, corresponding to wind speeds in miles per hour (mph). The left y-axis indicates the conditional probability (fragility), which reflects the likelihood that the displacement exceeds a specified threshold. The right y-axis shows the ten displacement responses obtained from FEM simulations using ten randomly selected nails installed on the wooden roof at the critical measurement location, illustrating the variability in local structural response due to random nail placement. Additionally, four experimental displacement values, measured at wind speeds ranging from 80 to 140 mph, are superimposed on the figures to assess the agreement between measured and FEM-predicted displacements. The results indicate that the experimental displacements fall well within the range of FEM predictions, further validating the suitability of the FEM approach for wind analysis of wood-framed structures.

The red dots represent displacement data points obtained from FEA simulations that incorporate time-dependent wind pressures and nail hysteresis behavior, based on wind tunnel measurements and cyclic nail pull-out test data, respectively. Each red dot corresponds to a specific wind pressure level. The lognormal distribution, shown as a solid red line, provides an excellent fit to the simulation data within the wind speed range of 80–145 mph, particularly in the probability range of 0.1 to 0.98. As the displacement threshold increases, from $d = 0.068\ in.$ to $d = 0.09\ in.$ for roof sheathing, or from $d = 0.04\ in.$ to $d = 0.09\ in.$ for roof-to-wall connections, the fragility curves shift to the right, as indicated by the thin red dashed lines. This shift reflects that greater wind pressures are required to reach the same probability of exceedance for higher displacement thresholds.

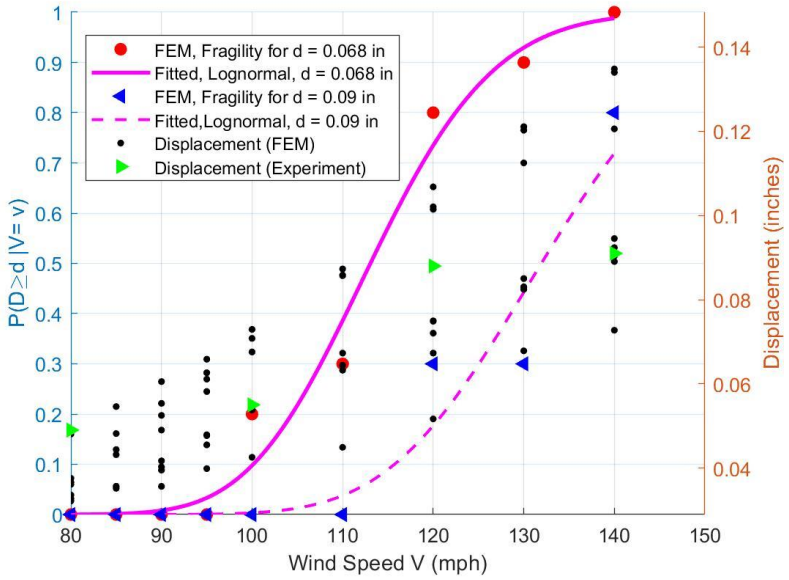

Figure 27. Fragility curves for connection LGS 009 (Nail 405).

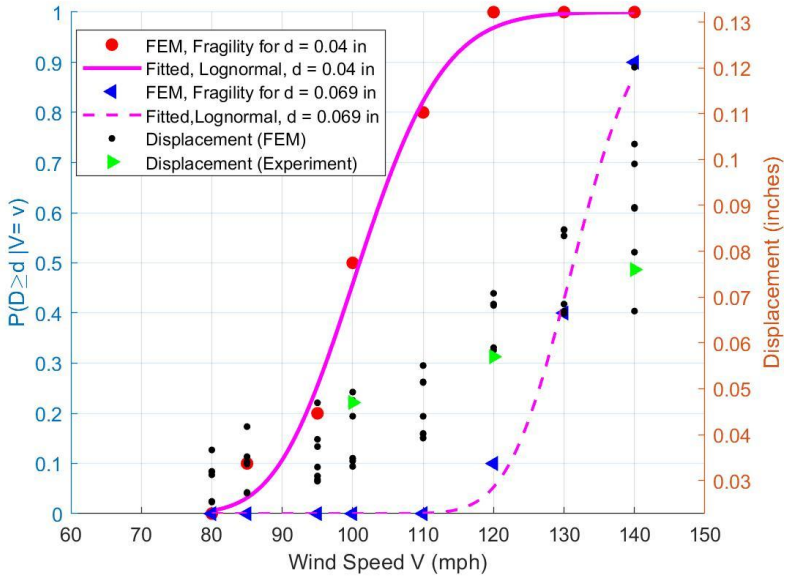

Figure 28. Fragility curves for connection LGS 007 (Nail 387).

The fragility of the panel, as illustrated in the preceding figures, is assessed using a probability-based equation that captures the likelihood of panel failure. The conditional probability of edge opening for LGS 009 (Nail 405) is higher than that for LGS 005 (Nail 387), indicating that the

roof sheathing edge (Nail 405) is more susceptible to wind-induced displacement than the roof-to-wall connection (Nail 492).

8. Conclusion

This report presents the validation of a 3D finite element method (FEM) developed to simulate the structural response of low-rise wood-frame buildings subjected to windstorms generated in a wind tunnel environment. The proposed general hysteresis model effectively addresses limitations of existing models by automatically fitting experimental data and ensuring consistent behavior across different materials and connection types. The new nail model offers a reliable tool for high-performance frame-building design, particularly in enhancing resilience against extreme wind events such as hurricanes and tornadoes.

The key contributions and insights from this study are summarized as follows:

- The proposed general nonlinear hysteresis model accurately predicts the force–displacement behavior and cumulative energy dissipation in structural components and materials.
- The model incorporates the extraction and condensation of key parameters, including loading, unloading, and backbone curves, while integrating a damage accumulation parameter. This allows the simulation of history-dependent, nonlinear nail behavior with strength degradation and pinching effects. The backbone curve is generated using an interpolated shape function, enabling the model to capture complex responses observed in experimental tests across various loading cycles and displacement magnitudes.
- The 3D FEM demonstrates strong capability in identifying damage locations, particularly at nail connections, under varying wind directions. It effectively captures large

deformations and potential failure in roof sheathing, confirming its accuracy and enhancing its applicability in performance-based design and research.

- The general nail model accounts for displacements and corresponding rotations, reducing the influence of misalignment stiffness. By improving alignment with monotonic test results, the model offers more realistic predictions than traditional scalar elastic nail models, which tend to overestimate displacements.
- This study represents a significant advancement in the dynamic analysis of lightweight frame structures subjected to turbulent cyclic wind loading. The 3D FEM framework provides a robust foundation for future research and development in the field of performance-based wind design.
- The comparison of cumulative probability (CDF) and fragility between FEM results and experimental measurements indicates that the proposed FEM model – incorporating 3D beam elements, shell elements, and a nonlinear six-degree-of-freedom nail model – is capable of accurately predicting the structural behavior of roof sheathing and nail failures under wind loading.
- The findings contribute to a deeper understanding of structural behavior under cyclic loading and support the development of advanced hysteresis modeling techniques. The newly developed model marks a major step forward in accurately capturing complex structural behaviors under dynamic loads, thereby enhancing the safety, reliability, and resilience of the built environment.

9. Analyzing for full-scale MHs (Phase 5 DEM and NSF RAPID project)

In Phase 5 of the DEM and NSF RAPID project, we continue to utilize the proposed FEM approach – previously validated through large-scale (1:4) wind tunnel tests at Florida International University (FIU) and nail withdrawal cyclic loading tests at the University of Kansas (KU)—to predict and evaluate the performance of manufactured housing units (MUs) under wind loads tested at the Wall of Wind (WOW) facility. This phase expands the methodology to full-scale modeling by incorporating input parameters from full-scale wind tunnel tests and maintaining collaboration with the KU team for additional cyclic loading experiments on connections and sub-components.

To support this, MU parameters – including dimensions, materials, and structural connections – will be documented and implemented in the FEM model. If certain data are not available from previous studies, additional component tests will be conducted at KU. Connection property data will be randomly assigned within each connection type in the FEM model to capture the statistical variability inherent in real structures.

Wind loads from the large-scale (1:4) wind tunnel tests will be scaled and interpreted for application to the full-scale FEM as time-history pressure loads on the building envelope. FEM simulations will be performed to evaluate displacements and damage levels for each randomly generated structural property dataset. The outcomes will be presented in the form of cumulative distribution functions (CDFs) and fragility curves to assess the wind performance of manufactured housing units. In addition, this method will enable the research team to evaluate the performance of roof-to-wall connections at the full scale – an analysis that was not feasible at the 1:4 scale, as

the wind loads in previous tests were insufficient to induce nonlinear behavior in these connections.

10. References

1. Sigma-Swiss Re, 2011. Natural Catastrophes and Man-Made Disasters in 2010. No. 1/2011. Swiss Reinsurance Company Ltd., Zurich, Switzerland.

2. Pielke, J., Roger, A., Gratz, J., Landsea, C.W., Collins, D., Saunders, M.A., Musulin, R., 2008. Normalized hurricane damage in the United States: 1900–2005. Natural Hazards Review 9 (1), 29–42.

3. Caracoglia, L., Jones, N.P., 2009. Analysis of full-scale wind and pressure measurements in a low-rise building. Journal of Wind Engineering and Industrial Aerodynamics 97 (5–6), 157–173.

4. Balderrama, J.A., Masters, F.J., Gurley, K.R., Prevatt, D.O., Aponte-Bermu´ dez, L.D., Reinhold, T.A., Pinelli, J.-P., Subramanian, C.S., Schiff, S.D., Chowdhury, A.G., 2011. The Florida Coastal Monitoring Program (FCMP): a review. Journal of Wind Engineering and Industrial Aerodynamics 99 (9), 979–995

5. Pavkovic K, Rajcic V, Haiman M. Large diameter fastener in locally reinforced and non-reinforced timber loaded perpendicular to grain. Eng Struct 2014;74:256–65

6. Gecys T, Daniunas A, Bader TK, Wagner L, Eberhardsteiner J. 3D finite element analysis and experimental investigations of a new type of timber beam-tobeam connection. Eng Struct 2015;86:134–45.

7. Wua GF, Zhu EC, Zhou HJ, Pan JL. Testing and modelling of shearwalls studded with small-diameter round timber under cyclic lateral load. Constr Build Mater 2015;77:288–96.

8. Branco JM, Araújo JP. Structural behaviour of log timber walls under lateral inplane loads. Eng Struct 2012;40:371–82.

9. Bolmsvik A, Linderholt A, Brandt A, Ekevid T. FE modelling of light weight wooden assemblies – parameter study and comparison between analyses and experiments. Eng Struct 2014;73:125–42.

10. Vessby J, Källsner B, Olsson A, Girhammar UA. Evaluation of softening behaviour of timber light-frame walls subjected to in-plane forces using simple FE models. Eng Struct 2014;81:464–79.

11. del Coz Díaz JJ, García Nieto PJ, Lozano Martínez-Luengas A, Suarez Domínguez FJ, Domínguez Hernández J. Non-linear numerical analysis of plywood board timber connections by DOE-FEM and full-scale experimental validation. Eng Struct 2013;49:76–90

12. Girhammar U, Kallsner B. Elasto-plastic model for analysis of influence of imperfections on stiffness of fully anchored light-frame timber shear walls. Eng Struct 2009; 31:2182–93.

13. Chui Y, Ni C, Jiang L. Finte-element model for nailed wood joints under reversed cyclic load. J Struct Eng 1998;124(1):96–103

14. Daudeville L, Davenne L, Yasumura M. Prediction of the load carrying capacity of bolted timber joints. Wood Sci Technol 1999:15–29

15. Richard N, Daudeville L, Prion H, Lam F. Timber shear walls with large openings: experimental and numerical prediction of the structural behaviour. Can J Civil Eng 2002:29:713–724

16. Xu J, Dolan J. Development of nailed wood joint element in abaqus. J Struct Eng 2009;135(8):968–76.

17. Kasal B, Leichti R. Nonlinear finite-element model for light-frame stud walls. J Struct Eng 1992;118(11):3122–35

18. Yasumura M, Kamada T, Imura Y, Uesugi M, Daudeville L. Pseudodynamic tests and earthquake response analysis of timber structures ii: two-level conventional wooden structures with plywood sheathed shear walls. J Wood Sci 2006;52:69–74.

19. Meireles H, Bento R, Cattaro S, Lagomarsino S. A hysteretic model for frontal walls in pombalino buildings. Bull Earthquake Eng 2012.

20. Ayoub A. Seismic analysis of wood building structures. Eng Struct 2007;29:213–23

21. Pang W, Rosowsky D, Pei S, Lindt JVD. Evolutionary parameter hysteretic model. J Struct Eng 2007;133(8):1118–29

22. Humbert J. Characterization of the behavior of timber structures with metal fasteners undergoing seismic loadings. Ph.D. thesis, Grenoble University; 2010

23. U.S. Department of Housing and Urban Development (HUD) (2022). 24 Code of Federal Regulations Part 3280, Manufactured Home Construction and Safety Standards. Washington, D.C

24. National Design Specification (NDS) (2018). National Design Specification for Wood Construction, 2018 Edition. ANSI/AWC-NDS 2018. American Wood Council, Leesburg, VA.

25. Nikhil Kumar, Vinay Dayal, Partha P. Sarkar. Failure of wood-framed low-rise buildings under tornado wind loads. Engineering Structures 39 (2012) 79–88

26. Zisis I, Stathopoulos T. Wind load transfer mechanisms on a low wood building using full-scale load data. J Wind Eng Ind Aerodyn 2012;104–106:65–75.

27. Zisis, I., Stathopoulos, T., Smith, I., Doudak, G., 2011. Cladding pressures and primary structural system forces of a wood building exposed to strong winds. Canadian Journal of Civil Engineering—NRC Research Press 38, 974–983

28. Dao, T.N. and van de Lindt, J. W. (2008). "New Nonlinear Roof Sheathing Fastener Model for Use in Finite-Element Wind Load Applications." ASCE Journal of Structural Engineering, 134 (10) 1668-1674.

29. Jing He, Fang Pan, C.S. Cai, Filmon Habte, Arindam Chowdhury, Finite-element modeling framework for predicting realistic responses of light-frame low-rise buildings under wind loads. Engineering Structures 164 (2018) 53–69

30. American Plywood Association (APA)–The Engineered Wood Association. (2001). "Diaphragms and shear walls: Design/construction guide." APA–The Engineered Wood Association, Tacoma, Wash.

31. National Design Specification (NDS) (2018). National Design Specification for Wood Construction, 2018 Edition. ANSI/AWC-NDS 2018. American Wood Council, Leesburg, VA.

32. American Society of Civil Engineers (ASCE) (2022). Minimum Design Loads for Buildings and Other Structures, Standard 7. American Society of Civil Engineers, Reston, VA.

FIU International Hurricane Research Center

FLORIDA INTERNATIONAL UNIVERSITY

A Resource for the State of Florida

SECTION 4:

Torsional Loads on Irregular-Shaped Buildings

Report for the Period 2024-2025

A Research Project Funded by:

Florida Division of Emergency Management

Prepared by

Ioannis Zisis, PhD.

Graduate Student

Mahmoud Abdallah

July 31, 2025

Executive Summary

This study investigates how building shape and height affect wind pressures and structural forces in low-rise buildings through wind tunnel testing conducted at the Natural Hazards Engineering Research Infrastructure (NHERI) Wall of Wind Experimental Facility (WoW EF). Three building configurations, rectangular, L-shaped, and T-shaped, were evaluated at 1- and 3-story heights under simulated open terrain conditions. Pressure taps distributed across the building surfaces captured detailed pressure fields, allowing for the computation of mean ($\bar{C}_p$) and peak ($\hat{C}_p$, $\check{C}_p$) pressure coefficients. These data were integrated to derive directional base force coefficients, including torsional moments (C_T), lateral shear (C_{Sx}, C_{Sy}), and resultant force magnitudes (C_V).

The findings show that non-rectangular buildings (L- and T-shaped) experience significantly higher torsional and shear demands than rectangular baselines, with amplification becoming more pronounced at increased heights. Peak suction pressures were notably stronger near inward corners and projections of irregular plans, with pressure coefficients reaching values as low as –4.26, indicating intense suction forces capable of stressing or lifting roof and wall elements. Resultant shear coefficients and torsional moments increased by up to 43% compared to rectangular counterparts, with taller configurations exhibiting more persistent asymmetries and stronger directional peaks under oblique winds. Vertical extension was found to intensify flow separation, pressure differentials, and vortex shedding effects, especially in buildings with asymmetric outlines.

This study offers critical insights for Florida's building codes, particularly regarding low-rise structures in hurricane-prone areas. These findings will enable engineers and architects to design more resilient irregular buildings, ultimately enhancing structural integrity and improving public safety against severe wind events, leading to reduced property damage and more effective disaster preparedness for citizens.

Keywords: Wind tunnel testing; Irregular building geometry; Torsional wind loads; Shear force coefficients; Pressure coefficients; MWFRS; NHERI Wall of Wind.

Table of Contents

List of Figures

List of Tables

List of Symbols

Symbol	Description
α	Power-law exponent in velocity profile
$BLUE\ peak$	Statistically extrapolated peak (Lieblein, 1974)
C_p	Pressure coefficient
C_{Sx}, C_{Sy}	Shear force coefficients in x- and y-directions
C_T	Torsional moment coefficient
C_V	Resultant base shear coefficient
F_x, F_y	Base shear forces along building-fixed axes
$f_i(t)$	In-plane force at tap i at time t
h	Model roof height
$I_u(z)$	Turbulence intensity at height z
μ	Mean value
n	Sampling frequency
Pxx	Power spectral density
RMS	Root mean square
r_i	Moment arm from tap i to building centroid
σ	Standard deviation
$\sigma_u(z)$	Standard deviation of longitudinal velocity fluctuations at height z
$S_n(f)$	Spectral density of longitudinal velocity fluctuations
θ	Resultant load angle
$U(z)$	Mean velocity at height z
V	Resultant base shear
z_0	Surface roughness length

1. INTRODUCTION

Wind acting on buildings generates complex force systems that include not only along-wind and across-wind pressures but also torsional moments whenever pressure distributions become unsymmetric about the plan centroid. Early code provisions (e.g., NBCC 1995, ASCE 7-98) treated torsion in a simplified manner, typically using partial-load approximations (Isyumov & Case, 2000). However, wind-tunnel studies have shown that such simplifications often underpredict torsional demands, particularly for low- and mid-rise buildings (Isyumov & Poole, 1983; Tamura et al., 2001). While more advanced approaches like high-frequency base balance and pressure integration have improved predictions for tall buildings (Tallin & Ellingwood, 1985; Xie & Irwin, 2000), low-rise structures have historically received less focused attention.

In the past two decades, several studies have helped clarify torsional behavior in rectangular footprints, including the influence of roof slope, height, and terrain exposure (M. Elsharawy et al., 2012; M. R. Elsharawy, 2014; M. Elsharawy et al., 2015). These investigations established shear–torsion relationships and informed improvements in code-based eccentricity rules (Stathopoulos et al., 2013). However, most of this work remains limited to regular, symmetric plans.

In contrast, real-world low-rise buildings often feature L-, T-, or other nonrectangular geometries that introduce significant flow asymmetries and pressure concentration near reentrant corners. Prior studies have shown that these irregular shapes can lead to elevated cladding pressures and increased structural demands (Shao et al., 2018, 2019; Sarma et al., 2023, In Press; Matus & Zisis, In Press), but they typically stop short of quantifying global torsional effects or offering generalized design guidance.

This study addresses that gap by conducting wind-tunnel experiments on scaled L- and T-shaped buildings at multiple heights, using high-frequency pressure integration (HFPI) to derive global torsional loads. The analysis quantifies how plan geometry and height influence the magnitude and variability of torsion, shear, and uplift forces. Directional sensitivities are assessed to identify wind angles most critical for design. Current wind design standards, including ASCE 7, do not provide explicit provisions for torsional loads on irregular building plans such as L- and T-shapes. This study fills that gap by establishing empirical amplification trends based on wind

tunnel experiments. The results lay the groundwork for developing torsion-aware load combinations and design guidance, which are intended to inform future updates to existing code frameworks.

2. LITERATURE REVIEW

2.1. Code Prescriptions for Torsion in Rectangular Plans

Building codes have historically treated wind-induced torsion on rectangular footprints through simplified "partial-load" and eccentricity approaches, rather than directly measuring pressure-induced moments. In NBCC 1995, designers apply a 25 % unilateral reduction on one lateral face ("partial loading") to represent unbalanced pressures; this yields an effective eccentricity of only about 4 % of the plan width (Isyumov & Case, 2000). ASCE 7-98 and its successor ASCE 7-10 prescribe a 15 % eccentricity of the plan dimension, achieved by combining 75 % loading on one half of the façade with 25 % on the other ("envelope" method). Eurocode EN 1991-1-4 adopts a triangular loading distribution with a 6 % eccentricity rule for rectangular buildings (Isyumov & Poole, 1983; Isyumov & Case, 2000).

These code-based eccentricities were intended as conservative surrogates for actual torsional moments. However, wind-tunnel investigations have repeatedly shown that they often misrepresent true torsional demands. Isyumov & Poole (1983) used weighted pneumatic averaging to measure mean and fluctuating torque on square and 2:1 rectangular prisms in suburban and urban boundary layers; they found that small deviations in wind angle produce mean eccentricities far exceeding 4–6 % of plan width. For a square prism in suburban terrain, mean torsion coefficients peaked at wind angles of about 10°, with moment arms that doubled compared to face-normal flow (Isyumov & Poole, 1983). These results indicate that NBCC's 4 % eccentricity and Eurocode's 6 % rule underpredict mean torsion, especially near oblique wind angles.

Isyumov & Case (2000) further quantified code-accurate versus measured torsion for low (≤ 60 ft [18.3 m]) and intermediate-height (≈ 100–200 ft [30.5–61.0 m]) buildings. They demonstrated that NBCC 1995's partial-load pattern often underestimates C_T by up to 80 % for low-rise rectangles. In one example, a 32 ft × 32 ft × 16 ft (9.75 m × 9.75 m × 4.88 m) building yielded a measured $C_T \approx 0.24$, whereas NBCC partial loading predicted only $C_T \approx 0.09$ (Isyumov & Case, 2000). ASCE 7-98's 15 % eccentricity improved predictions for medium-rise buildings

but still failed to capture peak torsion at specific wind angles. Moreover, ASCE's approach becomes nonconservative when roof slope or terrain changes, as subsequent studies confirmed (Xie & Irwin, 2000).

For tall, flexible towers, Tallin & Ellingwood (1985) examined how high-frequency force-balance (HFFB) measurements overestimate generalized torsion; their mode-shape weighting analysis revealed that base-torque spectra from HFFB tests must be multiplied by approximately 0.66 to obtain true modal torque for a uniform first mode. Although Tallin & Ellingwood did not propose specific code changes, their work underscores that even when codes specify eccentricities, designers should be aware that HFFB can exaggerate torsional estimates if mode shapes are ignored.

Xie & Irwin (2000) reviewed torsional factors for tall buildings, identifying equivalent eccentricities of 6–8 % B for square plans and up to 25–30 % B for skewed or rounded footprints. They argued that ASCE 7-10's 4–6 % rules are often nonconservative for tall, torsionally sensitive geometries and recommended high-frequency pressure integration (HFPI) to capture actual C_p distributions. For rectangular towers, they suggested using $e \approx 10\text{–}15\,\%\,B$ and applying a load-reduction factor $r \approx 0.5\text{–}0.8$ (such that $M_T = e \cdot r \cdot F_H$) when wind-tunnel data are unavailable.

In summary, NBCC, ASCE 7, and Eurocode historically rely on 4–15 % eccentricity rules for rectangular torsion, implemented through partial-load or envelope load cases. Wind-tunnel evidence (Isyumov & Poole, 1983; Isyumov & Case, 2000) shows these prescriptions sometimes underpredict actual C_T by 50–80 %, particularly for low and intermediate heights. Tallin & Ellingwood (1985) and Xie & Irwin (2000) highlighted the need to weight HFFB data by mode shape and to adopt larger equivalent eccentricities for taller or skewed plans. These discrepancies between code assumptions and measured behavior set the stage for more detailed, experimental shear-torsion correlations that appear in subsequent rectangular-plan studies. In the state of Florida, ASCE 7 is the governing wind load standard referenced by the Florida Building Code, making it the most directly applicable among the standards discussed.

2.2. Wind-Tunnel Findings on Rectangular Low- and Medium-Rise Buildings

Wind-tunnel experiments on rectangular footprints have provided detailed insight into how shear (C_p) and torsion (C_T) coefficients vary with building height, roof slope, and exposure, and

have given rise to generalized shear-torsion combinations that outperform traditional code eccentricities.

Elsharawy et al. (2012) initiated this sequence by testing three 1:400 scale, gabled-roof models (full-scale eave heights of 19.7 ft and 39.4 ft [6 m and 12 m]) with plan aspect ratios (L/B) of 1, 2, and 3 in open-country and urban simulated terrains. Using 76–126 pressure taps per "half-face" and 312.5 Hz sampling, they computed peak torsion coefficients (C_T) for wind directions from 0° to 180° in 15° increments. Their results showed that increasing roof slope from 0° to 45° produced a ~ 20 % rise in C_T (open terrain) and ~ 40 % increase in C_p (Elsharawy et al., 2012). They also demonstrated that urban terrain turbulence can double both shear and torsional coefficients compared to open-country results. When comparing code predictions, ASCE 7-10's directional method matched measured torsions most closely, whereas NBCC 2010 underpredicted C_T by up to ~ 50 % and Eurocode EN 1991-1-4 by nearly 100 % for the same geometries (Elsharawy et al., 2012).

Building on these findings, Elsharawy (2014) expanded the parameter space by testing four full-scale heights—19.7 ft, 39.4 ft, 82.0 ft, and 164.0 ft (6 m, 12 m, 25 m, and 50 m)—again at 1:400 scale, with roof slopes of 0°, 18.4°, and 45°. Their instrumentation included 146 wall taps sampling at 300 Hz for 27 s (equivalent to one hour full-scale). Across all heights and slopes, nondimensional shear (C_S) and torsion (C_T) coefficients remained nearly invariant with height, as raw forces and reference velocities both scaled proportionally (Elsharawy, 2014). Crucially, peak-C_T events consistently occurred simultaneously with approximately 80 % of peak transverse shear (C_{Sy}) and 45 % of peak longitudinal shear (C_{Sx}), regardless of height or slope. Analytically, Elsharawy (2014) proposed replacing fixed eccentricities with $C_T = 0.3\ C_{Sy}$ for transverse winds and $C_T = 0.15\ C_{Sx}$ for longitudinal winds, arguing that these ratios more faithfully represent measured simultaneous peaks than code eccentricities of 6–18 % B.

Elsharawy et al. (2015) confirmed these shear-torsion ratios specifically for flat roofs (0° slope). They tested four heights—19.7 ft, 39.4 ft, 82.0 ft, and 164.0 ft (6 m, 12 m, 25 m, 50 m)—of a 200 ft × 128 ft (61 m × 39 m) plan in open terrain with 146 wall taps at 300 Hz sampling over 27 s per direction. For winds transverse to the long dimension, peak $C_T \approx 0.27$ coincided with concurrent transverse shear $C_{Sx} \approx 0.81$ (≈ 80 % of its own maximum ≈ 0.90) and longitudinal shear $C_{Sy} \approx 0.45$ (≈ 45 % of its maximum ≈ 1.0) (Elsharawy et al., 2015). When longitudinal shear

peaked, concurrent $C_T \approx 0.32$ (≈ 35 %–40 % of its peak ≈ 0.90). Comparing to codes, NBCC 2010's partial-load approach underpredicted C_T by ~ 60 % for the low-rise case (19.7 ft [6 m]) but overpredicted by ~40%–60% for medium heights (82.0 ft and 164.0 ft [25 m and 50 m]). ASCE 7-10's 15 % eccentricity envelope was conservative for flat roofs (overpredicting C_T by ~ 15 %–25 %) but became nonconservative when slope changed (underpredicting by ~ 10 %–20 % at 45°) (Elsharawy et al., 2015). Eurocode's 6 % eccentricity consistently underpredicted C_T by ~ 50 %–70 %.

Stathopoulos et al. (2013) also tested rectangular, medium-rise models (20 m–60 m full scale) at 1:400 scale, comparing flat (0°) and gabled (45°) roofs in open terrain. Using 146 wall taps at 300 Hz over 27 s per direction, they defined peak shear C_{Sx}, C_{Sy}, and torsion C_T as the average of the top ten one-hour extremes, and recorded corresponding shear/torsion at those instants. For flat roofs, their results echoed Elsharawy's findings: peak $C_T \approx 0.27$ aligned with concurrent $C_{Sx} \approx 0.81$ (≈ 80 % of max ≈ 0.90) and $C_{Sy} \approx 0.45$ (≈ 45 % of max ≈ 1.0). They further quantified that when C_{Sx} peaked (≈ 0.90), concurrent $C_T \approx 0.32$ (≈ 35 %–40 % of max ≈ 0.90), and analogous ratios held for C_{Sy} peaks. On gabled roofs, peak C_T rose by ~ 15 %–20 %, and peak shears by ~ 30 %–40 % compared to flat (Stathopoulos et al., 2013). Code comparisons showed NBCC 2010 underpredicting C_T by ~ 60 % at 20 m, but overpredicting by ~ 40 %–60 % at 40–60 m; ASCE 7-10's 15 % eccentricity was conservative for flat, but nonconservative for gabled; Eurocode remained ~ 50 % low across heights (Stathopoulos et al., 2013).

Tamura et al. (2001) focused on low-rise (≤ 10 m) square and rectangular models in both urban ($\alpha = 1/4$) and open ($\alpha = 1/6$) terrains, mapping instantaneous C_p distributions corresponding to peak along-wind (F_D), across-wind (F_L), and torsion (M_T). They found that extreme C_T events produced C_p patterns nearly identical to extreme F_D, large positive pressures on one windward half and intense local suctions near leading corners, confirming strong F_D–M_T coupling (Tamura et al., 2001). Their ensemble-averaged C_p fields showed that quasi-steady GC_p (mean C_p × gust factor) underpredicts asymmetry and thus underestimates torsion by up to 100 % (Tamura & Hibi, 2001). Using these extreme C_p maps on a four-column frame, they demonstrated as much as a 30 %–75 % underestimation in column stresses when ignoring torsion and cross-wind (Tamura et al., 2001).

Tamura et al. (2003) extended this analysis by correlating peak M_T with concurrent F_D and F_L for low- and middle-rise buildings—41.0 ft and 164.0 ft (12.5 m and 50 m) full-scale—based

on 50 mm and 200 mm models at 1:250 scale square/rectangular models. Data revealed that when F_D peaked, M_T could range from 0 % to 100 % of its peak value, whereas when F_L peaked, M_T stayed between 0 % and 30 % of its peak. Conversely, peak M_T correlated with ~ 80 % of peak F_D and ~ 20 % of peak F_L (Tamura et al., 2003). Cross-correlation analysis of instantaneous C_p time series confirmed high $|C_D|$–$|C_M|$ correlation (~ 0.8) but low $|C_L|$–$|C_M|$ (~ 0.2), explaining why torsion aligns closely with along-wind rather than across-wind extremes. Their structural load study for a four-column frame showed that including all six wind components (F_D, F_L, M_T, M_D, M_L, F_T) increased column stresses by up to 75 % compared to considering F_D alone (Tamura et al., 2003).

Nguyen et al. (2018) examined NBCC 2015's classification of low-rise ($H \leq 65.6$ ft [20 m], $H/D_s < 1$) and medium-rise (65–200 ft [20–60 m] or $1 \leq H/Ds \leq 4$) rectangles. They showed that NBCC 2015's partial-load Cases B and D lack explicit definitions for tributary lengths, leading to wide C_T variability when different interpretations are applied. For a low-rise 32.8 ft × 65.6 ft × 16.4 ft (10 m × 20 m × 5 m) building, NBCC 2015 and ASCE 7-10 predicted similar C_S but diverged by > 30 % in C_T. For five medium-rise cases, 66 ft × 66 ft to 66 ft × 197 ft (20 m × 20 m to 20 m × 60 m) with heights of 82.0 ft, 131.2 ft, and 196.9 ft (25 m, 40 m, and 60 m), NBCC 2015 and ASCE 7-10 produced shear and torsion within 5 % of each other, but ambiguity remained for low-rise. Nguyen et al. recommended adopting ASCE 7-10's 25 % reduced-loading partial-load method over NBCC's triangular load for low height (Nguyen et al., 2018).

Together, these wind-tunnel findings establish firm shear-torsion relations for rectangular low- to medium-rise buildings: peak $C_T \approx 0.3\, C_{Sy}$ (transverse winds) and $C_T \approx 0.15\, C_{Sx}$ (longitudinal winds), invariant with height (6 m–60 m) and robust to roof slope (0°–45°) (Stathopoulos et al., 2013; Elsharawy, 2014; Elsharawy et al., 2015). They also reveal that code provisions for NBCC 2010/2015 possess inconsistencies—underpredicting torsion for low-rise and overpredicting for certain medium-rise cases—whereas ASCE 7-10's 15 % eccentricity is conservative for flat roofs but fails when slope or terrain changes. Finally, Tamura et al. (2001) and Tamura et al. (2003) highlight the dominant role of along-wind pressures in driving torsion and demonstrate the shortcomings of quasi-steady C_p methods for torsion prediction. These comprehensive rectangular-plan studies laid the groundwork for explicit code-oriented

shear-torsion combination factors, yet leave unaddressed the behavior of irregular footprints—an issue tackled in the subsequent subsection.

2.3. Pressure & Cladding Studies on Irregular Footprints

Real-world low-rise structures often deviate from simple rectangles, exhibiting L-, T-, C-, or S-shapes that alter both local pressure distributions and global structural demands. Although few studies have measured torsional moments on such footprints, several wind-tunnel investigations have quantified how cladding pressures concentrate near reentrant corners and impact member loads.

Shao et al. (2019) tested eight 1:200 scale, hip-roofed models—four rectangular and four irregular (L-, T-, and C-shaped)—in open terrain to map both cladding pressures and resulting structural loads. Their instrumentation included 144 roof taps and 64 wall taps per model, sampled at 300 Hz over 27 s per wind direction. On rectangular hip roofs, peak suctions reached Cp ≈ –2.0 near corners, but non-rectangular models exhibited even deeper suction peaks (Cp ≈ –2.0 to –2.3) at reentrant corners, depending on wind angle. When these pressure distributions were applied in 3D finite element simulations (ABAQUS), intermediate frames on L-shaped models experienced moments that were approximately 25% larger than the corresponding rectangular case; similarly, T-shaped models showed 20–25% higher shears and moments on their side wings. These findings were consistent with earlier work by Shao et al. (2018), who also investigated L- and T-shaped hip-roof buildings with 4:12 slopes using 1:100 scaled wind tunnel models. That study showed strong sensitivity of local Cp distributions to wind direction, especially around internal corners and junctions between roof segments. They further observed that L-shaped models exhibited increased turbulence-induced fluctuations and asymmetry in roof pressures, contributing to elevated cladding loads in those zones. Together, the 2018 and 2019 studies demonstrate that irregular hip-roof footprints not only generate localized suction concentrations but also produce elevated global frame forces, effects not captured by conventional torsion correlations developed for rectangular plans.

For gable-roofed low-rise irregulars, Matus et al. (In Press) carried out an extensive experimental program at the Wall of Wind, testing a wide variety of non-rectangular plan geometries at 1:50 and 1:100 scales. The study included both gable and hip roof configurations

across rectangular, L-, T-, C-, and S-shaped plans, with pressure data collected under simulated open-terrain boundary layer conditions. While the results of this experimental campaign are currently under peer review, the dataset has already served as the foundation for two subsequent analytical studies by Sarma et al.

The roof-level study, published by Sarma et al. (2023), focused on the wind vulnerability of roof sheathing panels. Using a subset of the Matus dataset, they analyzed six gable-roofed and four hip-roofed models, capturing pressures at 520 Hz over 60 s per wind direction. Their findings showed that peak roof Cp on rectangular eaves reached –3.0 to –3.5, whereas irregular plans exhibited Cp values between –2.5 and –3.0 under oblique winds. Irregular shapes also showed a broader spatial extent of high suction zones (Cp < –1.0), with wall pressures clustering near reentrant corners.

The load-path-level analysis, currently under review, expanded the scope to global wind effects and introduced five dimensionless shape factors to relate plan geometry to base shear (CV), torsion (CT), and lift (CL). These are defined as:

1) Rectangularity (β_R): Plan area divided by the area of the minimum bounding rectangle (value = 1 for a rectangle).
2) Convexity (β_C): Perimeter of convex hull divided by actual plan perimeter ($\beta_C < 1$ indicates reentrant indentations).
3) Angularity (β_A): Inverse Cox circularity, defined as $(P^2/A)/(4\pi)$, where P = perimeter and A = area (higher β_A denotes sharper corners).
4) Irregularity (β_I): area outside best-fit ellipse/area of ellipse (quantifies deviation from an ideal ellipse).
5) Elongation (β_E): diameter of circumcircle/diameter of equal-area circle (measures plan stretch).

Their regression models achieved strong correlation ($R^2 \approx 0.85–0.92$), confirming convexity, irregularity, and angularity as dominant predictors of wind-induced loading. The best-fit expressions are:

- Peak vertical load coefficient:

$$C_{V,max} = -1.21 + 3.79\,\beta_C + 0.97\,\beta_I - 0.66\,\beta_E$$

- Peak torsional load coefficient:

$$C_{T,max}=0.184-1.14\,\beta_C-0.72\,\beta_A+2.49\,\beta_I$$

- Peak lateral load coefficient:

$$C_{L,max}=0.283-0.238\,\beta_C+0.115\,\beta_R+0.44\,\beta_E$$

These results reinforce the role of geometric complexity in driving extreme wind effects on irregular plans. However, both studies are limited to rigid, low-rise models; the influence of structural flexibility and height remains unaddressed.

While the work of Shao et al. (2019), Sarma et al. (2023, In Press), and Matus et al., (In Press) have significantly advanced understanding of how reentrant corners and shape irregularity elevate local C_p and global frame loads, none of these studies experimentally capture the resulting torsional moments (M_T). In particular, while Sarma et al. estimate C_T from pressure integration over vertical walls, they do not measure instantaneous M_T, nor do they explore how mode-shape weighting (Tallin & Ellingwood, 1985) or simultaneous shear-torsion correlations (Elsharawy, 2014) might influence combined load estimates. Consequently, a gap remains in determining true global torsion coefficients for L/T/C footprints in both low and medium-rise categories. This shortfall underscores the need for HFPI testing on irregular plans to capture instantaneous M_T, derive shear-torsion ratios, and ultimately propose codified design expressions that extend beyond rectangular approximations.

2.4. Dynamic & Mode-Shape Considerations

While most low- and medium-rise torsion studies rely on quasi-static pressure integration, dynamic effects and structural mode shapes can alter global torsional responses—particularly for taller or flexible buildings. Two key studies address how to account for these factors.

Tallin & Ellingwood (1985) investigated how high-frequency force-balance (HFFB) measurements, which inherently record base torque (i.e., assuming a uniform mode shape $\varphi(Z)=1$), overestimate the generalized torsional moment that a structure actually experiences under its first torsional mode ($\varphi(Z) \propto Z/H$). Using published wind-tunnel pressure data on a tall rectangular prism (full-scale aspect ratio 8.3:1:1), they recorded instantaneous torsional coefficients C_i at six discrete

elevations Z_i (ranging from H/12 to 11H/12) and determined pairwise correlations R_{ij} between those levels (Tallin & Ellingwood, 1985). By defining a modal weighting factor

$$w_i=\phi(Z_i)\, C_i\, \Delta Z_i H,$$

they showed that for a linear torsional mode ($\varphi(Z)=Z/H$), summing the top three levels (e.g., $Z_i \geq H/2$) captures ~ 82 % of the true modal RMS torsion, whereas the base-torque reading would imply 100 %. Thus, they derived a correction factor $K \approx 0.57$ (modal RMS ⁄ base RMS) for linear modes and K≈0.51 for cantilever modes ($\varphi(Z)=(Z/H)^{1.5}$). Their spectral analysis confirmed that, up to nondimensional frequencies $nB/U_H \approx 0.1$, the normalized modal-torque spectrum $G_M(nB/U_H)$ closely matches the base-torque spectrum $G_B(nB/U_H)$ when scaled by $K=\sigma_B/\sigma_M$ (Tallin & Ellingwood, 1985). Consequently, designers relying on HFFB data should multiply base-torque extremes by ~ 0.66 (i.e., $1/K=1/0.57$) to estimate true first-mode torsion for tall, flexible buildings. Although Tallin & Ellingwood focused on high-rise frames, their methodology underscores that mode shape matters: without appropriate weighting, base-torque readings can overestimate the torsional demand by ~ 75 %.

Xie & Irwin (2000) propose a simple way to estimate peak torsion on tall buildings when full high-frequency pressure integration is not available. They introduce an equivalent eccentricity, defined as the ratio of the maximum base torque to the sum of the orthogonal shear forces, and show from wind-tunnel tests that this eccentricity falls in the range of 6–8 % B for square plans, about 10 % B for 2:1 rectangles, and as high as 25–30 % B for skewed parallelogram footprints. Recognizing that the wind direction producing the worst torque rarely coincides with the worst shear, they also define a load-reduction factor, which for their case studies is roughly 0.7, meaning only about 70 % of the peak shear aligns with the peak torque direction. By combining these two parameters, they recommend the practical design shortcut

$$M_z \approx e\, B \times r\, F_{H,\max},$$

which delivers a conservative torsion estimate without the need for full-scale pressure integration.

On the dynamic side, Xie & Irwin examine how coupling between torsional and sway modes affects torsional demands. Their results indicate that moderate coupling (30–60 %) can

amplify peak torque by 10–20 %, but for geometries already highly torsionally sensitive—such as skewed or irregular plans—the static aerodynamic eccentricity remains the dominant driver. They therefore suggest that, in preliminary design, a baseline eccentricity of about 10 % B with a load-reduction factor near 0.5 offers a practical and sufficiently conservative estimate of torsional loads when HFPI is not feasible.

2.5. Identified Gaps & Motivation

Although the torsional behavior of rectangular low-rise buildings has been well characterized and cladding pressures on L- and T-shaped plans have been mapped, no experimental program has yet used high-frequency pressure integration to measure the global torsional moment on low-rise irregular footprints. Current code provisions still rely on eccentricity rules developed for rectangles or defer L- and T-shapes to generic wind-tunnel testing without explaining how to integrate local pressures into a net torsion. This study will close that gap by conducting high-frequency pressure integration on 1–3-story L- and T-shaped models, extracting true torsional moments, and deriving shear-torsion combination factors specifically for non-rectangular low-rise buildings, culminating in practical design expressions compatible with prevailing standards.

3. METHODOLOGY

3.1. Experimental Facility and Model Description

The experimental campaign was conducted at the NHERI Wall of Wind (WOW) Experimental Facility at Florida International University. The WOW EF is a large-scale open-jet facility capable of simulating hurricane-force winds using a twelve-fan array arranged in two curved, staggered rows. This system can generate sustained wind speeds of up to 157 mph (70 m/s), enabling realistic simulation of extreme wind conditions on scaled structures (Gan Chowdhury et al., 2017).

To replicate atmospheric boundary layers over different terrain types, the facility incorporates a flow-conditioning section upstream of the test area. This section includes modular spires and surface roughness elements that can be configured to produce velocity and turbulence profiles representative of open-country, suburban, or urban exposures (Abdallah & Zisis, 2025a, 2025b). The open-jet test section measures approximately 20 ft wide × 14 ft high (6.0 m × 4.3 m) and leads into a 16 ft (4.9 m) diameter turntable. This turntable allows precise model orientation in 15° increments, supporting full 360° directional testing.

Data acquisition is conducted using high-frequency pressure-scanning systems sampling at rates up to 625 Hz, while wind speed measurements are recorded at 2,000 Hz. These high-resolution sampling rates enable precise capture of both mean and fluctuating components of wind-induced loads. The overall blockage ratio of the system is maintained below 1%, minimizing interference effects on the flow and ensuring reliable aerodynamic measurements.

A schematic overview of the facility is shown in Figure 1, highlighting the fan array, terrain simulation elements, open-jet region, and rotating platform. A front-facing view of the twelve-fan system is presented in Figure 2, offering a visual of the full setup housed within the WoW EF building. These capabilities allow the WoW EF to support comprehensive studies of wind-induced pressures and loads on buildings and components, including investigations into the effects of plan irregularity and building height, as demonstrated in recent work by Abdallah and Zisis 2025a, 2025b).

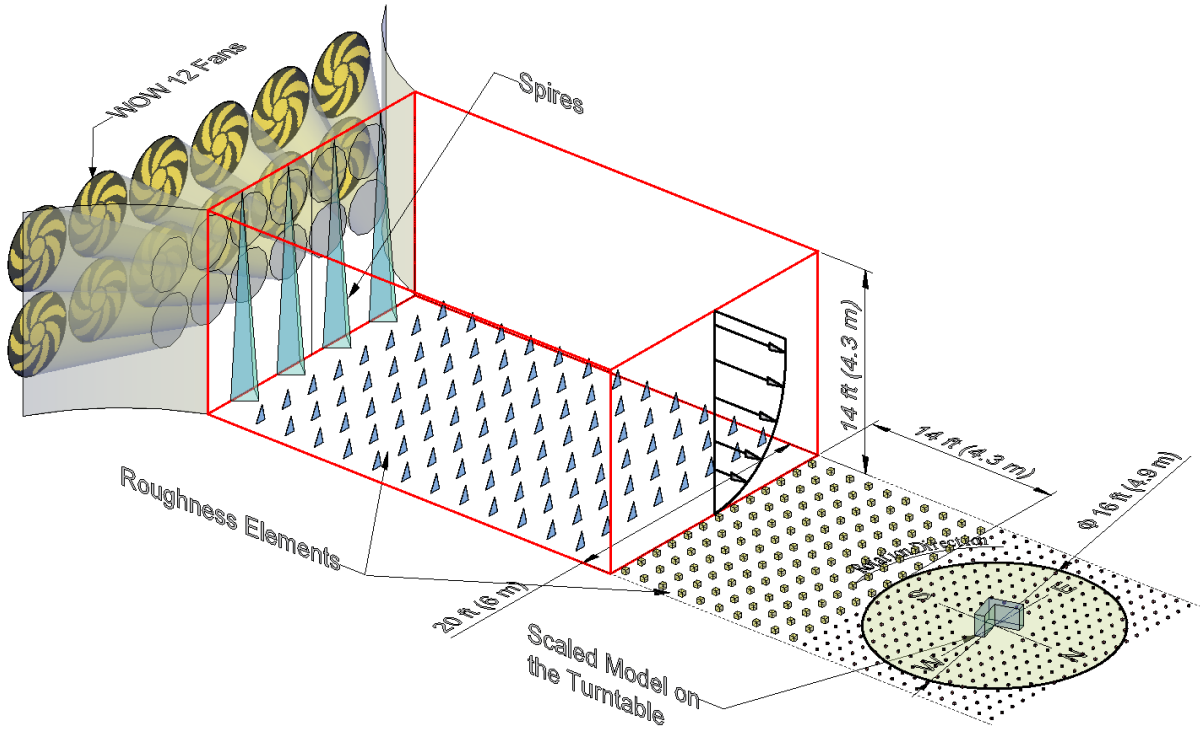

Figure 1. Schematic diagram of the NHERI Wall of Wind Experimental Facility setup (not to scale).

Figure 2. Front view of the 12-fan array inside the WoW EF at Florida International University.

3.2. Building Models

To evaluate how building geometry and height influence wind-induced loads, this study employed a set of simplified structures representing common low-rise residential buildings. Three distinct plan shapes—rectangular, L-shaped, and T-shaped—were selected to isolate the effects of plan irregularity, while keeping the overall footprint area approximately consistent across all configurations. These shapes are frequently encountered in residential and mixed-use developments, particularly in suburban and urban contexts.

Each shape was tested in 1-, 2-, and 3-story versions, reflecting the most prevalent height range of residential construction in hurricane-prone regions. This range captures key transitions in structural response due to increasing surface area, exposure, and potential for torsional amplification. All dimensions reported herein refer to full-scale values, based on a geometric scaling ratio of 1:50 from the physical models.

Each story corresponds to a full-scale height of 11.4 ft (3.475 m), resulting in total building heights of approximately 11.4 ft (3.5 m) for 1-story, 22.8 ft (7.0 m) for 2-story, and 34.2 ft (10.5 m) for 3-story configurations. The rectangular model has a footprint of 62.5 ft × 31.3 ft (19.05 m × 9.53 m). The L-shaped and T-shaped models, while preserving the same total plan area, were redistributed to introduce central projections and corner setbacks. Both had maximum dimensions of 62.5 ft × 46.9 ft (19.05 m × 14.29 m) in full scale.

Photographs of the models during testing are shown in Figure 3, while Figure 4 provides their corresponding plan dimensions. These idealized yet representative forms provided a systematic framework to assess the effects of building shape and height on wind pressures, force distribution, and torsional response.

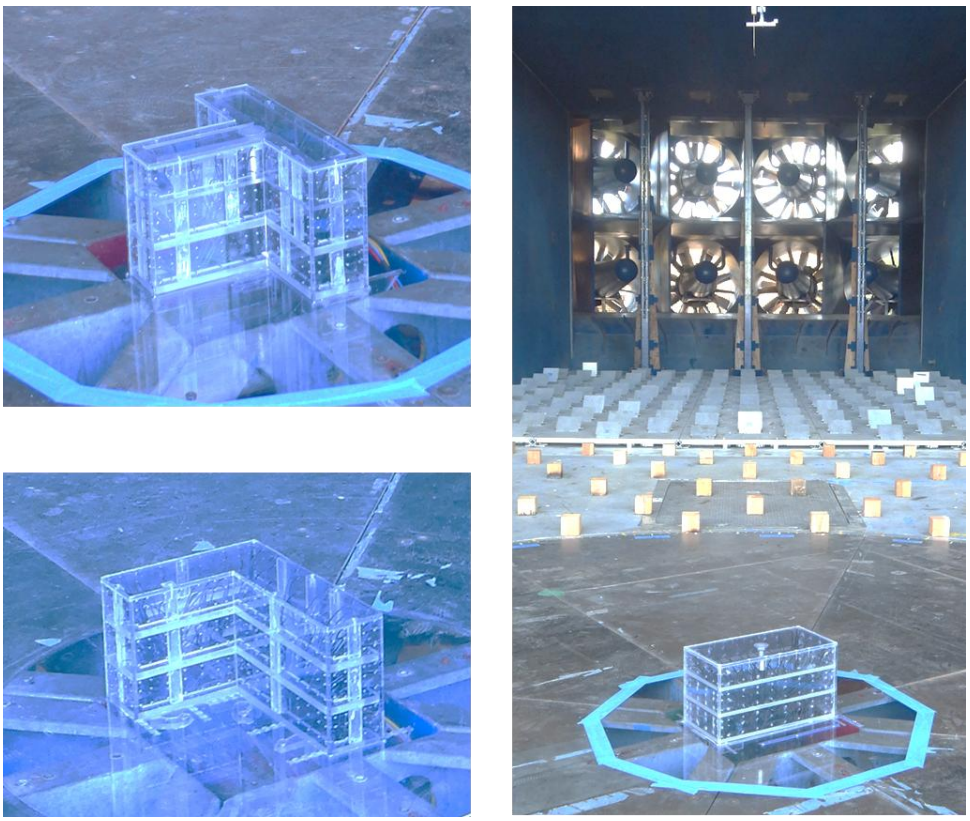

Figure 3. Rectangular, L-shaped, and T-shaped building models during wind tunnel testing at the NHERI Wall of Wind. Each shape was tested in 1-, 2-, and 3-story configurations to assess the effects of height and plan geometry on wind loads.

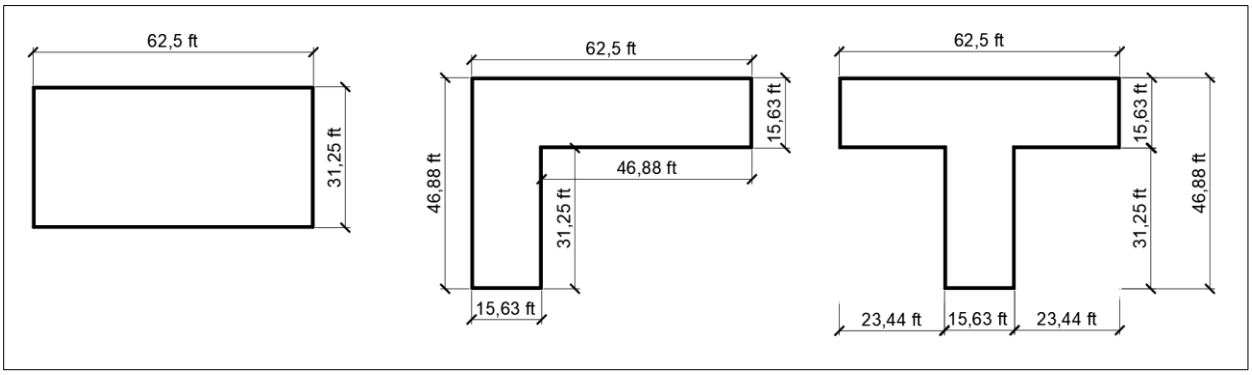

Figure 4. Plan dimensions of the rectangular, L-shaped, and T-shaped buildings. All values represent full-scale dimensions based on a 1:50 geometric scale.

3.2.1. Pressure Tap Layout for Single-Story Models

To capture wind-induced pressures across the building walls, each model was outfitted with a distributed array of wall-mounted pressure taps. Tap layouts were designed to maximize resolution in regions prone to flow separation and aerodynamic amplification, such as building

corners, intersections, and re-entrant zones. While the overall number of taps varied with plan shape, the layout strategy maintained symmetry and spatial coverage across all wall surfaces.

Figures 5 through 8 illustrate the pressure tap layouts used on the single-story rectangular, L-shaped, and T-shaped models, along with a representative wall segment (Wall#01) showing the vertical arrangement of tap rows. In each plan, taps were concentrated in areas of geometric complexity such as re-entrant corners and wall intersections to capture localized aerodynamic effects and torsional responses. While the overall tap count varied with plan shape, the layout maintained symmetry and uniform coverage along the facades. For all configurations, the same layout was replicated across additional story levels, with tap numbering continued accordingly. Vertically, each wall segment included three horizontal tap rows positioned at 2.98 ft, 4.10 ft, and 6.56 ft above floor level within the 11.4 ft story height. The total number of wall taps for each shape and story configuration is summarized in Table 1.

Although only the single-story layouts are shown, the same tap distribution was replicated vertically for the two- and three-story configurations, with taps added at each additional story level. The total number of taps per shape and height level is summarized in Table 1.

Table 1. Number of wall pressure taps per model configuration and story level.

Building Plan Shape	**1-Story**	**2-Story**	**3-Story**
Rectangular	96	192	288
L-shaped	120	240	360
T-shaped	126	252	378

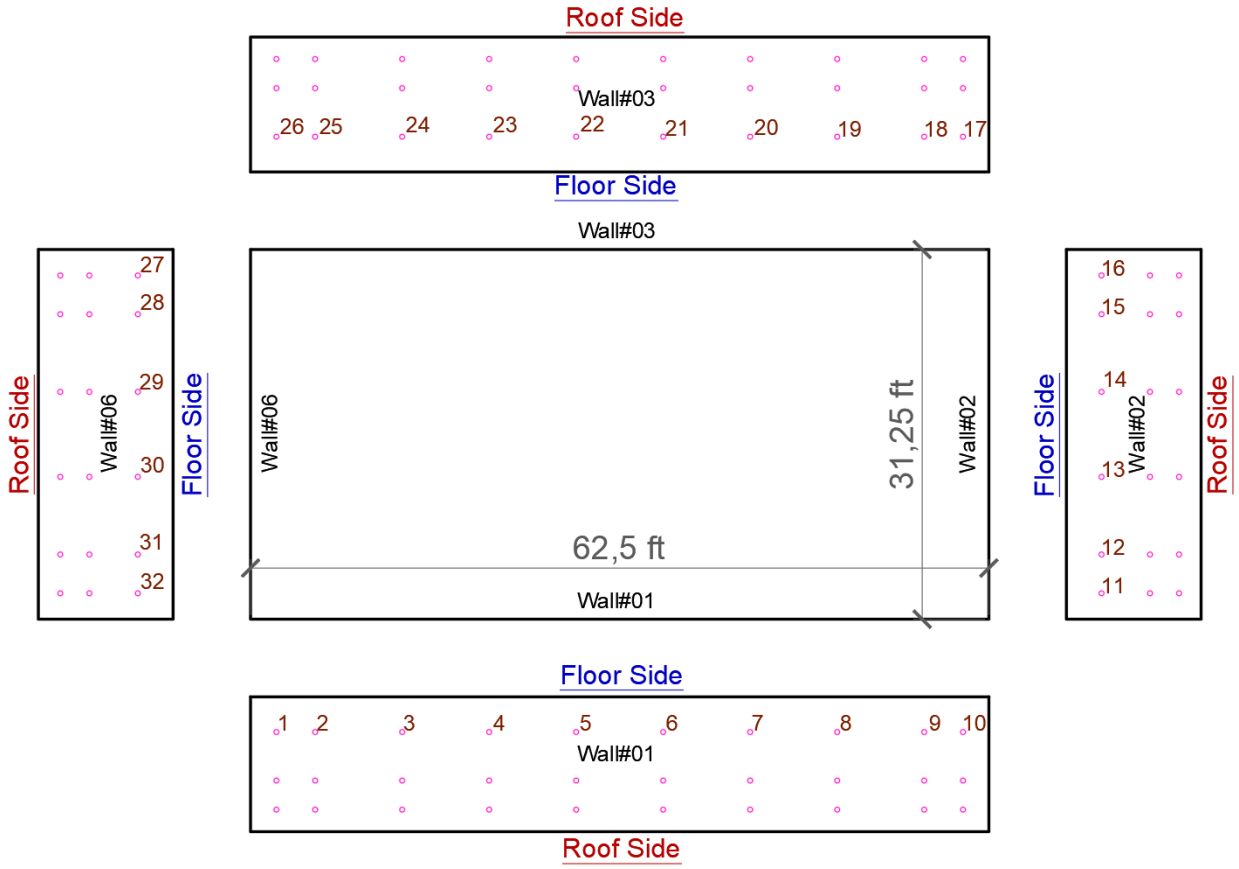

Figure 5. Pressure tap layout for the single-story Rectangular model. Tap numbers shown correspond to the first story only; upper stories repeat the same layout and continue the numbering. Tap rows are placed at 2.98 ft, 4.10 ft, and 6.56 ft above the floor, within the 11.4 ft story height. All dimensions are provided in full scale.

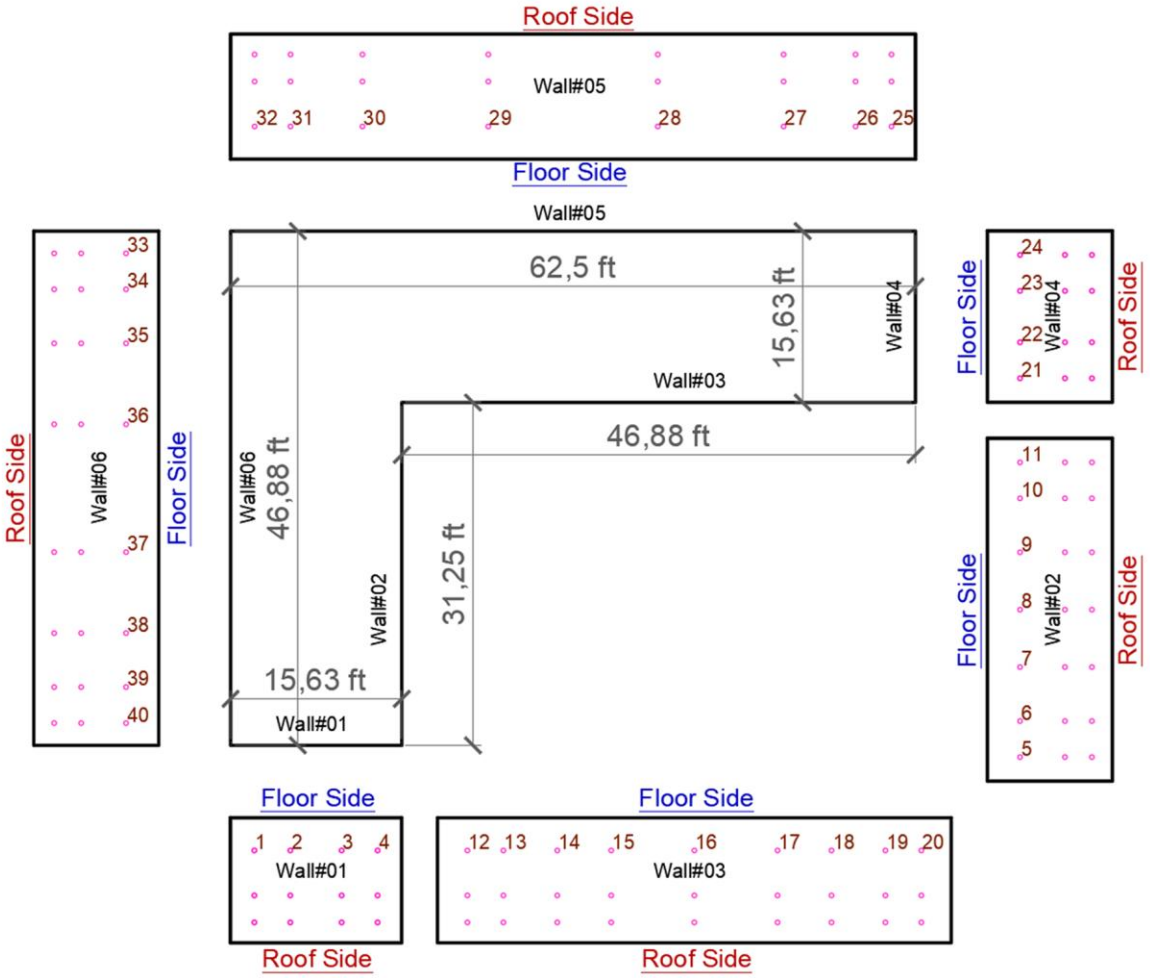

Figure 6. Pressure tap layout for the single-story L-shaped model. Tap numbers shown correspond to the first story only; the second and third stories replicate the layout and continue numbering. Tap rows are placed at 2.98 ft, 4.10 ft, and 6.56 ft above the floor, based on a story height of 11.4 ft. All dimensions are shown in full scale.

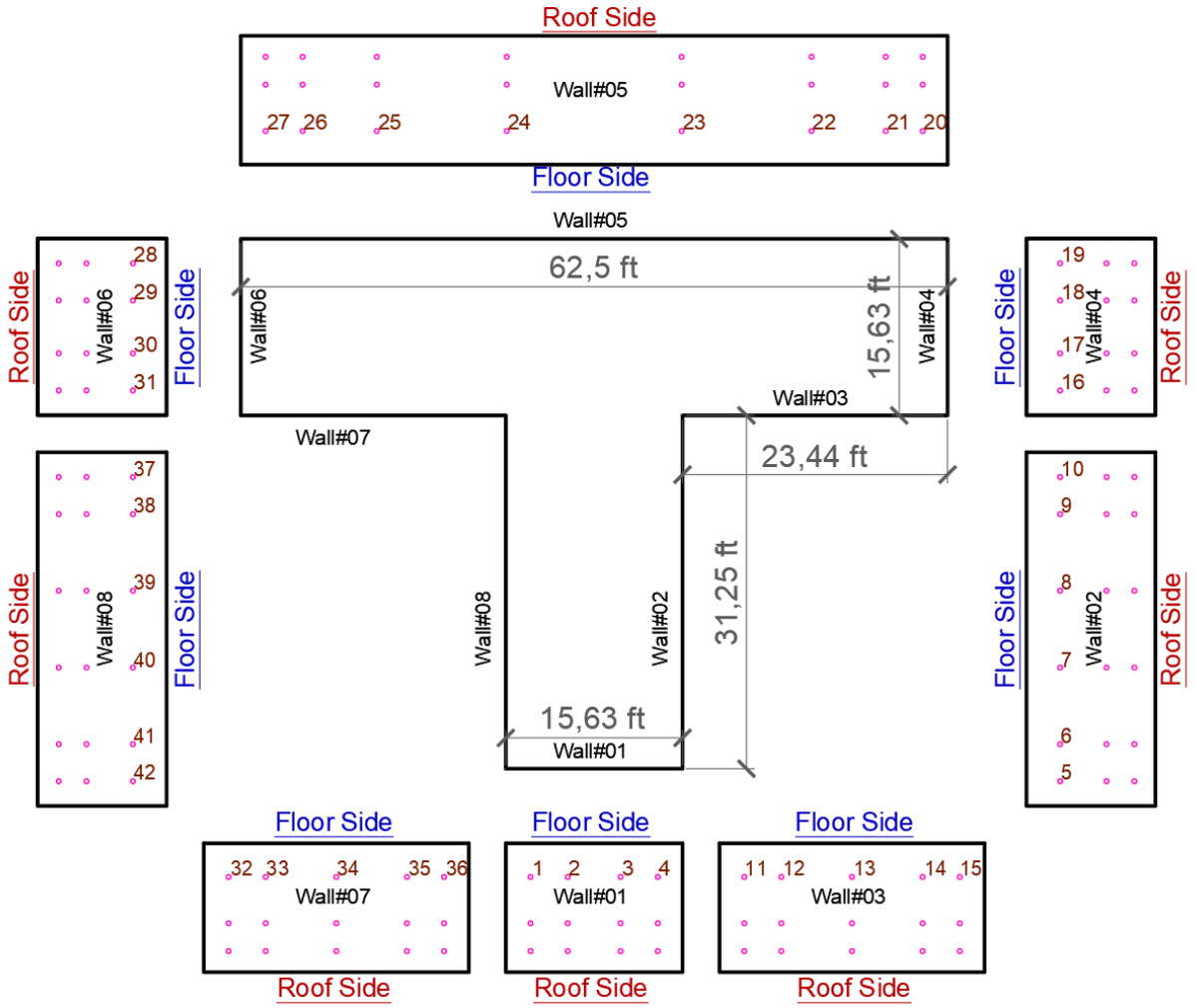

Figure 7. Pressure tap layout for the single-story T-shaped model. Wall identifiers and tap numbers are labeled for the first story only; upper stories follow the same layout and extend the numbering sequence. Tap elevations are located at 2.98 ft, 4.10 ft, and 6.56 ft above the floor, with a total story height of 11.4 ft. All dimensions are expressed in full-scale units.

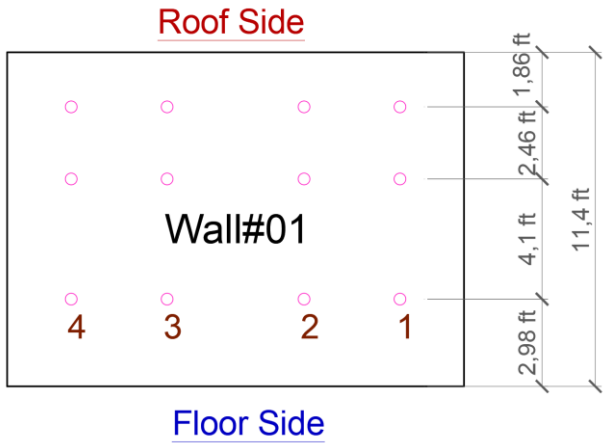

Figure 8. Vertical pressure tap layout on a representative wall (Wall#01), showing tap rows positioned at 2.98 ft, 4.10 ft, and 6.56 ft above floor level within the 11.4 ft story height.

3.3. Wind Simulation, Instrumentation, and Load Coefficients

3.3.1. Wind Simulation and Scaling

The wind field generated in the WOW facility was validated through detailed measurements of mean velocity, turbulence intensity, and spectral content. Data were collected using a Cobra probe sampling at 2,000 Hz at multiple elevations upstream of the models, including the roof height of the 3-story configuration.

The vertical profile of mean wind speed followed a power-law distribution:

$$\frac{U(z)}{U_{ref}} = \left(\frac{z}{z_{ref}}\right)^{\alpha}, \quad \alpha = \frac{1}{7} \tag{1}$$

where $U(z)$ is the mean velocity at height z, and U_{ref} is the reference wind speed at z_{ref} = 33 ft (10 m). The measured profile exhibited close agreement with ESDU 85020 reference profiles for open terrain, as shown in Figure 9a.

Turbulence intensity $I_u(z)$ was calculated as:

$$I_u(z) = \frac{\sigma_u(z)}{U(z)} \tag{2}$$

At the roof height of the 3-story model (10.42 m full scale), the measured turbulence intensity was approximately 19%, consistent with expected values for Exposure C. Velocity and turbulence intensity distributions were both compared against ESDU profiles for roughness lengths

z_0 = 0.01 m and 0.15 m, representing the lower and upper bounds of open terrain roughness, respectively.

To validate spectral content, the longitudinal velocity time series was converted to the frequency domain using a Fast Fourier Transform with a Hamming window and 50% overlap. The resulting spectrum was normalized and plotted as:

$$\frac{nS_n(f)}{U^2(z)} \; vs. \; \frac{nh}{U_{roof}} \tag{3}$$

where $S_n(f)$ is the spectral density at frequency f, n is the sampling frequency, and h is the 3-story roof height. The spectrum is shown in Figure 9b, compared against the Kaimal model at full scale for both roughness lengths. The experimental data fall within the expected bounds, especially in the inertial subrange, confirming that both the intensity and frequency content of the simulated turbulence are representative of full-scale atmospheric boundary layers over open terrain.

The geometric scale of the models was 1:50, and a corresponding time scale of 1:12 was adopted, yielding a velocity scale of $\lambda_v = 1{:}4.167$. Table 2 summarizes the wind speeds measured at the model roof height for each building height configuration (1-, 2-, and 3-story), as well as the corresponding full-scale equivalent mean and 3-second gust wind speeds. Full-scale gust speeds were derived from the mean using a conversion factor of 1.13 based on the Durst curve, appropriate for Exposure Category C and the 10 m height level. The resulting full-scale gust speeds ranged from approximately 164 mph to 178 mph, which is in close agreement with the ASCE 7–22 basic wind speed of 183 mph for Risk Category II structures in coastal Miami-Dade County, Florida, conditions that support the applicability of the test data to hurricane-prone environments.

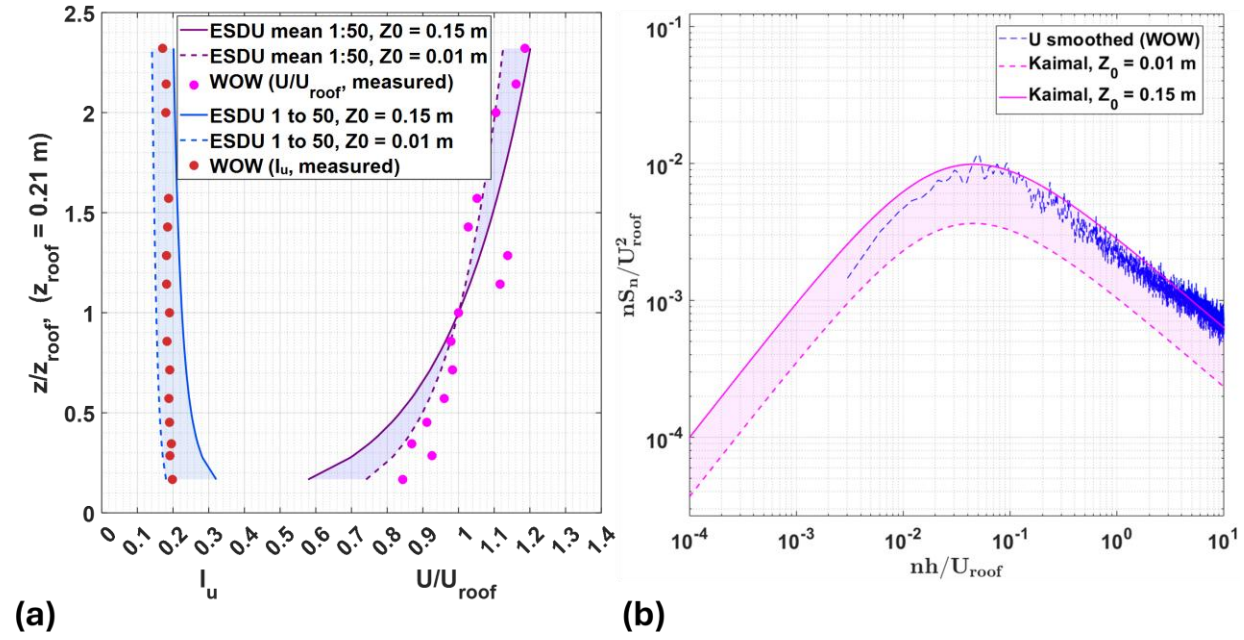

Figure 9. Wind field characterization and validation at the 3-story model roof height. (a) Measured velocity and turbulence intensity profiles compared with ESDU reference profiles for open terrain roughness bounds (z_0=0.01m and 0.15m). (b) Normalized longitudinal turbulence spectrum compared with Kaimal reference spectra at the same roughness bounds.

Table 2. Model wind speeds and equivalent full-scale gusts for each building height.

Building Height (Stories)	Building Height ft (m)	$\bar{U}_{MS}$ ft/s (m/s)	$\hat{U}_{FS}$ mph (m/s)
1	11.4 (3.47)	51.2 (15.60)	164.4 (73.5)
2	22.8 (6.95)	53.1 (16.20)	170.7 (76.3)
3	34.2 (10.42)	55.3 (16.86)	177.6 (79.4)

3.3.2. Pressure Measurement and Data Acquisition

Surface pressures on each building model were measured using pressure taps connected to a high-frequency pressure-scanning system (Scanivalve ZOC33/DSM4000). The system recorded pressure time histories over 120-second durations per wind direction at a sampling frequency of 625 Hz. A total of 24 wind directions, spaced at 15° intervals, were tested to enable full 360° directional coverage.

Each pressure tap was connected to the scanning modules via polyurethane tubing with an inner diameter of approximately 1.35 mm and an average length of 5 ft (1.52 m). To mitigate tubing-related distortion effects—such as signal attenuation and phase shift—a low-pass Butterworth filter with a 300 Hz cutoff was applied to the raw signals. Additionally, tubing transfer functions were characterized through calibration experiments, and corrections were applied using an inverse transfer function approach, following the methodology of Irwin et al. (1979) to ensure fidelity in the recovered pressure histories.

Tap distributions varied with both building height and plan geometry, with increased density in regions prone to flow separation and load amplification, such as reentrant corners, wall intersections, and perimeter edges (see Table 3).

Table 3. Number of pressure taps per model configuration and story level.

Building Plan Shape	1-Story	2-Story	3-Story
Rectangular	96	192	288
L-shaped	120	240	360
T-shaped	126	252	378

To facilitate load estimation, tributary areas were computed using Voronoi tessellation, a geometric partitioning technique originally developed by Voronoi (1908) and more recently adopted in wind engineering applications (Gierson et al., 2017; Simiu & Yeo, 2019). This method ensures that each pressure tap is associated with a spatially appropriate control area, rather than assuming uniformly distributed influence. Pressure measurements were non-dimensionalized as pressure coefficients relative to the static reference pressure and dynamic pressure at roof height:

$$C_{p,i}(t) = \frac{p_i(t) - p_{ref}}{q_h} \quad (4)$$

$$with\ q_h = \frac{1}{2}\rho U_h^2 \quad (5)$$

where $p_i(t)$ is the instantaneous measured pressure, p_{ref} is the reference static pressure, and U_h is the mean wind speed at roof height. Referencing all pressure coefficients to q_h ensures consistent comparison across buildings of different height and shape.

3.3.3. Force Derivation from Wall Pressure Taps

Pressure data collected from wall-mounted taps served as the basis for calculating in-plane loads and torsional effects. As no roof taps were instrumented in the present study, the analysis is limited to *in-plane loads* — namely, the base shear components along the building-fixed axes and the resulting torsional moments about the centroid. This approach remains consistent with the objective of assessing wind-induced plan asymmetries and allows for direct comparison with previous investigations such as those by Elsharawy et al. (2014) and Sarma et al. (In Press), who emphasized wall pressure contributions to lateral and torsional load estimation.

The instantaneous pressure $p_i(t)$ measured at each wall tap was converted to a time-varying force $f_i(t)$ using its associated tributary area A_i, estimated via Voronoi tessellation:

$$f_i(t) = p_i(t)\ .\ A_i \tag{6}$$

Each force was resolved into components along the building-fixed coordinate system: $f_{x,i}(t)$ and $f_{y,i}(t)$. The total base shear components in the longitudinal and transverse directions were then obtained as:

$$F_x(t) = \sum_{i \in X}^{N} x, f_i(t) \tag{7}$$

$$F_y(t) = \sum_{j \in Y}^{N} f_{y,j}(t) \tag{8}$$

and the resultant base shear was given by:

$$V(t) = \sqrt{F_x^2(t) + F_y^2(t)} \tag{9}$$

The torsional moment, $M_t(t)$, was computed as the vector cross product between the moment arm r_i (from the building centroid to tap (i) and the lateral force $f_i(t)$, summed over all taps:

$$M_T(t) = \sum_{i=1}^{N} (r_i \times f_i(t) \quad (10)$$

Since both r_i and f_i lie in the horizontal plane, the resulting moment acts about the vertical (z) axis, capturing the torsional effect directly from in-plane loads.

3.3.4. Peak Load Estimation

To account for the limited duration of wind tunnel records, peak load effects were estimated using the *Best Linear Unbiased Estimators (BLUE)* method developed by Lieblein (1974). This technique extrapolates representative peak values from finite-length time histories by combining observed data in a statistically optimal way, preserving unbiasedness, and minimizing estimation variance.

The BLUE method was applied to the directional time histories of base shear (C_V), torsional moment (C_T), and lateral force (C_L) to estimate peak responses for each wind direction. These peaks were used to evaluate and compare the sensitivity of different building shapes and heights to lateral and torsional wind effects.

Unlike cladding-level studies that benchmark against ASCE 7–22 (2022) pressure coefficient limits, this analysis focuses on main wind force-resisting system (MWFRS) behavior. The peak responses are interpreted in the context of system-level design load combinations, such as those specified in ASCE 7–22 (e.g., Load Cases 1–4 in Fig. 27.3-8), which combine wall pressures and torsional effects.

4. RESULTS

The experimental program generated an extensive dataset capturing the wind-induced pressures and resulting forces, moments, and torsional responses for nine building configurations. These configurations represented a factorial combination of three plan shapes (Rectangular, L-shape, and T-shape) and three heights (1-, 2-, and 3-story). Testing encompassed wind directions from 0° to 360° in 15° increments, enabling a detailed assessment of directional sensitivity and geometric effects.

Results are presented in two principal parts. The first addresses the local pressure coefficients (C_p) measured on the exterior walls, including mean distributions and statistical peak values. These findings characterize the spatial variation in wind suction and stagnation pressures due to shape and wind incidence.

The second part focuses on global load effects derived from the pressure data, reported in terms of nondimensional base shear coefficients (C_{Sx}, C_{Sy}), resultant base shear (C_V), and the torsional moment coefficient (C_T). These coefficients quantify the structural response of the buildings and enable direct comparisons across shapes and heights, independent of scale.

Subsequent subsections explore the variation of these coefficients with wind direction, present critical wind angles for peak responses, and introduce amplification factors to quantify the influence of geometric irregularity and building height. All results are based on wall pressure measurements and reflect exterior wind loading effects.

4.1. Pressure Coefficient (C_p) Results

The distribution of local pressure coefficients (C_p) across the exterior walls of the building models provides the foundation for understanding how wind pressures vary with geometry, height, and wind direction. This section presents both $\bar{C}_p$ distributions for selected wind directions and critical peak envelopes representing the most severe positive and negative pressures recorded across all tested wind angles.

4.1.1. Mean $\bar{C}_p$ Distributions

4.1.1.1. Single-Story Buildings:

a) 000° Wind Direction

The comparison of the 1-story T-shape, L-shape, and Rectangular buildings at 000° wind direction (Figure 10a, 10b, and 10c, respectively) highlights both similarities in overall pressure distribution and important differences driven by geometric complexity.

On the windward walls, all three shapes exhibit relatively low positive pressures or mild suction. The $\bar{C}_p$ values are approximately –0.3 for both the T-shape (Figure 10a) and Rectangular shape (Figure 10c), while the L-shape (Figure 10b) shows slightly stronger suction at around –

0.45. This suggests that geometric features, such as the re-entrant corner of the L-shape, reduce stagnation pressures by promoting flow separation or acceleration even on windward walls.

The side walls reveal more pronounced differences. For the T-shape and Rectangular buildings (Figure 10a and 10c), suction values increase progressively from the upstream corners toward the rear, with $\bar{C}_p$ values ranging from –0.3 to –0.9. The L-shape (Figure 10b), however, displays a more complex gradient, with suction values reaching –0.75 to –0.9 near the exposed edges. This can be attributed to flow acceleration around the open corner and varying sheltering effects, which are absent in the more symmetric Rectangular and T-shape plans.

Leeward wall suctions are significant across all shapes, with $\bar{C}_p$ values consistently reaching –0.9. However, the distribution is more uniform in the Rectangular case (Figure 10c), while the T-shape and especially the L-shape (Figure 10a and 10b) show greater variation due to geometry-induced flow separation and possible localized reattachment. The L-shape's asymmetry leads to slightly higher and more variable suctions compared to the other two shapes.

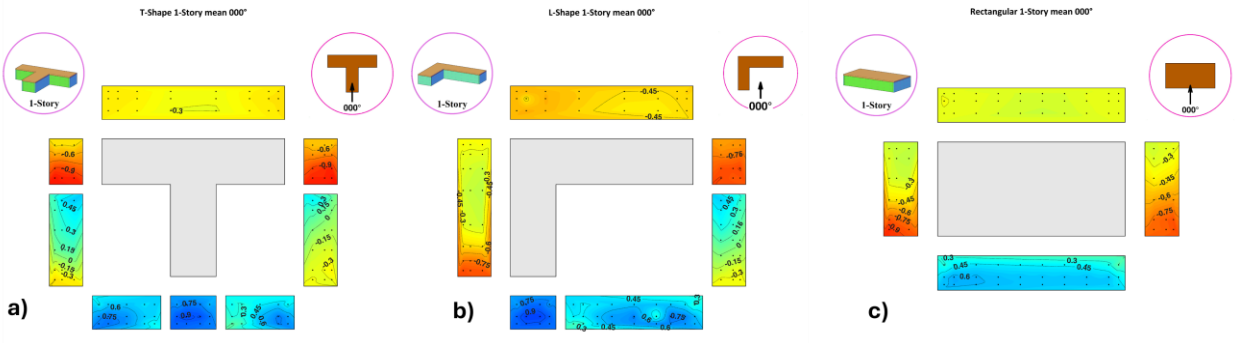

Figure 10. Mean pressure coefficient ($\bar{C}_p$) distributions for 1-story T-shape (a), L-shape (b), and Rectangular (c) buildings under 000° wind.

b) 135° Wind Direction

At a wind direction of 135°, the T-shaped 1-story building (Figure 11a) displays a pressure distribution reflecting the complex interaction of oblique wind and the building's protruding geometry. The windward walls, particularly the southeast-facing sections of the east and south façades, exhibit modest positive pressures with $\bar{C}_p$ values around 0 to +0.15. These pressures are lower than those typically observed under orthogonal wind loading (Figure 11a), indicating reduced stagnation effects due to early flow separation along the angled walls. The side walls show suctions increasing from approximately –0.3 near sheltered corners to –0.6 in more exposed

regions. The leeward walls, primarily facing northwest, experience suctions between –0.45 and –0.6. The roof-edge walls—also vertical walls—demonstrate suctions ranging from –0.45 to –0.6, with the strongest effects occurring near corners where vortex formation is likely. Compared to the 000° case, suctions are similar in magnitude but distributed with greater spatial variability, a direct result of the oblique wind angle.

The L-shaped 1-story building (Figure 11b) presents pressure patterns influenced by both the oblique wind and the plan's geometric asymmetry. The windward walls display positive pressures peaking at approximately +0.45, higher than those recorded for the T-shape (Figure 11a) due to the longer, continuous walls that better maintain stagnation pressure. The side walls show suctions increasing from near zero to approximately –0.45. Interestingly, these suctions are less severe than those in the T-shape, likely because the L-shape's re-entrant corner provides partial sheltering and moderates flow acceleration. The leeward walls experience suctions around –0.45, which are lower than the T-shape values. The roof-edge walls also show consistent suctions up to –0.45, with lower spatial variability than the T-shape. Compared to the L-shape under orthogonal wind (Figure 10b), the oblique wind reduces peak suctions but introduces more variability along the side and roof-edge walls.

The Rectangular 1-story building (Figure 11c) shows the most uniform pressure distribution of the three shapes. The windward walls sustain positive pressures up to +0.45, comparable to the L-shape (Figure 11b) and higher than the T-shape (Figure 11a). The side walls exhibit suctions progressing from near zero to –0.45, closely matching the L-shape values and slightly milder than the T-shape. The leeward wall experiences suctions between –0.45 and –0.75, similar in magnitude to the other two shapes but distributed more evenly, without localized peaks. The roof-edge walls (again, vertical walls rotated for visualization) display suctions ranging from –0.3 to –0.75. Compared to the Rectangular shape under orthogonal wind (Figure 10c), diagonal wind exposure slightly reduces peak suctions but increases spatial variability along the side and leeward walls.

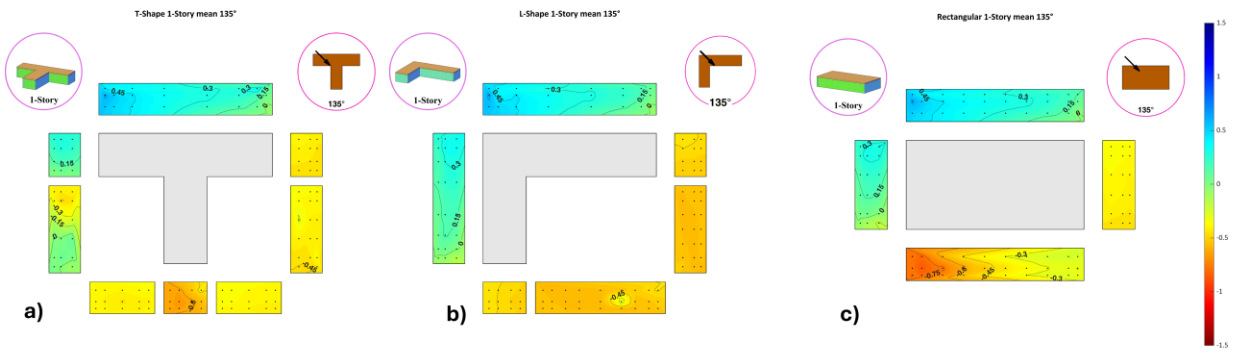

Figure 11. Mean pressure coefficient ($\bar{C}_p$) distributions for 1-story T-shape (a), L-shape (b), and Rectangular (c) buildings under 135° wind.

c) 315° Wind Direction

At a wind direction of 315°, the T-shaped 1-story building (Figure 12a) exhibits pressure distributions characterized by moderate positive pressures on the windward walls and typical suctions on the side and leeward walls. The windward walls, facing northwest in this case, display $\bar{C}_p$ values up to +0.15, with localized regions of suction reaching –0.3 to –0.45, suggesting early flow separation along some wall sections. The side walls demonstrate increasing suction toward the leeward regions, with $\bar{C}_p$ values ranging from approximately –0.3 to –0.6. The leeward walls experience suctions up to –0.6, slightly lower in magnitude than those observed under orthogonal winds (Figure 10a), likely due to more distributed wake effects at the oblique wind angle. The roof-edge walls (vertical walls at the roof perimeter) show suctions between –0.3 and –0.6, with increased spatial variability, particularly near corners where flow separation is intensified.

The L-shaped 1-story building (Figure 12b) demonstrates a more complex distribution of pressures, strongly influenced by the building's asymmetry and the oblique wind approach. The windward walls exhibit positive pressures reaching +0.3, with some areas showing mild suctions. The side walls experience suctions that range from approximately –0.3 to –0.75, with the most severe suctions occurring on the long, exposed wall sections where flow acceleration and corner vortex effects are most significant. The leeward walls show suctions up to –0.75, matching or slightly exceeding the magnitudes recorded for the T-shape (Figure 12a). The roof-edge walls also exhibit high suctions, particularly near the open corner where geometric effects amplify negative pressures. Compared to the 000° and 135° wind directions (Figures Figure 10b and Figure 11b),

the 315° wind results in both higher peak suctions and greater spatial variability, emphasizing the influence of wind direction and plan asymmetry.

The Rectangular 1-story building (Figure 12c) presents the most uniform pressure distribution of the three shapes. The windward walls maintain positive pressures between 0 and +0.3, comparable to the values seen in the L-shape (Figure 12b) and higher than those in the T-shape (Figure 12a). The side walls show suctions ranging from –0.15 to –0.6, while the leeward walls experience suctions up to –0.75, similar in magnitude to the other two shapes but with less pronounced peaks. The roof-edge walls sustain suctions from –0.15 to –0.75, with a notably even distribution across the façade segments. This uniformity reflects the aerodynamic stability of the rectangular geometry, which tends to minimize localized flow separation and vortex-induced pressure peaks, even under oblique wind loading.

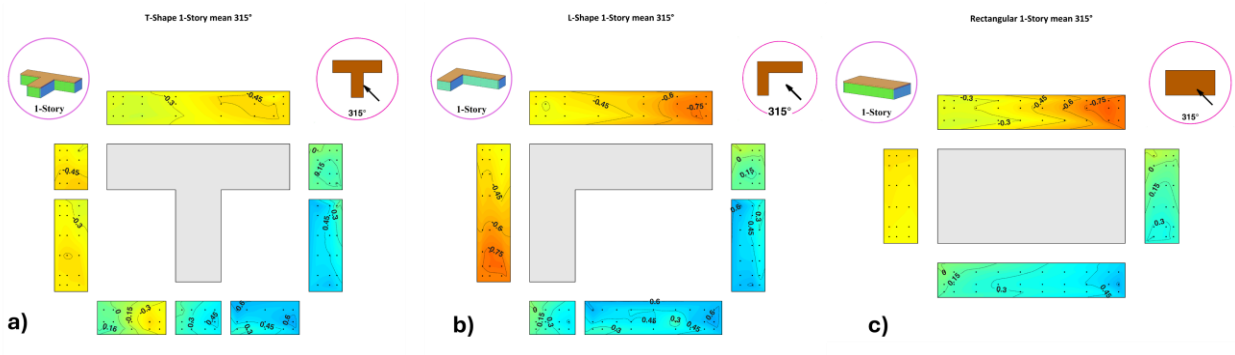

Figure 12. Mean pressure coefficient ($\bar{C}_p$) distributions for 1-story T-shape (a), L-shape (b), and Rectangular (c) buildings under 315° wind.

4.1.1.2. Two-Story Buildings:

a) 000° Wind Direction

At a wind direction of 000°, the T-shaped 2-story building (Figure 13a) displays pressure distributions that reflect the combination of orthogonal wind exposure and increased building height relative to the previously analyzed 1-story case (Figure 10a). The windward walls, facing north, experience mild positive pressures with $\bar{C}_p$ values reaching up to +0.45. This represents an increase over the 1-story case, consistent with the greater wind exposure and development of boundary layer flow separation at higher elevations. The side walls exhibit suctions increasing progressively toward the rear, ranging from approximately –0.3 to –0.75. The leeward walls sustain

strong suctions up to –0.75, slightly less than the peak suctions observed in the 1-story case but more uniformly distributed. The roof-edge walls, like all other walls in the contour plots, demonstrate moderate suctions, generally between –0.45 and –0.75, with stronger negative pressures occurring near corners where flow separation and vortex effects dominate.

The L-shaped 2-story building (Figure 13b) exhibits a more complex pressure distribution shaped by the asymmetric geometry and increased height. The windward walls show positive $\bar{C}_p$ values up to +0.45, with localized reductions due to flow acceleration around re-entrant corners. The side walls reveal suction values increasing from approximately –0.3 to –0.9, particularly along long, exposed wall sections where flow acceleration is most intense. The leeward walls exhibit suctions up to –0.9, matching or slightly exceeding those observed in the T-shape (Figure 13a). Notably, the most severe negative pressures occur along the longer wall segments where separation zones are sustained. The roof-edge walls show significant suctions between –0.45 and –1.05, with the most extreme values occurring near the open corner regions where geometric complexity amplifies flow separation and vortex shedding. Compared to the 1-story L-shape (Figure 10b), the increase in story height results in both greater suction magnitudes and more pronounced spatial variability.

The Rectangular 2-story building (Figure 13c) presents the most uniform pressure distribution among the three shapes. The windward walls sustain positive pressures up to +0.45, comparable to the L-shape (Figure 13b) and T-shape (Figure 13a). The side walls demonstrate suctions increasing from approximately –0.3 to –0.9. The leeward wall experiences consistent suctions up to –0.9, similar in magnitude to the L-shape but distributed more evenly without localized peaks. The roof-edge walls show suctions ranging from –0.45 to –0.9, with a remarkably uniform distribution across all vertical wall sections. Compared to the Rectangular 1-story building (Figure 10c), the increase in height has led to greater suctions, but the symmetric geometry continues to provide aerodynamic stability and limits spatial variability.

In summary, under 000° wind loading, the L-shape exhibits the highest suctions and greatest spatial variability, particularly along side and leeward walls exposed to flow acceleration and corner vortex effects. The T-shape shows intermediate behavior, with moderate suctions and some geometric amplification due to its protruding walls. The Rectangular building maintains the most uniform pressure distributions, underscoring the aerodynamic advantages of simple,

symmetric forms when subjected to orthogonal winds. Across all shapes, increasing the story height amplifies both the magnitude and spatial variability of suctions, especially in areas influenced by geometric irregularities or exposed corners.

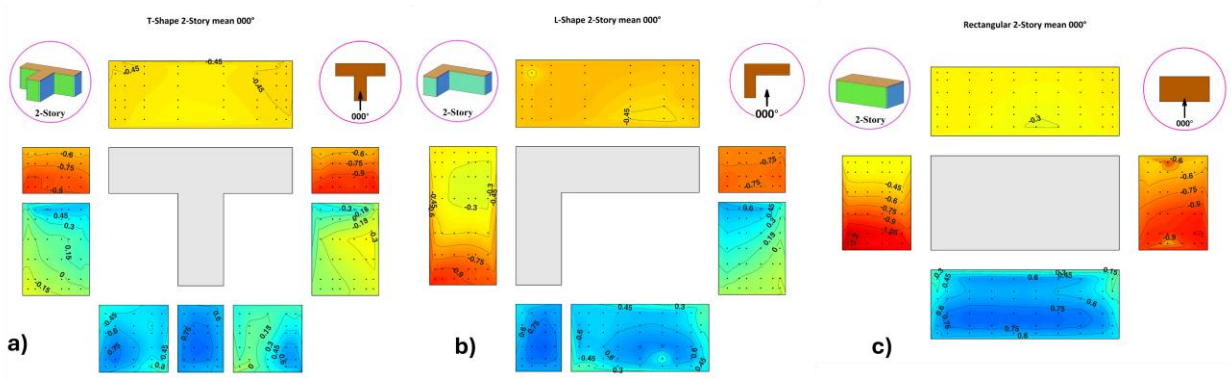

Figure 13. Mean pressure coefficient ($\bar{C}_p$) distributions for 2-story T-shape (a), L-shape (b), and Rectangular (c) buildings under 000° wind.

b) 000° Wind Direction

At a wind direction of 135°, the T-shaped 2-story building (Figure 14a) shows pressure distributions shaped by the diagonal wind exposure and the building's geometric complexity. The windward walls, facing southeast, exhibit positive pressures with $\bar{C}_p$ values up to +0.6, notably higher than those recorded for the same shape under 000° wind (Figure 13a, $C_p \approx +0.45$). This increase reflects stronger stagnation effects where the oblique wind impinges directly on extended wall sections. The side walls display suction values increasing from near zero up to –0.6, with some regions on the northeast and southwest walls experiencing enhanced suctions due to flow acceleration and separation. The leeward walls show suctions between –0.45 and –0.75, slightly lower than the peak suctions observed under orthogonal winds but distributed more uniformly. The roof-edge walls (vertical walls around the roof perimeter) experience suctions ranging from –0.45 to –0.75, with stronger negative pressures near corners and edges where vortex formation occurs.

The L-shaped 2-story building (Figure 14b) presents a more varied pressure distribution due to both the oblique wind approach and the inherent asymmetry of the plan. The windward walls sustain positive pressures up to +0.6, matching the T-shape (Figure 14a) but distributed more unevenly, particularly near the re-entrant corner where flow redirection reduces stagnation effects. The side walls exhibit suctions increasing from –0.15 to –0.75, with the most severe values occurring along long, exposed wall segments where flow acceleration and vortex formation are

prominent. The leeward walls also experience suctions up to –0.75, comparable to the T-shape, although more spatially variable. The roof-edge walls demonstrate suctions between –0.45 and –0.75, with amplified negative pressures near the open corner where geometric effects intensify flow separation. Compared to the L-shape's performance under orthogonal wind (Figure 13b), the diagonal wind has increased both the peak suctions and spatial variability of pressures.

The Rectangular 2-story building (Figure 14c) shows the most uniform pressure distribution of the three shapes. The windward walls display positive pressures up to +0.6, comparable to those in the T-shape and L-shape (Figures 14a and 14b), although distributed more evenly across the façade. The side walls experience suctions increasing from –0.15 to –0.6, while the leeward wall sustains suctions up to –0.75. The roof-edge walls exhibit suctions between –0.45 and –0.75, with a remarkably uniform distribution. Unlike the T- and L-shapes, the Rectangular geometry avoids localized peaks in suction, reflecting the aerodynamic advantages of symmetric, continuous walls. Compared to the 000° wind case (Figure 13c), the oblique wind exposure increases spatial variability but does not significantly raise the overall magnitude of suctions.

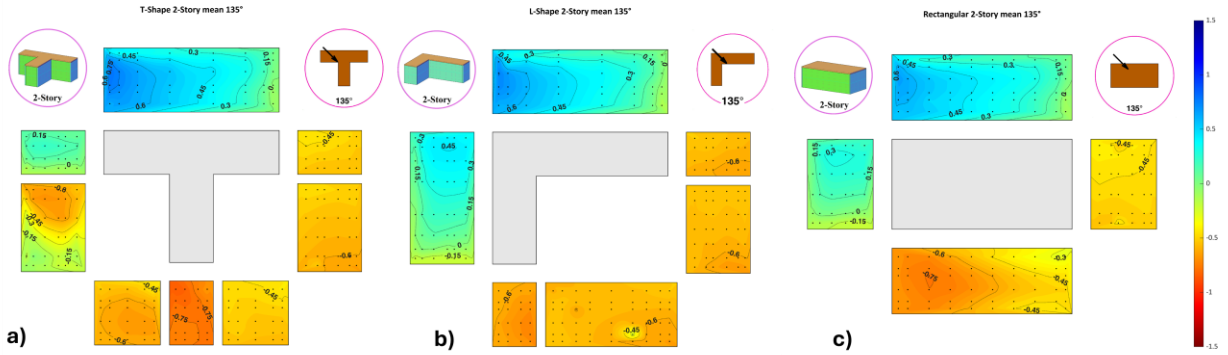

Figure 14. Mean pressure coefficient ($\bar{C}_p$) distributions for 2-story T-shape (a), L-shape (b), and Rectangular (c) buildings under 135° wind.

c) 000° Wind Direction

At a wind direction of 315°, the T-shaped 2-story building (Figure 15a) exhibits moderate positive pressures and substantial suction zones influenced by the oblique wind approach and the building's protruding geometry. The windward walls (northwest-facing) experience positive pressures up to approximately +0.15, lower than the values recorded for 135° wind (Figure 14a, $\bar{C}_p \approx +0.6$) but typical for oblique winds with flow deflection. The side walls show suction gradients ranging from approximately –0.3 to –0.75, with enhanced suctions occurring along

exposed wall sections subjected to flow acceleration and separation. The leeward walls sustain suctions between –0.6 and –0.75, slightly higher than under orthogonal winds (Figure 13a), indicating more persistent separation and recirculation at the oblique angle. The roof-edge walls display suctions from –0.3 to –0.75, with stronger negative pressures concentrated near building corners where vortex effects dominate.

The L-shaped 2-story building (Figure 15b) reveals a complex distribution of pressures shaped by the diagonal wind and geometric asymmetry. The windward walls exhibit positive pressures up to +0.3, higher than the T-shape (Figure 15a) and consistent with the longer, uninterrupted walls promoting greater stagnation. The side walls demonstrate suction gradients increasing from –0.15 to –0.75, particularly along long wall segments exposed to accelerated flow. The leeward walls experience suctions up to –0.75, matching or exceeding those seen in the T-shape. The roof-edge walls also show significant suctions (up to –0.75), especially near the open corner regions where corner vortex effects intensify negative pressures. Compared to the same building under 135° wind (Figure 14b), suction magnitudes are similar, but spatial variability is greater, driven by the different alignment between the oblique wind and the building's open corner geometry.

The Rectangular 2-story building (Figure 15c) again displays the most uniform pressure distribution among the three shapes. The windward walls exhibit positive pressures up to +0.3, comparable to the L-shape (Figure 15b) and higher than the T-shape (Figure 15a). The side walls show suction gradients increasing from –0.15 to –0.6, while the leeward wall sustains suctions up to –0.75. The roof-edge walls demonstrate suctions ranging from –0.3 to –0.75, with a notably uniform distribution across all wall segments. Unlike the T- and L-shapes, the Rectangular form avoids localized suction peaks, reflecting the aerodynamic benefits of continuous, symmetric walls. Compared to the same shape under 135° wind (Figure 14c), the overall magnitudes are similar, but suction distribution remains more consistent at 315°, indicating resilience to different oblique wind orientations.

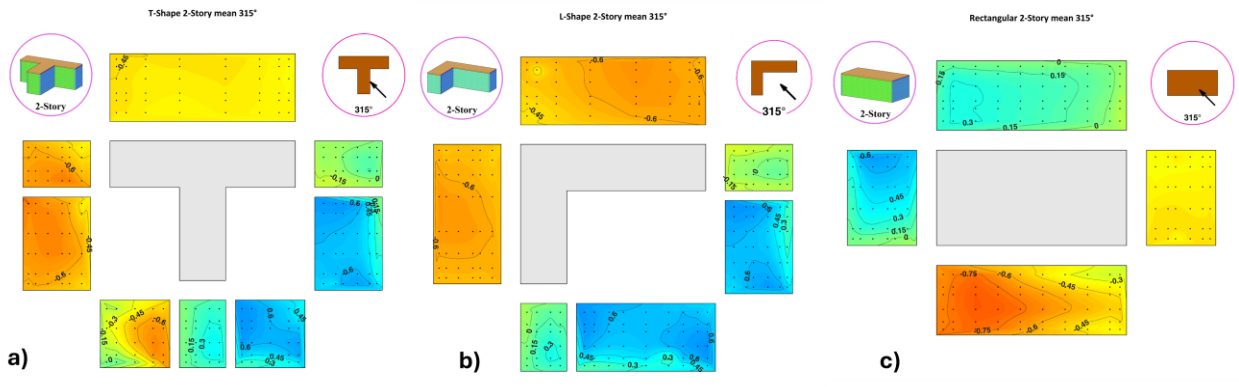

Figure 15. Mean pressure coefficient ($\bar{C}_p$) distributions for 2-story T-shape (a), L-shape (b), and Rectangular (c) buildings under 315° wind.

4.1.1.3. Three-Story Buildings:

a) 000° Wind Direction

At a wind direction of 000°, the T-shaped 3-story building (Figure 16a) exhibits increased positive pressures and suctions compared to its lower-height counterparts (Figures 10a and 13a), reflecting the amplified wind exposure and flow development at greater heights. The windward walls show positive pressures reaching up to +0.45, similar in magnitude to the 2-story case (Figure 13a) but distributed over a broader area. The side walls experience suctions increasing from –0.3 up to –0.9, with the strongest negative pressures occurring along the exposed segments where flow separation and acceleration are enhanced by the building's protrusions and greater elevation. The leeward walls sustain suctions around –0.75 to –0.9, similar to the 2-story case but slightly more uniformly distributed. The roof-edge walls display suctions ranging from –0.45 to –0.9, with the strongest effects concentrated near corners and edges where vortex shedding intensifies as the story height increases.

The L-shaped 3-story building (Figure 16b) demonstrates an even more varied pressure distribution due to both its asymmetric geometry and increased height. The windward walls sustain positive pressures up to +0.45, comparable to the T-shape (Figure 16a) and the 2-story L-shape (Figure 13b). However, the side walls show markedly increased suctions, progressing from –0.3 to as severe as –1.05, especially along long, uninterrupted wall segments where flow acceleration and corner vortices dominate. The leeward walls also experience strong suctions between –0.75 and –1.05. The roof-edge walls sustain suctions up to –1.05, with localized peaks near the open

corner regions where geometric effects lead to intensified flow separation. Compared to lower stories (Figures 10b and 13b), the 3-story L-shape exhibits both higher suction magnitudes and greater spatial variability, particularly where the building's asymmetry amplifies wind effects.

The Rectangular 3-story building (Figure 16c) once again displays the most uniform pressure distribution. The windward walls experience positive pressures up to +0.45, similar to the T- and L-shapes (Figures 16a and 16b). The side walls exhibit suction gradients increasing from –0.3 to –0.9, while the leeward wall sustains consistent suctions between –0.9 and –1.05. The roof-edge walls show the highest suctions among the three shapes, reaching values between –0.9 and –1.35. While the magnitude of suction increases with height, the spatial distribution remains relatively even due to the symmetry and continuity of the rectangular form. Compared to the lower stories (Figures 10c and 13c), suction values are significantly amplified, especially on the leeward and roof-edge walls, but variability remains low — highlighting the aerodynamic stability of the Rectangular shape even as height increases.

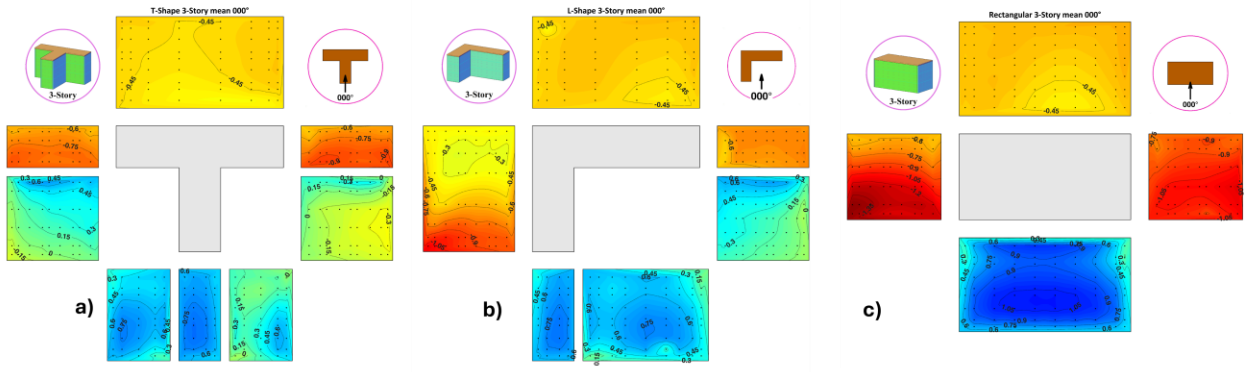

Figure 16. Mean pressure coefficient ($\bar{C}_p$) distributions for 3-story T-shape (a), L-shape (b), and Rectangular (c) buildings under 000° wind.

b) 135° Wind Direction

At a wind direction of 135°, the T-shaped 3-story building (Figure 17a) exhibits pressure distributions shaped by both the oblique wind exposure and increased building height. The windward walls (southeast-facing) experience positive pressures reaching up to +0.6, particularly where the oblique wind impinges directly on extended façade areas. These values are consistent with or slightly higher than the 2-story case (Figure 14a), reflecting stronger stagnation effects and the influence of greater wind exposure. The side walls show suction gradients increasing from near zero to –0.75, with intensified suctions occurring along exposed segments where flow acceleration

and separation are most pronounced. The leeward walls sustain suctions between –0.45 and –0.75, slightly lower in peak magnitude than under orthogonal winds (Figure 16a) but exhibiting greater spatial variability due to the diagonal flow path. The roof-edge walls exhibit suctions between –0.45 and –0.75, with the highest negative pressures concentrated near corners and edges where vortex formation is amplified by building height.

The L-shaped 3-story building (Figure 17b) reveals a more complex and spatially varied pressure distribution resulting from its asymmetric geometry and the oblique wind direction. The windward walls sustain positive pressures up to +0.6, comparable to the T-shape (Figure 17a), with the highest values occurring along uninterrupted wall sections. The side walls display suction gradients increasing from –0.15 to –0.75, with the most severe values occurring along long, exposed walls where flow acceleration and vortex formation dominate. The leeward walls also experience suctions up to –0.75, similar to the T-shape. The roof-edge walls demonstrate significant suctions (up to –0.75), especially near the open corner regions where geometric effects intensify flow separation and vortex shedding. Compared to the lower stories (Figures 11b and 14b), both suction magnitudes and spatial variability have increased, emphasizing the amplifying effects of building height and asymmetry under oblique winds.

The Rectangular 3-story building (Figure 17c) again displays the most uniform pressure distribution among the three shapes. The windward walls exhibit positive pressures up to +0.6, matching those seen in the T-shape and L-shape (Figures 17a and 17b). The side walls show suctions increasing from –0.15 to –0.6, while the leeward wall sustains suctions up to –0.75. The roof-edge walls exhibit suctions between –0.45 and –0.75, with a notably uniform distribution across all wall segments. Despite the increase in story height, the Rectangular form maintains consistent pressure patterns without localized peaks in suction, reflecting the aerodynamic benefits of symmetry and continuous walls. Compared to the same building under orthogonal wind (Figure 16c), overall suction magnitudes remain similar, but the spatial distribution becomes slightly more varied due to the oblique wind's diagonal flow path.

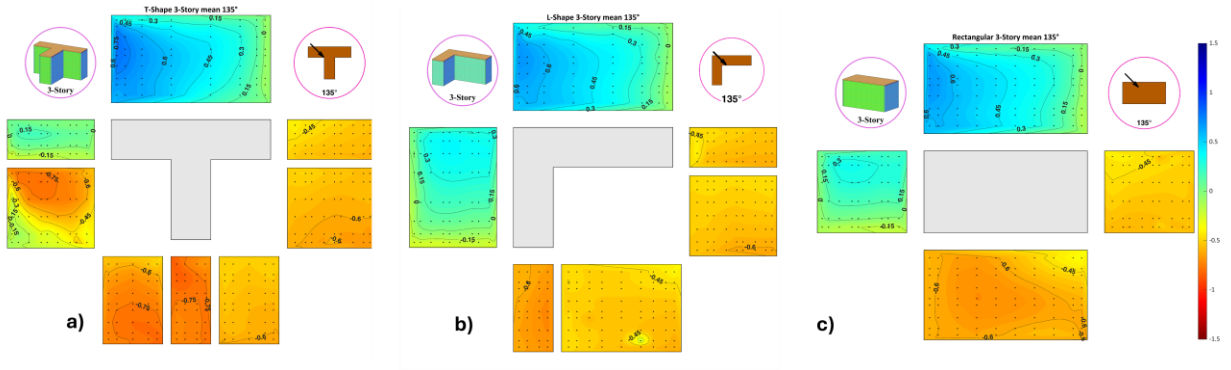

Figure 17. Mean pressure coefficient ($\bar{C}_p$) distributions for 3-story T-shape (a), L-shape (b), and Rectangular (c) buildings under 135° wind.

c) 315° Wind Direction

At a wind direction of 315°, the T-shaped 3-story building (Figure 18a) exhibits significant pressure variability shaped by the oblique wind and increased building height. The windward walls (northwest-facing) sustain positive pressures up to +0.15—lower than those observed under orthogonal or 135° winds (Figures 16a and 17a, $\bar{C}_p$ up to +0.45 to +0.6)—indicating reduced stagnation due to the flow deflection at this wind angle. The side walls demonstrate suction gradients increasing from –0.3 to –0.9, with the highest negative pressures concentrated along exposed segments where flow separation and acceleration dominate. Notably, the northeast and southwest walls experience pronounced suction zones, particularly at their upper regions and corners. The leeward walls exhibit consistent suctions ranging from –0.75 to –0.9, while the roof-edge walls show negative pressures between –0.45 and –0.9. Compared to the 2-story case (Figure 15a), suction magnitudes have increased with height, and spatial variability has become more pronounced.

The L-shaped 3-story building (Figure 18b) reveals a more complex pressure field driven by geometric asymmetry and diagonal wind effects. The windward walls display positive pressures up to +0.3, higher than the T-shape (Figure 18a) and consistent with longer wall sections promoting stronger stagnation effects. The side walls experience suction gradients increasing from –0.15 to –0.75, with severe suctions concentrated along long, exposed walls aligned obliquely to the flow. The leeward walls also exhibit suctions up to –0.75, while the roof-edge walls show significant negative pressures ranging from –0.45 to –0.75. The most intense suction occurs at the open corner regions where geometric effects amplify vortex shedding. Compared to the 2-story case (Figure

15b), both suction magnitudes and spatial variability have increased, especially on the side and leeward façades.

The Rectangular 3-story building (Figure 18c) once again demonstrates the most uniform pressure distribution of the three shapes. The windward walls exhibit positive pressures up to +0.3, similar to the L-shape (Figure 18b) and higher than the T-shape (Figure 18a). The side walls show suctions increasing from –0.15 to –0.6, while the leeward wall sustains suctions up to –0.75. The roof-edge walls display consistent negative pressures ranging from –0.45 to –0.75, with a relatively even distribution. While suction magnitudes have increased compared to the 2-story case (Figure 15c), the Rectangular building maintains lower spatial variability, reflecting the aerodynamic advantages of symmetry and continuous wall surfaces even at greater heights.

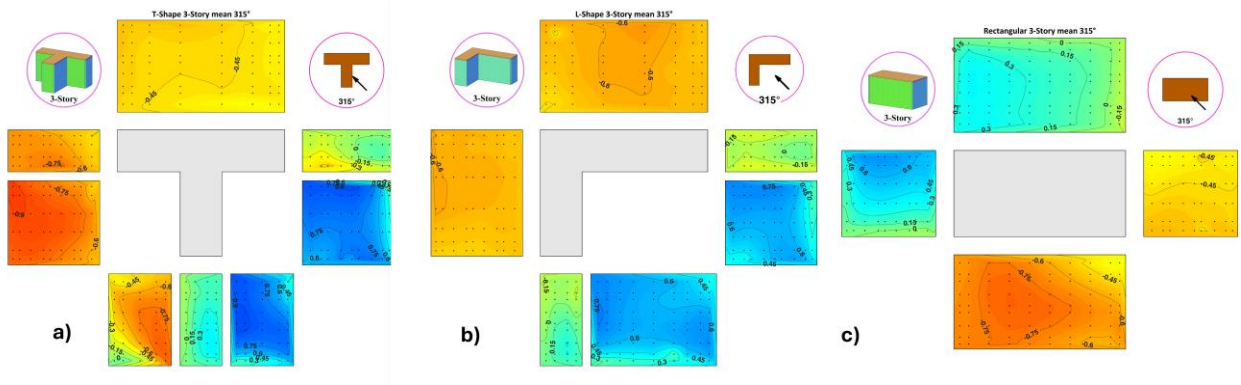

Figure 18. Mean pressure coefficient ($\bar{C}_p$) distributions for 3-story T-shape (a), L-shape (b), and Rectangular (c) buildings under 315° wind.

4.1.2. Peak C_p Envelopes

This section presents the critical peak pressure coefficients, including both the minimum ($\check{C}p$) and maximum ($\hat{C}p$) values, compiled from all tested wind directions for each shape and story height. These envelopes represent the most severe negative (suction) and positive pressures experienced on the exterior walls across the full directional spectrum, highlighting the combined effects of plan geometry, building height, and multidirectional wind exposure.

4.1.2.1. Critical $\check{C}_p$ Distribution

The peak suction pressures ($\check{C}_p$) for each shape and story height are presented in the following subsections, representing the most severe negative values recorded across all wind directions.

a) Single-Story Buildings:

The 1-story T-shape (Figure 19a) exhibits $\check{C}_p$ values predominantly ranging from –1.0 to –1.8 across most walls, with isolated regions reaching up to –2.2. These most intense suctions are concentrated at the ends of the projecting walls and external corners. The complex plan geometry of the T-shape promotes flow separation and vortex formation in these regions, amplifying negative pressures by approximately 25% to 40% compared to the central wall sections where $\check{C}_p$ values typically remain around –1.2 to –1.4.

In contrast, the L-shape (Figure 19b) shows $\check{C}_p$ values generally between –1.2 and –2.0, with isolated peaks approaching –2.4. The open-corner configuration promotes more extensive suction zones, particularly along the longer walls and at corners exposed to potential flow separation from multiple wind directions. Compared to the T-shape, the L-shape's peak suctions are approximately 10% to 15% higher, especially along the longer wall sections where pressure amplification occurs due to the combination of plan asymmetry and re-entrant geometries.

The Rectangular building (Figure 19c) demonstrates the most uniform suction distribution. $\check{C}_p$ values are mostly in the range of –1.0 to –1.6, with localized peaks at wall ends and corners reaching –2.0. Compared to both the T-shape and L-shape, the peak suctions are 15% to 20% lower. This reduction highlights the aerodynamic stability of the rectangular plan, which minimizes

localized flow acceleration and separation effects. The simple continuous walls distribute suctions more evenly, preventing extreme negative pressure concentrations.

When comparing across the three shapes, the L-shape consistently experiences the highest peak suctions, followed by the T-shape, and then the Rectangular shape. The differences between the most and least severe cases exceed 30%. This trend emphasizes the impact of plan complexity, with geometric irregularities and corner configurations significantly increasing the potential for localized suction amplification under multidirectional wind loading.

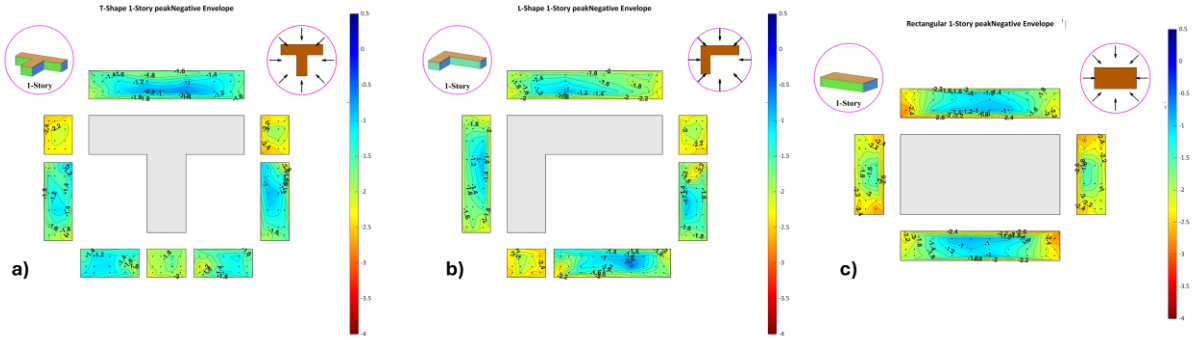

Figure 19. Peak negative pressure coefficients (Čp) distributions for 1-story T-shape (a), l-shape (b), and Rectangular (c) buildings.

b) Two-Story Buildings:

The 2-story T-shape (Figure 20a) shows peak negative C_p values that predominantly range from –1.2 to –2.2 across most wall areas, with localized peaks reaching –2.8 to –3.0 at the ends of projecting walls and the external corners. Compared to the 1-story configuration (Figure 19), suctions have increased by approximately 30% to 35%, reflecting the heightened exposure and increased wind speed with elevation. Notably, suction amplification is especially severe at corners and intersections where abrupt geometry changes cause flow separation and vortex formation.

The L-shape (Figure 20b) exhibits even stronger suctions, with $\check{C}_p$ values between –1.6 and –2.8 over the majority of the wall surfaces, and localized peaks surpassing –3.2 near re-entrant corners and exposed edges. Relative to the T-shape, the peak negative pressures are approximately 10% to 15% higher. This amplification is consistent with the plan's geometric asymmetry and the additional flow acceleration and corner vortex effects occurring where two walls meet at internal and external corners. Compared to the 1-story L-shape, the suction magnitudes have increased by 40% to 45%, reinforcing the significant influence of building height on suction intensification.

The Rectangular building (Figure 20c) continues to demonstrate the most uniform negative pressure distribution, with most wall regions experiencing $\check{C}_p$ values from –1.2 to –2.0, while peak suctions reach –2.6 at wall ends and corners. Even though suctions have increased by roughly 25% to 30% compared to the 1-story rectangular case, the overall distribution remains relatively smooth and exhibits fewer extreme peaks than the T- and L-shaped configurations. The simple, continuous wall geometry effectively reduces areas where separation and flow reattachment can amplify suctions.

Across all three shapes, the increase in suctions from 1-story to 2-story configurations ranges from 25% to 45%, with the largest increase occurring in zones of geometric irregularity and at wall corners. The L-shape consistently demonstrates the highest peak suctions, followed by the T-shape and the Rectangular form. These findings highlight how both building height and plan complexity interact to increase the severity and variability of negative wind pressures on building walls when considering worst-case wind directions.

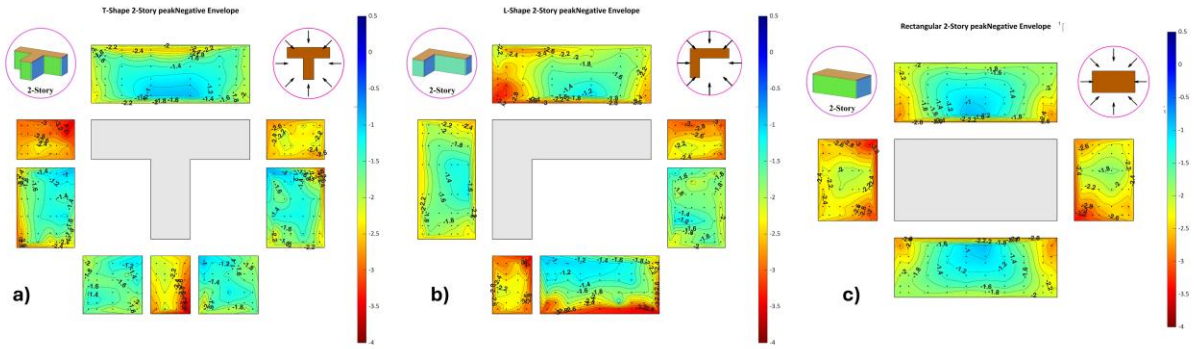

Figure 20. Peak negative pressure coefficient (Čp) distributions for 2-story T-shape (a), L-shape (b), and Rectangular (c) buildings.

c) Three-Story Buildings:

At the 3-story level, the T-shape (Figure 21a) experiences peak negative C_p values predominantly between –1.4 and –2.4 across most wall surfaces, with extreme suctions intensifying to –3.0 to –3.4 at projecting wall ends and corners. Compared to the 2-story configuration (Figure 20), suction magnitudes have increased by 15% to 25%, particularly on the upper regions and edges where wind exposure is amplified. The increases reflect both the higher elevation and more developed corner vortex effects. Notably, the transition from 2 to 3 stories results in a more pronounced gradient between central and edge zones, highlighting the growing importance of corner and edge effects as height increases.

The L-shape (Figure 21b) demonstrates the highest suctions among the three configurations, with widespread $\check{C}_p$ values from –1.8 to –2.8, and local peaks exceeding –3.6 at re-entrant corners and free ends. These values represent an approximate 20% to 30% increase over the 2-story L-shape case. The geometry's asymmetric plan continues to promote severe suction zones where flow accelerates around complex edges and intersections. Particularly, the re-entrant corners exhibit increases up to 40%, underscoring the compounding influence of plan complexity and building height on suction amplification.

The Rectangular building (Figure 21c), maintaining its typical uniformity, presents negative pressures generally between –1.4 and –2.0, with peak suctions reaching –2.8 to –3.0 at wall ends and corners. While suction levels have increased by 15% to 20% relative to the 2-story rectangular case, the rectangular plan continues to mitigate extreme peak suctions compared to the T- and L-shaped layouts. This uniform response emphasizes the aerodynamic advantage of continuous, regular geometries in resisting suction amplification, especially at greater heights.

Across all three shapes, transitioning from 2 to 3 stories yields an overall suction increase ranging from 15% to 30%, with the highest amplification at geometric discontinuities—namely, edges, corners, and re-entrant zones. The L-shape continues to be the most susceptible to severe suction effects, followed by the T-shape, with the Rectangular shape exhibiting the most stable pressure distribution.

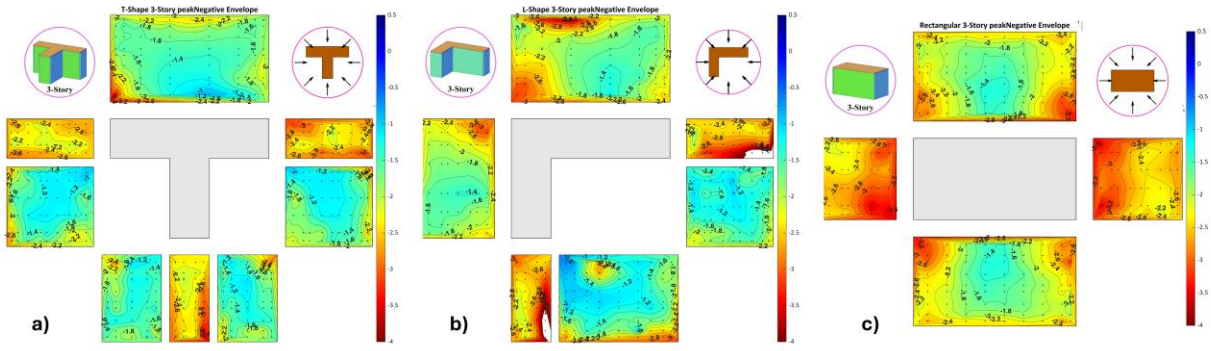

Figure 21. Peak negative pressure coefficient (Čp) distributions for 3-story T-shape (a), L-shape (b), and Rectangular (c) buildings.

4.1.2.2. Critical $\hat{C}_p$ Distribution

a) Single-Story Buildings:

At the 1-story level, the peak positive pressure coefficients ($\hat{C}_p$) exhibit distinct patterns among the three shapes. Across all cases, values reflect the worst-case pressures aggregated from all wind directions (0°–360°), ensuring that each wall has experienced windward exposure at some point.

The T-shape (Figure 22a) walls present moderate $\hat{C}_p$ values. Most walls register between +1.3 to +1.9, with isolated areas reaching up to +2.1. The north wall and parts of the eastern projections show the highest pressures. Despite geometric irregularity, positive pressures are relatively evenly distributed across the walls, indicating that flow separation effects do not significantly suppress pressure build-up in any zone. Compared to the Rectangular shape (Figure 22c), the T-shape's peak $\hat{C}_p$ values are approximately 20–25% higher. When compared to the L-shape (Figure 22b), the T-shape exhibits roughly 10–15% higher positive pressures.

The L-shaped (Figure 22b) shows a similar overall range of +1.3 to +1.9, with peak values up to +1.9 along the west wall and the south leg. Local amplifications are seen near the re-entrant corner, likely due to stagnation where oblique winds encounter the concave geometry. Compared to the Rectangular building (Figure 22c), the L-shape experiences roughly 10–15% higher peak pressures.

The Rectangular configuration (Figure 22c) has the lowest $\hat{C}p$ values, generally between +1.2 and +1.5, with occasional peaks reaching +1.7. Peak pressures are concentrated on the east and south façades due to wind alignment. The simple geometry promotes uniform flow, minimizing localized amplification and resulting in the lowest positive pressures among the three shapes.

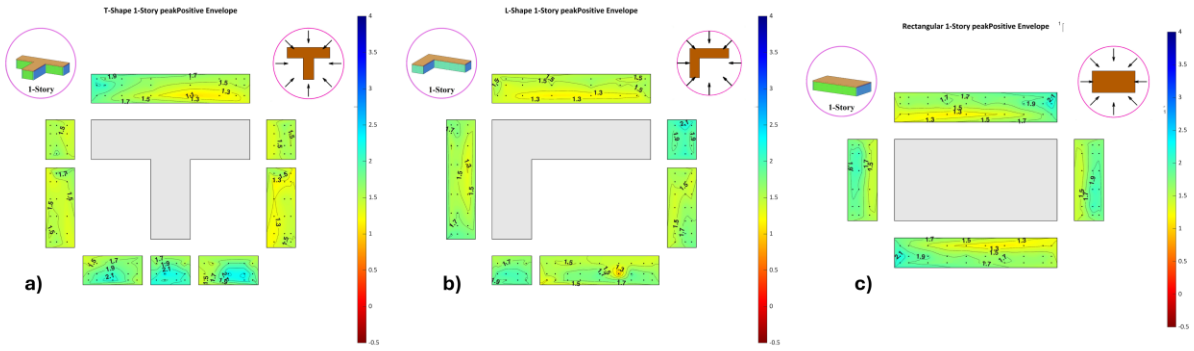

Figure 22. Peak positive pressure coefficient (Ĉp) distributions for 1-story T-shape (a), L-shape (b), and Rectangular (c) buildings.

b) Two-Story Buildings:

For the 2-story buildings, the T-shape (Figure 23a) shows $\hat{C}p$ values between +1.5 and +1.9, with peaks up to +2.1. This marks a 10–15% increase over the 1-story T-shape (Figure 22a), especially near upper wall regions and outer corners, where stagnation accumulates under oblique wind approach.

The L-shape (Figure 23b) also displays $\hat{C}p$ values in the +1.5 to +1.9 range, with isolated regions—typically along long walls and re-entrant corners—reaching +2.1. Compared to the 1-story case (Figure 22b), this constitutes a 15–20% increase, driven by greater surface area and wind exposure.

The Rectangular building (Figure 23c) registers most $\hat{C}p$ values from +1.5 to +1.7, with a few zones approaching +1.9. Compared to its 1-story version (Figure 22c), the increase is modest (5–10%). Unlike the T- and L-shapes, the Rectangular plan exhibits limited local amplification, again due to its aerodynamic regularity.

Across all shapes, the T- and L-shaped configurations exhibit up to 25% higher positive pressures than the Rectangular baseline, emphasizing the influence of geometry.

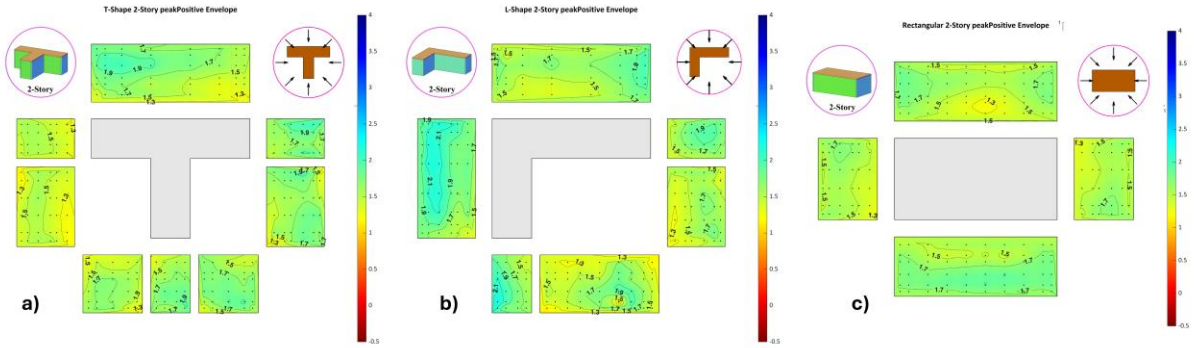

Figure 23. Peak positive pressure coefficient ($\hat{C}p$) distributions for 2-story T-shape (a), L-shape (b), and Rectangular (c) buildings.

c) Three-Story Buildings:

The T-shape (Figure 24a) shows the most significant amplification, with most walls registering between +1.7 and +2.1, and peaks up to +2.3. This reflects a 10–15% increase over the 2-story T-shape (Figure 23a) and up to 25% over the 1-story version (Figure 22a). The most pronounced peaks are observed at upper wall sections and corners.

The L-shape (Figure 24b) similarly exhibits $\hat{C}p$ values from +1.7 to +2.1, with localized peaks at +2.3—typically at re-entrant corners and exposed wall segments. Compared to the 2-story L-shape (Figure 23b), the increase is around 12–18%, and up to 30% over the 1-story case (Figure 22b).

The Rectangular configuration (Figure 24c) maintains consistent aerodynamic behavior, with $\hat{C}p$ values from +1.5 to +1.9 and isolated peaks up to +2.1. Pressure amplification from the 2-story case (Figure 23c) is limited to 8–12%, and overall performance remains more stable than in irregular shapes.

Comparatively, the T- and L-shapes experience 15–20% higher peak pressures than the Rectangular geometry, especially as building height increases and re-entrant features compound stagnation effects.

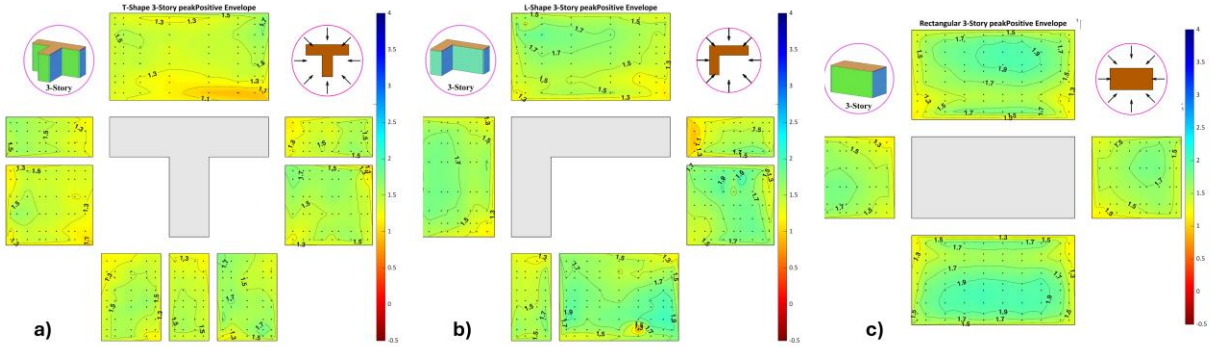

Figure 24. Peak positive pressure coefficient (Ĉp) distributions for 3-story T-shape (a), L-shape (b), and Rectangular (c) buildings.

Table 4 summarizes the typical and peak critical pressure coefficients (Čp and Ĉp) for all shapes and story heights, illustrating how suction and positive pressure magnitudes vary with plan geometry and building height.

Table 4. Summary of typical and peak critical pressure coefficients (Čp and Ĉp) for all shapes and story heights.

Story	Shape	Typical $\check{C}p$	Peak $\check{C}p$	Δ $\check{C}p$ vs. Prev. Height	Typical $\hat{C}p$	Peak $\hat{C}p$	Δ $\hat{C}p$ vs. Prev. Height	Notable Geometric Effects
1	T	–1.0 to –1.8	–2.2	–	+1.3 to +1.9	+2.1	–	Suctions are amplified at projecting walls and corners. Positive pressure evenly distributed.
1	L	–1.2 to –2.0	–2.4	–	+1.3 to +1.9	+1.9	–	Open corner amplifies suctions. Re-entrant stagnation boosts $\hat{C}_p$.
1	R	–1.0 to –1.6	–2.0	–	+1.2 to +1.5	+1.7	–	Uniform response, minimal amplifications.
2	T	–1.2 to –2.2	–3.0	+30–35%	+1.5 to +1.9	+2.1	+10–15%	Height increases suction and stagnation at corners.
2	L	–1.6 to –2.8	–3.2	+40–45%	+1.5 to +1.9	+2.1	+15–20%	Re-entrant corners show 40% Ĉp amplification.
2	R	–1.2 to –2.0	–2.6	+25–30%	+1.5 to +1.7	+1.9	+5–10%	Simple plan reduces local peaks.
3	T	–1.4 to –2.4	–3.4	+15–25%	+1.7 to +2.1	+2.3	+10–15%	Suction gradients intensify at higher walls and edges.
3	L	–1.8 to –2.8	–3.6	+20–30%	+1.7 to +2.1	+2.3	+12–18%	Plan complexity amplifies Ĉp by up to 40%.
3	R	–1.4 to –2.0	–3.0	+15–20%	+1.5 to +1.9	+2.1	+8–12%	Uniform pressures, limited amplification.

4.2. Force and Moment Results

This section presents the derived force and moment coefficients computed from wall pressure data for all building configurations. The analysis captures the directional variation and magnitude of base shear and torsional effects, enabling a detailed evaluation of how wind direction, building shape, and height influence global structural demands.

Four nondimensional coefficients are examined: the longitudinal and transverse base shear coefficients (C_{Sx} and C_{Sy}), the resultant base shear coefficient (C_V), and the torsional moment coefficient (C_T). These were obtained by integrating wall pressures into force and moment time histories, then normalized with respect to dynamic pressure and relevant geometric quantities, as defined in Section 3.3.

The mean directional trends for each story height are presented in Figures 25-27, which display C_{Sx}, C_{Sy}, C_V, and C_T as functions of wind direction (0°–360°) for the 1-, 2-, and 3-story buildings, respectively. These plots highlight the influence of height on the directional distribution of aerodynamic loads.

The corresponding peak directional envelopes—representing the maximum response values across all time histories for each direction—are shown in Figures 28-30. These figures identify the critical wind angles that generate extreme structural responses and illustrate how peak magnitudes evolve with increasing building height.

To isolate the effect of plan geometry, Figures 31–33 compare the mean coefficients across the three plan shapes (T-shape, L-shape, and Rectangular) at each story level. These comparisons elucidate the relative sensitivity of each geometry to directional wind effects under average loading conditions.

Finally, Figures 34–36 provide parallel comparisons for the peak coefficients across all shapes and heights. These plots serve to quantify shape-induced amplification effects under worst-case wind loading scenarios, particularly with respect to torsion and resultant shear.

All results are based exclusively on external wall pressure measurements and are therefore consistent with the pressure coefficient (C_p) analysis reported in Section 4.1. Roof pressures were not instrumented in this study. As such, the reported force and moment coefficients reflect wind-induced in-plane loading behavior—namely base shear and torsion—relevant to main wind force-resisting system (MWFRS) design considerations.

4.2.1. Variation of Forces and Torsional Moment with Wind Direction

4.2.1.1. Longitudinal and Transverse Shear Coefficients (C_{Sx}, C_{Sy})

Across all shapes and building heights, the base shear coefficients in the longitudinal (C_{Sx}) and transverse (C_{Sy}) directions revealed pronounced sensitivity to wind direction (Figures 25a–b, 26a–b, and 27a–b for 1-, 2-, and 3-story models, respectively).

The Rectangular building displayed stable and symmetric shear responses, with peak C_{Sx} and C_{Sy} values occurring around 0°, 90°, 180°, and 270° — wind directions aligned with the

building's principal axes. This pattern reflects the expected directional regularity of a symmetric plan and confirms its baseline aerodynamic performance.

In contrast, the T-shaped and especially the L-shaped buildings exhibited elevated and asymmetric shear responses under oblique (quartering) winds such as 45°, 135°, 225°, and 315°. These variations are attributable to geometric irregularities that induce unbalanced pressure distributions and localized flow separation.

The L-shape showed particularly strong fluctuations in C_{Sy}, with both positive and negative peaks intensifying with building height. For example, at the 3-story level (Figure 27b), C_{Sy} fell below –0.4 under certain directions, indicating a sharp transverse load reversal driven by asymmetric plan features. Simultaneously, C_{Sx} peaked near 0.3 — more than double the maximum observed for the Rectangular model — under winds oblique to the vertical leg of the "L."

4.2.1.2. Resultant Base Shear and Torsional Coefficients (C_V, C_T)

The resultant base shear coefficient (C_V) and the torsional moment coefficient (C_T) provide system-level measures of wind loading (Figures 25c–d, 26c–d, and 27c–d). While C_V combines the vector magnitude of shear forces in both directions, C_T isolates the rotational component arising from eccentric pressure distributions.

The Rectangular building consistently exhibited low and stable C_T values across all wind directions and building heights, affirming its inherent torsional neutrality due to geometric symmetry. Correspondingly, C_V values remained moderate and showed limited directional fluctuation, with values generally bounded below 1.5.

By contrast, the T-shaped configuration revealed moderate amplification in both C_V and C_T, particularly at the 2- and 3-story levels under quartering winds (e.g., 45°, 60°, 135°). Peak C_T values for the T-shape reached approximately 0.08 to 0.10 at 3-story height, indicating directional asymmetries despite partial geometric balance. C_V values for the T-shape increased with height and reached 2.0 in the 3-story case, reflecting the combined effect of increased surface area and flow separation around re-entrant corners.

The most pronounced torsional behavior occurred in the L-shaped buildings. At the 3-story level (Figure 27d), peak C_T values exceeded 0.25 under winds from 45°, 225°, and 315°—

directions that engage both legs of the “L” in an unbalanced manner. These torsional demands were more than five times higher than those of the T-shape and nearly tenfold those of the Rectangular configuration. This trend reflects how re-entrant geometry and plan asymmetry amplify rotational loading beyond what would be inferred from shear alone.

The high C_V values for the L-shape further highlight the compounding effects of plan irregularity and building height. In the 3-story configuration (Figure 27c), C_V exceeded 2.5 at wind angles near 45°, indicating that irregular geometry not only intensifies torsion but also raises resultant shear demands. Similar trends were observed in the 1- and 2-story cases (Figures 25c–d and 26c–d), though the magnitude and directional sensitivity became more pronounced with increased height.

Importantly, the wind directions producing peak C_T did not always align with those generating peak C_V, particularly in the L-shaped models. This directional decoupling emphasizes the need to evaluate torsional effects independently, as reliance on shear trends alone may mask critical torsional demands. For instance, in the L-shape at 3-story height, maximum torsion occurred at 225°, whereas maximum base shear occurred at 45°, illustrating distinct aerodynamic mechanisms driving each response.

These findings align with prior experimental work (e.g., Elsharawy et al., 2015; Sarma et al., 2025) and reinforce the importance of explicitly considering torsion in the wind-resistant design of irregularly shaped, low-rise buildings, especially in hurricane-prone regions where directional wind variability and geometric eccentricity combine to elevate structural demands.

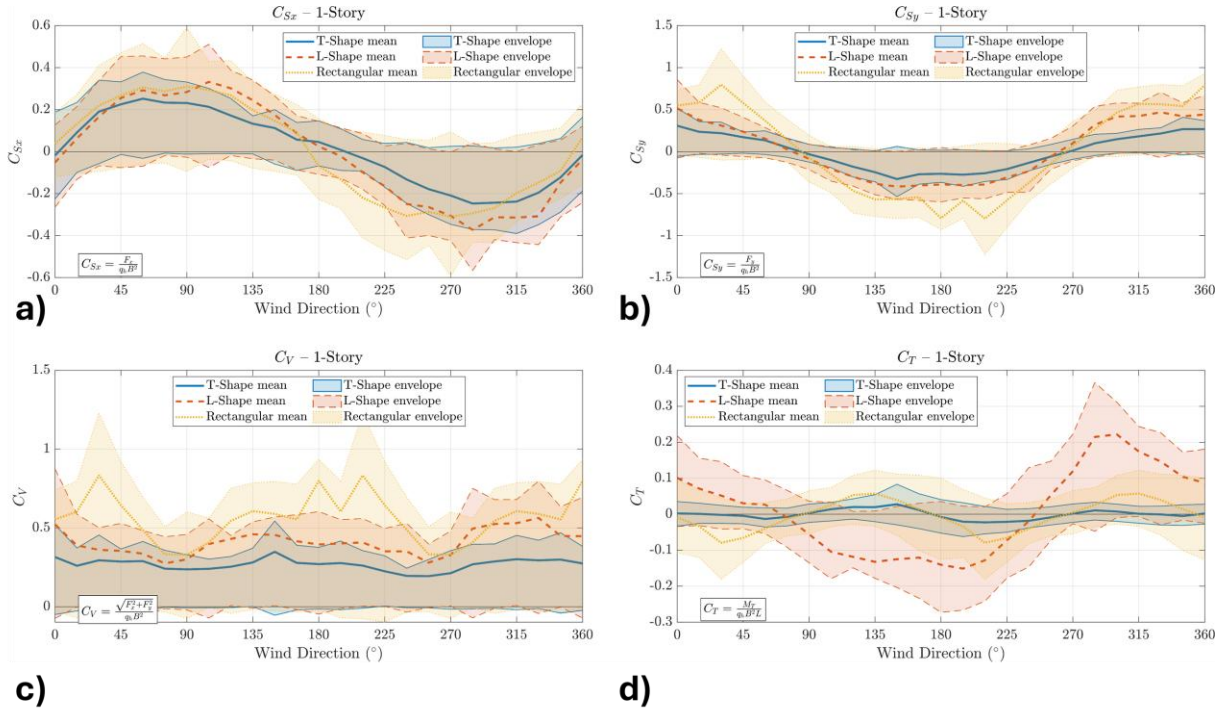

Axes are independently scaled across stories to improve resolution clarity. Use coefficient magnitudes for comparison.

Figure 25. Mean and peak envelope of base shear and torsional load coefficients (CSx, CSy, CV, and CT), versus wind direction for 1-story T-, L-, and Rectangular buildings.

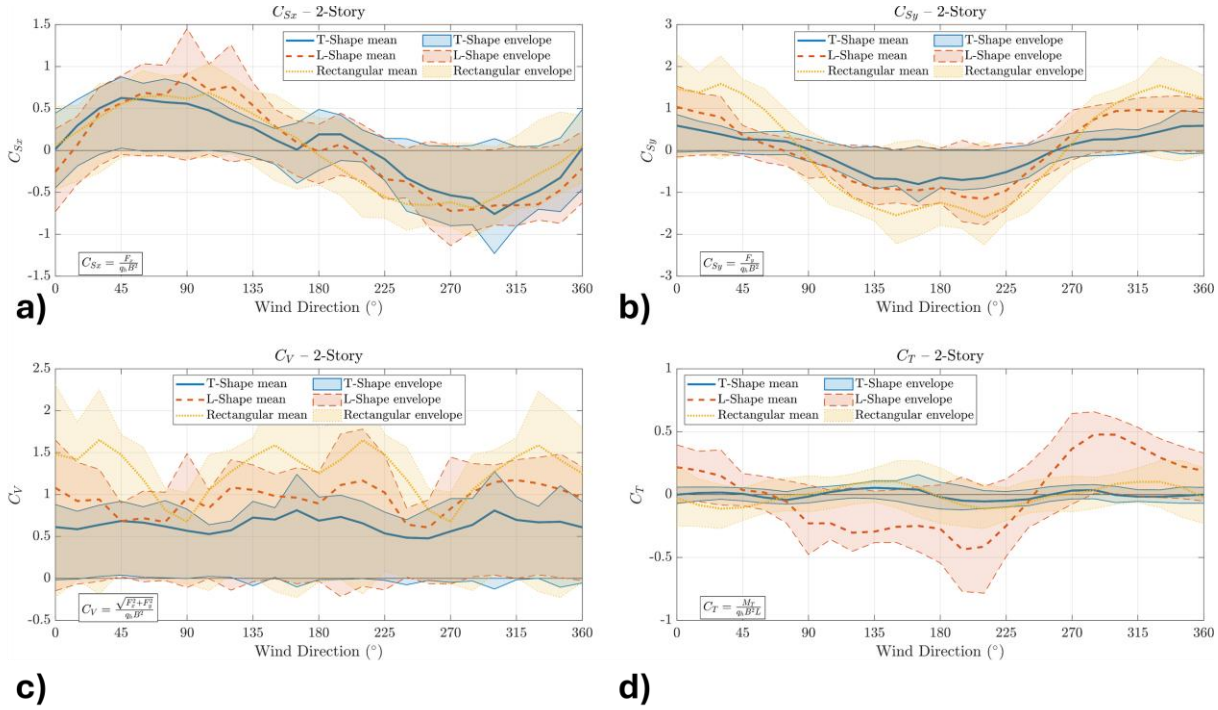

Axes are independently scaled across stories to improve resolution clarity. Use coefficient magnitudes for comparison.

Figure 26. Mean and peak envelope of base shear and torsional load coefficients (CSx, CSy, CV, and CT), versus wind direction for 2-story T-, L-, and Rectangular buildings.

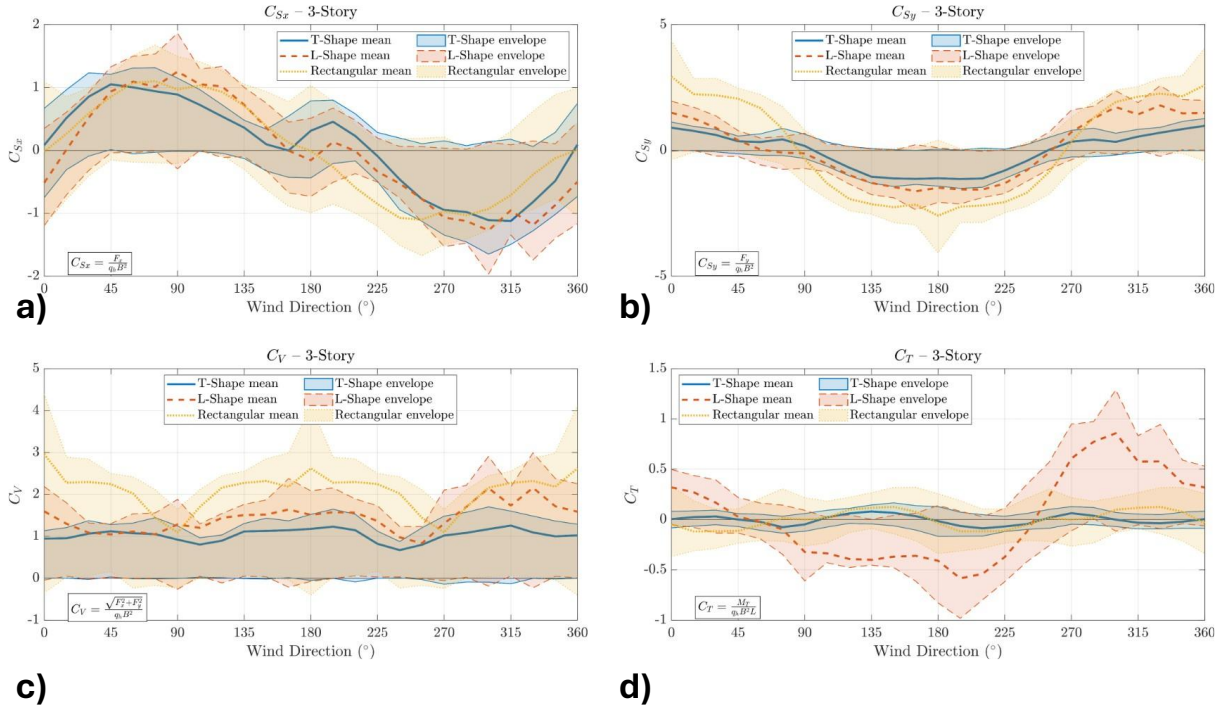

Axes are independently scaled across stories to improve resolution clarity. Use coefficient magnitudes for comparison.

Figure 27. Mean and peak envelope of base shear and torsional load coefficients (CSx, CSy, CV, and CT), versus wind direction for 3-story T-, L-, and Rectangular buildings.

4.2.2. Influence of Building Height on Shear and Torsional Coefficients

The effect of building height on wind-induced shear and torsional response was evaluated by comparing the base shear coefficients (C_{Sx}, C_{Sy}), resultant shear (C_V), and torsional moment coefficient (C_T) across the 1-, 2-, and 3-story configurations for each plan geometry. Figures 28 through 30 present these trends for the T-shaped, L-shaped, and Rectangular buildings, respectively.

In the T-shaped buildings (Figure 28), increasing the story height resulted in noticeable amplification in both shear and torsional responses. The C_{Sx} and C_{Sy} envelopes widened progressively with height, particularly under oblique wind directions (e.g., 45°, 135°, 225°), indicating greater wind sensitivity at higher elevations. The resultant base shear C_V also increased with height, with the 3-story model exhibiting values nearly twice as large as the 1-story model in several directions. Torsional amplification was most evident in the higher-story cases, with C_T reaching values around 0.15 in the 3-story configuration—especially near 225° and 315°, where asymmetric vortical flows are intensified by the plan geometry.

For the L-shaped buildings (Figure 29), the influence of height was even more pronounced. The C_{Sx} and C_{Sy} coefficients showed increasingly irregular and asymmetric patterns with height. Under quartering winds, the 3-story L-shape reached transverse shear coefficients beyond ±2.5—significantly higher than its lower-story counterparts. The resultant shear coefficient C_V followed a similar trend, growing steadily with height and exhibiting a broader envelope. Notably, the torsional coefficient C_T revealed the strongest height dependency among all configurations: the 3-story model displayed peaks of 0.3–0.35 under winds from 45°, 135°, and 270°, representing more than a fivefold increase over the 1-story configuration. This emphasizes the compounding effect of plan irregularity and vertical extension on torsional demands.

By contrast, the Rectangular buildings (Figure 30) showed relatively minimal sensitivity to building height. The C_{Sx} and C_{Sy} profiles remained consistent across stories, with peak values occurring at principal wind directions (0°, 90°, etc.) and maintaining symmetric trends. While there was some increase in C_V with height, it was modest compared to the irregular shapes. The torsional response remained low across all heights, with C_T values rarely exceeding ±0.05 even in the 3-story configuration, underscoring the torsional stability inherent to symmetric plan geometries.

These results collectively highlight how geometric irregularity and height interact to amplify lateral and torsional loads, particularly in plan-asymmetric buildings. They underscore the importance of evaluating these effects explicitly in design, especially under oblique wind directions.

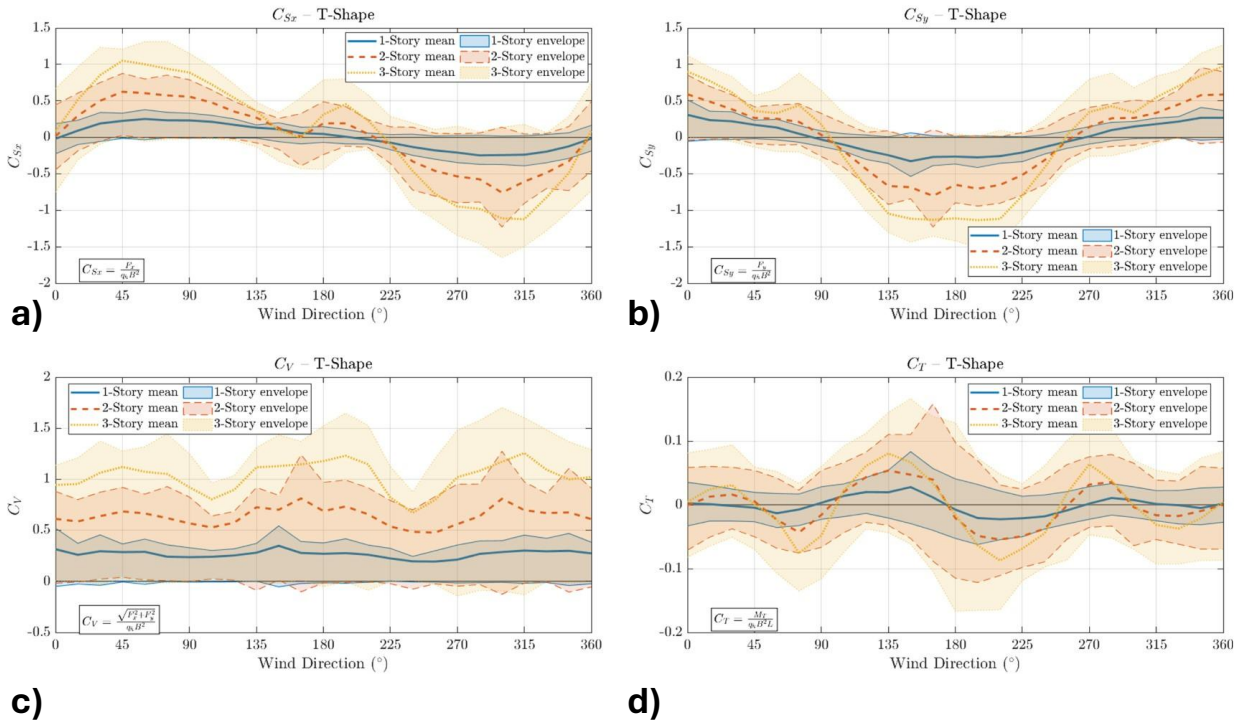

Axes are independently scaled across stories to improve resolution clarity. Use coefficient magnitudes for comparison.

Figure 28. Variation of base shear coefficients (C_{Sx}, C_{Sy}), resultant shear coefficient (C_V), and torsional moment coefficient (C_T) with wind direction for the T-shaped building across 1-, 2-, and 3-story configurations. Results include mean trends and peak envelopes at each height level.

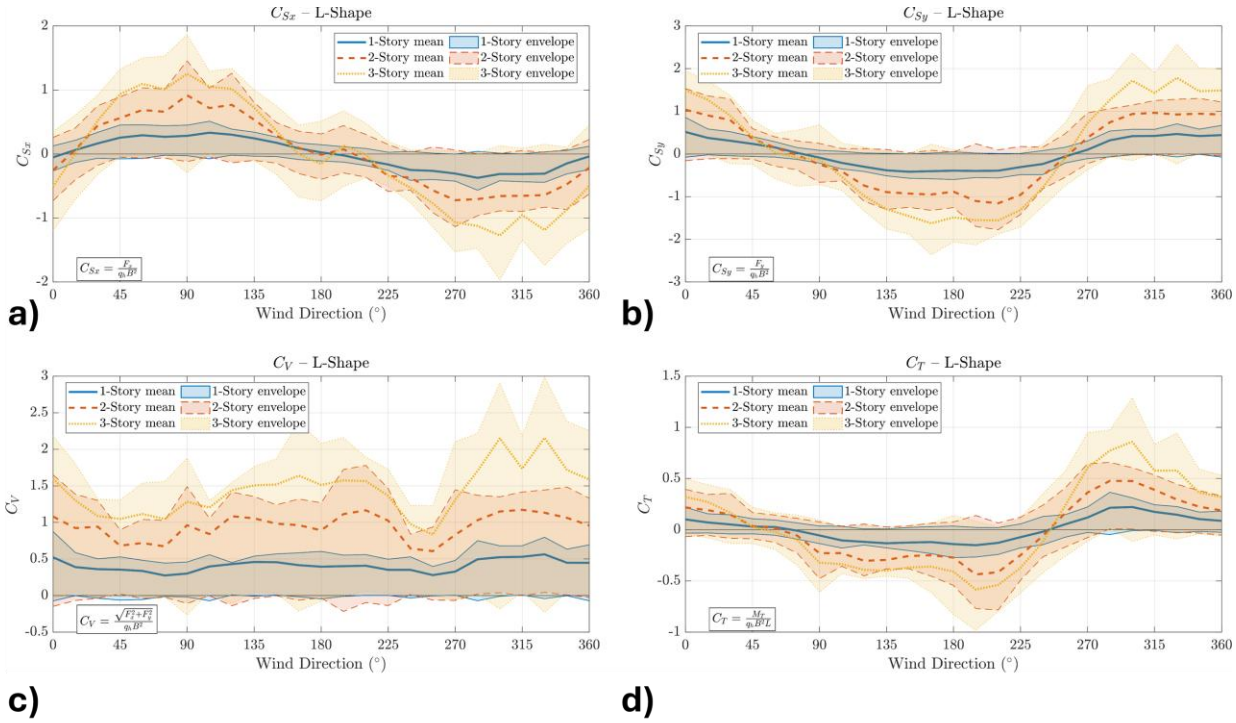

Axes are independently scaled across stories to improve resolution clarity. Use coefficient magnitudes for comparison.

Figure 29. Variation of base shear coefficients (C_{Sx}, C_{Sy}), resultant shear coefficient (C_V), and torsional moment coefficient (C_T) with wind direction for the L-shaped building across 1-, 2-, and 3-story configurations. Irregular trends and large peaks in C_T highlight strong sensitivity to building height.

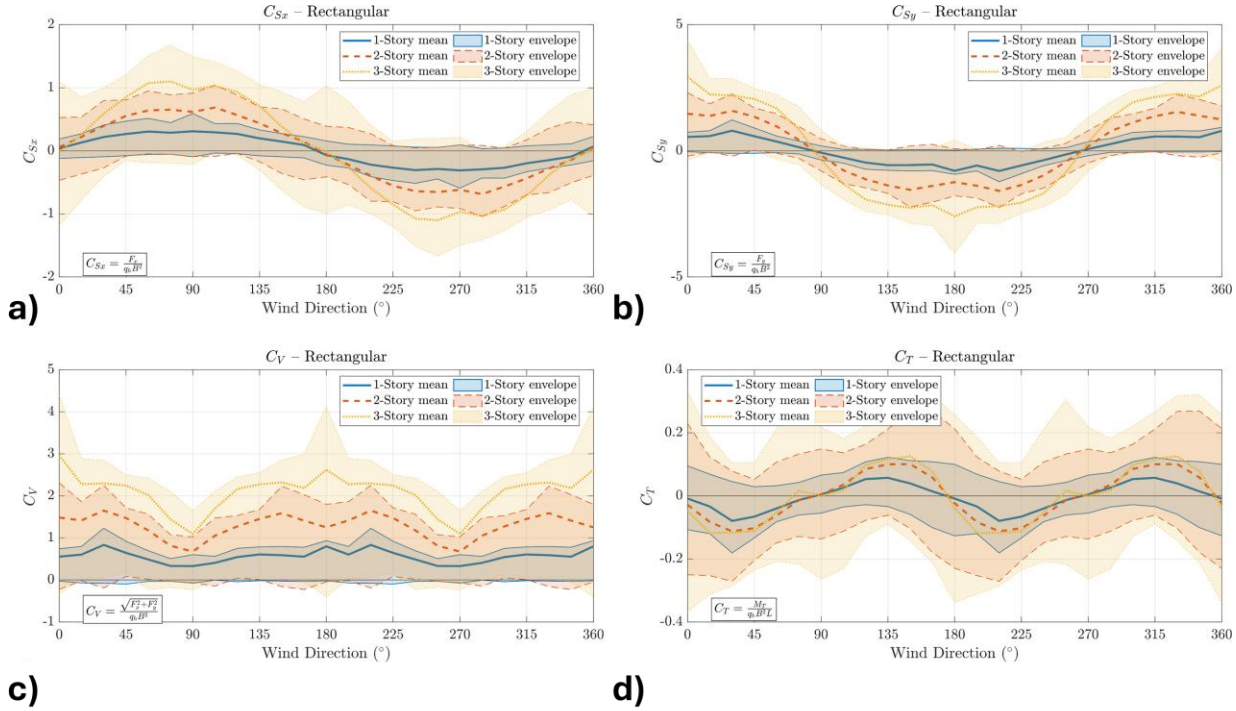

Figure 30. Variation of base shear coefficients (C_{Sx}, C_{Sy}), resultant shear coefficient (C_V), and torsional moment coefficient (C_T) with wind direction for the Rectangular building across 1-, 2-, and 3-story configurations. Minimal variation in C_T confirms the torsional stability of symmetric plan geometries.

4.2.3. Directional Peaks and Critical Wind Directions

4.2.3.1. Mean Directional Coefficients

The directional distribution of mean force and moment coefficients provides insight into how wind loading patterns evolve with building shape and height. Figures 31 through 33 present polar plots of the mean base shear coefficients C_{Sx} and C_{Sy}, the resultant base shear C_V, and the torsional moment coefficient C_T for the 1-, 2-, and 3-story models, respectively.

For all shapes and heights, the base shear coefficients (C_{Sx}, C_{Sy}) exhibit clear directional sensitivity. In the rectangular model, these coefficients maintain a regular four-lobe pattern with peaks near 0°, 90°, 180°, and 270° (see Figures 31a–b), reflecting the aerodynamic stability of symmetric geometry. As building height increases (Figures 32a–b and 33a–b), these patterns remain consistent in shape but grow slightly in magnitude.

In contrast, the T-shaped and L-shaped buildings show more irregular and distorted directional trends. Notably, C_{Sx} for the T-shape exhibits amplified lobes near 90° and 270°,

particularly in the 2- and 3-story cases (Figures 32a and 33a). These correspond to winds perpendicular to the vertical stem of the T, where the extended plan area increases drag forces. The L-shape shows its strongest signature in C_{Sy}, with consistent peaks at oblique angles such as 45° and 225° (Figures 31b, 32b, and 33b), attributed to the lateral imbalance and flow separations caused by its asymmetric plan.

The resultant base shear coefficient C_V consolidates the effects of C_{Sx} and C_{Sy}. While the rectangular building exhibits a smooth, elliptical response at all heights (Figures 31c, 32c, and 33c), both the T- and L-shaped buildings develop distorted patterns with elevated values in quadrant winds. The L-shape, in particular, shows nearly 2× higher C_V in critical directions by the 3-story level (Figure 33c), indicating intensified loading as vertical exposure increases.

Torsional response, captured by C_T, further highlights the impact of irregular geometry. As expected, the rectangular shape maintains negligible torsion across all wind directions (Figures 31d–33d), confirming its torsional symmetry. The T-shape introduces moderate torsional moments in quartering winds, with noticeable lobes in Figures 32d and 33d. The L-shape shows the most significant torsional asymmetry, with dominant lobes at 45°, 225°, and 315°, reaching mean C_T values near 0.2 in the 3-story case (Figure 33d). These values are approximately 10× higher than those for the rectangular building, underscoring the influence of asymmetric plan geometry and increased building height.

These trends affirm that mean directional effects can produce substantial wind-induced demands, especially torsional, in buildings with irregular plans. This highlights the need to consider shape-induced asymmetries not only in peak loading conditions but also in the average structural response when evaluating the wind-resisting system.

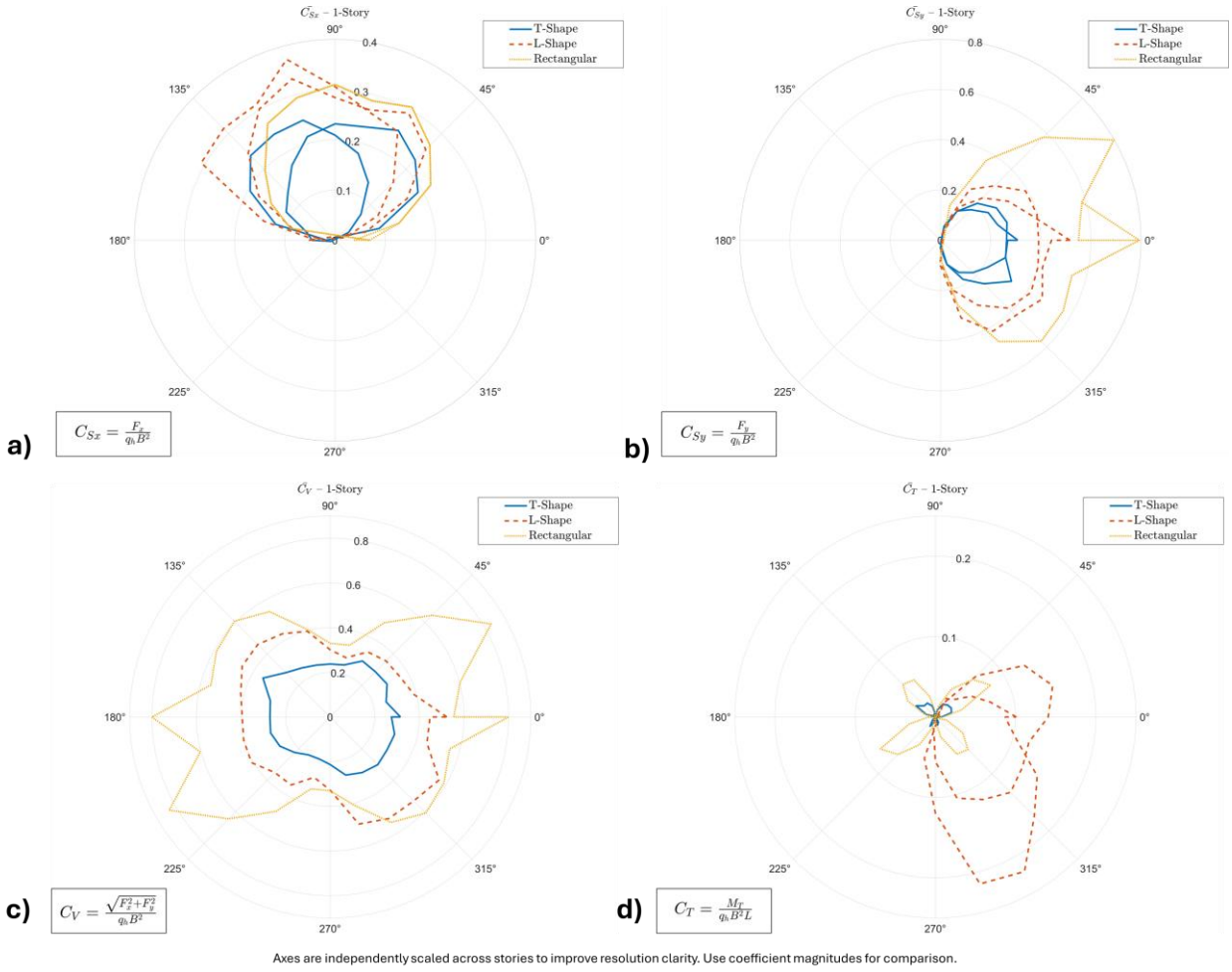

Figure 31. Directional mean coefficients for the 1-story buildings: (a) longitudinal base shear $\bar{C}_{Sx}$,(b) transverse base shear $\bar{C}_{Sy}$, (c) resultant base shear $\bar{C}_V$, and (d) torsional moment coefficient $\bar{C}_T$.

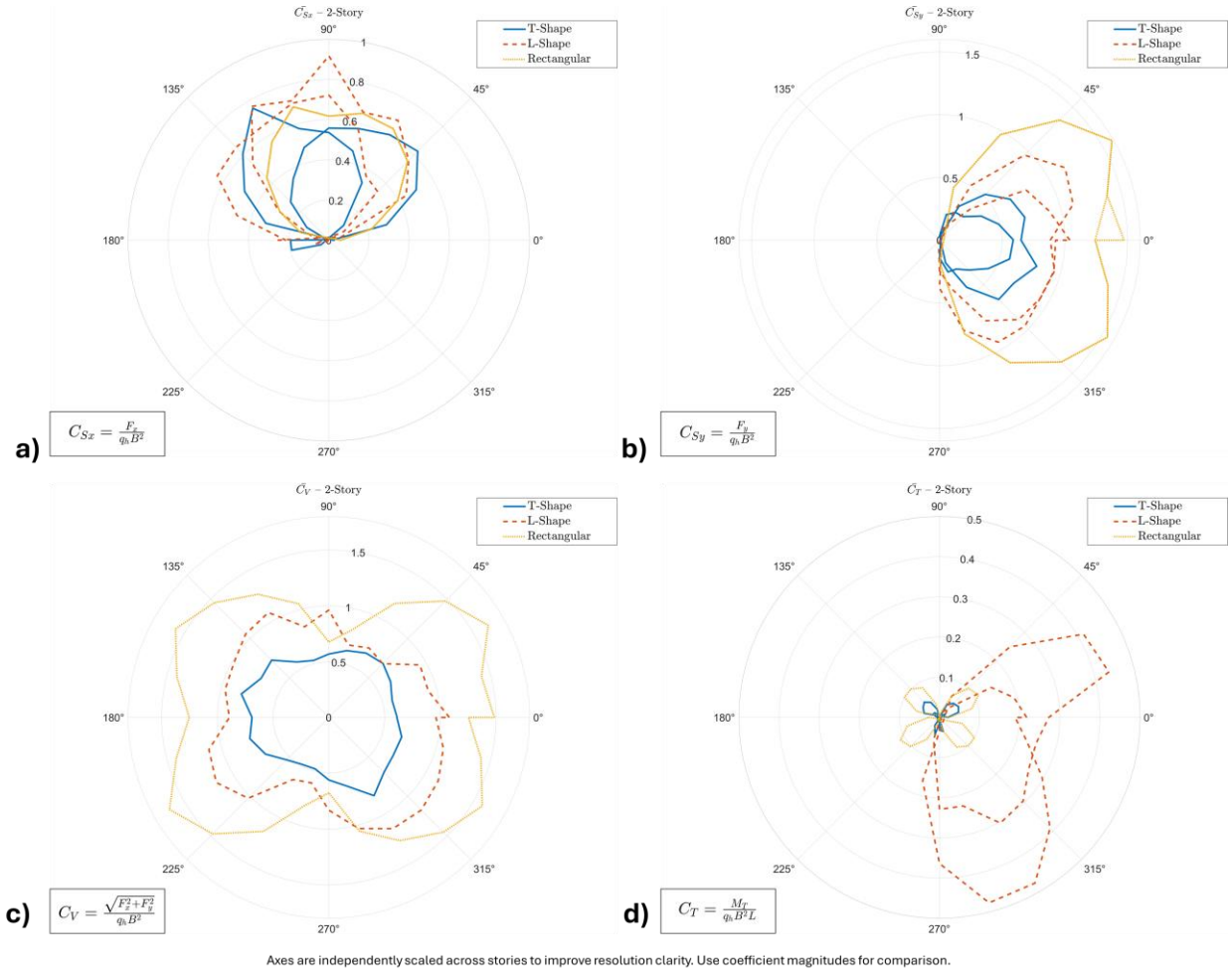

Figure 32. Directional mean coefficients for the 2-story buildings: (a) $\bar{C}_{Sx}$,(b) $\bar{C}_{Sy}$, (c) $\bar{C}_V$, and (d) $\bar{C}_T$.

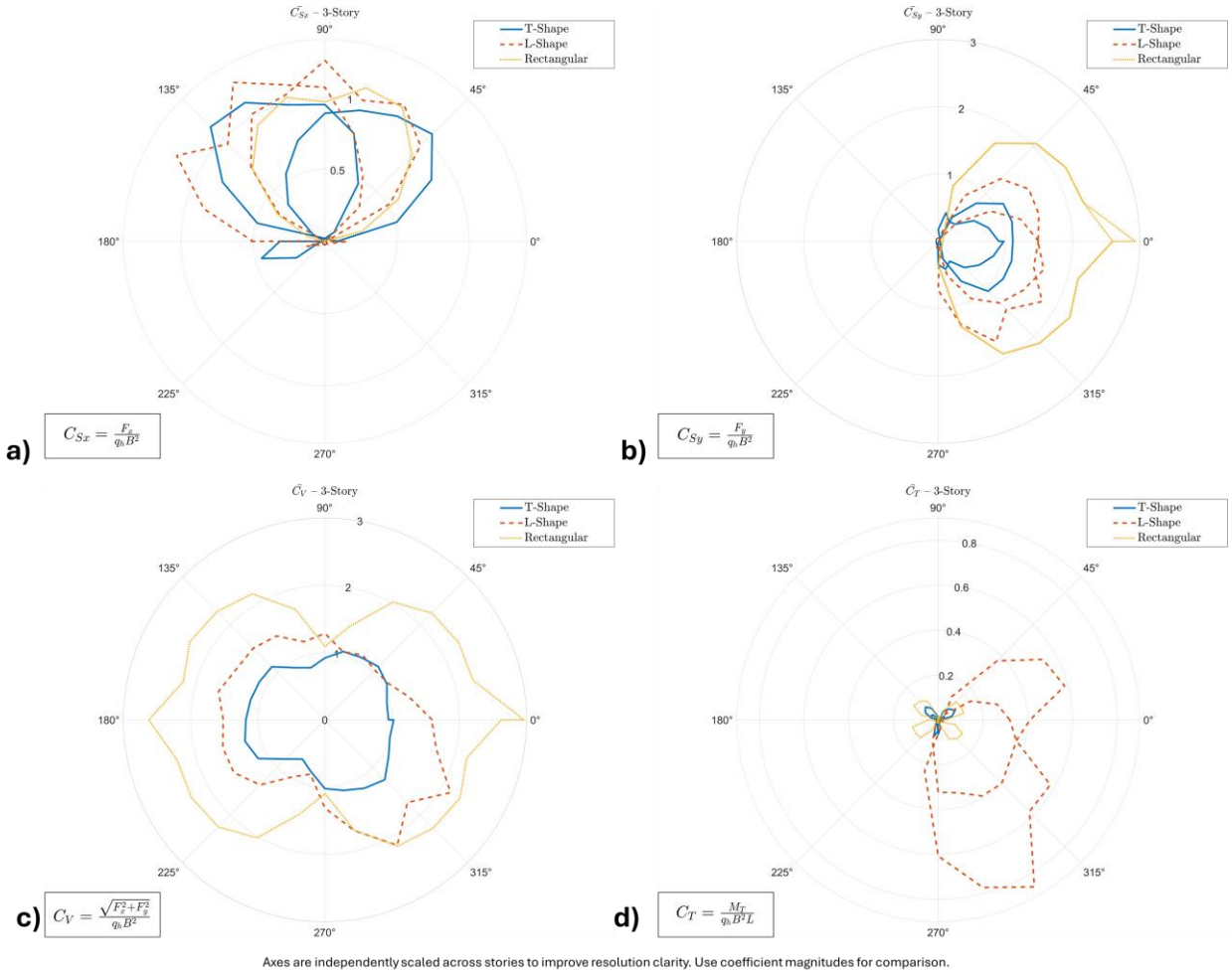

Figure 33. Directional mean coefficients for the 3-story buildings: (a) $\bar{C}_{Sx}$,(b) $\bar{C}_{Sy}$, (c) $\bar{C}_V$, and (d) $\bar{C}_T$.

4.2.3.2. Peak Directional Coefficients

The peak directional coefficients reflect the extreme wind-induced demands across all orientations, offering critical insight into the most vulnerable loading directions for each configuration. Figures 34 through 36 illustrate the peak base shear coefficients C_{Sx} and C_{Sy} the resultant shear C_V , and the torsional moment coefficient C_T for the 1-, 2-, and 3-story buildings, respectively.

For the rectangular building, peak shear coefficients (Figures 34a–b) remain largely aligned with the principal axes (0°, 90°, 180°, 270°), and the response retains its symmetric pattern across all heights. However, the magnitude increases with story count, particularly for C_{Sx}, reflecting the higher exposure and greater tributary area of taller models. The peak C_V values (Figure 34c) also

grow with height but remain smooth and directionally predictable, indicating the rectangular configuration maintains consistent aerodynamic behavior even under extreme conditions.

In contrast, the T-shaped building exhibits pronounced direction-dependent amplification. For instance, in the 3-story case (Figure 36a–b), peak C_{Sx} and C_{Sy} exceed 0.3 in multiple off-axis directions, particularly near 60°, 240°, and 270°. These peaks correspond to flow orientations that expose large frontal areas or activate plan irregularities. The peak resultant shear C_V (Figure 36c) reveals elongated lobes in these same directions, indicating compound amplification of forces.

The L-shaped configuration demonstrates the most severe and asymmetric peak responses. In Figures 34a–b through 36a–b, peak base shear coefficients are dominated by responses at diagonal wind angles (e.g., 45°, 135°, 225°, 315°), where flow separation and reattachment become highly unbalanced. This is especially evident in the 3-story model (Figure 36b), where C_{Sy} drops below –0.5 and C_{Sx} exceeds 0.35 — values that significantly surpass the rectangular benchmark by more than a factor of two.

The torsional coefficient C_T, shown in Figures 34d through 36d, further amplifies these trends. The rectangular model again shows minimal peaks, with values generally below 0.05 across all wind directions. The T-shaped building begins to show directional torsional spikes by the 2- and 3-story levels (Figures 35d–36d), especially around 45° and 225°. However, the L-shaped model exhibits the most extreme torsional peaks, reaching values near 0.3 at 3 stories (Figure 36d). These occur at quartering winds and align closely with the plan asymmetry, signaling a high potential for torsional instability if not addressed in design.

In summary, while mean directional coefficients reveal consistent shape effects, peak coefficients highlight how geometry and building height interact to produce extreme, direction-specific wind demands. The escalation of peak C_V and C_T in the T- and L-shaped buildings—particularly under oblique winds—emphasizes the importance of evaluating directional extremes during design, rather than relying solely on mean or axis-aligned loads.

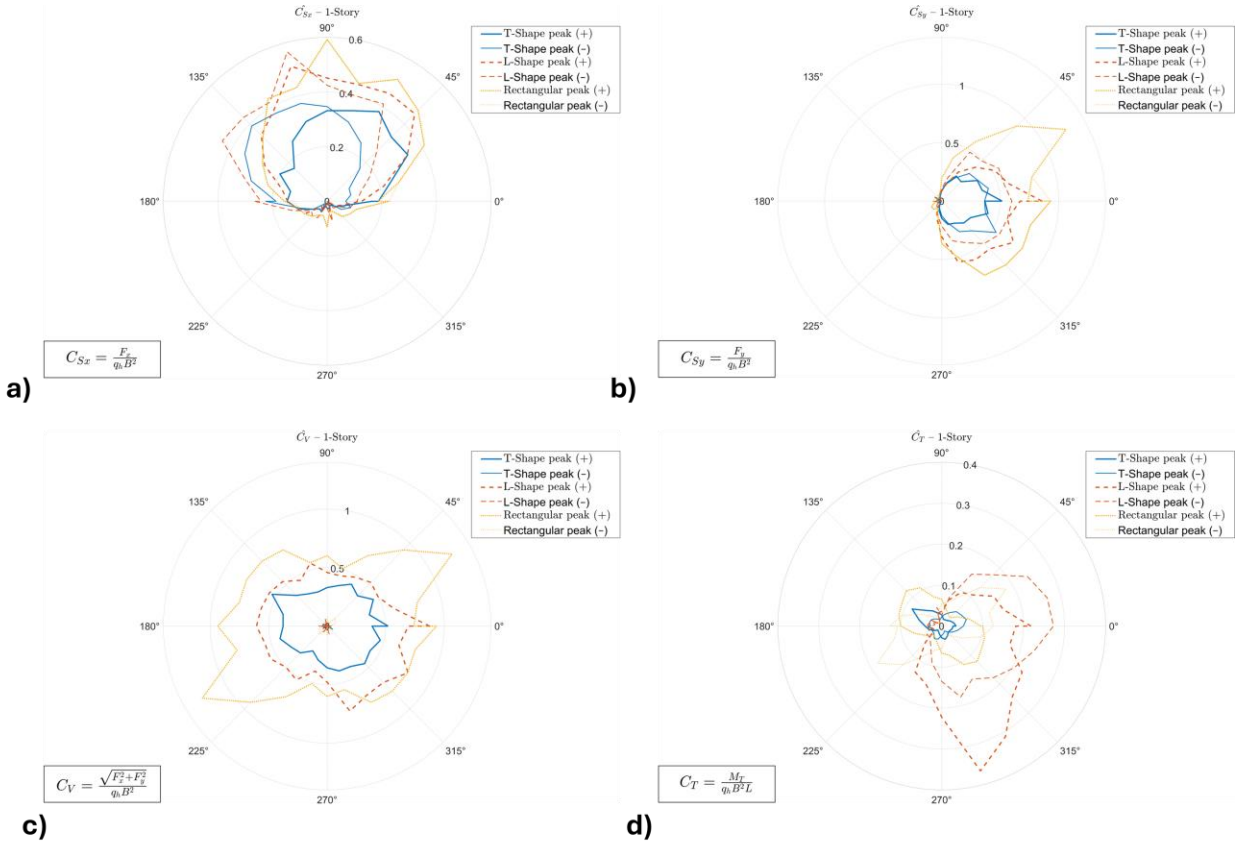

Figure 34. Directional peak coefficients for the 1-story buildings: (a) $\hat{C}_{Sx}$,(b) $\hat{C}_{Sy}$, (c) $\hat{C}_V$, and (d) $\hat{C}_T$.

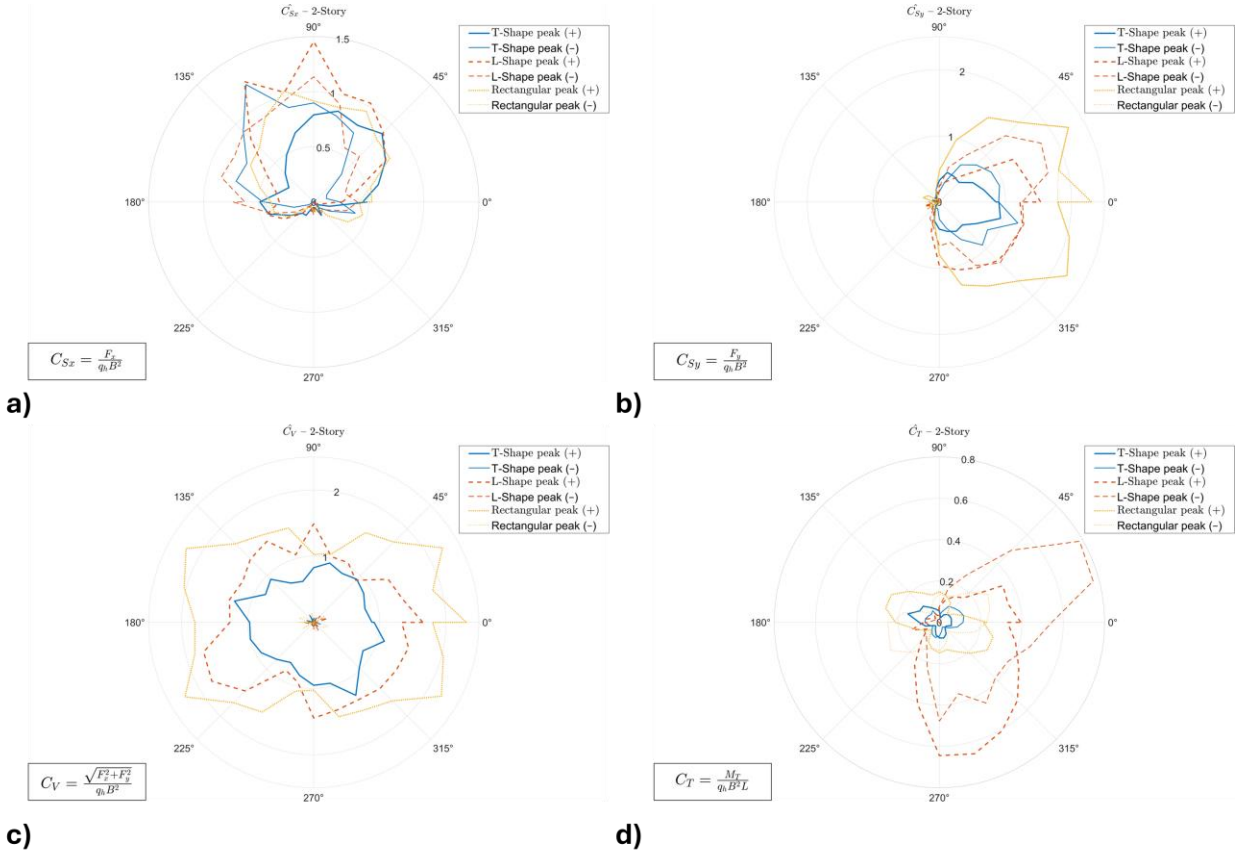

Figure 35. Directional peak coefficients for the 2-story buildings: (a) $\hat{C}_{Sx}$,(b) $\hat{C}_{Sy}$, (c) $\hat{C}_V$, and (d) $\hat{C}_T$.

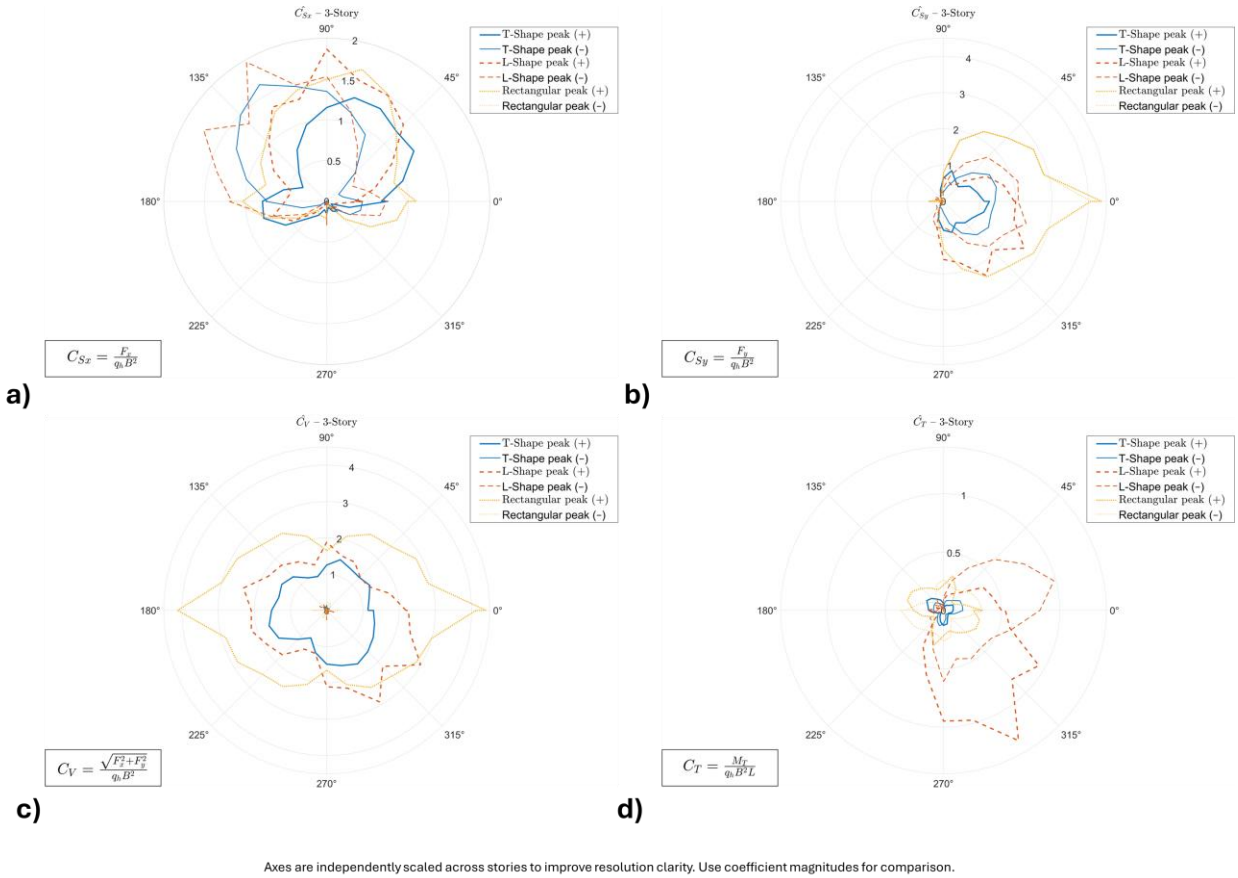

Figure 36. Directional peak coefficients for the 3-story buildings: (a) $\hat{C}_{Sx}$,(b) $\hat{C}_{Sy}$, (c) $\hat{C}_V$, and (d) $\hat{C}_T$.

5. DISCUSSION

5.1. Pressure (C_p) Coefficient Behavior

5.1.1. Influence of Plan Geometry

Irregular plans exhibited more severe mean suction than the rectangular configuration. At the 2-story level, the L-shaped building recorded $\bar{C}_p$ =−0.83 in critical wall zones, compared to $\bar{C}_p$ = −0.61 for the rectangular case—representing a 36% amplification. For the T-shaped configuration at 1 story, the mean suction along the upper roof edge was $\bar{C}_p$ = −0.71, compared to $\bar{C}_p$ = −0.59 in the rectangular model (20% increase). These results highlight the increased suction demands induced by re-entrant corners and asymmetric flow paths in irregular plans.

Plan geometry also influenced the peak values substantially. At 1 story, the L-shaped model reached $\check{C}_p$ = −3.75, whereas the rectangular configuration exhibited $\check{C}_p$ =−2.15, corresponding to

a 1.74× amplification. For the T-shaped building, the peak positive pressure coefficient was $\hat{C}_p$= +1.66, compared to $\hat{C}_p$ = +1.48 for the rectangular case, a 12% increase. The amplification effects were primarily concentrated near re-entrant corners and roof-wall intersections, where strong vortex generation and flow detachment were observed.

Matus (2024) reported similar trends for plan geometry at a fixed low-rise height. For L-shaped configurations, values of $\check{C}_p$ ranged from –2.8 to –3.2, and $\hat{C}_p \approx +1.5$. T-shaped buildings exhibited $\check{C}_p$ = –2.6 to –2.9 and $\hat{C}_p \approx +1.4$. For the rectangular benchmark, pressures remained within –2.1 to –2.3 (negative) and +1.4 to +1.5 (positive). The present rectangular results fall within this envelope, while the L- and T-shaped configurations exceed the previously reported extremes—likely due to finer spatial resolution, sharper re-entrant corners, and more detailed local capture using the 1:50 model scale. Nonetheless, the relative differences and directional trends are in strong agreement.

5.1.2. Effect of Building Height

Building height influenced mean pressures most notably for the irregular configurations. In the T-shaped model, suction along the roof edge increased from $\bar{C}_p$ =−0.71 at 1 story to $\bar{C}_p$= −0.98 at 3 stories—a 38% increase. For the L-shaped building, wall-zone mean pressures deepened similarly, whereas the rectangular model showed limited height sensitivity, with changes in $\bar{C}_p$ typically below 10%.

Additionally, building height had a pronounced effect on the peak pressure coefficients, particularly in irregular configurations. For the L-shaped model, the peak negative coefficient increased from $\check{C}_p$ = −3.75 at 1 story to $\check{C}_p$ =−4.26 at 3 stories, representing a 13.6% amplification. The corresponding positive peak also increased from $\hat{C}_p$ = +1.52 to $\hat{C}_p$ = +1.66, a 9.2% increase. Similarly, the T-shaped configuration exhibited an increase in $\hat{C}_p$ from +1.45 to +1.60 (10.3%) and in $\check{C}_p$ from –3.40 to –3.91 (15.0%). In contrast, the rectangular model showed limited height sensitivity: $\check{C}_p$ increased from –2.15 to –2.30 (7%), while $\hat{C}_p$ remained nearly unchanged, varying slightly from +1.48 to +1.50 (1.4%). These findings confirm that vertical exposure amplifies localized suctions and stagnation pressures more strongly in irregular geometries than in regular ones.

5.1.3. Height-Based Shape Disparity

In addition to the within-shape amplification discussed above, the disparity between irregular and regular configurations widened with increasing building height. At 1 story, the L-shaped model exhibited a peak negative pressure coefficient $\check{C}_p$ that was 1.74× greater than that of the rectangular model. At 3 stories, this ratio increased to 1.85×, indicating that the aerodynamic penalty associated with the L-shaped plan was not only preserved but intensified with height. A similar pattern was observed for the T-shaped configuration, where the amplification in $\check{C}_p$ relative to the rectangular model increased from 1.58× at 1 story (–3.40 vs. –2.15) to 1.70× at 3 stories (–3.91 vs. –2.30).

The same trend was evident in the positive peak pressures. At 1 story, the $\hat{C}_p$ ratio between the T-shaped and rectangular models was approximately 1.10× (+1.45 vs. +1.32), increasing to 1.13× at 3 stories (+1.60 vs. +1.42). Although the absolute differences in $\hat{C}_p$ were smaller than those in suction, the directional consistency reinforces the conclusion that plan irregularity has a compounding influence as building height increases.

This height-dependent divergence suggests a nonlinear interaction between flow structures induced by plan geometry and the vertical wind profile. At higher elevations, irregular configurations are more exposed to elevated turbulence intensities and shear layers, which exacerbate flow separation at re-entrant corners and create deeper suction zones. The combination of these effects result in pressure distributions that are not simply scaled versions of the 1-story case, but reflect amplified aerodynamic instability.

The implications for design are significant. Height not only increases pressure magnitude within a given shape but also widens the performance gap between regular and irregular plans. This highlights the importance of treating geometric irregularity as a dynamic rather than static design penalty, one that may become increasingly critical for taller low-rise buildings subjected to boundary layer wind profiles.

5.2. Shear and Torsional Force Coefficients

5.2.1. Influence of Geometry on Mean Shear and Torsional Coefficients

Plan geometry had a significant influence on the distribution and magnitude of wind-induced force coefficients. Compared to the rectangular baseline, both L-shaped and T-shaped

buildings exhibited amplified responses in the principal shear directions ($\bar{C}_{Sx}$, $\bar{C}_{Sy}$) and torsional moment ($\bar{C}_T$), with the degree of amplification strongly dependent on the orientation and asymmetry of the plan.

At 1 story, the L-shaped model exhibited a mean torsional coefficient $\bar{C}_T = 0.019$, which was 1.36× higher than the rectangular counterpart ($\bar{C}_T = 0.014$). The T-shaped model showed a comparable amplification, reaching $\bar{C}_T = 0.020$, a 1.43× increase. The influence on transverse shear ($\bar{C}_{Sy}$) was also notable: the L-shaped building showed a 28% increase relative to the rectangular configuration, while the T-shaped model displayed a 34% increase. These differences are attributed to the inherently asymmetric flow patterns around the protruding wings and re-entrant corners of the irregular plans, which enhance lateral pressure differentials and unbalanced moment generation.

These observations are consistent with the findings of Nguyen et al. (2018), who reported that torsional moment coefficients for L-shaped buildings exceeded those of rectangular buildings by up to 40% under oblique wind conditions. Similarly, Elsharawy et al. (2015) concluded that plan irregularity substantially increased the net torque on flat-roof buildings, with L-shaped cases producing higher torsional responses than both T-shaped and rectangular models. Their experimental results showed the highest torsional coefficients near 45° and 135°, matching the dominant oblique flow interaction zones, a directional trend also supported by the current findings.

The peak force coefficients followed similar trends but with even stronger shape dependence. The peak torsional coefficients $\check{C}_T$ for the L-shaped model at 1 story reached values as low as –0.054, compared to –0.039 for the rectangular model, reflecting a 38% amplification. Likewise, the peak positive values $\hat{C}_T$ showed a noticeable increase in the irregular plans, especially under oblique wind angles (see Figures 30–32). The largest torsional peaks were generally recorded between 30°–60° and 120°–150°, consistent with expected corner vortex shedding. These extremes further confirm the role of plan asymmetry in amplifying rotational imbalance.

A similar pattern emerged in the shear coefficients. The L-shaped model showed extreme peaks in $\check{C}_{Sy}$ and $\hat{C}_{Sy}$ that exceeded the rectangular baseline by over 35% under certain wind directions. These differences are clearly illustrated in the peak envelopes of Figures 21–26, where

the shaded bounds around the mean curves represent the directional maxima and minima. The envelope width was consistently larger in irregular plans, reinforcing that non-rectangular geometries not only shift the mean behavior but also widen the range of expected extreme responses.

In addition to torsion and shear, plan geometry also influenced the vertical force coefficient $\bar{C}_V$, particularly in the L-shaped configuration. At 1 story, the L-shaped model exhibited a $\bar{C}_V$ approximately 27% more negative than that of the rectangular configuration, indicating stronger uplift forces over re-entrant zones. Peak uplift values $\check{C}_V$ for the L-shaped model reached –1.29, compared to –1.00 for the rectangular building, a 29% increase. These patterns are attributed to localized suction effects induced by flow separation and downwash near internal corners, which intensify vertical pressure differentials. Comparable trends were observed by Elsharawy (2014) and Nguyen et al. (2018), who both noted that re-entrant geometries generate enhanced uplift loads due to disturbed flow reattachment and unbalanced roof pressures.

Beyond amplitude comparisons, the directional behavior of the force coefficients further illustrates the aerodynamic complexity introduced by plan irregularity. In the L-shaped 3-story configuration, for instance, the peak torsional coefficient C_T occurred at 225°, while the peak base shear C_V was observed at 45°, highlighting a clear misalignment between dominant torsional and translational load directions. This decoupling suggests that simplified co-directional assumptions may underestimate torsional effects when applied to irregular geometries. Furthermore, in extreme cases, torsional amplification reached nearly ten times the baseline rectangular values, underscoring the significant rotational vulnerability of asymmetric plans under oblique winds. These findings emphasize that shape-induced torsional amplification is not only substantial in magnitude but also highly sensitive to wind angle, particularly at elevated building heights.

Overall, the influence of plan geometry on force coefficients is both significant and multifaceted. The current results confirm that torsional, shear, and vertical responses, particularly $\bar{C}_T$, $\check{C}_T$, and $\check{C}_V$, are highly sensitive to shape asymmetry, and validate trends reported in prior experimental and analytical studies. These effects are not only observable in mean behavior but are even more pronounced in peak values, reinforcing the need to incorporate shape amplification factors in MWFRS-level wind load estimations.

5.2.2. Height Effects on Shear, Torsional, and Vertical Force Coefficients

Increasing building height had a consistent amplifying effect on wind-induced shear and torsional loads, with the degree of amplification varying by plan geometry. Across all configurations, mean torsional coefficients $\bar{C}_T$ increased with height, reflecting greater exposure to oblique flow and enhanced pressure differentials over taller walls.

For the L-shaped model, $\bar{C}_T$ rose from 0.019 at 1 story to 0.023 at 3 stories—an increase of 21%. The T-shaped configuration followed a nearly identical trend (0.020 to 0.024, 20%), while the rectangular case exhibited more modest growth (0.014 to 0.016, 14%). These observations suggest that irregular configurations, especially those with re-entrant corners and extended arms, are more sensitive to height-based amplification. Taller buildings present longer pressure lever arms and larger separated flow regions, particularly near asymmetric plan features.

Transverse shear coefficients $\bar{C}_{Sy}$ exhibited similar behavior. The L-shape showed a 17% increase in $\bar{C}_{Sy}$, and the T-shape grew by 19%, compared to only 8% for the rectangular configuration. Once again, plan irregularity magnifies the effect of height on wind loads, particularly in the lateral direction.

Amplification in vertical force coefficients $\bar{C}_V$ was also evident but less pronounced. In the L-shaped building, $\bar{C}_V$ became more negative, shifting from –0.62 to –0.69 (11%), while the rectangular model increased only slightly in magnitude (–0.49 to –0.52, 6%). The added height intensifies flow separation and suction at re-entrant zones, though these effects are somewhat constrained in regular geometries.

Peak force coefficients showed even stronger height dependence. Peak negative torsion $\check{C}_T$ for the L-shaped model increased from –0.054 to –0.064 (18.5%), while the rectangular case grew from –0.039 to –0.044 (12.8%). Directional peaks in torsion ($\hat{C}_T$) followed the same trend, with taller irregular shapes consistently producing higher peak loads due to more persistent asymmetric pressure fields.

In transverse shear, the L-shaped model saw $\check{C}_{Sy}$ grow from –0.126 to –0.145 (15.1%), with the T-shape showing a comparable increase (~17%). The rectangular building, by contrast, changed by less than 8% over the same height range. These results again reinforce the observation that height amplifies shape sensitivity, particularly in lateral load paths.

Vertical peak loads followed a similar pattern. Peak uplift coefficients $\check{C}_V$ for the L-shape increased from –1.29 to –1.41 (9.3%), with the T-shape showing a similar magnitude of increase. The rectangular model, however, changed only slightly (–1.00 to –1.05), suggesting that the contribution of height to vertical force amplification is largely dependent on plan irregularity.

In addition to magnitude increases, building height also influenced the directional sensitivity of wind-induced forces. For all shapes (but especially the L-shaped configuration) the wind directions producing peak torsion (C_T) did not align with those producing peak base shear (C_V), and this misalignment became more pronounced at higher elevations. For example, at 3-story height, the L-shape exhibited its maximum torsional response at 225°, while the peak base shear occurred around 45°, reflecting distinct aerodynamic mechanisms governing rotation and translation. This divergence suggests that taller buildings with irregular plans not only amplify wind loads but also experience more complex directional dependencies, further underscoring the limitations of simplified design approaches that assume co-directionality of force components.

These findings are in agreement with prior studies. Nguyen et al. (2018) and Elsharawy et al. (2015) reported that medium-rise buildings tend to experience amplified torsion and shear as height increases, especially in buildings with asymmetric plans. In both studies, peak loads shifted toward oblique wind directions with height, a pattern also observed in the present data. Overall, height increases both the magnitude of wind-induced forces and the disparity between regular and irregular plans, with irregular shapes exhibiting greater amplification in all components, especially torsion. While vertical uplift also increases with height, its rate of amplification remains more subdued compared to torsional and lateral effects.

5.2.3. Cross-Configuration Disparity with Height

Beyond the individual effects of geometry and height, it is instructive to examine how the disparity between plan configurations evolves as buildings become taller. At 1 story, the L- and T-shaped models exhibited substantially higher values of mean torsional coefficients $\bar{C}_T$ than the rectangular baseline—by 36% and 43%, respectively. At 3 stories, this disparity widened slightly: the L-shaped building exceeded the rectangular by 44%, and the T-shaped by 50%. This incremental divergence suggests that the amplification effect of height acts more strongly on

irregular plans, possibly due to enhanced interaction between oblique wind directions and asymmetric plan features over longer façade extents.

A similar pattern emerged in shear. Mean transverse shear coefficients $\bar{C}_{Sy}$ in L- and T-shaped models were 28% and 34% higher than rectangular at 1 story, but this difference expanded to 35% and 39% at 3 stories. The rectangular model, by contrast, displayed more limited sensitivity to height, with relatively modest increases across all force components. These trends reinforce that building height not only amplifies individual responses but also amplifies the disparity between plan shapes, especially for lateral loading paths.

For torsional peaks, the differences were more pronounced. At 1 story, the peak negative torsional coefficient $\check{C}_T$ for the L-shaped model was 38% more severe than the rectangular counterpart. At 3 stories, this grew to 45%, with a similar escalation observed in $\hat{C}_T$ values. The T-shaped building exhibited nearly identical height-driven disparity amplification. These increases are consistent with the larger vortex imbalance and cross-plan pressure differentials induced by height in irregular configurations.

Vertical load disparities also followed this trend, albeit to a lesser extent. At 1 story, $\check{C}_V$ in the L-shaped model was 29% more negative than in the rectangular case; at 3 stories, the difference increased slightly to 34%. The directional amplification remained dominant near re-entrant corners and extended wings, where suction effects become more energetic with height.

Taken together, these results show that the gap between regular and irregular plans is not constant but expands with height. Irregular configurations, already more sensitive to oblique flows and asymmetric vortex generation, become increasingly susceptible to torsional and lateral amplification in taller forms. This height-shape interaction underscores the necessity of jointly evaluating geometry and elevation in MWFRS design, rather than treating them as independent modifiers.

6. SUMMARY AND CONCLUSIONS

This study examined the influence of plan geometry and building height on wind-induced loads—specifically shear, torsional, and vertical forces—acting on low-rise buildings. A series of wind tunnel tests were conducted on three plan configurations (rectangular, L-shaped, and T-

shaped), across three building heights (1-, 2-, and 3-story), under boundary layer flow representative of open terrain. The resulting data were used to derive mean and peak force coefficients, identify directional trends, and evaluate amplification effects tied to geometry and height. Below is a consolidated summary of the main findings:

➢ **Key Conclusions**

- **Plan geometry has a pronounced effect** on both the magnitude and variability of wind-induced forces:
    - Irregular shapes (L and T) exhibited consistently higher torsional and lateral shear coefficients than the rectangular baseline.
    - At 1 story, torsional coefficients $\bar{C}_T$ in L- and T-shaped buildings exceeded those of rectangular buildings by ~36–43%. Peak torsional loads $\check{C}_T$, $\hat{C}_T$ showed even larger disparities.
    - Vertical uplift $\check{C}_V$ was more negative in irregular plans, especially near re-entrant corners, with up to 29% higher suction than the rectangular case.
- **Building height amplifies wind loads,** especially in irregular buildings:
    - As height increased from 1 to 3 stories, all force components—torsion, shear, and vertical—also increased.
    - Height-based amplification was strongest in torsion and shear. For instance, mean $\bar{C}_T$ increased by over 20% in irregular models, compared to only 14% in the rectangular one.
    - Peak coefficients followed a similar pattern, with amplification more pronounced in L and T shapes due to greater exposure to oblique flow and enhanced vortex generation.
- **The disparity between regular and irregular shapes grows with height:**
    - Not only do irregular buildings experience higher forces, but the gap between them and rectangular buildings becomes more significant as height increases.
    - For example, the torsional disparity ($\check{C}_T$, $\hat{C}_T$) between L and rectangular plans grew from 38% at 1 story to 45% at 3 stories.
- **Directional effects matter:**

- The largest force coefficients were typically observed under oblique (quartering) wind angles centered on 45°, 135°, 225°, and 315° for irregular plans; rectangular peaks remain near principal axes, confirming the role of asymmetry and corner vortex interactions in governing peak responses.
- Peak shear and torsion values were most sensitive in these ranges, suggesting that structural systems should be especially robust for winds approaching at diagonal angles.

7. BENEFITS THE STATE OF FLORIDA AND PRACTICAL APPLICATIONS:

This study advances the understanding of torsional wind effects on non-rectangular low-rise buildings, addressing a critical gap in current design practices for hurricane-prone regions like Florida. Irregular plan geometries, specifically L- and T-shaped configurations, exhibited significantly elevated torsional responses compared to rectangular baselines, with amplification increasing systematically with building height. These findings are especially relevant to ASCE 7—the primary wind load standard referenced in the Florida Building Code—which currently lacks explicit provisions for torsional loads in irregular low-rise structures. Future incorporation of experimentally derived torsion amplification factors into ASCE 7 or Florida-specific amendments could improve the accuracy and safety of wind design for such buildings.

The integration of high-resolution pressure measurements (Cp) into the global load analysis allowed for a more complete characterization of how asymmetric pressure distributions, particularly near re-entrant corners and wall projections, contribute to torsional moment development. While pressure coefficient results were not the primary focus, they provided critical insight into the spatial origins of load asymmetry and supported the identification of torsion-critical regions.

For Florida, where irregular building footprints are increasingly common in public, residential, and mixed-use developments, these results offer practical guidance to structural engineers, building designers, and code officials for improving the wind performance of essential infrastructure. The findings support the refinement of load paths, diaphragm design, and anchorage detailing in torsion-sensitive regions of the building, and underscore the importance of directional analysis under oblique wind angles.

By establishing experimentally grounded amplification factors and directional trends, this study supports more resilient, torsion-aware design practices that align with Florida's efforts to reduce hurricane risk and extend infrastructure life. These practices can improve the structural reliability of essential buildings, helping minimize wind-related damage and enabling faster recovery after major storms. The findings will be shared through peer-reviewed publications, technical presentations, and engagement with structural engineers and code development committees, with the goal of informing future design standards and practical guidance.

ACKNOWLEDGMENT

The authors gratefully acknowledge the financial support provided by the Florida Division of Emergency Management (FDEM). The experimental work was conducted at the NSF NHERI Wall of Wind Experimental Facility (WOW EF) at Florida International University, whose technical capabilities and staff expertise were essential to the success of this study. Special thanks are extended to the WOW operations team for their assistance throughout the testing campaign. The views expressed herein are those of the authors and do not necessarily reflect those of the funding agency or affiliated institutions.

Refences

Abdallah, M., & Zisis, I. (2025a). Investigating the Influence of PV Panel Sizes on Wind-Induced Loads. *Structures Congress*, 403–412. https://doi.org/10.1061/9780784486085.036

Abdallah, M., & Zisis, I. (2025b). Wind-induced loads on photovoltaic (PV) panels on low-sloped gable roofs: Panel size effects. *Journal of Wind Engineering and Industrial Aerodynamics*, *263*, 106129. https://doi.org/10.1016/j.jweia.2025.106129

ASCE 7. (2022). *Minimum Design Loads and Associated Criteria for Buildings and Other Structures*. American Society of Civil Engineers. https://doi.org/10.1061/9780784415788

Elsharawy, M., Galal, K., & Stathopoulos, T. (2015). Torsional and shear wind loads on flat-roofed buildings. *Engineering Structures*, *84*, 313–324. https://doi.org/10.1016/j.engstruct.2014.11.028

Elsharawy, M. R. (2014). *Wind-Induced Torsional Loads on Low- and Medium-Rise Buildings* [Thesis (PhD), Concordia University]. https://spectrum.library.concordia.ca/id/eprint/978514/1/elsharawy_PhD_S2014.pdf

Elsharawy, M., Stathopoulos, T., & Galal, K. (2012). Wind-induced torsional loads on low buildings. *Journal of Wind Engineering and Industrial Aerodynamics*, *104–106*, 40–48. https://doi.org/10.1016/j.jweia.2012.03.011

Gan Chowdhury, A., Zisis, I., Irwin, P., Bitsuamlak, G., Pinelli, J.-P., Hajra, B., & Moravej, M. (2017). Large-Scale Experimentation Using the 12-Fan Wall of Wind to Assess and Mitigate Hurricane Wind and Rain Impacts on Buildings and Infrastructure Systems. *Journal of Structural Engineering*, *143*(7), 04017053. https://doi.org/10.1061/(ASCE)ST.1943-541X.0001785

Gierson, M. L., Phillips, B. M., Duthinh, D., & Ayyub, B. M. (2017). Wind-Pressure Coefficients on Low-Rise Building Enclosures Using Modern Wind-Tunnel Data and Voronoi Diagrams. *ASCE-ASME Journal of Risk and Uncertainty in Engineering Systems, Part A: Civil Engineering*, *3*(4), 04017010. https://doi.org/10.1061/AJRUA6.0000915

Isyumov, N., & Case, P. C. (2000). Wind-Induced Torsional Loads and Responses of Buildings. *Advanced Technology in Structural Engineering*, 1–8. https://doi.org/10.1061/40492(2000)83

Isyumov, N., & Poole, M. (1983). WIND INDUCED TORQUE OM SQUARE AND RECTANGULARBUILDING SHAPES. *Journal of Wind Engineering and Industrial Aerodynamics*, *13*, 183–196. https://doi.org/10.1016/0167-6105(83)90140-X

Matus, M., & Zisis, I. (In Press). Wind-induced Pressure Distribution on Non-rectangular Shaped Low-rise Buildings. *ASCE Journal of Structural Engineering*.

Nguyen, T. S., Stathopoulos, T., & Tirca, L. (2018). Wind-induced shear and torsion in low-rise and medium-rise buildings: Provisions of National Building Code of Canada 2015. *Canadian Journal of Civil Engineering*, *45*(5), 339–350. https://doi.org/10.1139/cjce-2017-0107

Sarma, H., Matus, M., Lee, S. J., & Zisis, I. (In Press). Influence of Building Shape-factor on Wind Loads for Non-Rectangular Low-Rise Structures. *Journal of Wind Engineering and Industrial Aerodynamics*.

Sarma, H., Zisis, I., & Matus, M. (2023). Effect of roof shape on wind vulnerability of roof sheathing panels. *Structural Safety*, *100*, 102283. https://doi.org/10.1016/j.strusafe.2022.102283

Shao, S., Stathopoulos, T., Yang, Q., & Tian, Y. (2018). Wind Pressures on 4:12-Sloped Hip Roofs of L- and T-Shaped Low-Rise Buildings. *Journal of Structural Engineering*, *144*(7), 04018088. https://doi.org/10.1061/(ASCE)ST.1943-541X.0002077

Shao, S., Tian, Y., Yang, Q., & Stathopoulos, T. (2019). Wind-induced cladding and structural loads on low-rise buildings with 4:12-sloped hip roofs. *Journal of Wind Engineering and Industrial Aerodynamics*, *193*, 103948. https://doi.org/10.1016/j.jweia.2019.103948

Simiu, E., & Yeo, D. (2019). *Wind Effects on Structures: Modern Structural Design for Wind* (1st ed.). Wiley. https://doi.org/10.1002/9781119375890

Stathopoulos, T., Xypnitou, E., & Zisis, I. (2013). Wind Loads on Solar Collectors and PV Panels on Roofs. *Structures Congress 2013*, 1545–1554. https://doi.org/10.1061/9780784412848.136

Tallin, A., & Ellingwood, B. (1985). Analysis of torsional moments on tall buildings. *Journal of Wind Engineering and Industrial Aerodynamics*, *18*(2), 191–195. https://doi.org/10.1016/0167-6105(85)90097-2

Tamura, Y., Kikuchi, H., & Hibi, K. (2001). Extreme wind pressure distributions on low-rise building models. *Journal of Wind Engineering and Industrial Aerodynamics*, *89*(14–15), 1635–1646. https://doi.org/10.1016/S0167-6105(01)00153-2

Tamura, Y., Kikuchi, H., & Hibi, K. (2003). Quasi-static wind load combinations for low- and middle-rise buildings. *Journal of Wind Engineering and Industrial Aerodynamics*, *91*(12–15), 1613–1625. https://doi.org/10.1016/j.jweia.2003.09.020

Voronoi, G. (1908). New applications of continuous parameters to the theory of quadratic forms. *Journal of Pure and Applied Mathematics*, *133*(133), 97–178. https://doi.org/10.1515/crll.1908.133.97

Xie, J., & Irwin, P. A. (2000). Key Factors for Torsional Wind Response of Tall Buildings. *Advanced Technology in Structural Engineering*, 1–9. https://doi.org/10.1061/40492(2000)86

FIU International Hurricane Research Center
FLORIDA INTERNATIONAL UNIVERSITY

A Resource for the State of Florida

SECTION 5:

Education and Outreach Programs to Convey the Benefits of Various Hurricane Loss Mitigation Devices and Techniques

A Report Submitted to:
The State of Florida Division of Emergency Management

Prepared By:
Erik Salna

July 31, 2025

Executive Summary:

The FIU International Hurricane Research Center developed and coordinated education and outreach activities to build on the foundation of previous work under this grant and showcased the hurricane-loss mitigation objectives of the RCMP.

For the 2024-2025 performance period, the below mentioned educational partnerships, community events, and outreach programs were developed:

Wall of Wind Mitigation Challenge (WOW! Challenge): March 20th, 2025
The International Hurricane Research Center (IHRC), located on the campus of Florida International University (FIU), has developed the Wall of Wind Mitigation Challenge (WOW! Challenge), a judged competition for South Florida high school students. As the next generation of engineers to address natural hazards and extreme weather, this STEM education event features a competition between high school teams to develop innovative wind mitigation concepts and real-life human safety and property protection solutions. The mitigation concepts are tested live at the FIU NSF-NHERI Wall of Wind (WOW) Experimental Facility (EF), located on FIU's Engineering Campus.

- The objective of the 2025 Wall of Wind Mitigation Challenge was for student teams to design a way to reduce the impact of wind scouring on a building's flat roof. Each team's task was to develop a mitigation solution that would improve the flat roof's aerodynamic performance to prevent pea gravel on the roof from being blown away by up-to-hurricane-force winds.
- The flat roof models were wind tested by the NSF-NHERI Wall of Wind experimental research facility at FIU to evaluate their performance.
- The high school teams prepared three components for the competition: a physical test, an oral presentation, and a written technical paper.
- The competition involved teams from nine South Florida high schools, including 135 students and nine teachers.
- *First Place* was awarded to TERRA Environmental Research Institute.
  Second Place was awarded to Florida Christian School.
  Third Place was awarded to South Miami Senior High School.
- A complete scoring summary can be found on the following link:
  2025_CHALLENG_FINAL_SCORES.pdf

Special Guests:

- Jeanette M. Nuñez, President, Florida International University
- Kevin Guthrie, Director, Florida Division of Emergency Management
- Jillian Holzman, HLMP Program Manager, Bureau of Mitigation, Florida Division of Emergency Management

Media exposure resulted in great positive visibility for the IHRC, FIU and FDEM's message of mitigation:

- 2025 WOW Challenge Highlights Video:
  https://youtu.be/aGM7zTjtwm0?si=gN0f_W2Ep3T5bbYB
- THE BULLETIN, FDEM Mitigation Bureau, June 2025: Bulletin Volume 15 Issue 2

- CBS4-Miami: https://www.ihrc.fiu.edu/media/latest-media-coverage/cbs4-miami-fiu-wall-of-wind-challenge/

NOAA Hurricane Awareness Tour, Sarasota/Bradenton Airport: May 9th, 2025 (Cancelled)
The entire 2025 Hurricane Hunter Awareness Tour was cancelled.

Eye of the Storm (Science, Mitigation & Preparedness) Event: May 31st, 2025
The Museum of Discovery & Science (MODS), located in Fort Lauderdale, FL, assisted the IHRC in planning, coordinating, and facilitating this free admission public education event that showcased special hands-on, interactive activities and demonstrations teaching hurricane science, mitigation and preparedness.

- 6,105 visitors attended Eye of the Storm, showcasing special interactive activities and demonstrations teaching hurricane science, mitigation and preparedness.
- A Participant Post Survey showed 79.5% of respondents increased their knowledge about wind engineering and mitigating hurricane damage and 89.2% will be taking steps to mitigate hurricane damage.
- Event Flyer: 2025 Eye of the Storm – Hurricane (Science, Mitigation & Preparedness) Free Museum Event, Saturday, May 31st, 10am to 5pm | IHRC Website

Special FDEM Guests:

- Kevin Guthrie, Director, Florida Division of Emergency Management
- Jillian Holzman, HLMP Program Manager, Bureau of Mitigation, Florida Division of Emergency Management

FDEM Press Conference at Eye of the Storm: 20250531 Florida Division of Emergency Management Hosts Press Conference at the Eye of the Storm Event, Highlighting Hurricane Preparedness | Florida Disaster

FDEM Press Conference at Eye of the Storm Video:
https://youtu.be/Q3QpZFB8B3c?si=S0A4z7OSBVDjYCPX

Media exposure resulted in great positive visibility in the community for the IHRC, FIU and FDEM's message of mitigation.

- https://wsvn.com/news/local/broward/eye-of-the-storm-event-at-mods-in-fort-lauderdale-aims-to-ensure-floridians-are-hurricane-ready/#google_vignette
- https://www.news4jax.com/news/local/2025/05/31/fdem-hosts-press-conference-urges-floridians-to-make-final-preps-for-hurricane-season/
- https://app.criticalmention.com/app/#clip/view/022a8609-37e0-4245-acc2-5173459dc314?token=0e57270d-1c85-448e-b3ca-0788817604d7

Education and Outreach Programs:

Wall of Wind Mitigation Challenge (WOW! Challenge): March 20th, 2025

Overview of Wall of Wind Mitigation Challenge:

The WOW! Challenge requires problem solving, teamwork, and creativity, and it includes aspects of science, technology, engineering, mathematics, architectural design, and business entrepreneurship. The high school students are inspired to pursue STEM education and careers in wind engineering and hurricane mitigation. The competition has real world applications and benefits society by developing hurricane mitigation techniques that can lead to enhanced human safety, property loss reduction, insurance cost reduction, and a culture of hurricane preparedness. There is no other competition like it in the entire country, and it's a once in a lifetime opportunity for the high school students – *an experience they never forget*.

"The WOW! Challenge is a platform to educate high school students in our community with regards to hurricane engineering and community resilience. Student teams are given real-world wind engineering problems, and they conceive and validate wind mitigation concepts to solve such problems. The WOW! Challenge informs students about the importance of mitigation and community resilience to prepare them as future leaders in disaster mitigation. We see these young students become motivated toward STEM careers and possibly enrolling at FIU with the dream of performing research at our national NSF-NHERI Wall of Wind Experimental Facility."
Arindam Gan Chowdhury, professor of civil and environmental engineering and director of the NHERI Wall of Wind Experimental Facility.

<u>2025 Wall of Wind Mitigation Challenge:</u>
The objective of the 2025 Wall of Wind Mitigation Challenge was for student teams to design a way to reduce the impact of wind scouring on a building's flat roof (see Figure 1). Each team's task was to develop a mitigation solution that will improve the flat roof's aerodynamic performance to prevent pea gravel on the roof from being blown away by up-to-hurricane-force winds. The mitigation solutions were tested by the NSF-NHERI Wall of Wind in a controlled wind field to evaluate the effectiveness of the flat roof mitigation solutions.

Special Guests:

- Jeanette M. Nuñez, President, Florida International University
- Kevin Guthrie, Executive Director, Florida Division of Emergency Management
- Jillian Holzman, HLMP Program Manager, Bureau of Mitigation, Florida Division of Emergency Management

"In the face of nature's most damaging winds, innovation becomes our strongest protection," said Executive Director Kevin Guthrie. "The Wall of Wind Mitigation Challenge is where science, innovation and preparation come together to build a stronger, smarter and more resilient Florida. Hurricanes don't wait — and neither should we."
Kevin Guthrie, Executive Director, Florida Division of Emergency Management

Wall of Wind Mitigation Challenge media exposure resulted in great positive visibility for the IHRC, FIU and FDEM's message of mitigation:

- 2025 WOW Challenge Highlights Video: https://youtu.be/aGM7zTjtwm0?si=gN0f_W2Ep3T5bbYB
- THE BULLETIN, FDEM Mitigation Bureau, June 2025: Bulletin Volume 15 Issue 2
- CBS4-Miami: https://www.ihrc.fiu.edu/media/latest-media-coverage/cbs4-miami-fiu-wall-of-wind-challenge/

Teams from nine South Florida high schools participated in the competition involving over 135 students and nine teachers. They were from School for Advanced Studies-West Campus, Miramar High School, Florida Christian School, Booker T. Washington Senior High School, Christopher Columbus High School, South Miami Senior High School, MAST Academy, Miami Carol City Senior High School, and TERRA Environmental Research Institute.

Student teams prepared three components for the competition: a written technical paper, an oral presentation, and a physical test of their wind mitigation barrier model. All the details of the rules and guidelines for the three required components are on the WOW Mitigation Challenge web page located at: http://www.ihrc.fiu.edu/outreach-education/wall-of-wind-challenge/.

Written technical papers and oral presentations had to include the following:

- Effectively communicate some scientific processes or analysis and include any scientific or mathematical analysis involved with the development of their flat roof mitigation solution.
- What is wind mitigation?
- What is the importance of wind mitigation?
- How is wind mitigation being addressed with your flat roof mitigation solution?
- In addition to wind engineering, other disciplines could be included, such as architecture, business, economics, finance, marketing, geosciences, insurance, political science, sociology, and urban planning.
- Details for the written technical paper guidelines can be found at: https://www.ihrc.fiu.edu/wp-content/uploads/2025/03/2025_WOW_CHALLENGE_RESEARCH_PAPER_GUIDELINES.pdf

The Oral Presentation Description:

- Oral presentations were done live at FIU to a panel of judges who then computed a score for the Team.
- Oral presentations could not exceed 7 minutes and were strictly enforced.
- Judges had some follow-up questions for each high school team after their oral presentation.
- Details for the oral presentation guidelines can be found at: https://www.ihrc.fiu.edu/wp-content/uploads/2025/03/2025_WOW_CHALLENGE_ORAL_GUIDELINES.pdf

The Physical Test Description:

- Each high school team designed and constructed a flat roof mitigation solution, and it was tested by the NSF-NHERI Wall of Wind (see Figure 1).
- Each team's task was to develop a mitigation solution that would improve the flat roof's aerodynamic performance to prevent pea gravel on the roof from being blown away by up-to-hurricane-force winds (see Figure 2).
- Teams were provided with the top portion of the cube 36 x 36 x 6 inches (L x W x H), which represented the flat roof, on which they attached their mitigation system (see Figure 3).

- The mitigation system was restricted to the area shaded in red in Figure 4, which extends up to 6 inches above the roof surface; up to 1 inch inward from the roof edge; up to 2 inches outward from the wall; and up to 4 inches downward from the roof surface along the outer wall.
- In the 3-inch x 6-inch area shaded in red in Figure 4, the mitigation system had to be 50% porous or greater at all locations, including the corners. Porosity was visually inspected by the Judges and had to meet the 50% or greater porosity requirement within any given 3-inch x 3-inch section. Examples of valid and invalid porosity are shown in Figure 5.
- A proof of 50% porosity was also required in the Appendix of the team's written technical paper.
- The physical wind tests occurred on a uniform cube 36 x 36 x 36 inches (L x W x H) at the NSF-NHERI Wall of Wind. These cubes represented a building with a flat roof (see Figure 6). Pea gravel was applied on top of the flat roof.
- All flat roofs were tested with a 45° wind angle of incidence during the wind test.
- Prior to the wind testing, Judges inspected the flat roof and mitigation system to verify that the design followed the requirements and restrictions.
- Scoring for the wind test reflected the ability of the mitigation system to mitigate scouring on the flat roof by measuring the scoured area.
- Judged parameters also included the following: Fit & Finish, Innovation, and Practicality.
- Teams were able to watch the wind tests from the WOW Operations & Control Center.
- The number of small blocks that were blown over were counted by FIU.
- Each flat roof was tested by a predefined wind speed profile. The same profile was used for all the flat roofs.
- Details for the physical test guidelines can be found at: https://www.ihrc.fiu.edu/wp-content/uploads/2025/03/2025_CHALLENGE_PHYSICAL_GUIDLINES.pdf

***Figure 1**. The NSF-NHERI Wall of Wind at FIU.*

***Figure 2**. Example of scouring caused by wind on a flat roof.*

***Figure 3**. Flat roof test specimen that was provided to each team.*

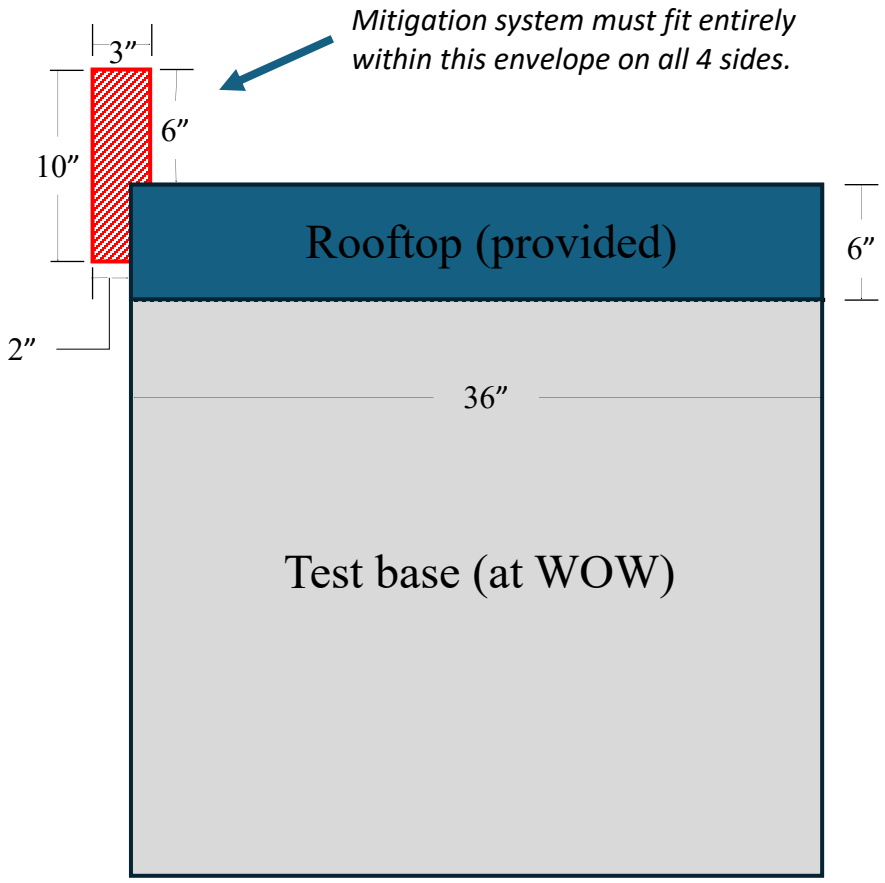

Figure 4. Design envelope for the flat roof mitigation solution (side view).

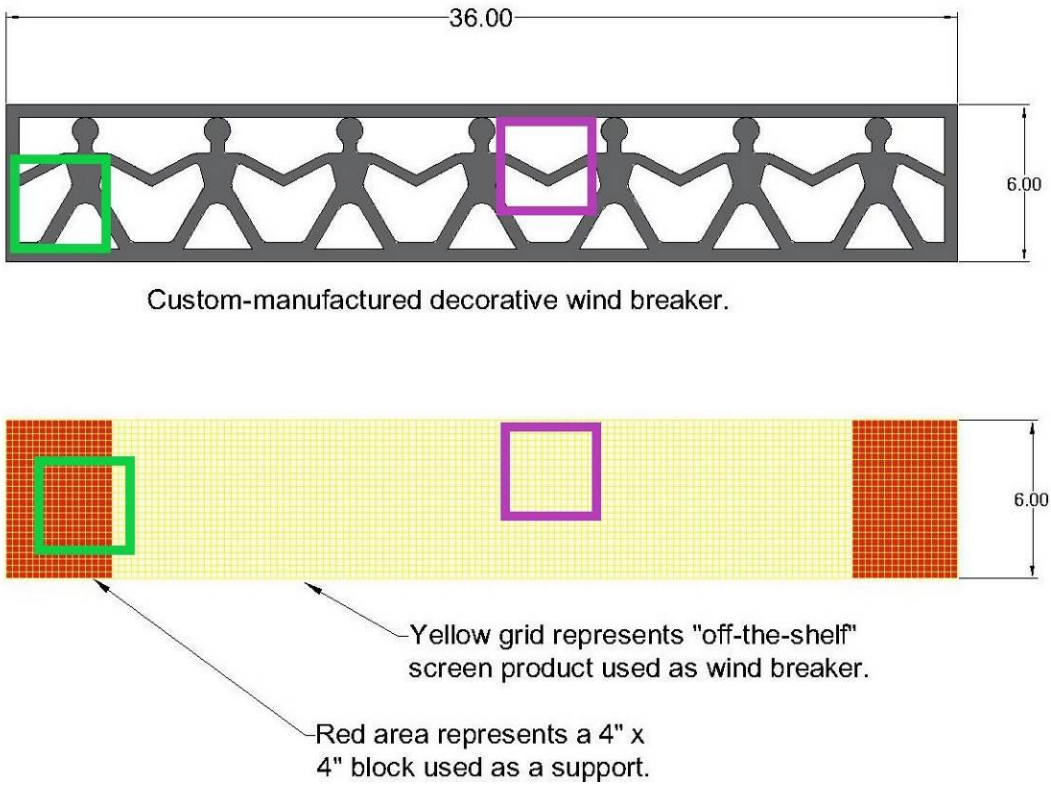

Figure 5. *Examples of porosity. The top image shows at least 50% porosity in both squares. In the bottom image, the purple square shows 50% porosity, but the green square shows less than 50% porosity, as the screen is blocked by the solid support.*

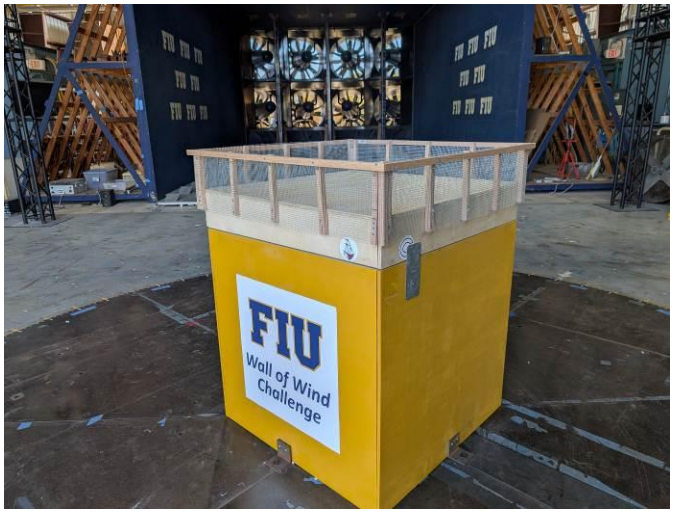

Figure 6*. The flat roof was wind tested on a uniform cube 36 x 36 x 36 inches (L x W x H) at the NSF-NHERI Wall of Wind. These cubes represented a building with a flat roof.*

There was a cumulative and weighted scoring point scale for the written technical paper (25%), oral presentation (25%), and physical test of the roof model (50%) to determine the top three winning teams:

- *First Place* was awarded to TERRA Environmental Research Institute.
- *Second Place* was awarded to Florida Christian School.
- *Third Place* was awarded to South Miami Senior High School.

A complete scoring summary can be found on the following link: https://www.ihrc.fiu.edu/wp-content/uploads/2025/05/2025_CHALLENG_FINAL_SCORES.pdf

All three required components of the competition were judged and scored by a combination of IHRC NSF-NHERI Wall of Wind faculty, Florida Division of Emergency Management, FIU wind engineering alumni, local emergency management, community educators, partners, and media:

- Jillian Holzman, HLMP Program Manager, Bureau of Mitigation, Florida Division of Emergency Management
- Dana McGeehan, Region 10 Recovery/Mitigation Coordinator, Florida Division of Emergency Management
- Maggie Steenburg, MPS, Assistant Director, Miami-Dade County Emergency Management
- Annette Flores, MPH, Assistant Director, Department of Emergency Management, Florida International University
- Amal Elawady, PhD, Associate Professor, Department of Civil & Environmental Engineering, College of Engineering and Computing, Lab. Wind Engineering Research, Extreme Events Institute, Florida International University
- Ioannis Zisis, PhD., F.SEI, Associate Professor, Dept. of Civil & Environ. Engineering PI and Site Director, NSF IUCRC for Wind Hazard and Infrastructure Performance (WHIP), Co-Director, Lab. Wind Engineering Research, Extreme Events Institute, Florida International University
- Steven W. Diaz, PhD, PE, Program Director/Site Operations Manager, NSF-NHERI Wall of Wind Experimental Facility, International Hurricane Research Center, Extreme Events Institute, Florida International University
- Dejiang Chen, Ph.D., Research Specialist, NSF-NHERI Wall of Wind Experimental Facility, International Hurricane Research Center, Extreme Events Institute, Florida International University
- Ziad Azzi (FIU Alum), PhD, PE, Principal Forensic Engineer, DDA Forensics
- Francis J. Bain (FIU Alum), PE, FDOT Approved Specialty Engineer, Specialty Engineering / Bridge Construction Manager, EAC Consulting, Inc.
- Carlos E. Melchor (FIU Alum), PE, Melchor Consultation Services, LLC
- David E. Milton (FIU Alum), Director of Operations, TelaClaims
- Brett Dexter, PE, Vice President of Engineering, Quick Tie Products, Inc.
- Carlos de la Camara, Director, Science Curriculum Support Specialist, HS, Department of Mathematics and Science, Miami-Dade County Public Schools
- JP Keener, Science Department, Broward County Schools
- Ana Torres-Vazquez, Meteorologist, NOAA/National Weather Service, Miami-South Florida WFO

- Brandy Campbell, Multimedia Journalist - Miami Based, FOX Weather National Network
- Dave Warren, CBS 4 Meteorologist
- Anthony Duarte, Meteorologist, Weather Producer, Univision

Evaluation and Assessment:

- Teachers rated all aspects of the WOW Challenge – materials, communication, training, feedback and educational value - from 'good' to 'excellent'. Six teachers said that the challenge greatly exceeded their expectations.
- All teachers said that the WOW Challenge contributed to an overall increase in knowledge of wind engineering, with seven teachers reporting a significant increase in knowledge.
- All teachers said students reported that they would 'definitely' study wind engineering in college.

Teacher Testimonials:

- *"I truly appreciate how this challenge initiates critical thinking, allows students to practice public speaking skills, professionalism, research, and construction of an idea agreed upon with peers."*
- *"An incredible opportunity to participate in something beyond the classroom. As this was not the norm for a classroom environment, there was a lot more interest by the students who participated."*
- *"The testimonies from my students showed how much they loved the WOW Challenge."*
- *"Those that attended the competition, came away with a much better idea of what engineering entails and realized that they have the capability to do it if they so choose. I can't wait to see how they grow their STEM knowledge next year."*
- *"The ability to be able to take the lessons learned in the classroom and apply them to real world situations is priceless. Nothing piques the curiosity of students more than being able to see the results for themselves."*

Student Testimonials:

- *"It was a very fun and great learning experience. It allowed me to get an insight into the civil engineering career which is what I will be majoring in college. I wish more schools would participate in such a fun project."*
- *"Engineering meets purpose when we try to solve a real-world problem. The Wall of Wind Challenge reminds us that progress is measured not just in awards, but in ability to withstand pressure and refine our skills."*

Sponsorships:

The Wall of Wind Mitigation Challenge also received sponsor support for bus transportation, trophies, lunch, event video, and additional materials and supplies for each high school team. The sponsor support came from the FIU alumni serving as judges and their companies: DDA Forensics, CONNECT Engineering, Melchor Consultation Services, LLC, Quick Tie Products, Inc., TelaClaims, EAC Consulting, Inc., and The Biltmore School.

Kevin Guthrie, FDEM Executive Director

Jeanette Nuñez, FIU President discusses test.

Booker T. Washington HS reviews their test.

South Miami HS watching their wind test.

Christopher Columbus High School

Miami Carol City Senior High School

MAST Academy with their roof model.

Miramar High School with their roof model.

1st Place Team: TERRA Env. Res. Inst.

2nd Place Team: Florida Christian School

3rd Place Team: South Miami Senior HS

WOW Challenge Flat Roof Models

Eye of the Storm (Science, Mitigation & Preparedness) Event: May 31st, 2025

The Museum of Discovery & Science (MODS), located in Fort Lauderdale, FL, assisted the IHRC in planning, coordinating and facilitating this free admission public education event. A total of 6,105 visitors attended Eye of the Storm, showcasing special interactive activities and demonstrations teaching hurricane science, mitigation and preparedness. This included special learning activities for parents and children providing family fun throughout the day.

Event Flyer: 2025 Eye of the Storm – Hurricane (Science, Mitigation & Preparedness) Free Museum Event, Saturday, May 31st, 10am to 5pm | IHRC Website

Key Messages Communicated to the museum visitors:
1. Know Your Risk
2. Know Your Evacuation Zone
3. Complete Your Hurricane Plan
4. Address Any Special Needs
5. Assemble Your Supply Kit
6. Prepare Your Pets
7. Get an Insurance Check-Up
8. Protect Your Home
9. Help Your Neighbor

Special FDEM Guests:

- Kevin Guthrie, Director, Florida Division of Emergency Management
- Jillian Holzman, HLMP Program Manager, Bureau of Mitigation, Florida Division of Emergency Management

FDEM Press Conference at Eye of the Storm:
20250531 Florida Division of Emergency Management Hosts Press Conference at the Eye of the Storm Event, Highlighting Hurricane Preparedness | Florida Disaster

FDEM Press Conference at Eye of the Storm Video:
https://youtu.be/Q3QpZFB8B3c?si=S0A4z7OSBVDjYCPX

The Eye of the Storm received great coverage from the local South Florida media. This resulted in great positive visibility in the community for IHRC, FIU and FDEM's message of hurricane preparedness and mitigation.

- https://wsvn.com/news/local/broward/eye-of-the-storm-event-at-mods-in-fort-lauderdale-aims-to-ensure-floridians-are-hurricane-ready/#google_vignette
- https://www.news4jax.com/news/local/2025/05/31/fdem-hosts-press-conference-urges-floridians-to-make-final-preps-for-hurricane-season/
- https://app.criticalmention.com/app/#clip/view/022a8609-37e0-4245-acc2-5173459dc314?token=0e57270d-1c85-448e-b3ca-0788817604d7

The following local South Florida media representatives participated in person:

- Brandon Orr, Meteorologist, WPLG-TV Local 10 News

- Jenniffer Guerra, Meteorologist, Telemundo
- Anthony Duarte, Meteorologist, Weather Producer, Univision

Various distinguished hurricane experts participated:
- Neal Dorst, Hurricane Researcher, NOAA/AOML/HRD
- Stanley B. Goldenberg, Research Meteorologist, NOAA/AOML/HRD
- Robert Molleda, Warning Coordination Meteorologist, National Weather Service-Miami

Special interactive exhibits and demonstrations included:
- IHPA Live Air Cannon Demonstrations Showing Debris Impact of Shutters and Windows
- BECON-TV Hurricane Broadcast Center
- FIU NSF-NHERI Wind Tunnel Exhibit and Researcher Talks
- FIU Meteorology Student Demonstrations
- MODS Live Weather Science Demonstrations
- MODS Windy Weather Activities for Kids
- Special Showings of Built to Last: Buyer Beware, Resilience Documentary in IMAX Theater
- Weather Jeopardy Game
- Touch a Truck – Emergency Response and Recovery Vehicles

Special live interactive live theater presentations:
- Tsunami Tim Live Weather Education Theater Show
- NWS Owlie Skywarn Weather Theater Show

Weather Jeopardy Categories:
- Hurricanes 101
- Know Your Zone
- Don't Blow Away
- Whacky Weather

Partner Mascots:
- *NWS Owlie Sywarn* – NOAA-NWS
- *Sparky the Fire Dog* - City of Fort Lauderdale Emergency Management
- *Spot* - Museum of Discovery and Science
- *Roary* – Florida International University

Assessment Activities:
Participant Post Survey Questions for Event Attendees:
1. Did you attend the 2023 Eye of the Storm event?
2. To what extent did this event increase your knowledge about how wind engineering can mitigate hurricane damage?
3. To what extent are you interested in learning more about wind engineering?
4. To what extent will you be taking steps to mitigate hurricane damage to your property?
5. How many times have you attended the Eye of the Storm Event?

Positive Survey Results:

- 79.5% increased their knowledge about wind engineering and mitigating hurricane damage.
- 90.0% would like to learn more about wind engineering.
- 89.2% will be taking steps to mitigate hurricane damage.
- 87% were first time attendees of the event.

Attendee Feedback:

- *"The event was nothing short from amazing!! Thank you for having it I'm so glad I attended."*
- *"It was good, and I learned something at the outside impact test against windows, and shutters that I did not know. That test is a real eye opener to protecting windows against wind driven objects."*
- *"The event was great. Letting everyone have access to the whole museum was amazing."*
- *"It's always a good event with lots of information & resources for newbies."*

Message Board #1 During Event:
What did you learn today about protecting your home from hurricanes?

- *Put up shutters BEFORE the storm!*
- *Shutters are better than tape.*
- *I helped build a hurricane-safe model house.*

Message Board #2 During Event:
Would you like to study wind engineering in school?

- *Yes! I want to make buildings safer.*
- *I want to help with hurricane research.*
- *I want to protect people from hurricanes.*

Message Board #3 During Event:
What are your thoughts on today's events?

- *Wind tunnels rock!*
- *My favorite part was the air-cannon window explosions.*
- *Storms don't seem so scary now.*

This collaborative community education outreach project partnered the IHRC and MODS with:

- Florida Division of Emergency Management
- Broward County Emergency Management
- Broward County CERT
- Broward County Office of Resilience
- Broward County Property Appraiser
- City of Fort Lauderdale Emergency Management
- City of Fort Lauderdale Fire Rescue and Fire Explorers
- City of Fort Lauderdale Police Department
- Fort Lauderdale Fire and Safety Museum
- Miami-Dade County Emergency Management

- NOAA National Hurricane Center
- NOAA Atlantic Oceanographic and Meteorological Laboratory and Hurricane Research Division
- NOAA National Weather Service – Miami Office
- U.S. Coast Guard Air Station Miami
- BECON-TV (Broward Education Communications Network)
- International Hurricane Protection Association
- Florida Power & Light
- American Red Cross
- Salvation Army
- Humane Society of Broward County
- United Way of Broward County
- AARP
- AshBritt, Inc.
- TTI
- Cox Media Group Miami
- FIU Meteorology Club
- FIU Engineering on Wheels
- Nova Southeastern University
- Global Protection Products, LLC
- Hospital Manager for Veterinary Emergency Group
- DDA Forensics
- LAN Infotech
- Port Nexus Corporation
- Local Relief
- Resilience Action Fund

<u>Digital Marketing Campaign Summary:</u>

- Total Potential Impressions: 2,367,060+

Facebook Posts

- Potential Impressions: 1,286,695+

X Posts

- Potential Impressions: 238,000+

Instagram Posts

- Potential Impressions: 828,435+

LinkedIn Posts

- Potential Impressions: 13,925+

Influencer and Media Posts

- Potential Influencer and Media Impressions: 2,403,358+

<u>Eye of the Storm Video Series:</u>

The Eye of the Storm 12-episode "evergreen" video series was re-promoted in conjunction with the Eye of the Storm in-person event on June 1st. The video series continues to be promoted during the current hurricane season by MODS, IHRC, and many of the partners who attended on May 31st.

All the videos are listed on the MODS virtual Eye of the Storm webpage and YouTube page:
Virtual Eye of the Storm - Museum of Discovery & Science | IMAX AutoNation (mods.org)
Eye of the Storm 2020 - YouTube
All the videos are also listed on the following MyFloridaCFO web-page:
Plan Prepare Protect: Are You Disaster Ready? Resources (myfloridacfo.com)

The Eye of the Storm videos have resulted in a hugely successful digital marketing campaign and has expanded the reach and impact beyond South Florida to other states on the Gulf of Mexico and the U.S. eastern seaboard at risk of a hurricane landfall.

FDEM Press Conference

FDEM Director Kevin Guthrie and Team

Jillian Holzman, FDEM

Fort Lauderdale CERT Team

Fort Lauderdale Police Explorers

Broward County Emergency Management

FPL Hurricane Information Team

National Weather Service – Miami Office

Making a storm cloud!

6,105 visitors attended Eye of the Storm!

MODS EcoExplorers

Emergency Response and Recovery Vehicles

Sparky the Fire Safety Dog

Windy Weather Activities for Kids

FIU Roary and NWS Owlie Skywarn

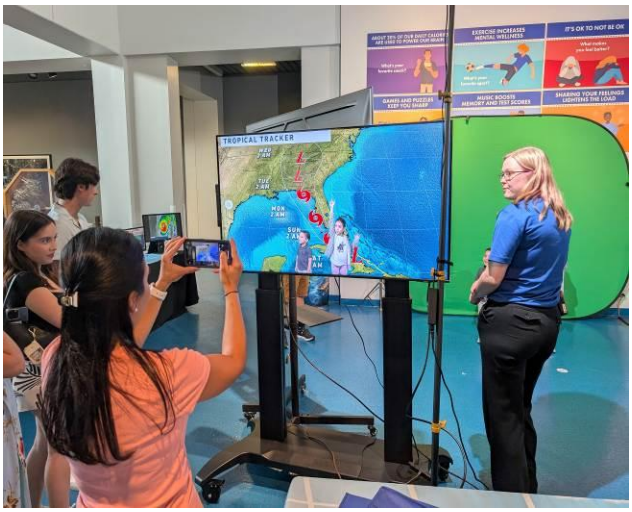

BECON-TV Hurricane Broadcast Center

WLRN – PBS Hurricane Team

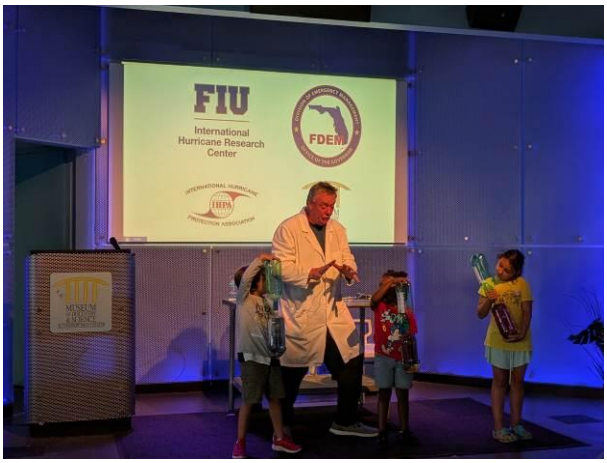

Live Weather Education Theater Show

FIU Wall of Wind students with wind tunnel.

FIU Meteorology Club